

UNIVERSITY OF BIRMINGHAM

Development of Ceramics for use in Proton Conducting Ceramic Cells

by

Abubakr Siddiq

A Thesis Submitted to the University of Birmingham for the Degree of

DOCTOR OF PHILOSOPHY

Centre for Hydrogen and Fuel Cell Research

School of Chemical Engineering

College of Engineering and Physical Sciences

University of Birmingham

December 2023

UNIVERSITY OF
BIRMINGHAM

University of Birmingham Research Archive

e-theses repository

This unpublished thesis/dissertation is copyright of the author and/or third parties. The intellectual property rights of the author or third parties in respect of this work are as defined by The Copyright Designs and Patents Act 1988 or as modified by any successor legislation.

Any use made of information contained in this thesis/dissertation must be in accordance with that legislation and must be properly acknowledged. Further distribution or reproduction in any format is prohibited without the permission of the copyright holder.

Abstract

Proton conducting ceramics (PCCs) can incorporate water molecules into oxide ion vacancies and then transfer protons (H+) via the oxide ions. Thus, enabling these PCCs to be implemented as part of a fuel cell or an electrolyser, that can operate within the intermediate temperature range of 500°C to 700°C. Within a proton conducting ceramic electrolyser (PCCE) dry H_2 is able to be produced, unlike in oxide conducting solid oxide electrolyser (OC-SOE).

The electrolyte materials used in these cases have been firmly established, however there is still an array of materials that can be explored as electrodes for proton conducting ceramic cells (PCCCs). Previously, compositions used for oxide conducting solid oxide cells (OC-SOCs) have been utilised in PCCCs. This thesis aims to develop electrode materials that can be utilised in PCCC within the intermediate temperature range.

The electrode material barium ferrite ($BaFeO_{3-\delta}$) was synthesised and doped with niobium (Nb) and bismuth (Bi); their lattice parameters were confirmed by X-ray diffraction (XRD). Nb-doped samples were chemically stable in humid N_2 atmospheres. Conversely, Bi doped samples only remained stable in humid N_2, in dry N_2 these samples formed two phases.

Ruddlesden-Popper; $La_{2-x}(Ba/Sr)_xNiO_{4+\delta}$, $La_{3-x}Pr_xNi_2O_{7-\delta}$ and $La_{4-x}Pr_xNi_3O_{10-\delta}$ were synthesised for electrode materials; again XRD confirmed their lattice parameters. Under humid N_2, $La_2NiO_{4+\delta}$, $La_{1.5}Sr_{0.5}NiO_{4+\delta}$, $La_3Ni_2O_{7-\delta}$, $La_2PrNi_2O_{7-\delta}$, $La_4Ni_3O_{10-\delta}$, $La_{3.75}Pr_{0.25}Ni_3O_{10-\delta}$ and $La_3PrNi_3O_{10-\delta}$ were shown to maintain their XRD pattern.

$BaCe_{0.6}Zr_{0.3}Y_{0.1}O_{3-\delta}$ electrolyte pellets were manufactured by pressing and sintering with 1 wt% nickel oxide (NiO) as a sintering aid. Symmetrical cells tests were performed in dry and humid air conditions. $La_2NiO_{4+\delta}$ and $La_{1.5}Sr_{0.5}NiO_{4+\delta}$ were shown to have a decrease in polarisation resistance when measurements were taken in humid air, below 600°C. All other samples showed an increase in polarisation resistance when measurements were taken in humid air, suggesting p-type conductivity.

Following symmetrical cell testing, fuel cell tests were performed on $La_2NiO_{4+\delta}$. A power density of 4.94 $mWcm^{-2}$ was achieved, the cell was then tested in electrolyser mode and a current density of -3.29 $mAcm^{-2}$ was achieved at 700°C. Electrolysis testing was then performed using $La_3Ni_2O_{7-\delta}$ as the air electrode -21.3 $mAcm^{-2}$ was achieved at 700°C, suggesting $La_3Ni_2O_{7-\delta}$ to be a better performing electrode then $La_2NiO_{4+\delta}$ for electrolysis.

Overall, it has been shown that $La_2NiO_{4+\delta}$ and $La_3Ni_2O_{7-\delta}$ can be utilised in PCCCs. Implying other Ruddlesden-Popper compositions may also be viable for use in a fuel cell or electrolyser, such as $La_{3-x}Pr_xNi_2O_{7-\delta}$ and $La_{4-x}Pr_xNi_3O_{10-\delta}$. With $La_4Ni_3O_{10-\delta}$ possibly being a better performing air electrode, for electrolysis, than $La_3Ni_2O_{7-\delta}$, as it has a greater number of corner linked NiO_6 octahedra.

Acknowledgements

To begin with a thanks to Professor Robert Steinberger-Wilckens for the opportunity and support over the last couple of years, despite him always finding me eating. Thanks to Professor Peter Slater for all his advice, ideas and guidance over the last few years, it was much appreciated.

Thanks goes to the various lab members on the fifth floor in Haworth (School of Chemistry), past and present. A special thanks goes to Abbey Jarvis, Lizzie Driscoll, Tzu-Yu Chen and Josh Deakin for all the help, training and guidance in all thing's lab based. Thanks also goes to Matt James, Laura Driscoll, Mark Stockham, Bo Dong for all the helpful advice. Luke Sweeney, Dan Butler, Jamie Price, Dom Gardner, Alex Sargent and Will Lima da Silva for making the lab entertaining.

From the Fuel Cell group a special thanks goes to Pushpa Patel and Sam Eardley for all their advice and entertaining chats in the office. Zeyu Jian and Chris Harrison for all things rig and solid oxide cell based. Bhargav Pandya, Naser Uddin and Ahmed Hammad for always willing to help. Finally, thanks to Abdul Hye for his delightful aspect on things. Also, from the School of Chemical Engineering thanks goes to Dan Baiocco, Andy Ingram, Eddie Pelan, Marcos Fernandez-Villamarin and Daniel Kgautlhe for the cheerful conversations.

A special thanks must go to Munir (Chow) Ahmed for always willing to help despite being in a different school and always having everything you would ever need in his Physics stores. Thanks to Ian Bodfish and Brian Thomas for help with delivers (there were a lot of them over the years) and just being a hilarious duo.

Thanks to Husnain Ali-Abid, Hasant Ali-Abid and Alvin Dawati for all the walks and random discussions, I'm sure they truly appreciated me getting them lost. Samir Shabir, who I often bumped into and chatted to on my late nights home from uni.

Finally, thanks to my parents for all the food these last few years. All the homemade chips, chicken wings, barbeques and tiramisu. My brother for his awful yet entertaining puns, also my sister who always gave the best disapproving looks.

‘Anything that can go wrong will go wrong.’

Murphy’s Law

Abbreviations

8YSZ	8 mol% yttrium stabilised zirconium
AFC	Alkaline fuel cells
ASR	Area specific resistance
BSE	Back-scattered electrons
BSED	Back-scattered electron detectors
CCS	Carbon capture and storage
CEM	Controlled evaporator mixer
CHP	Combined heat and power
DMFC	Direct methanol fuel cells
EDXS	Energy dispersive X-ray spectroscopy
EIS	Electrochemical impedance spectroscopy
GDC	Gadolinium-doped cerium
GDL	Gas diffusion layer
GHG	Greenhouse gases
HSE	Health and Safety Executives
LSCF	Lanthanum strontium ferrite doped with cobalt
LSM	Lanthanum manganite
MCFC	Molten carbonate fuel cell
MEA	Membrane electrode assembly

MIEC	Mixed ionic electronic conductor
MS	Mass spectrometry
OC-SOC	Oxide conducting solid oxide cell
OC-SOE	Oxide conducting solid oxide electrolyser
ORR	Oxygen reduction reaction
PAFC	Phosphoric acid fuel cells
PCC	Proton conducting ceramic
PCCC	Proton conducting ceramic cell
PCCE	Proton conducting ceramic electrolyser
PCCFC	Proton conducting ceramic fuel cell
PEMC	Polymer exchange membrane fuel cell
PEME	Polymer exchange membrane electrolyser
PEMFC	Polymer exchange membrane fuel cell
PGM	Platinum group metals
PROX	Preferential oxidation
PSA	Pressure swing absorption
R_{exp}	R-expected
R_O	Ohmic Resistance
R_p	R-pattern
R_{pol}	Polarisation resistance
$R_{pol\ dry}$	Polarisation resistance in dry air

$R_{pol\ humid}$	Polarisation resistance in humid air
R_{wp}	R-weighted pattern
ScSZ	Scandium-stabilised zirconium
SED	Secondary electron detector
SEM	Scanning electron microscope
SMR	Steam methane reforming
SOC	Solid oxide cell
SOE	Sold oxide electrolyser
SOFC	Solid oxide fuel cell
TGA	Thermogravimetric analysis
TPB	Triple phase boundary
UK	United Kingdom
USA	United States of America
VT-XRD	Variable temperature X-ray diffraction
WGS	Water gas shift
XRD	X-ray diffraction
YSZ	Yttria-stabilised zirconia

Table of Contents

Chapter 1: Introduction 1

1.1 Climate Change 1

1.2 Energy System 3

1.3 Hydrogen Economy 5

1.4 Fuel Cells 5

1.4.1 Fuel Cells 5

1.5 Hydrogen Production 8

1.5.1 Production from Fossil Fuels 9

1.5.2 Coal Gasification 10

1.5.3 Water Electrolysis 10

1.6 Thesis Outline 15

Chapter 2: Literature Review 17

2.1 Introduction 17

2.2 Electrolyte 18

2.2.1 Barium Cerates 18

2.2.2 Barium Zirconates 20

2.2.3 Barium Cerate-Zirconates 21

2.3 Cathode 25

2.3.1 Mixed Ionic Electronic Conductors 26

2.3.2 Triple Conductor 31

2.4 Anode 34
2.5 Fabrication 34
2.5.1 Synthesis 35
2.5.2 Sintering Aids 35
2.5.3 Electrolyte and Anode Manufacturing 40
2.6 Steam Electrolysis 46
2.7 Conclusion 48
2.8 Project Objectives 49
Chapter 3: Experimental Techniques 50
3.1 Material Synthesis 50
3.1.1 Solid State 50
3.1.2 Sol-Gel Synthesis 51
3.1.3 Pellet Pressing 53
3.2 Characterisation 53
3.2.1 X-ray Diffraction 53
3.2.2 Heating in Various Gases 58
3.2.3 Thermogravimetric Analysis 59
3.2.4 Scanning Electron Microscopy and Energy Dispersive X-Ray Spectroscopy Analysis . 60
3.2.5 4 Probe Direct Current (DC) Conductivity 61
3.3 Cell Manufacturing 62
3.3.1 Electrolyte Sintering 62
3.3.2 Symmetrical Cells 64

3.3.3 Full Cell Fabrication 65
3.4 Cell Testing 66
3.4.1 Symmetrical Cell Testing 66
3.4.2 Fuel Cell/Electrolyser Testing 76
Chapter 4: Bi and Nb Doping in $BaFeO_{3-\delta}$ 85
4.1 Introduction 85
4.2 Experimental 87
4.3 Bismuth Doped Systems $BaFe_{1-x}Bi_xO_{3-\delta}$ 88
4.3.1 Investigation into the Effect of Heating Under Humid Nitrogen 91
4.3.2 Investigation into the Effect of Heating under Dry Nitrogen 97
4.3.3 Conductivity data 101
4.4 Niobium Doped Systems $BaFe_{1-x}Nb_xO_{3-\delta}$ 102
4.4.1 Investigation into the Effect of Heating under Humid Nitrogen 104
4.4.2 Investigation into the Effect of Heating under Dry N_2 109
4.4.3 Conductivity Data 111
4.5 Conclusions 113
Chapter 5: Ba and Sr Doping in $La_2NiO_{4+\delta}$ 114
5.1 Introduction 114
5.2 Experimental 115
5.3 Ba Doped and Sr Doped $La_2NiO_{4+\delta}$; $La_{2-x}Ba_xNiO_{4+\delta}$ and $La_{2-x}Sr_xNiO_{4+\delta}$ 116
5.3.1 Investigation of Heating under Humid Nitrogen, Dry Nitrogen and Humid Oxygen 120
5.3.2 Analysis of Variable Temperature XRD on Samples treated in a Humid Atmosphere 132

5.3.3 Conductivity Data 139
5.3.4 Conclusion 140
Chapter 6: Pr Doping in $La_{n+1}Ni_nO_{3n+1}$; n=2 and 3 142
6.1 Introduction 142
6.2 Experimental 143
6.3 Pr doped $La_3Ni_2O_{7-\delta}$; $La_{3-x}Pr_xNi_2O_{7-\delta}$ 145
6.3.1 Investigation of Heating under Humid Nitrogen, Dry Nitrogen and Humid Oxygen ... 148
6.3.2 Analysis of Variable Temperature XRD on Samples treated in a Humid Atmosphere 161
6.3.3 Conductivity Data 170
6.3.4 Conclusion 172
6.4 Pr doped $La_4Ni_3O_{10-\delta}$; $La_{4-x}Pr_xNi_3O_{10-\delta}$ 173
6.4.1 Investigation of Heating under Humid Nitrogen, Dry Nitrogen and Humid Oxygen ... 177
6.4.2 Analysis of Variable Temperature XRD on Samples treated in a Humid Atmosphere 187
6.4.3 Conductivity Data 197
6.4.4 Conclusions 198
6.5 Summary 199
Chapter 7: Proton Conducting Ceramic Cell Fabrication and Testing 201
7.1 Introduction 201
7.2 Experimental 202
7.3 Investigation of the Chemical Stability of Various Electrolyte Materials in Humid Nitrogen 204
7.4 Investigation into Developing Dense Electrolyte Pellets through the Addition of Sintering Aids 206

7.4.1 Exploration of LiF as a Sintering Aid 206
7.4.2 Exploration of ZnO as a Sintering Aid 208
7.4.3 Exploration of CuO as a Sintering Aid 213
7.4.4 Exploration of NiO as a Sintering Aid 214
7.5 Investigation into the Effect of Dry Air and Humid Air on Symmetrical Cells 216
7.6 Cell Fabrication and Testing 221
7.6.1 Attempt at Co-Pressing of Anode and Electrolyte 221
7.6.2 Anode Supported Cell 223
7.6.3 Electrolyte Supported Cell 224
7.7 Electrolysis Testing 240
7.8 Conclusions 242
Chapter 8: Conclusion and Future Work 243
8.1 Summary and Conclusions 243
8.1.1 Chapter 4 243
8.1.2 Chapter 5 244
8.1.3 Chapter 6 244
8.1.4 Chapter 7 246
8.2 Future Work 247
Chapter 9: References 248
Chapter 10: Appendix 273
10.1 Chapter 4 273
10.2 Chapter 5 275

10.3 Chapter 6 276

10.4 Chapter 7 280

List of Figures

Figure 1.1: Global average annual temperature relative to the period between 1961 – 1990 (red) plotted alongside the global average annual CO_2 released since 1979 (dark red). Data adapted from [3, 4]. 2

Figure 1.2: Global energy supply by source between 1990 and 2019 data taken from IEA [9]. Oil (gold), coal (black), natural gas (brown), biofuels and waste (dark green), nuclear (green), hydro (blue) and wind and solar (yellow). 3

Figure 2.1: Figure showing various cathodes types a) pure electronic conductor b) mixed ionic electronic conductor, and c) triple conductor..... 26

Figure 2.2: Figure showing lanthanum nickelate Ruddlesden-Popper structure. Showing $La_2NiO_{4+\delta}$ on the left, $La_3Ni_2O_{7-\delta}$ in the middle and $La_4Ni_3O_{10-\delta}$ on the right. 33

Figure 2.3: Impact of the various sintering aids employed by Babilo *et al.* [146]. Reproduced from [146] with permission from John Wiley and Sons..... 36

Figure 2.4: Field emission electron probe microanalysis showing the cross section of the cells sintered at a) 1300°C, b)1320°C c) 1350°C and d) 1400°C. Dotted lines indicate the electrolyte surface. The images show low quantities of nickel (blue) are present throughout the pellet. Reproduced from [158] with permission from Elsevier. 40

Figure 2.5: Reproduced from [163] with permission from American Ceramic Society. a) shows the anode supported cells, b)shows the cross-sectional images of the PCCFC after testing, c) shows cross-section image of the cell but focused on the various layers, where the cathode, the porous and dense electrolytes can be seen, d) shows all four layers and e) shows the interface between the anode and dense electrolyte. 45

Figure 3.1: Relationship between crystal planes and the angles of incident/diffraction x-rays. 56

Figure 3.2: Setup used for heating samples in humid N_2, dry N_2 and humid O_2..... 59

Figure 3.3: Pellet setup for 4-probe and the rig it is placed in. On the left is enlarged image of the pellet with the 4 electrodes connected. The pellet is then connected to a Keithley 6220 Precision Current

Source and Keithley 2182A Nanovoltmeter and placed in a vertical furnace. A LabVIEW program is used to collect experimental data. 62

Figure 3.4: Program used for the sintering of $BaCe_{0.6}Zr_{0.3}Y_{0.1}O_{3-\delta}$ pellets. 64

Figure 3.5: Program used for the sintering of cathodes for $BaCe_{0.6}Zr_{0.3}Y_{0.1}O_{3-\delta}$ symmetrical cells..... 65

Figure 3.6: Diagrams of rig for symmetrical cell testing. Left, is a diagram when the rig is not in use notice the separation of the two tubes. Right, is a diagram when the rig is in use, notice the two tubes have come together. 67

Figure 3.7: Nyquist plots for a) a single resistor, b) a single capacitor, c) a single inductor, d) a CPE and e) a resistor and capacitor in parallel. 74

Figure 3.8: Example of a Nyquist plot and the equivalent circuit associated with it. 76

Figure 3.9: Diagrams of rig for fuel cell and electrolyser testing. Left, is a diagram when the rig is not in use notice the separation of the two tubes. Right, is a diagram when the rig is in use, notice the two tubes have come together. 77

Figure 3.10: Voltage (square) and power density (circle) verses current density of commercial OC-SOC, measurements taken at 700°C. OC-SOC consisted of LSCF and GDC cathode, 8YSZ electrolyte and 50:50 wt% of NiO:8YSZ anode. 79

Figure 3.11: The expected outcome with varying vales of enthalpy, entropy and Gibbs free energy. . 80

Figure 3.12: Graph showing the relationship between Gibbs free energy/enthalpy and temperature [178, 179] 82

Figure 3.13: Polarisation curve for a PEMCs. The three distinct regions can be clearly seen for PEMCs, unlike with an SOC where the activation loss is negligible due to the high operating temperature. 84

Figure 4.1: Example of a cubic *Pm*-3*m* space group perovskite, with the general formula ABO_3. Where the grey orbs represent the A-site, the red orbs represent the B-site and the blue orbs represent oxygen atoms. 86

Figure 4.2: XRD of $BaFe_{1-x}Bi_xO_{3-\delta}$ where x = 0.075, 0.1 and 0.15. 89

Figure 4.3: Example of observed (blue cross), calculated (green) and difference (cyan) profiles for Rietveld refinement performed (cubic *Pm*-3*m* space group, R_w=4.21%). 90

Figure 4.4: Variation of cell parameter of $BaFe_{1-x}Bi_xO_{3-\delta}$ with Bi content. Samples were refined against a cubic *Pm*-3*m* space group. Circle indicates *a* parameter. Triangle indicates the volume of the unit cell. 91

Figure 4.5: XRD of $BaFe_{1-x}Bi_xO_{3-\delta}$ where x = 0.075, 0.1 and 0.1, after samples were exposed to humid N_2..... 92

Figure 4.6: XRD of $BaFe_{0.925}Bi_{0.075}O_{3-\delta}$ before (bottom) and after humid N_2 (top). 92

Figure 4.7: Lattice parameter (cubic *Pm-3m*) of $BaFe_{1-x}Bi_xO_{3-\delta}$ doped samples. Circles indicate the *a* parameters and triangles indicate the volume of the cell. 93

Figure 4.8: Lattice parameter (cubic *Pm*-3*m*) of $BaFe_{1-x}Bi_xO_{3-\delta}$ doped samples. Circles indicate the a parameters and triangles indicate the volume of the cell. Black indicated original samples, blue indicated sample heated in humid N_2..... 94

Figure 4.9: TGA and MS data for humidified $BaFe_{0.925}Bi_{0.075}O_{3-\delta}$ when heated to 1000°C showing mass loss (black) and H_2O loss (blue)..... 95

Figure 4.10: TGA and MS data for humidified $BaFe_{0.9}Bi_{0.1}O_{3-\delta}$ of sample when heated to 1000°C showing mass loss (black) and H_2O loss (blue). 96

Figure 4.11: TGA and MS data for humidified $BaFe_{0.85}Bi_{0.15}O_{3-\delta}$ of sample when heated to 1000°C showing mass loss (black) and H_2O loss (blue). 96

Figure 4.12: XRD pattern of $BaFe_{1-x}Bi_xO_{3-\delta}$ where x = 0.075, 0.1 and 0.15 after heating in dry N_2. Left shows the shoulders on the 110 reflection. 97

Figure 4.13: Example of observed (blue cross), calculated (green) and difference (cyan) profiles for Rietveld refinement performed (two cubic *Pm*-3*m* space group, R_w=4.67%). 98

Figure 4.14: Lattice parameters for $BaFe_{1-x}Bi_xO_{3-\delta}$ doped samples. Samples were refined against a cubic *Pm*-3*m* space group. Blue shows the sample heated in humid N_2. Dark green shows the sample heated in dry N_2 and is the larger cell. Green shows the sample heated in dry N_2 and is the smaller cell. 100

Figure 4.15: Volume for $BaFe_{1-x}Bi_xO_{3-\delta}$ doped samples. Samples were refined against a cubic *Pm*-3*m* space group. Blue shows the sample heated in humid N_2. Dark green shows the sample heated in dry N_2 and is the larger cell. Green shows the sample heated in dry N_2 and is the smaller cell..... 101

Figure 4.16: Conductivity results of $BaFe_{1-x}Bi_xO_{3-\delta}$ samples dependent of temperature. Red fill indicates heating and cyan fill indicates cooling; data shown between 250°C to 700°C. Measurements taken in air. 102

Figure 4.17: XRD of $BaFe_{1-x}Nb_xO_{3-\delta}$ where x = 0.4, 0.45 and 0.5. 103

Figure 4.18: Lattice parameter of $BaFe_{1-x}Nb_xO_{3-\delta}$ doped samples, (*Pm*-3*m* space group). Circles indicate the a parameters and triangles indicate the volume of the cell. 104

Figure 4.19: XRD of $BaFe_{1-x}Nb_xO_{3-\delta}$ where x = 0.4, 0.45 and 0.5, after samples were exposed to humid N_2 105

Figure 4.20: Lattice parameter of $BaFe_{1-x}Nb_xO_{3-\delta}$ doped samples (cubic *Pm*-3*m* space group). Black indicates the parent sample, blue indicates the sample heated in humid N_2. 106

Figure 4.21: Volume of $BaFe_{1-x}Nb_xO_{3-\delta}$ doped samples (cubic *Pm*-3*m* space group). Black indicates the parent sample, blue indicates the sample heated in humid N_2. 106

Figure 4.22: TGA and MS of humidified $BaFe_{0.6}Nb_{0.4}O_{3-\delta}$ when heated to 1000°C. Mass loss (black) and H_2O loss (blue). 107

Figure 4.23: TGA and MS of humidified $BaFe_{0.55}Nb_{0.45}O_{3-\delta}$ when heated to 1000°C. Mass loss (black) and H_2O loss (blue). 108

Figure 4.24: TGA and MS of humidified $BaFe_{0.5}Nb_{0.5}O_{3-\delta}$ when heated to 1000°C. Mass loss (black) and H_2O loss (blue). 108

Figure 4.25: XRD of $BaFe_{1-x}Nb_xO_{3-\delta}$ where x = 0.4, 0.45 and 0.5, after samples were exposed to dry N_2. 109

Figure 4.26: Lattice parameters for $BaFe_{1-x}Nb_xO_{3-\delta}$ doped samples (cubic *Pm*-3*m* space group). Blue shows the sample heated in humid N_2. Dark green shows the sample heated in dry N_2 and is the larger cell. Green shows the sample heated in dry N_2 and is the smaller cell. 110

Figure 4.27: Volume of $BaFe_{1-x}Nb_xO_{3-\delta}$ doped samples (*Pm*-3*m* space group). Blue shows the sample heated in humid N_2. Dark green shows the sample heated in dry N_2 and is the larger cell. Green shows the sample heated in dry N_2 and is the smaller cell. 111

Figure 4.28: Conductivity results of $BaFe_{1-x}Nb_xO_{3-\delta}$ samples. Red fill indicates heating and cyan fill indicates cooling; data shown between 300°C to 700°C. Measurements taken in air. 112

Figure 5.1: XRD pattens of $La_{2-x}Ba_xNiO_{4+\delta}$ and $La_{2-x}Sr_xNiO_{4+\delta}$ where x =0, 0.25 and 0.5. In ascending order $La_2NiO_{4+\delta}$ (black), $La_{1.75}Ba_{0.25}NiO_{4+\delta}$ (red), $La_{1.5}Ba_{0.5}NiO_{4+\delta}$ (green), $La_{1.75}Sr_{0.25}NiO_{4+\delta}$ (blue) and $La_{1.5}Sr_{0.5}NiO_{4+\delta}$ (pink). 117

Figure 5.2: Example of observed (blue cross), calculated (green) and difference (cyan) profiles for Rietveld refinement performed on $La_2NiO_{4+\delta}$ (orthorhombic *Fmmm* space group, R_{wp}=5.83%). 117

Figure 5.3: Variation of *a* and *b* lattice parameters for $La_{2-x}Ba_xNiO_{4+\delta}$ and $La_{2-x}Sr_xNiO_{4+\delta}$ with Ba/Sr content (x). Black circles indicates *a* parameter for Ba doped samples. Black stars indicates *b* parameter for Ba doped samples. Empty circle indicates *a* parameter for Sr doped samples. Empty star indicates *b* parameter for Sr doped samples..... 119

Figure 5.4: Variation of *c* lattice parameter and cell volume for $La_{2-x}Ba_xNiO_{4+\delta}$ and $La_{2-x}Sr_xNiO_{4+\delta}$ with Ba/Sr content (x). Black squares indicate *c* parameter for Ba doped samples. Black triangles indicates volume for Ba doped samples. Empty squares indicate *c* parameter for Sr doped samples. Empty triangles indicate volume for Sr doped samples..... 120

Figure 5.5: XRD patterns of $La_2NiO_{4+\delta}$ annealed in various conditions. In ascending order humid N_2 (black), dry N_2 (red) and humid O_2 (green)..... 121

Figure 5.6: TGA and MS, up to a temperature of 1000°C, performed on $La_2NiO_{4+\delta}$ heated in humid N_2. Mass loss (black), H_2O loss (blue) and O_2 loss (red). 122

Figure 5.7: TGA and MS, up to a temperature of 1000°C, performed on $La_2NiO_{4+\delta}$ heated in humid N_2. Mass loss (black) and CO_2 loss (dark red). 123

Figure 5.8: TGA and MS of La_2O_3 annealed in air, data profile for the temperature range between 550°C and 1000°C. Mass loss (black) and CO_2 loss (dark red). 124

Figure 5.9: XRD pattern of $La_{2-x}Ba_xNiO_{4+\delta}$ where x=0.25 and 0.5, heated in humid N_2. In ascending order $La_{1.75}Ba_{0.25}NiO_{4+\delta}$ (black) and $La_{1.5}Ba_{0.5}NiO_{4+\delta}$ (red). Impurities are shown by circles. 125

Figure 5.10: XRD patterns of $La_{1.75}Sr_{0.25}NiO_{4+\delta}$ annealed in various conditions. In ascending order humid N_2 (black), dry N_2 (red) and humid O_2 (green). 126

Figure 5.11: TGA and MS, up to a temperature of 1000°C, performed on $La_{1.75}Sr_{0.25}NiO_{4+\delta}$ heated in humid N_2. Mass loss (black), H_2O loss (blue) and O_2 loss (red). 128

Figure 5.12: TGA and MS, up to a temperature of 1000°C, performed on $La_{1.75}Sr_{0.25}NiO_{4+\delta}$ heated in humid N_2. Mass loss (black) and CO_2 loss (dark red). 128

Figure 5.13: XRD patterns of $La_{1.5}Sr_{0.5}NiO_{4+\delta}$ annealed under various conditions. In ascending order humid N_2 (black), dry N_2 (red) and humid O_2 (green). 129

Figure 5.14: TGA and MS, up to a temperature of 1000°C, performed on $La_{1.5}Sr_{0.5}NiO_{4+\delta}$ heated in humid N_2. Mass loss (black), H_2O loss (blue) and O_2 loss (red). 131

Figure 5.15: TGA and MS, up to a temperature of 1000°C, performed on $La_{1.5}Sr_{0.5}NiO_{4+\delta}$ heated in humid N_2. Mass loss (black) and CO_2 loss (dark red). 131

Figure 5.16: VT-XRD pattern of humidified $La_2NiO_{4+\delta}$ showing no change in XRD patterns during heating. In ascending order the temperatures 125°C (black), 325°C (red) and 725°C (green) are represented. 132

Figure 5.17: VT-XRD data showing the variation in *a* (circle) and *b* (star) parameter of humidified $La_2NiO_{4+\delta}$ versus temperature. The black line indicated the change in phase..... 133

Figure 5.18: VT-XRD data showing the variation in *c* parameter of humidified $La_2NiO_{4+\delta}$ verses temperatures. Slight deviations in results are highlighted in blue. The black line showing the change in phase..... 133

Figure 5.19: VT-XRD data showing the variation in cell volume of humidified $La_2NiO_{4+\delta}$ versus temperatures. The black line showing the change in phase. 134

Figure 5.20: VT-XRD data showing the variation in lattice parameters of humidified $La_{1.75}Sr_{0.25}NiO_{4+\delta}$ versus temperature. 135

Figure 5.21: VT-XRD pattern of humidified $La_{1.5}Sr_{0.5}NiO_{4+\delta}$ showing no change in XRD patterns during heating. In ascending order the following temperatures 125°C on heating (black), 425°C on heating (red) and 775°C on heating (green), 425°C on cooling (blue) and 125°C on cooling (pink) are shown. Visible

phase change in XRD patterns are not observed during heating or cooling. Specifically, between 31° and 34° shoulders are still present on peaks. 136

Figure 5.22: VT-XRD data showing the variation in a parameter of humidified $La_{1.5}Sr_{0.5}NiO_{4+\delta}$ versus temperature. Deviations from the linear trend are highlighted in blue. 137

Figure 5.23: VT-XRD data showing the variation in *b* parameter of humidified $La_{1.5}Sr_{0.5}NiO_{4+\delta}$ versus temperature. Deviations from the linear trend are highlighted in blue. 137

Figure 5.24: VT-XRD data showing the variation in *c* parameter of humidified $La_{1.5}Sr_{0.5}NiO_{4+\delta}$ versus temperature. Deviations from the linear trend are highlighted in blue. 138

Figure 5.25: VT-XRD data showing the variation in cell volume parameter of humidified $La_{1.5}Sr_{0.5}NiO_{4+\delta}$ verses temperature. Deviations from the linear trend are highlighted in blue. 138

Figure 5.26: Conductivity data for $La_{2-x}Sr_xNiO_{4+\delta}$ where x=0 (circle) , 0.25 (triangle) and 0.5 (square). Red fill indicates heating and cyan fill indicates cooling; data shown between 200°C to 750°C. Measurements taken in air. 139

Figure 6.1: XRD patterns of $La_{3-x}Pr_xNi_2O_{7-\delta}$ samples where x =0, 0.5 and 0.75 and 1. In ascending order $La_3Ni_2O_{7-\delta}$ (black), $La_{2.75}Pr_{0.25}Ni_2O_{7-\delta}$ (red), $La_{2.5}Pr_{0.5}Ni_2O_{7-\delta}$ (green) and $La_2PrNi_2O_{7-\delta}$ (blue). 145

Figure 6.2: Example of observed, calculated and difference profiles for Rietveld refinement performed on $La_3Ni_2O_{7-\delta}$ (orthorhombic *Fmmm* space group, R_{wp}=7.44%). 146

Figure 6.3: Variation of *a* and *b* lattice parameters for $La_{3-x}Pr_xNi_2O_{7-\delta}$ (x=0, 0.25, 0.5 and 1). Black circles indicate a parameter. Black stars indicate *b* parameter. 147

Figure 6.4: Variation of *c* lattice parameter and volume for $La_{3-x}Pr_xNi_2O_{7-\delta}$ (x=0, 0.25, 0.5 and 1). Black squares indicate *c* parameter. Black triangles indicate volume. 148

Figure 6.5: XRD patterns of $La_3Ni_2O_{7-\delta}$ heated in various conditions. In ascending order humid N_2 (black), dry N_2 (red) and humid O_2 (green). 149

Figure 6.6: TGA and MS, up to a temperature of 1000°C, performed on $La_3Ni_2O_{7-\delta}$ heated in humid N_2. Mass loss (black), H_2O loss (blue) and O_2 loss (red). 150

Figure 6.7: TGA and MS, up to a temperature of 1000°C, performed on $La_3Ni_2O_{7-\delta}$ heated in humid N_2. Mass loss (black) and CO_2 loss (dark red). 151

Figure 6.8: XRD patterns of $La_{2.75}Pr_{0.25}Ni_2O_{7-\delta}$ heated in various conditions. In ascending order humid N_2 (black), dry N_2 (red) and humid O_2 (green). (0 0 6), (0 0 10) and (0 0 12) reflections shown..... 152

Figure 6.9: Example of observed (blue cross), calculated (green) and difference (cyan) profiles for Rietveld refinement performed on $La_{2.75}Pr_{0.25}Ni_2O_{7-\delta}$ (orthorhombic *Fmmm* space group, R_{wp}=8.11%). 153

Figure 6.10: TGA and MS, up to a temperature of 1000°C, performed on $La_{2.75}Pr_{0.25}Ni_2O_{7-\delta}$ heated in humid N_2. Mass loss (black), H_2O loss (blue) and O_2 loss (red). 154

Figure 6.11: TGA and MS, up to a temperature of 1000°C, performed on $La_{2.75}Pr_{0.25}Ni_2O_{7-\delta}$ heated in humid N_2. Mass loss (black) and CO_2 loss (dark red). 155

Figure 6.12: XRD patterns of $La_{2.5}Pr_{0.5}Ni_2O_{7-\delta}$ heated in various conditions. In ascending order humid N_2 (black), dry N_2 (red) and humid O_2 (green). (0 0 6), (0 0 10) and (0 0 12) reflections are shown. 156

Figure 6.13: TGA and MS, up to a temperature of 1000°C, performed on $La_{2.5}Pr_{0.5}Ni_2O_{7-\delta}$ heated in humid. Mass loss (black), H_2O loss (blue) and O_2 loss (red). 157

Figure 6.14: TGA and MS, up to a temperature of 1000°C, performed on $La_{2.5}Pr_{0.5}Ni_2O_{7-\delta}$ heated in humid N_2. Mass loss (black) and CO_2 loss (dark red). 157

Figure 6.15: XRD patterns of $La_2PrNi_2O_{7-\delta}$ heated in various conditions. In ascending order humid N_2 (black), dry N_2 (red) and humid O_2 (green). 159

Figure 6.16: TGA and MS, up to a temperature of 1000°C, performed on $La_2PrNi_2O_{7-\delta}$ heated in humid N_2. Mass loss (black), H_2O loss (blue) and O_2 loss (red). 160

Figure 6.17: TGA and MS, up to a temperature of 1000°C, performed on $La_2PrNi_2O_{7-\delta}$ heated in humid N_2. Mass loss (black) and CO_2 loss (dark red). 160

Figure 6.18: VT-XRD pattern of humid $La_3Ni_2O_{7-\delta}$ showing phase change, from orthorhombic to tetragonal, during heating. Specifically, peaks between 32.5° and 33.5° form a singular peak. In ascending order temperatures are 125°C on heating (black), 225°C on heating (red), 375°C on heating (green) and 725°C on heating (blue). 162

Figure 6.19: VT-XRD data showing the variation in a (circle) and b (star) parameter of humidifed $La_3Ni_2O_{7-\delta}$ versus temperature. At 325°C, the orthorhombic phase turns tetragonal. A black line is drawn to show this change in symmetry. 163
Figure 6.20: VT-XRD data showing the variation in c parameter (diamond) of humidified $La_3Ni_2O_{7-\delta}$ verses temperature. At 325°C, the orthorhombic phase turns tetragonal. A black line is drawn to show this change in symmetry..... 163
Figure 6.21: VT-XRD data showing the variation in volume (triangle) of humidifed $La_3Ni_2O_{7-\delta}$ versus temperature. At 325°C, the orthorhombic phase turns tetragonal. A black line is drawn to show this change in symmetry. 164
Figure 6.22: VT-XRD pattern of humid $La_{2.5}Pr_{0.5}Ni_2O_{7-\delta}$ showing phase change, from orthorhombic to tetragonal, during heating. Specifically, peaks between 32.5° and 33.5° form a singular peak. During cooling the tetragonal phase reverts to an orthorhombic structure. In ascending order, the temperatures are 125°C on heating (black), 625°C on heating (red), 725°C on heating (green), 625°C on cooling (blue) 575°C on cooling (pink)..... 165
Figure 6.23: VT-XRD data showing the variation in *a* (circle) and *b* (star) parameter of humidified $La_{2.5}Pr_{0.5}Ni_2O_{7-\delta}$ versus temperature. Slight deviations in linearity are highlighted in blue..... 166
Figure 6.24: VT-XRD data showing the variantion in *c* parameter of humidified $La_{2.5}Pr_{0.5}Ni_2O_{7-\delta}$ against temperature. Deviations in results are highlighted. Deviations in linearity are highlighted in blue. .. 166
Figure 6.25: VT-XRD data showing the variation in volume of humidified $La_{2.5}Pr_{0.5}Ni_2O_{7-\delta}$ versus temperature..... 167
Figure 6.26: VT-XRD pattern of humid $La_2PrNi_2O_{7-\delta}$. Sample is orthorhombic at lower temperatures. During heating the distance between 32.5° and 33.5° peaks reduced. During cooling the previously mentioned peaks separated. In ascending order the temperatures are 125°C on heating (black), 425°C on heating (red), 775°C on heating (green), 425°C on cooling (blue) 125°C on cooling (pink). 168
Figure 6.27: VT-XRD data showing the variation in *a* (circle) and *b* (star) parameters of humidified $La_2PrNi_2O_{7-\delta}$ versus temperature. Red fill indicates heating and cyan fill indicates cooling. 169

Figure 6.28: VT-XRD data showing the variantion in *c* parameter of humidified $La_2PrNi_2O_{7-\delta}$ versus temperature. Deviations in linearity of results are highlighted in blue. 169

Figure 6.29: VT-XRD data showing the variation in volume of humidified $La_2PrNi_2O_{7-\delta}$ versus temperature..... 170

Figure 6.30: Conductivity data for $La_{3-x}Pr_xNi_2O_{7-\delta}$ where x=0 (circle), 0.25 (triangle) and 0.5 (square) and 1 (diamond). Red fill indicates heating and cyan fill indicates cooling, data shown between 200°C and 750°C..... 171

Figure 6.31: XRD pattens of $La_{4-x}Pr_xNi_3O_{10-\delta}$ samples where x =0, 0.5 and 0.75 and 1. In ascending order $La_4Ni_3O_{10-\delta}$ (black), $La_{3.75}Pr_{0.25}Ni_3O_{10-\delta}$ (red), $La_{3.5}Pr_{0.5}Ni_3O_{10-\delta}$ (green) and $La_3PrNi_3O_{10-\delta}$ (blue). 174

Figure 6.32: Example of observed (blue cross), calculated (green) and difference (cyan) profiles for Rietveld refinement performed on $La_4Ni_3O_{10-\delta}$ (orthorhombic *Fmmm* space group, R_{wp}=10.00%). . 175

Figure 6.33: Variation of *a* (circle) and *b* (star) lattice parameters for $La_{4-x}Pr_xNi_3O_{10-\delta}$ (x=0, 0.25, 0.5 and 1). Black circles indicate a parameter. Black stars indicate *b* parameter. The highlighted region shows an initial decrease in the *b* parameter. 176

Figure 6.34: Variation of *c* lattice parameter and volume for $La_{4-x}Pr_xNi_3O_{10-\delta}$ (x=0, 0.25, 0.5 and 1). Black squares indicate *c* parameter. Black triangles indicate volume..... 177

Figure 6.35: XRD patterns of $La_4Ni_3O_{10-\delta}$ heated in various conditions. In ascending order humid N_2 (black), dry N_2 (red) and humid O_2 (green)..... 178

Figure 6.36: TGA and MS, up to a temperature of 1000°C, performed on $La_4Ni_3O_{10-\delta}$ heated in humid N_2. Mass loss (black), H_2O loss (blue) and O_2 loss (red). 179

Figure 6.37: TGA and MS, up to a temperature of 1000°C, performed on $La_4Ni_3O_{10-\delta}$ heated in humid N_2. Mass loss (black) and CO_2 loss (dark red). 180

Figure 6.38: XRD patterns of $La_{3.75}Pr_{0.25}Ni_3O_{10-\delta}$ heated in various conditions. In ascending order humid N_2 (black), dry N_2 (red) and humid O_2 (green). 181

Figure 6.39: TGA and MS, up to a temperature of 1000°C, performed on $La_{3.75}Pr_{0.25}Ni_3O_{10-\delta}$ heated in humid N_2. Mass loss (black), H_2O loss (blue) and O_2 loss (red). 182

Figure 6.40: TGA and MS, up to a temperature of 1000°C, performed on $La_{3.75}Pr_{0.25}Ni_3O_{10-\delta}$ heated in humid N_2. Mass loss (black) and CO_2 loss (dark red). 183

Figure 6.41: XRD patterns of $La_{3.5}Pr_{0.5}Ni_3O_{10-\delta}$ heated in various conditions. In ascending order humid N_2 (black), dry N_2 (red) and humid O_2 (green). $La_4Ni_3O_{10-\delta}$ phase shown by black circle, $Pr_2NiO_{4-\delta}$ shown by black triangle. 184

Figure 6.42: XRD patterns of $La_3PrNi_3O_{10-\delta}$ heated in various conditions. In ascending order humid N_2 (black), dry N_2 (red) and humid O_2 (green). 185

Figure 6.43: TGA and MS, up to a temperature of 1000°C, performed on $La_3PrNi_3O_{10-\delta}$ heated in humid N_2. Mass loss (black) and H_2O loss (blue). 186

Figure 6.44: TGA and MS, up to a temperature of 1000°C, performed on $La_3PrNi_3O_{10-\delta}$ heated in humid. Mass loss (black) and O_2 loss (red). 186

Figure 6.45: TGA and MS, up to a temperature of 1000°C, performed on $La_3PrNi_3O_{10-\delta}$ heated in humid N_2. Mass loss (black) and CO_2 loss (dark red). 187

Figure 6.46: VT-XRD pattern of humid $La_4Ni_3O_{10-\delta}$ showing phase change, from orthorhombic to tetragonal, during heating. Specifically, peaks between 32.5° and 33.5° form a singular peak. In ascending order the temperatures are 125°C on heating (black), 325°C on heating (red), 425°C on heating (green) and 725°C on heating (blue). 188

Figure 6.47: VT-XRD data showing the variation in *a* (circle) and *b* (star) parameter of humidifed $La_4Ni_3O_{10-\delta}$ versus temperature. At 425°C, the orthorhombic phase turns tetragonal. A black line is drawn to show this split in symmetry. 189

Figure 6.48: VT-XRD data showing the variation in *c* parameter of humidifed $La_4Ni_3O_{10-\delta}$ versus temperatures. At 425°C, the orthorhombic phase turns tetragonal. A black line is drawn to show this change in symmetry. 189

Figure 6.49: VT-XRD data showing the variation in volume (triangle) of humidifed $La_4Ni_3O_{10-\delta}$ versus temperatures. At 425°C, the orthorhombic phase turns tetragonal. A black line is drawn to show this change in symmetry. 190

Figure 6.50: VT-XRD pattern of humid $La_{3.75}Pr_{0.25}Ni_3O_{10-\delta}$ showing phase change, from orthorhombic to tetragonal, during heating. Specifically, peaks between 32.5° and 33.5° form a singular peak. During cooling the tetragonal phase reverted to an orthorhombic structure. In ascending order the temperatures are 125°C on heating (black), 325°C on heating (red), 475°C on heating (green), 725°C on heating (blue), 425°C on cooling (pink) and 275°C on cooling (cyan). 191

Figure 6.51: VT-XRD data showing the variation in *a* (circle) and *b* (star) parameter of humidified $La_{3.75}Pr_{0.25}Ni_3O_{10-\delta}$ versus temperature..... 192

Figure 6.52: VT-XRD data showing the variantion in *c* parameter of humidified $La_{3.75}Pr_{0.25}Ni_3O_{10-\delta}$ against temperature. Deviations in the linearity of results are highlighted in blue. 192

Figure 6.53: VT-XRD data showing the variation in volume of humidified $La_{3.75}Pr_{0.25}Ni_3O_{10-\delta}$ versus temperature..... 193

Figure 6.54: VT-XRD pattern of humid $La_3PrNi_3O_{10-\delta}$. The sample is orthorhombic at lower temperatures. During heating the distance between 32.5° and 33.5° peaks reduced. During cooling the previously mentioned peaks separated. In ascending order the temperatures are 125°C on heating (black), 425°C on heating (red), 775°C on heating (green), 425°C on cooling (blue) 125°C on cooling (pink). 194

Figure 6.55: VT-XRD data showing the variation in *a* (circle) and *b* (star) parameter of humidified $La_3PrNi_3O_{10-\delta}$ versus temperature. 195

Figure 6.56: VT-XRD data showing the variantion in *b* parameter of humidified $La_3PrNi_3O_{10-\delta}$ against temperature. Slight deviations in linearity of results are highlighted in blue. 195

Figure 6.57: VT-XRD data showing the variation in *c* parameter of humidified $La_3PrNi_3O_{10-\delta}$ versus temperature..... 196

Figure 6.58: VT-XRD showing the variation in volume parameter of humidified $La_3PrNi_3O_{10-\delta}$ versus temperature..... 196

Figure 6.59: Conductivity data for $La_{4-x}Pr_xNi_3O_{10-\delta}$ where x=0 (circle) , 0.25 (triangle) and 0.5 (square) and 1 (diamond). Red fill indicates heating and cyan fill indicates cooling, data shown between 200°C and 750°C. 197

Figure 7.1: XRD of $BaCe_{0.9}Y_{0.1}O_{3-\delta}$ as synthesised (black), heated in humid N_2 and removed from furnace at room temperature (red), heated in humid N_2 and removed from furnace at 200°C. 205

Figure 7.2: LiF doped samples a) 1 mol%, b) 2 mol% and c) 4 mol%. 206

Figure 7.3: XRD patterns of $BaZr_{0.8}Y_{0.3}O_{3-\delta}$ pellets, sintered with varying quantities of LiF: 1 mol% (black), 2 mol% (red) and 4 mol% (green). 207

Figure 7.4: a) 1 mol% of ZnO sintered at 1300°C for 4 h. b) 4 mol% of ZnO sintered at at 1300°C for 4 h. c) 10 mol % of ZnO sintered at 1300°C for 4h d) 1 mol% of ZnO sintered at 1400°C for 4 h. e) 4 mol% of ZnO sintered at 1400°C for 4 h. f) 10 mol % of ZnO sintered at 1400°C for 4 h. 208

Figure 7.5: XRD patterns of $BaZr_{0.8}Y_{0.3}O_{3-\delta}$ pellets sintered at 1300°C for 4 h with ZnO as a sintering aid. 1 mol% ZnO (black), 4 mol% ZnO (red) and 10 mol% ZnO (green). 209

Figure 7.6: XRD patterns of $BaZr_{0.8}Y_{0.3}O_{3-\delta}$ pellets sintered at 1400°C for 4 h with ZnO as a sintering aid. 1 mol% ZnO (black), 4 mol% ZnO (red) and 10 mol% ZnO (green). 210

Figure 7.7: XRD pattern of $BaZr_{0.8}Y_{0.3}O_{3-\delta}$ with 1 mol% $BaCO_3$ (black) and 10 mol% $BaCO_3$ (red) sintered at 1300°C for 10 h. 211

Figure 7.8: Images of $BaZr_{0.8}Y_{0.3}O_{3-\delta}$ containing 1 mol% ZnO, sintered at 1500°C for 12 h. a) 1 mol% $BaCO_3$, b) 10 mol% $BaCO_3$. 212

Figure 7.9: XRD patterns of $BaZr_{0.8}Y_{0.3}O_{3-\delta}$, 1 mol% ZnO with 1 mol% $BaCO_3$ (black), 2 mol% $BaCO_3$ (red) and 10 mol% $BaCO_3$ (green). 212

Figure 7.10: XRD pattern of $BaZr_{0.8}Y_{0.3}O_{3-\delta}$ with 4 wt% CuO. 1 mol% $BaCO_3$ (black) and 10 mol% $BaCO_3$ (red). 213

Figure 7.11: $BaCe_{0.6}Zr_{0.3}Y_{0.1}O_{3-\delta}$ sintered with 1 wt% NiO. 10 mol% $BaCO_3$ added (black) and 20 mol% $BaCO_3$ (red). 215

Figure 7.12: $BaCe_{0.6}Zr_{0.3}Y_{0.1}O_{3-\delta}$ with 1 wt% NiO sintered pellets. a) shows sintered pellet with no weight on top b) shows pellet with weight applied c) SEM surface image of $BaCe_{0.6}Zr_{0.3}Y_{0.1}O_{3-\delta}$ with 1 wt% NiO. 215

Figure 7.13: Image showing $BaCe_{0.6}Zr_{0.3}Y_{0.1}O_{3-\delta}$ pellets after sintering with 4 wt% NiO. The image shows the bed of $BaCe_{0.6}Zr_{0.3}Y_{0.1}O_{3-\delta}$ that the pellets were placed on during sintering, the cracked pellets and the sacrificial powder (that has fused to the alumina weights) used to cover the pellets. 216

Figure 7.14: Nyquist plot for $La_2NiO_{4+\delta}$, at 500°C in dry air (black filled circle), and humid air (black open circle), and at 600°C in dry air (red filled circle), and humid air (red open circle). 217

Figure 7.15: $R_{pol,\ air}$ (filled circle) and $R_{pol,\ humid}$ (empty circle) for $La_2NiO_{4+\delta}$ (black) and $La_{1.5}Sr_{0.5}NiO_{4+\delta}$ (red). 218

Figure 7.16: $R_{pol,\ air}$ (filled circle) and $R_{pol,\ humid}$ (empty circle) for $La_3Ni_2O_{7-\delta}$ (black) and $La_2PrNi_2O_{7-\delta}$ (red). 219

Figure 7.17: $R_{pol,\ air}$ (filled circles) and $R_{pol,\ humid}$ (open circles) for $La_4Ni_3O_{10-\delta}$ (black) and $La_{3.75}Pr_{0.25}Ni_3O_{10-\delta}$ (red) and $La_3PrNi_3O_{10-\delta}$ (green) 220

Figure 7.18: Nyquist plot for $La_4Ni_3O_{10-\delta}$, at 500°C in dry air (black filled circles), humid air (black open circles). The tail is observed coming from a semi-circle at low frequencies, possibly due to mass-transfer diffusion processes [9]. 220

Figure 7.19: Image of co-pressed $BaCe_{0.6}Zr_{0.7}Y_{0.1}O_{3-\delta}$ fuel electrode and electrolyte. The surface layer is the fuel electrode which has broken into various segments 222

Figure 7.20: SEM and EDXS of co-pressed $BaCe_{0.6}Zr_{0.7}Y_{0.1}O_{3-\delta}$. a) shows the electrolyte side of the pellet, b) shows the anode side of the pellet at x300 magnification, c) shows x1000 magnification of the anode with EDXS analysis of the image in the following. 222

Figure 7.21: SEM images of the spin coated electrolyte after sintering a) and b) are the electrolyte with 33% solid loading, c) and d) are the electrolyte with 58% solid loading, e) and f) are the electrolyte with 66% solid loading. 224

Figure 7.22: Images of spin coated half cells a) before sintering b) after sintering. 225

Figure 7.23: SEM images of the sintered half-cell. a) is the electrolyte, b) is the anode at x150 magnification, c) is the fuel electrode at x800 magnification followed by EDXS of the same surface. 225

Figure 7.24: Voltage (square) and power density (circle) verses current density of the cell tested using the various flow rate profiles at 500°C..... 227
Figure 7.25: SEM image of cell before testing. The more porous section, to the left side of the larger image, is the fuel electrode. While the denser section is the electrolyte. 227
Figure 7.26: Voltage (square) and power density (circle) against current density of the cell tested using the various flow rate profiles, from Table 7.4, at 700°C. 228
Figure 7.27: Voltage (square) and power density (circle) verses current density of the cell tested using the various flow rate profiles at 700°C. Fuel electrode was sintered at 1300°C for 6 h. 229
Figure 7.28: Voltage verses current density of cell before and after introduction of bubbler. 230
Figure 7.29: : Power density verses current density of cell before and after introduction of bubbler. 231
Figure 7.30: SEM of fuel electrode after sintering without sacrificial powder covering. a) x300 magnification and b) x800 magnification followed by EDXS of the image. 232
Figure 7.31: Voltage (square) and power density (circle) verses current density of the cell tested before and after introducing the bubbler. Measurements taken at 700°C. 233
Figure 7.32: SEM images of surface of $BaCe_{0.6}Zr_{0.3}Y_{0.1}O_{3-\delta}$ pellet after polishing each image shows one side of the pellet. 234
Figure 7.33: Voltage (square) and power density (circle) verses current density of the cell where the electrolyte was polished before the fuel electrode was applied. The cell was tested before and after introducing the bubbler, in the H_2 flowpath. Measurements taken at 700°C. 234
Figure 7.34: SEM images of new fuel electrode composition after sintering but before reducing a) x50 magnification b) x150 magnification and c) x1000 magnification followed by EDXS of image..... 236
Figure 7.35: Voltage (square) and power density (circle) against current density of the cell with new fuel electrode compositions. Measurements taken at 700°C. 237
Figure 7.36: SEM images of the four layer anode after sintering. a) x100 magnification and b) x1000 magnification, followed by EDXS of the image. 238
Figure 7.37: Voltage (square) and power density (circle) verses current density of the cell with four layers of fuel electrode spin coated on. Measurements taken at 500°C (black) and 600°C (red). 239

Figure 7.38: Voltage (square) and power density (circle) verses current density of the cell with four layers of fuel electrode spin coated on, measurements taken at 700°C..... 239

Figure 7.39: Electrolysis voltage against current density for cell with $La_2NiO_{4+\delta}$ air electrode. Measurements taken at 600°C (black square), 650°C (red square) and 700°C (green square)..... 241

Figure 7.40: Electrolysis voltage against current density for cell with $La_3Ni_2O_{7-\delta}$ air electrode. Measurements taken at 600°C (black square), 650°C (red square) and 700°C (green square)..... 241

Figure 10.1: TGA and MS data for humidified $BaFe_{0.925}Bi_{0.075}O_{3-\delta}$ when heated to 1000°C showing mass loss (black) and O_2 loss (red). 273

Figure 10.2: TGA and MS data for humidified $BaFe_{0.9}Bi_{0.1}O_{3-\delta}$ of sample when heated to 1000°C showing mass loss (black) and O_2 loss (red)..... 274

Figure 10.3: TGA and MS data for humidified $BaFe_{0.85}Bi_{0.15}O_{3-\delta}$ of sample when heated to 1000°C showing mass loss (black) and O_2 loss (red)..... 274

Figure 10.4: XRD pattern of $La_{2-x}Ba_xNiO_{4+\delta}$ where x=0.25 and 0.5, heated in dry N_2. In ascending order $La_{1.75}Ba_{0.25}NiO_{4+\delta}$, $La_{1.5}Ba_{0.5}NiO_{4+\delta}$..... 275

Figure 10.5: VT-XRD data showing the variation in a (circle) parameter of humidified $La_{2.5}Pr_{0.5}Ni_2O_{7-\delta}$ versus temperature, between 625°C and 725°C..... 276

Figure 10.6: VT-XRD data showing the variantion in c parameter of humidified $La_{2.5}Pr_{0.5}Ni_2O_{7-\delta}$ against temperature, between 625°C and 725°C. 277

Figure 10.7: VT-XRD data showing the variation in volume of humidified $La_{2.5}Pr_{0.5}Ni_2O_{7-\delta}$ versus temperature, between 625°C and 725°C. 278

Figure 10.8: VT-XRD data showing the variation in a (circle) parameter of humidified $La_{3.75}Pr_{0.25}Ni_3O_{10-\delta}$ versus temperature, between 425°C and 725°C. 278

Figure 10.9: VT-XRD data showing the variantion in c parameter of humidified $La_{3.75}Pr_{0.25}Ni_3O_{10-\delta}$ against temperature, between 425°C and 725°C..... 279

Figure 10.10: VT-XRD data showing the variation in volume of humidified $La_{3.75}Pr_{0.25}Ni_3O_{10-\delta}$ versus temperature, between 425°C and 725°C. 279

Figure 10.11: XRD pattern of $BaZr_{0.8}Y_{0.2}O_{3-\delta}$ original (black) and heated in humid N_2 (red)..... 280

Figure 10.12: Example of observed (blue cross), calculated (green) and difference (cyan) profiles for Rietveld refinement performed on $BaZr_{0.8}Y_{0.2}O_{3-\delta}$ (cubic *Pm-3m* space group, R_w=5.72%)..... 281
Figure 10.13: XRD pattern of $BaCe_{0.6}Zr_{0.3}Y_{0.1}O_{3-\delta}$ original (black) and heated in humid N_2 (red).... 282
Figure 10.14: Example of observed (blue cross), calculated (green) and difference (cyan) profiles for Rietveld refinement performed on $BaCe_{0.6}Zr_{0.3}Y_{0.1}O_{3-\delta}$ (orthorhombic *Imma* space group, R_w=6.89%). 282

List of Tables

Table 1.1: The different capacity factors for renewable energy technologies for the UK, published by the UK Department for Business, Energy & Industrial Strategy for the years 2018, 2019, 2020 and 2021 [11]. 4
Table 1.2 part 1: Showing the most common types of fuel cells with their respective electrolytes, electrode reactions, charge carriers, operating temperature, efficiency and fuel [19-25]. 6
Table 1.3: Commonly referenced colours to describe H_2 production. Generalized CO_2 emissions are also stated as actual varies will vary depending on feed inputs [30, 31]. 9
Table 1.4: Data compiled from various sources [14, 33, 44-49]. [a] Efficiency is the lower heating value of hydrogen produced divided by the electrical energy that is supplied to the electrolyser. [b] Efficiency considers the efficiency of the thermal energy source. [c] Efficiency ignores the efficiency of the thermal energy source. [d] Insufficient experimental data so efficiency is theoretical. Efficiencies taken from [45, 48] 12
Table 2.1: Table showing various PCC material compositions with the power densities achieved in fuel cell testing. Data given in descending order of power density. 23
Table 2.2: Table showing various cells that used MIECs. Cells split in terms of cathode used, followed by power density. 28

Table 2.3: Table showing the sintering aids used with various electrolytes. The sintering aids with no density given belong samples where the electrolyte was part of a cell, so no density was given. 37

Table 2.4: Table showing various methods of applying the electrolyte layer, along with sintering temperature and layer thickness. 41

Table 3.1: List of chemicals used for solid state synthesis, as well as their purities. 50

Table 3.2: List of chemicals used for sol-gel synthesis, as well as their purities. 52

Table 3.3: Showing various crystal systems and the conditions defining them. 54

Table 3.4: Metal paint, maximum experimental temperature and drying temperature. 61

Table 3.5: Electrical components and their respective equations for voltage. 70

Table 3.6: Impedance equations for the electrical components shown in Table 3.5. 71

Table 3.7: Capacitance values and their respective phenomenon [177]. 75

Table 4.1: Samples synthesised at Synthesis temperature used. 88

Table 4.2: Unit cell parameters for $BaFe_{1-x}Bi_xO_{3-\delta}$ where x = 0.075, 0.1 and 0.15. The structure presented was refined against a cubic *Pm*-3*m* space group. 89

Table 4.3: Unit cell parameters for $BaFe_{1-x}Bi_xO_{3-\delta}$ where x = 0.075, 0.1 and 0.15. The structure presented was refined against a tetragonal space group *P*4/*mmm* space group. 90

Table 4.4: Unit cell parameters for $BaFe_{1-x}Bi_xO_{3-\delta}$ samples heated in humid N_2; where x = 0.075, 0.1 and 0.15. (cubic *Pm*-3*m* space group). 93

Table 4.5: $BaFe_{1-x}Bi_xO_{3-\delta}$ oxygen content determined by Rietveld refinement and moles of H_2O incorporated into the Bi doped samples, obtained from TGA data analysis. 95

Table 4.6: Unit cell parameters for $BaFe_{1-x}Bi_xO_{3-\delta}$ samples heated in dry N_2; where x = 0.075, 0.1 and 0.15. Data presented are for the larger unit cell (top) and smaller unit cell (bottom) and was the structure refined using a cubic *Pm*-3*m* space group. 99

Table 4.7: $BaFe_{1-x}Bi_xO_{3-\delta}$ where x = 0.075, 0.1 and 0.15, conductivity at 487°C, 629°C and 700°C. 102

Table 4.8: Unit cell parameters for $BaFe_{1-x}Nb_xO_{3-\delta}$ where x = 0.4, 0.45 and 0.5, (cubic *Pm*-3*m* space group). 103

Table 4.9: Unit cell parameters for $BaFe_{1-x}Nb_xO_{3-\delta}$ samples heated in humid N_2; where x = 0.4, 0.45 and 0.5 (cubic *Pm*-3*m* space group). 105

Table 4.10: Unit cell parameters for $BaFe_{1-x}Nb_xO_{3-\delta}$ samples heated in dry N_2; where x = 0.4, 0.45 and 0.5 (cubic *Pm*-3*m* space group). 110

Table 4.11: Conductivity at 300°C, 342°C and 700°C for $BaFe_{1-x}Nb_xO_{3-\delta}$. 112

Table 5.1: Final heating temperatures for $La_{2-x}(Ba/Sr)_xNiO_{4+\delta}$. 115

Table 5.2: Lattice parameters (orthorhombic *Fmmm*) for Rietveld refinement performed on $La_{2-x}Ba_xNiO_{4+\delta}$ and $La_{2-x}Sr_xNiO_{4+\delta}$ (x =0, 0.25 and 0.5) samples 118

Table 5.3: Lattice parameters (orthorhombic *Fmmm*) for Rietveld refinement performed on $La_2NiO_{4+\delta}$ heated in various conditions. 121

Table 5.4: Lattice parameters (orthorhombic *Fmmm*) for Rietveld refinement performed on $La_{2-x}Ba_xNiO_{4+\delta}$ where x=0.25 and 0.5, annealed in various conditions. 125

Table 5.5: Lattice parameters (orthorhombic *Fmmm*) for Rietveld refinement performed on $La_{1.75}Sr_{0.25}NiO_{4+\delta}$ heated in various conditions. 127

Table 5.6: Lattice parameters (orthorhombic *Fmmm*) for Rietveld refinement performed on $La_{1.5}Sr_{0.5}NiO_{4+\delta}$ annealed in various conditions. 130

Table 5.7: Conductivity of $La_{2-x}Sr_xNiO_{4+\delta}$ where x=0, 0.25 and 0.5, conductivity at 475°C, 711°C and 750°C. 140

Table 5.8: Conductivity and H_2O loss from $La_{2-x}Sr_xNiO_{4+\delta}$ (x=0, 0.25 and 0.5). 141

Table 6.1: Final heating temperatures for $La_{3-x}Pr_xNi_2O_{7-\delta}$ and $La_{4-x}Pr_xNi_3O_{10-\delta}$. 144

Table 6.2: Lattice parameters (orthorhombic *Fmmm*) from Rietveld refinement performed for $La_{3-x}Pr_xNi_2O_{7-\delta}$ (x =0, 0.5 and 0.75 and 1) samples. 147

Table 6.3: Lattice parameters (orthorhombic *Fmmm*) for Rietveld refinement performed on $La_3Ni_2O_{7-\delta}$ heated in various conditions. 150

Table 6.4: Lattice parameters (orthorhombic space group) for Rietveld refinement performed on $La_{2.75}Pr_{0.25}Ni_2O_{7-\delta}$ heating in various conditions. 154

Table 6.5: Lattice parameters (orthorhombic *Fmmm*) for Rietveld refinement performed on $La_{2.5}Pr_{0.5}Ni_2O_{7-\delta}$ heated in various conditions. 156

Table 6.6: Lattice parameters (orthorhombic *Fmmm*) for Rietveld refinement performed on $La_2PrNi_2O_{7-\delta}$ heated in various conditions. 159

Table 6.7: Maximum H_2O and CO_2 loss from TGA/MS of samples heated in humid N_2. 161

Table 6.8: Conductivity for $La_{3-x}Pr_xNi_2O_{7-\delta}$ where x=0, 0.25, 0.5 and 1, conductivity at 200°C, 239°C, 554°C and 750°C. 171

Table 6.9: Summary of the effect of different heating conditions on $La_{3-x}Pr_xNi_2O_{7-\delta}$ (x=0, 0.25, 0.5 and 1) as well as H_2O loss (below 600°C) of humid samples and maximum electrical conductivity. 173

Table 6.10: Lattice parameters (orthorhombic *Fmmm*) from Rietveld refinement performed on $La_{4-x}Pr_xNi_3O_{10-\delta}$ (x =0, 0.5 and 0.75 and 1) samples. 176

Table 6.11: Lattice parameters (orthorhombic *Fmmm*) for Rietveld refinement performed on $La_4Ni_3O_{10-\delta}$ heated in various conditions. 178

Table 6.12: Lattice parameters (orthorhombic *Fmmm*) for Rietveld refinement performed on $La_{3.75}Pr_{0.25}Ni_3O_{10-\delta}$ heated in various conditions. 181

Table 6.13; Lattice parameters (orthorhombic *Fmmm*) for Rietveld refinement performed on $La_{3.5}Pr_{0.5}Ni_3O_{10-\delta}$ heated in various conditions. 184

Table 6.14: Lattice parameters (orthorhombic *Fmmm*) for Rietveld refinement performed on $La_3PrNi_3O_{10-\delta}$ heated in various conditions. 185

Table 6.15: Conductivity for $La_{4-x}Pr_xNi_3O_{10-\delta}$ (x=0, 0.25, 0.5 and 1), conductivity at 200°C, 357°C and 750°C. 198

Table 6.16: H_2O loss (below 600°C) and CO_2 loss of $La_{4-x}Pr_xNi_3O_{10-\delta}$ (x=0, 0.25, 5 and 1) heated in humid N_2 as well as electrical conductivity. 199

Table 6.17: Summary of compositions which were chemically stable when heated in various atmospheres along with their maximum electrical conductivity and temperature at which orthorhombic-tetragonal phase change occurred. 200

Table 7.1: Fuel electrode composition used for cell fabrication. 204

Table 7.2: Table showing the densities of the $BaZr_{0.8}Y_{0.3}O_{3-\delta}$ sintered pellets using LiF as a sintering aid. 207

Table 7.3: Table showing the sintering temperatures and densities of $BaZr_{0.8}Y_{0.3}O_{3-\delta}$ pellets using ZnO as a sintering aid..... 210

Table 7.4: Flow rate profiles used when testing cells as a fuel cell. 226

Table 7.5: Composition of new anode, with greater percentage of NiO and lower percentage of pore former. 235

Table 10.1: Lattice parameters for $La_3PrNi_3O_{10-\delta}$ at 725°C, during heating and cooling. 280

Table 10.2: Lattice parameters (cubic *Pm-3m*) for Rietveld refinement performed on $BaZr_{0.8}Y_{0.2}O_{3-\delta}$. 281

Table 10.3: Lattice parameters (orthorhombic *Imma*) for Rietveld refinement performed on $BaCe_{0.6}Zr_{0.3}Y_{0.1}O_{3-\delta}$..... 283

Chapter 1: Introduction

1.1 Climate Change

The industrial revolution began in the 18th century and saw quicker and more efficient manufacturing of goods. At the core of this propulsion of manufacturing and economic development were fossil fuels. The harnessing of fossil fuels, through combustion, led to great advancements in manufacturing goods and improved global interconnectivity. Fossil fuels soon became pivotal to society and reliance deepened as further technological advancements were made. The cost of advancement was the release of pollutants into the atmosphere, such as carbon dioxide (CO_2), known as greenhouse gases (GHGs). They have been shown to aid in the insulation of thermal radiation, known as the greenhouse effect, leading to global warming and thus climate change [1, 2]. Land and sea temperatures have been increasing since the industrial revolution and it is widely acknowledged that this increase is largely due to the release of CO_2 into the atmosphere since the industrial revolution which can be seen in Figure 1.1[3, 4].

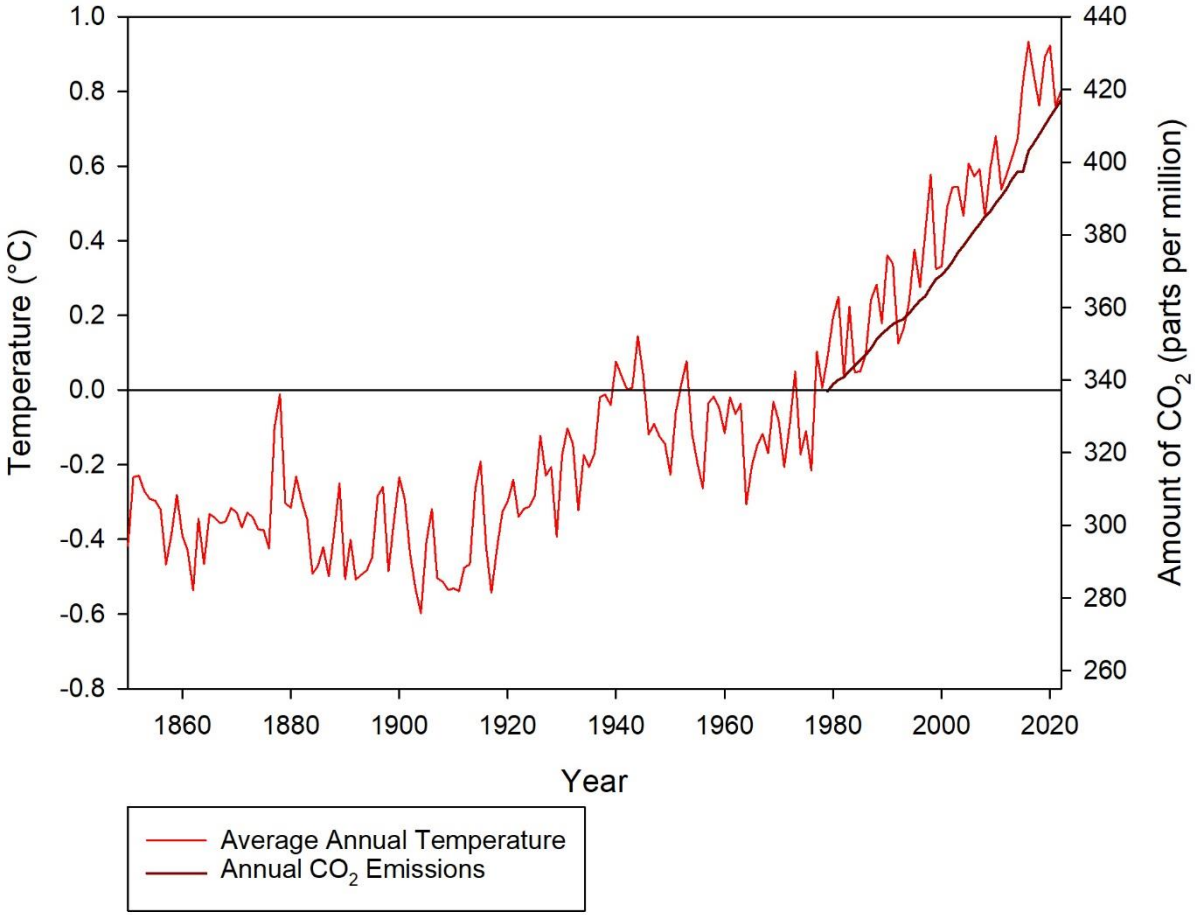


Figure 1.1: Global average annual temperature relative to the period between 1961 – 1990 (red) plotted alongside the global average annual CO_2 released since 1979 (dark red). Data adapted from [3, 4].

The issue regarding the reliance on fossil fuels and the effect they have on climate change has been brought to the forefront with various countries agreeing to tackle the problem through the Kyoto Protocol (1997), followed by the Paris Agreement (2015) [5, 6]. The Kyoto Protocol was the first international agreement to globally reduce GHGs [5]. The Paris Agreement followed, with the goal of ensuing that global temperatures remained below 2°C above pre-industrial levels [6]. The UK in particular set its goal through the Climate Change Act 2008 to reduce carbon emissions by 80% of what was produced in 1990 by 2050, which was then further increased in 100% in 2019, thus achieving a new zero economy [7].

1.2 Energy System

Primary energy demand for the world increased by 5.8% in 2021 and 82% of this primary energy coming from fossil fuels [8]. Fossil fuel use has increased by 65% between 1990 and 2021, constantly being the highest energy contributors as seen by Figure 1.2 [9]. Despite the constant increase in fossil fuel consumption, CO_2 release from primary energy has been decreasing since 2018 [8]. If all polluting sectors are included, such as transport and industrial processes, then CO_2 emissions have not, however, decreased since 2015 [10].

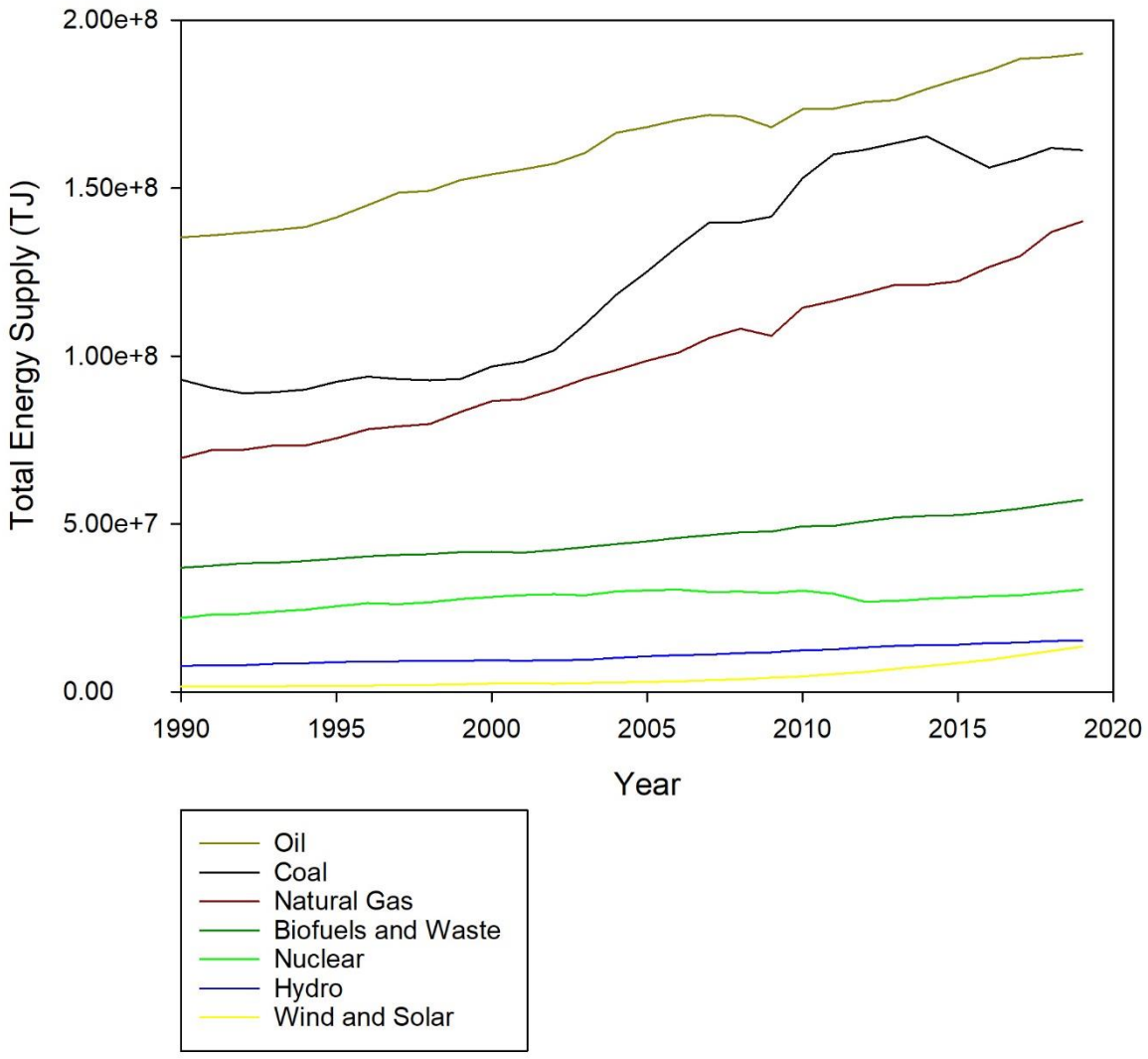


Figure 1.2: Global energy supply by source between 1990 and 2019 data taken from IEA [9]. Oil (gold), coal (black), natural gas (brown), biofuels and waste (dark green), nuclear (green), hydro (blue) and wind and solar (yellow).

Energy demand can be met with the aid of renewable energy, reducing the use of fossil fuels and GHG emissions. On the world scale, energy from renewables (including biofuels but excluding hydro) has grown by 15% in 2021 [8]. For the UK, reliance on fossil fuels has decreased by 4% in 2019 [9]. Energy demand was complemented by renewables, which were seen to increase by 9% in 2019 [9]. 2019 is used as a comparison as all energy demand decreased in 2020 due to the Coronavirus disease (COVID-19).

Even though renewable energy can aid in reducing CO_2 emissions they are only able to produce energy when the correct environmental conditions are met. In terms of their energy output, the ratio between the actual output of the energy technology against the theoretical maximum output is known as the capacity factor [11]. The variation in capacity factor can be seen for the UK in Table 1.1, which shows the capacity factors for various renewable energy technologies between 2018 and 2021 [11]. As energy output varies with weather conditions, an energy storage system would ideally be integrated, allowing energy to be stored when supply is greater than demand. The stored energy can then be utilised when demand is greater than supply.

Table 1.1: The different capacity factors for renewable energy technologies for the UK, published by the UK Department for Business, Energy & Industrial Strategy for the years 2018, 2019, 2020 and 2021 [11].

Renewable Energy Technology	2018	2019	2020	2021
Bioenergy	58.6	55.4	58.7	56.6
Hydropower	33.2	36.1	41.5	33.1
Offshore Wind	39.9	40.4	45.7	37.4
Onshore Wind	26.7	26.5	28.3	23.2
Solar Photovoltaics	11.2	10.7	10.9	10.0

1.3 Hydrogen Economy

The hydrogen (H_2) economy is the decarbonisation of various polluting sectors of the economy, through the incorporation of H_2 as an alternative to fossil fuels [12]. The H_2 can be produced from fossil fuels with CO_2 as a by-product. Implementing carbon capture and storage (CCS) into this process will classify the hydrogen as low carbon. This type of hydrogen is key if the world is to reduce its carbon emissions [10]. In an ideal hydrogen economy, hydrogen is produced through electrolysis therefore not producing any CO_2. Electrolysis would be powered using renewable energy technologies when these technologies are producing a surplus of energy, this is known as power-to-hydrogen [12-14]. When there is a deficit in energy supply, hydrogen fuel cells be used to supplement the available energy [13].

Alternatively, the combustion of H_2 can be used to produce heat. H_2 can also be blended with methane (CH_4) and burnt, reducing the amount of CH_4 used and thus reducing the amount of carbon produced. The UK's Health and Safety Executive (HSE) reported that modern gas appliances would be able to burn 20 vol% of H_2 in CH_4 without modifications [15]. With various blending projects are being implemented in Germany, France, Netherlands, the UK and the United States of America (USA) [14, 16-18]. In these cases little or no modifications were required to the grid infrastructure to accommodate this level of H_2 [14, 15, 18].

1.4 Fuel Cells

1.4.1 Fuel Cells

Fuel cells are an electrochemical device that produces electricity and water (H_2O) through the use of a catalysis for the hydrogen-oxygen reaction. The electrochemical reaction can occur at various temperatures, depending on the setup and composition of the fuel cell. Fuel cells are named according to their electrolytes. They include alkaline fuel cell (AFC), polymer exchange membrane fuel cell (PEMFC), direct methanol fuel cell (DMFC), phosphoric acid fuel cell (PAFC), molten carbonate fuel cell (MCFC), solid oxide fuel cell (SOFC) and proton conducting ceramic fuel cell (PCCFC) [19, 20]. These fuel cells and their respective properties are shown in Table 1.2.

Table 1.2 part 1: Showing the most common types of fuel cells with their respective electrolytes, electrode reactions, charge carriers, operating temperature, efficiency and fuel [19-25].

Fuel Cell	Electrolyte	Anode Reaction	Cathode Reaction	Ion	Operating Temperature (°C)	Efficiency (%)	Fuel
Direct Methanol	Nafion ®	$CH_3OH + H_2O \rightarrow CO_2 + 6H^+ + 6e^-$	$6H^+ + \frac{3}{2}O_2 + 6e^- \rightarrow 3H_2O$	H^+	20 – 90	35 – 60	Methanol – water solution,
Polymer Electrolyte	Nafion ®	$H_2 \rightarrow 2H^+ + 2e^-$	$\frac{1}{2}O_2 + 2H^+ + 2e^- \rightarrow H_2O$	H^+	30 – 100	40 – 60	H_2
Alkaline	Potassium hydroxide	$2H_2 + 4(OH)^- \rightarrow 4H_2O + 2e^-$	$O_2 + 2H_2O + 4e^- \rightarrow 4(OH)^-$	OH^-	50 – 200	60 – 70	H_2
Phosphoric Acid	Phosphoric acid	$H_2 \rightarrow 2H^+ + 2e^-$	$\frac{1}{2}O_2 + 2H^+ + 2e^- \rightarrow H_2O$	H^+	160 – 220	36 – 45	H_2
Molten Carbonate	Liquid alkali carbonate	$H_2 + {CO_3}^{2-} \rightarrow H_2O + CO_2 + 2e^-$	$\frac{1}{2}O_2 + CO_2 + 2e^- \rightarrow {CO_3}^{2-}$	CO_3^{2-}	600 – 700	55 – 65	H_2, CH_4

Table 1.2 part 2: Continuation of Table 1.2 part 1. Showing the most common types of fuel cells with their respective electrolytes, electrode reactions, charge carriers, operating temperature, efficiency and fuel [19-25].

Fuel Cell	Electrolyte	Anode Reaction	Cathode Reaction	Ion	Operating Temperature (°C)	Efficiency (%)	Fuel
Oxide Conducting Solid Oxide	Ceramic	$H_2 + O^{2-} \rightarrow H_2O + 2e^-$	$\frac{1}{2}O_2 + 2e^- \rightarrow O^{2-}$	O^{2-}	600 – 850	55 – 65	H_2, CH_4
Proton Conducting Ceramic	Ceramic	$H_2 \rightarrow 2H^+ + 2e^-$	$2H^+ + O_2 + 2e^- \rightarrow H_2O$	H^+	500 – 700	55 – 65	H_2, Ammonia

Fuel cells consist of two electrodes, an anode and a cathode, separated by an electrolyte. The most common fuel cell characteristics are shown in Table 1.2. The fuel, either hydrogen or a hydrocarbon gas, enters at the anode and air at the cathode. Depending on the fuel cell, either anions (negatively charged ions) or cations (positively charged ions) transfer across the electrolyte. Possible anions are carbonate ions (CO_3^{2-}), hydroxide ions (OH^-) and oxygen ions (O^{2-}), while the cation is protons (H^+). If cations migrate across the electrolyte, then H_2O is produced at the cathode, while if anions migrate across the electrolyte, then H_2O is produced on the anode side. Most fuel cells utilise hydrogen, although SOFCs and MCFCs can utilise methane due to their higher operating temperature, which are more tolerant to impurities [19-21].

On average, a fuel cell will operate between 0.6 – 0.7 V, to preserve the lifetime of the cell, while maintaining adequate performance [22, 26]. As this voltage is technically not very useful, the cells are connected in series i.e. combined into stacks. Fuel cell stacks produce higher voltages and power. They are seen as an alternative to the traditional combustion engine. Currently stacks are being implemented into society for mobility uses such as passenger vehicles, buses, aeroplanes, and ships [27, 28]. SOFCs and MCFCs are more often used in stationary applications, where the high-grade heat can used as part of a combined heat and power (CHP) system for energy supply to buildings [12, 27].

1.5 Hydrogen Production

H_2 is a colourless gas and is one of the most abundant elements in the universe [29]. However, on Earth hydrogen is primarily bonded to other atoms such as oxygen or carbon. To produce H_2 these bonds must be broken which can be done through various chemical processes, thus classing it as a secondary fuel [12].

In 2021 94 Mt of H_2 was produced mainly from fossil fuels, known as grey H_2 [16, 30, 31]. The colour used to describe H_2 is a way of signifying the process in which it was made, Table 1.3 shows the various colours used to describe H_2 as well as the process associated with it [30, 31]. By 2030 it is expected that 24 Mt of the H_2 produced can be classified as low-carbon, of this 60% will be green and the rest will be

blue H_2 [10, 16]. Various projects around the world are currently under development to meet the expected H_2 demand, with many expected to be completed by 2030 [18, 32].

Table 1.3: Commonly referenced colours to describe H_2 production. Generalized CO_2 emissions are also stated as actual varies will vary depending on feed inputs [30, 31].

Hydrogen Colour	Process
Black/Brown	Gasification using hard and lignite coal, respectively
Grey	Steam methane reforming of natural gas
Blue	Steam methane reforming of natural gas with carbon, capture and storage
Green	Renewable electricity integrated with water electrolysis
Pink	Nuclear energy integrated with water electrolysis
Turquoise	Methane pyrolysis

1.5.1 Production from Fossil Fuels

Currently the prevalent way to produce hydrogen is through steam methane reforming (SMR) of natural gas followed by the water gas shift reaction (WGS), shown in equation (1.1) and (1.2) respectively [33]. In 2021, approximately 58 Mt of hydrogen were produced through this process [16]. These reactions occur at higher temperatures, with varying temperatures and pressures reported, having efficiencies between 60% and 85% [29]. The temperature and pressure range are between 700°C and 1450°C and 3 to 25 bar with a nickel-based catalyst [34-37]. SMR produces carbon monoxide (CO). To improve the yield of H_2, a WGS reaction is performed on the product stream of the SMR reactor [38].

$$CH_4 + H_2O \leftrightarrow 3H_2 + CO \quad (1.1)$$

$$CO + H_2O \leftrightarrow H_2 + CO_2 \quad (1.2)$$

The WGS reaction shown in equation (1.2) occurs over two reactors. The first reactor operates above 300°C, with an iron-based catalyst (often paired with chromium), while the second operates between 210°C and 330°C, with a copper-based catalyst [37, 38].

To achieve 99% hydrogen in the product stream, CO and CO_2 must be removed. This can be achieved through pressure swing adsorption (PSA), amine scrubbing or preferential oxidation (PROX) [35, 39, 40]. Due to the reactions that occur and the separation of the CO and CO_2, the process releases carbon emissions, with interest in preventing these adding to greenhouse gas levels through carbon capture and storage (CCS) [40].

1.5.2 Coal Gasification

Gasification is the process of turning solid carbon containing material into gases by heating the reactants to high temperatures, while controlling the concentration of O_2 and steam [41]. Coal gasification occurs above 750°C, with the operating temperature varying depending on the reactor and feedstock [41]. The process occurs in two steps. In the first the carbon present in the coal becomes partially oxidised, through the introduction of air, to form CO_2 [31, 42], shown by equation (1.3). The second, begins with stopping the air feed and injecting steam, so that reaction (1.4) can take place [31, 42]. Any CO produced can be further processed through the WGS reaction, increasing the concentration of H_2 in the product stream [42]. The final gas is a mixture of: H_2, CO, CO_2, CH_4 and other hydrocarbons, with the ratio of these products varying depending on the reactors used [41]. Further separation of H_2 is required, and despite this higher effort, the process is preferred to SMR when coal is more abundant than natural gas [42].

$$C + O_2 \rightarrow CO_2 \quad (1.3)$$

$$C + H_2O \rightarrow CO + H_2 \quad (1.4)$$

1.5.3 Water Electrolysis

Hydrogen can be produced from the electrochemical splitting of H_2O, shown by equation (1.5) [33]. The process is known as H_2O electrolysis. Under standard conditions the enthalpy for the electrolysis of H_2O is 286 kJ mol^{-1} [43]. Low temperature (<100°C) electrolysers use platinum-group metals (PGMs)

to facilitate the reaction. Alternatively, nickel (Ni) can be used as a catalyst, however a higher operating temperature is required in this [12].

$$H_2O \rightarrow H_2 + \frac{1}{2}O_2 \quad (1.5)$$

In the presence of H_2O, a potential applied to the electrodes of the electrolyser which allows for oxidation and reduction reactions to occur at the anode and cathode respectively. The type of electrolyser will affect which ions are transferred across the electrolyte. Table 1.4 shows the respective electrolyser cells alongside the ions transferred through the electrolyte. H_2 produced in this way can be zero-carbon if the applied current came from a source that did not produce carbon itself, for example solar power [40].

Table 1.4: Data compiled from various sources [14, 33, 44-49]. [a] Efficiency is the lower heating value of hydrogen produced divided by the electrical energy that is supplied to the electrolyser. [b] Efficiency considers the efficiency of the thermal energy source. [c] Efficiency ignores the efficiency of the thermal energy source. [d] Insufficient experimental data so efficiency is theoretical. Efficiencies taken from [45, 48] .

Electrolyser	**Electrolyte**	**Cathode**	**Anode**	**Ion**	**Operating Temperature (°C)**	**Efficiency (%)**
Alkaline	KOH or NaOH	Nickel coated stainless steel	Nickel coated stainless steel	OH^-	60 – 90	50 – 60 [a]
Polymer Electrolyte Membrane	Nafion®	Platinum on carbon black	Iridium	H^+	50 – 80	55 – 70 [a]
Oxide Conducting – Solid Oxide	Yttrium stabilised zirconium (YSZ) or Scandium stabilised zirconium (ScSZ)	Ni – YSZ/ Ni – ScSZ	La,Sr,Co,$FeO_{3-\delta}$ or La,Sr,$MnO_{3-\delta}$	O^{2-}	700 – 850	40 – 60 [b]/ 90 [c]
Proton Conducting Ceramic Cell	$Ba(Ce/Zr)_{1-x}Y_xO_{3-\delta}$	Ni – $Ba(Ce/Zr)_{1-x}Y_xO_{3-\delta}$	Ba,Sr,Co,$FeO_{3-\delta}$	H^+	400 – 700	50 – 95 [d]

1.5.3.1 Alkaline Electrolyser

Alkaline electrolysers operate between 60°C and 90°C [33, 44, 47]. They consist of a potassium hydroxide (KOH) or sodium hydroxide (NaOH) liquid electrolyte, separated by an asbestos diaphragm from stainless steel electrodes coated with a nickel (Ni) catalyst [44, 47]. Hydroxide ions (OH^-) and hydrogen (H_2) are produced from the alkaline electrolyte solution, equation (1.6). The OH^- transfer across the diaphragm from the cathode to the anode, resulting in the formation of O_2 and water (H_2O), equation (1.7) . The H_2 rich product is dried, and this final product is between 99.5% and 99.9% pure H_2 [44, 50].

$$2H_2O + 4e^- \rightarrow 2H_2 + 4OH^- \quad (1.6)$$

$$4OH^- \rightarrow O_2 + 2H_2O + 4e^- \quad (1.7)$$

Alkaline electrolysers are the most mature electrolyser technology [51]. They are able to operate for extended periods of time and have been successfully commercialised since the 1960s [44]. Nearly 70% of installed electrolysers in 2021 were alkaline electrolysers [16]. Despite this, alkaline electrolysers are being challenged by other electrolyser technologies, as they are only able to operate at relatively low current densities ranging from 0.2 A cm^{-2} to 0.8 A cm^{-2} [44].

1.5.3.2 Proton Exchange Membrane Electrolyser (PEME)

A proton exchange membrane electrolyser (PEME) consists of a polymer electrolyte which is generally made of Nafion® [46]. Located on either side of the Nafion® is a gas diffusion layer (GDL) and a catalyst layer [46]. All these components together are known as the membrane electrode assembly (MEA). One side of the MEA acts as an anode and the other side as a cathode. At the anode side an oxygen reduction reaction, equation (1.8), occurs. At the cathode side a hydrogen evolution reaction, (1.9), occurs.

$$2H_2O \rightarrow O_2 + 4H^+ + 4e^- \quad (1.8)$$

$$4H^+ + 4e^- \rightarrow 2H_2 \quad (1.9)$$

The operating temperature is between 50°C to 80°C, with an efficiency of 55% to 70% [45, 51]. H_2O enters the cell at the anode side of the MEA, passes through the GDL, where it encounters an iridium

(Ir) or ruthenium (Ru) based catalyst [46, 52]. The H_2O dissociates into oxygen, hydrogen ions and electrons, Equation (1.8). The hydrogen ions pass through the Nafion®, which must be kept hydrated and acidic, to allow the transport of hydrogen ions. At the cathode the positive ions and electrons interact with a platinum (Pt) based catalyst (often on a carbon support) forming hydrogen, shown by equation (1.9) [46].

PEME are becoming more commercially viable. It is expected that by 2030, the total capacity of the electrolyser market will be split equally between PEME and alkaline electrolysers [16]. Making them one of the dominant electrolysers in the market; despite the cost of the catalyst [44, 46]. They are favourable as they are better suited for fluctuating electricity input, thus is ideal for being paired with renewables.

1.5.3.3 Oxide Conducting Solid Oxide Electrolyser (OC-SOE)

An oxide conducting solid oxide electrolyser (OC-SOE) has a similar setup to an SOFC. These high temperature cells are able to be operated as an electrolyser or fuel cell, similar to that of lower temperature fuel cells [53]. OC-SOEs operate between 700°C to 850°C and consist of electrodes and an electrolyte made from ceramic oxides [54]. Oxide conductors use either yttria-stabilised zirconia (YSZ) or scandium-stabilised zirconium (ScSZ) as the electrolyte. YSZ has lower ionic conductivity, compared to ScSZ, and ideally operates between 700°C to 900°C [54-56]. The cathode used is a mixture of Ni and the electrolyte material. The Ni acts as a catalyst for the oxidation H_2O splitting that occurs [54, 57]. Due to the high operating temperature and presence of steam, Ni has been seen to re-oxidise [56, 57]. The anode material consists of strontium doped lanthanum manganite (LSM) with YSZ or of lanthanum strontium ferrite doped with cobalt (LSCF) [54]

H_2O enters at the cathode as steam, a potential is applied, and the steam dissociates into hydrogen and oxygen ions, shown by equation (1.10) [13, 56]. The oxide ions can migrate to the anode, through the electrolyte, where the reaction shown by (1.11) occurs [13, 56]. Leading to the formation of O_2 molecules at the anode and hydrogen on the cathode, with an efficiency of 70 – 90% [29]. As the steam enters at the cathode, where hydrogen is produced, the hydrogen will require further separation.

OC-SOE are in the early stages of being commercialised [53]. They are advantageous to lower temperature electrolysers as they have higher efficiencies and do not require expensive catalysts. It is expected that 4% of manufactured electrolyser will be OC-SOE in 2030 [16].

$$H_2O + 2e^- \rightarrow H_2 + O^{2-} \quad (1.10)$$

$$O^{2-} \rightarrow \frac{1}{2}O_2 + 2e^- \quad (1.11)$$

1.5.3.4 Proton Conducting Ceramic Electrolyser (PC-SOEC)

Proton conducting ceramic electrolyser (PCCE), are also made from ceramics, where the main transport mechanism, is due to protons. PCCEs are operated between 400°C and 700°C temperature range, often referred to as intermediate temperature [49]. Operating at the lower temperature spectrum of SOE's allows PCCE's to avoid issues that may arise at higher temperatures such as degradation of the cell during long-term testing [48, 49]. Efficiencies for these electrolysers range between 50% to 95% [48].

The electrolyte material of choice tends to be a composition of $Ba(Ce/Zr)_{1-x}Y_xO_{3-\delta}$ [49]. Unlike in OC-SOE, steam enters at the anode, also known as the steam electrode. When a potential is applied the steam dissociates into oxygen ions, protons and electrons [13]. The protons transfer across the steam electrode followed by the electrolyte and then the cathode (also known as the fuel electrode). Due to the transport of protons, hydrogen is produced at the fuel electrode, without the presence of H_2O [48, 56]. Therefore, further separation of H_2 from H_2O is not required and can be used directly, aiding in reducing costs. Unlike other forms of electrolyser technology, PCCE's have not yet been commercialised, as the technology is still under research and development.

1.6 Thesis Outline

Chapter 2: This chapter will explore the current literature, looking at the various electrolytes, cathodes and anodes used in PCCC. Looking at the some of the popular methods for fabrication and the power densities achieved.

Chapter 3: In this chapter the synthesis method used along with characterisation techniques. Followed by the apparatus used for symmetrical cell, fuel cell and electrolyser testing.

Chapter 4: This chapter will look at synthesising bismuth and niobium doped barium ferrites and looking at their chemical stability in humid and dry nitrogen (N_2), along with the possibility of any H_2O incorporation, followed by electrical conductivity measurements.

Chapter 5: In this chapter the doping of strontium and barium, into $La_2NiO_{4+\delta}$ will be explored. The effect on lattice parameters from heating in humid N_2, dry N_2 and humid O_2 will also be investigated. H_2O incorporation of the samples heated in humid N_2 will be assessed and compared to variable temperature X-ray diffraction data to.

Chapter 6: This chapter will look at praseodymium doping in $La_3Ni_2O_{7-\delta}$ and $La_4Ni_3O_{10-\delta}$. Successfully doped samples are then heated in humid N_2, dry N_2 and humid O_2 and lattice parameters determined. H_2O incorporation in investigated for the samples that remained chemically stable in humid N_2, with TGA/MS data compared to variable temperature X-ray diffraction data.

Chapter 7: In this chapter the previously made samples from chapter 5 and 6 will be incorporated into a symmetrical cell and electrochemical impedance spectroscopy performed in humid and dry air. Following this $La_2NiO_{4+\delta}$ will be explored with $BaCe_{0.6}Zr_{0.3}Y_{0.1}O_{3-\delta}$ as a fuel cell. With the chapter ending with electrolyser testing.

Chapter 2: Literature Review

2.1 Introduction

The first ceramic to have its proton conducting properties discovered was $SrCeO_3$ in 1981 [58]. Iwahara [59, 60] further found that barium cerate ($BaCeO_3$) was also a proton conductor in 1988. Currently most common proton conductors are based on $BaCeO_3$ and barium zirconate ($BaZrO_3$). Proton transport was proposed as occurring through hydroxide ions (OH^-) by Norby *et al.* [61], following the mechanism shown in equation (2.1). Where water from a humid atmosphere dissociates into hydroxide ions (OH^-), the OH^- occupies oxygen vacancies in the ceramic. The proton is then able to transfer through the ceramic by hopping or rotating between oxide ions using the Grotthuss mechanism [62]. The transport of protons requires a lower activation energy than that of oxide conduction, as protons are smaller in size [61]. Therefore, proton conducting cells (PCCCs) have been suggested for the use at lower temperatures than typical oxide conducting electrolyte solid oxide cells (OC-SOC).

$$H_2O + V_O^{\bullet\bullet} + O_O^{\times} \leftrightarrow 2OH_O^{\bullet} \qquad (2.1)$$

Perovskites, with the formula ABO_3, are often used as proton conducting ceramics (PCCs). The A site is often a large cation such a barium (Ba) or strontium (Sr), while the B site is often cerium (Ce) or zirconium (Zr). Further additions can be made using yttrium (Y) or ytterbium (Yb). The result is the difference between the large ionic radius on the A-site and the smaller ionic radius of the B-site aids in the formation of oxygen vacancies, as the structure is not as closely packed.

Throughout this chapter various materials for PCCCs are discussed. Within Sections 2.2, 2.3 and 2.4 when quoting the various materials and their application, as well as the current densities and power densities, they are in respect to the them being operated as a fuel cell at 700°C. The anode, of the fuel cell, unless stated otherwise is a mixture of NiO with the specified electrolyte material. The inlet feed for the anode is H_2 with 3 vol% H_2O and the inlet feed for the cathode is air. While in Section 2.5 discussion of the fabrication of PCCC can be applied to both fuel cells and electrolysers, however unless

stated will apply to fabrication of fuel cells. Finally, Section 2.6 is in regard to operation as an electrolyser where the fuel electrode is a mixture of the specified electrolyte and NiO

2.2 Electrolyte

Electrolyte materials for PCCCs must meet certain requirements. Electrolyte material should be dense, so that the gaseous reactants are not able to diffuse across the electrolyte. Instead, reactants should dissociate into their respective ions and migrate through the ceramic using oxygen vacancies. They are also required to have high ionic conductivity, while maintaining low electronic conductivity.

As the electrolyte is the layer to separate the gaseous reactants, one side containing hydrogen (H_2), the other oxygen (O_2) and water (H_2O), they must also be chemically stable in reducing and oxidising conditions. For long term testing, ideal proton conducting electrolytes can withstand humid conditions, with this sometimes being a factor in why specific materials are used [63]. Another factor to consider regarding electrolyte materials is their thermal stability, including their thermal expansion in comparison to the electrodes being used, although this is rarely covered within the literature.

2.2.1 Barium Cerates

Although $SrCeO_3$ was one of the first proton conductors discovered it has been overshadowed by barium-based compositions. Which have higher ionic conductivity, in part due to the larger ionic radius of Ba^{2+} compared to Sr^{2+}. The larger ionic radius allows a greater quantity of oxygen vacancies for OH^- to bind to, thus allowing the migration of protons.

Further improvements can be made by doping barium cerates with Y or Yb [64, 65] . By doping with either Y or Yb the conductivity, at 600°C, has been previously shown to increase to 0.0211 Scm^{-1} and 0.016 Scm^{-2} respectively [64], with the $BaCe_{1-x}Y_xO_{3-\delta}$ composition showing the better performance. Conductivity studies are performed either in humid or dry atmospheres and a comparison done between the two data sets, to observe the proton conductivity of the samples [64]. The conductivity is often seen to increase in humid atmosphere, although various reports have been shown where the conductivity of the sample decreases denoting p-type conductivity [64, 66, 67].

Barium cerate compositions, despite having high ionic conductivity, tend to have poor chemical stability when exposed to CO_2 (2.2) or H_2O (2.3) [49, 68, 69]. This has restricted their versatility so that they are mainly used with H_2 [70]. If alternative fuels, such as methane, are to be used then the barium cerates must be further doped to improve their chemical stability [70]. Similar chemical reactions occur with strontium cerate compositions (2.4), (2.5) and (2.6).

$$BaCeO_3 + CO_2 \rightarrow BaCO_3 + CeO_2 \quad (2.2)$$

$$BaCeO_3 + H_2O \rightarrow Ba(OH)_2 + CeO_2 \quad (2.3)$$

$$SrCeO_3 + CO_2 \rightarrow SrCO_3 + CeO_2 \quad (2.4)$$

$$SrCO_3 + CO_2 \rightarrow SrO + 2CO_2 \quad (2.5)$$

$$SrCeO_3 + H_2O \rightarrow Sr(OH)_2 + CeO_2 \quad (2.6)$$

$BaCeO_3$ is often doped with Y to improve its ionic conductivity. $BaCe_{0.9}Y_{0.1}O_{3-\delta}$ has been shown to be a possible electrolyte material despite its poor chemical stability [71, 72]. Further doping elements such as niobium (Nb), tin (Sn) and titanium (Ti) have been shown to improve the chemical stability in H_2O and CO_2 at the expense of decreasing the conductivity, thought to be due to a decrease in oxygen vacancies [69, 73, 74].

When observing the functional ability of the Nb. Doped electrolyte in a proton conducting ceramic fuel cell (PCCFC), high power densities have been observed, with values ranging from 345 to 660 $mWcm^{-2}$ [73, 75]. The difference in power densities is possibly due to the difference in the electrolyte and cathodes used. Xie *et al.* [73] used an electrolyte with a lower concentration of Ce ($BaCe_{0.6}Y_{0.3}Nb_{0.1}O_{3-\delta}$) and a $Nd_{0.7}Sr_{0.3}MnO_{3-\delta}$ cathode. While Wang *et al.* [75] used a higher concentration of Ce ($BaCe_{0.8}Y_{0.15}Nb_{0.05}O_{3-\delta}$) and a composite electrode of $SmBaCo_2O_{5+\delta}$ and $Ce_{0.8}Sm_{0.2}O_{2-\delta}$. The lower Ce would have an adverse impact on the ionic conductivity and therefore the power density.

Whilst Ti doping to obtain $BaCe_{0.7}Ti_{0.1}Y_{0.1}O_{3-\delta}$ cells was able to achieve 295 $mWcm^{-2}$ [74]. The cell used a $Nd_{0.7}Sr_{0.3}MnO_{3-\delta}$ cathode similar to Xie *et al.* [73]. Other dopants have been explored although

not as extensively: gadolinium (Gd), indium (In), and tantalum (Ta) are known to have varying effects on grain size, sintering ability and conductivity [64, 75, 76].

2.2.2 Barium Zirconates

An alternative to $BaCeO_3$ are the barium zirconate ($BaZrO_3$) set of materials. These have better chemical stability when compared to their cerate counterparts, being stable in CO_2 and H_2O conditions. Barium zirconates do not have the same level of conductivity as the barium cerates. These materials also require high temperatures in order to be successfully sintered. Grain boundary size can play an important role in the conductivity of a sample, with smaller grain sizes leading to greater grain boundary resistance, a factor that is often considered to be the cause of the low ionic conductivity of the $BaZrO_3$ electrolyte [77, 78].

Dopants have been explored to improve the ionic conductivity of these samples, in particular Y. Despite this, the sintering ability of these samples was still poor [79]. Alternative studies have investigated further dopants to improve the sintering properties. In particular $BaZr_{0.8}Y_{0.2-x}In_xO_{3-\delta}$ has been explored as an alternative, where doping with In has improved densities up to 99.8% of the theoretical values [80, 81]. Despite this, a conductivity of 0.01 Scm^{-1} was achieved, which is considered relatively low, although a separate study found that $BaZr_{0.8}Y_{0.05}In_{0.15}O_{3-\delta}$ electrolyte with a $Sm_{0.5}Sr_{0.5}CoO_{3-\delta}$-$Ce_{0.8}Sm_{0.2}O_{2-\delta}$ composite cathode achieved current densities of 379 $mWcm^{-2}$, which can be considered quite high when using a barium zirconate base as the electrolyte [80, 82].

$BaZr_{0.7}Sn_{0.1}Y_{0.2}O_{3-\delta}$ has been explored as a possible electrolyte material that would be chemically stable and have good chemical conductivity. Sn was used as a dopant to improve the conductivity of the barium zirconate electrolyte and once again a good peak power density of 360 $mWcm^{-2}$ [83]. Although the power output was not as high as other PCCC electrolytes $BaZr_{0.7}Sn_{0.1}Y_{0.2}O_{3-\delta}$ were shown to remain stable in humid 3% CO_2 atmosphere at 600°C for 10 h, compared to $BaCe_{0.7}Zr_{0.1}Y_{0.2}O_{3-\delta}$ which, when exposed to the same conditions displayed, was show to degrade [83].

Neodymium (Nd) doping has been shown to improve the sintering ability and conductivity of $BaZr_{1-x}Y_xO_{3-\delta}$ [84] . While its tolerance to CO_2 remained the same. Pr doping onto the B site, along side Y, can be done to improve the CO_2 tolerance of the sample as well [85]. However the performance of the cell remained fairly low, reaching 124 $mWcm^{-2}$ at 600°C using a $Sm_{0.5}Sr_{0.5}CoO_{3-\delta}$-$Ce_{0.8}Sm_{0.2}O_{2-\delta}$ cathode [85].

2.2.3 Barium Cerate-Zirconates

Compounds with a mixture of Ce and Zr on the B site have been explored as possible electrolytes. These compositions are able to complement the shortfalls of each other. They are able to have ionic conductivity, while remaining chemically stable [86-88]. Once again Y doping has been shown to improve the ionic conductivity of these systems [88]. A commonly occurring composition appears to be $Ba(Ce/Zr)_{1-x}Y_xO_{3-\delta}$, with a large amount of literature stating it as the electrolyte used (Table 2.1). A delicate balance must be considered with Zr, as its introduction has been shown to reduce conductivity and mean grain size [89].

The chemical stability of $BaCe_{0.8-x}Zr_xY_{0.2}O_{3-\delta}$ has been explored and showed that increasing Zr content could improve the chemical stability of the material [63]. In particular it was seen that increasing the content of Zr past x=0.2 allowed the compound to remain chemically stable in a CO_2 atmosphere. While $BaCe_{0.4}Zr_{0.4}Y_{0.2}O_{3-\delta}$, $BaCe_{0.2}Zr_{0.6}Y_{0.2}O_{3-\delta}$ and $BaZr_{0.8}Y_{0.2}O_{3-\delta}$ remained chemically stable. Although with increasing Zr the ionic conductivity of the samples was seen to decrease. In effect the qualities of the barium zirconate samples were adopted by the new composition. $BaCe_{0.55}Zr_{0.3}Y_{0.15}O_{3-\delta}$ has shown to be used a successful electrolyte material, in a PCCFC, on two separate occasions producing high current densities [90, 91]. A power density of 1100 $mWcm^{-2}$ and 1300 $mWcm^{-2}$ was achieved by Bae *et al.* [90] and An *et al.* [91] respectively, both at 600°C. Bae *et al.* [90] used an anode consisting of Ni with yttrium-stabilised zirconia (YSZ) followed by a layer of NiO with $BaCe_{0.55}Zr_{0.3}Y_{0.15}O_{3-\delta,}$ and a $La_{0.6}Sr_{0.4}CoO_{3-\delta}$ cathode. While An *et al.* [91] used an anode consisting of NiO with $BaCe_{0.55}Zr_{0.3}Y_{0.15}O_{3-\delta}$ and a $Ba_{0.5}Sr_{0.5}Co_{0.8}Fe_{0.2}O_{3-\delta}$ cathode.

Y has previously been shown to improve ionic conductivity, in part due to its small ionic radius compared to the A site cation, ranging from 0.9 to 1.075 Å. Yb has a smaller ionic radius, ranging from 0.868 to 1.042 Å. Therefore, it was hoped that Yb doping would further improve the ionic conductivity. A cell with a composition of $BaCe_{0.7}Zr_{0.1}Y_{0.1}Yb_{0.1}O_{3-\delta}$, with a $Sm_{0.5}Sr_{0.5}Fe_{0.8}O_{3-\delta}$-$Ce_{0.8}Sm_{0.2}O_{2-\delta}$ cathode, has been shown to produce a power output of 505 $mWcm^{-2}$ [92].

Introducing cobalt (Co) into the structure was seen to improve the conductivity of the sample and power density, as seen by Wan *et al.* [93] who fabricated a PCCFC with $BaCe_{0.5}Co_{0.2}Zr_{0.1}Y_{0.1}Yb_{0.1}O_{3-\delta}$ as the electrolyte and $PrBaCo_2O_{5+\delta}$-$BaCe_{0.7}Zr_{0.1}Y_{0.1}Yb_{0.1}O_{3-\delta}$ as the composite cathode achieved 670 $mWcm^{-2}$ [93]. Co-doping In and Bi, improves the sintering ability of the ceramic material therefore denser pellets are formed. Bi doping of an electrolyte material, in particular, has been shown to improve the power density of the cell, Ling *et al.* [94] compared $BaZr_{0.75}In_{0.2}Bi_{0.05}O_{3-\delta}$ electrolyte with that of $BaZr_{0.8}In_{0.2}O_{3-\delta}$. The PCCFC consisting of a $BaZr_{0.75}In_{0.2}Bi_{0.05}O_{3-\delta}$ electrolyte and $PrBaCo_2O_{5+\delta}$-$Sm_{0.2}Ce_{0.8}O_{1.9}$ composite cathode had a power output of 340 $mWcm^{-2}$. While the maximum power output of a $BaZr_{0.8}In_{0.2}O_{3-\delta}$ electrolyte was 85 $mWcm^{-2}$. It showed by noted that the comparison performed by Ling *et al.* [94] did not note the cathode used for $BaZr_{0.8}In_{0.2}O_{3-\delta}$.

Zn and potassium (K) can also improve the sintering ability and density of the samples [95, 96]. Ruiz-Trejo *et al.* [95] used a Zn based electrolyte for CO_2 electrolysis. However, Duan *et al.* [70] showed that it is not necessary to incorporate Zn into the electrolyte for use for CO_2 electrolysis, as they used $BaCe_{0.7}Zr_{0.1}Y_{0.1}Yb_{0.1}O_{3-\delta}$.

Table 2.1: Table showing various PCC material compositions with the power densities achieved in fuel cell testing. Data given in descending order of power density.

Electrolyte	Anode	Cathode	Power density ($mW\ cm^{-2}$)	Temperature (°C)	Ref
$BaCe_{0.55}Zr_{0.3}Y_{0.15}O_{3-\delta}$	NiO – $BaCe_{0.55}Zr_{0.3}Y_{0.15}O_{3-\delta}$	$Ba_{0.5}Sr_{0.5}Co_{0.8}Fe_{0.2}O_{3-\delta}$	1300	600	[91]
$BaCe_{0.7}Zr_{0.1}Y_{0.1}Yb_{0.1}O_{3-\delta}$	NiO – $BaCe_{0.7}Zr_{0.1}Y_{0.1}Yb_{0.1}O_{3-\delta}$	$BaFe_{0.5}Sn_{0.2}Bi_{0.3}O_{3-\delta}$	1277	700	[97]
$BaCe_{0.55}Zr_{0.3}Y_{0.15}O_{3-\delta}$	NiO – $BaCe_{0.55}Zr_{0.3}Y_{0.15}O_{3-\delta}$	$La_{0.6}Sr_{0.4}CoO_{3-\delta}$	1100	600	[90]
$BaCe_{0.7}Zr_{0.1}Y_{0.1}Yb_{0.1}O_{3-\delta}$	NiO – $BaCe_{0.7}Zr_{0.1}Y_{0.1}Yb_{0.1}O_{3-\delta}$	LSF, composition not given	838	700	[98]
$BaCe_{0.7}Zr_{0.1}Y_{0.2}O_{3-\delta}$	NiO – $BaCe_{0.7}Zr_{0.1}Y_{0.2}O_{3-\delta}$	$Sm_{0.5}Sr_{0.5}CoO_3$ – $BaCe_{0.7}Zr_{0.1}Y_{0.2}O_{3-\delta}$	780	700	[99]
$BaCe_{0.68}Zr_{0.1}Y_{0.1}Yb_{0.1}Co_{0.02}O_{3-\delta}$	NiO – $BaCe_{0.7}Zr_{0.1}Y_{0.1}Yb_{0.1}O_{3-\delta}$	$PrBaCo_2O_{5+\delta}$	670	700	[93]
$BaCe_{0.7}Zr_{0.1}Y_{0.2}O_{3-\delta}$	NiO - $BaCe_{0.7}Zr_{0.1}Y_{0.2}O_{3-\delta}$	$La_{0.25}Pr_{0.25}Sr_{0.5}FeO_{3-\delta}$	616	700	[100]
$BaZr_{0.8}Y_{0.2}O_{3-\delta}$	NiO – $BaCe_{0.7}Zr_{0.2}Y_{0.1}O_{3-\delta}$	$Sm_{0.5}Sr_{0.5}CoO_{3-\delta}$ – $Ce_{0.8}Sm_{0.2}O_{2-\delta}$	550	600	[101]
$BaCe_{0.7}Zr_{0.1}Y_{0.1}Yb_{0.1}O_{3-\delta}$	NiO – $BaCe_{0.7}Zr_{0.1}Y_{0.1}Yb_{0.1}O_{3-\delta}$	$Sm_{0.5}Sr_{0.5}Fe_{0.8}Cu_{0.2}O_{3-\delta}$ – $Ce_{0.8}Sm_{0.2}O_{2-\delta}$	505	700	[92]

Table 2.1 part 2: Table showing various PCC material compositions with the power densities achieved in fuel cell testing. Data given in descending order of power density.

Electrolyte	Anode	Cathode	Power density ($mW\ cm^{-2}$)	Temperature (°C)	Ref
$BaCe_{0.7}Zr_{0.1}Y_{0.2}O_{3-\delta}$	NiO – $BaCe_{0.7}Zr_{0.1}Y_{0.2}O_{3-\delta}$	$LaNi_{0.6}Fe_{0.4}O_{3-\delta}$ – $La_2NiO_{4+\delta}$	490	700	[102]
$BaCe_{0.7}Zr_{0.1}Y_{0.1}Yb_{0.1}O_{3-\delta}$	NiO – $BaCe_{0.7}Zr_{0.1}Y_{0.1}Yb_{0.1}O_{3-\delta}$	$BaCe_{0.6}Zr_{0.3}Y_{0.1}O_{3-\delta}$ – $BaCo_{0.4}Fe_{0.4}Zr_{0.1}Y_{0.1}O_{3-\delta}$	455	500	[103]
$BaCe_{0.4}Zr_{0.4}Y_{0.2}O_{3-\delta}$	NiO – $BaCe_{0.4}Zr_{0.4}Y_{0.2}O_{3-\delta}$	$La_{0.7}Sr_{0.3}Mn_{0.7}Ni_{0.3}O_{3-\delta}$	386	700	[104]
$BaZr_{0.8}Y_{0.05}In_{0.15}O_{3-\delta}$	NiO – $BaZr_{0.8}Y_{0.05}In_{0.15}O_{3-\delta}$	$Sm_{0.5}Sr_{0.5}CoO_{3-\delta}$ – $Ce_{0.8}Sm_{0.2}O_{2-\delta}$	379	700	[80]
$BaZr_{0.7}Sn_{0.1}Y_{0.2}O_{3-\delta}$	NiO – $BaZr_{0.7}Sn_{0.1}Y_{0.2}O_{3-\delta}$	$Sm_{0.5}Sr_{0.5}CoO_{3-\delta}$ – $Ce_{0.8}Sm_{0.2}O_{2-\delta}$	360	700	[83]
$BaCe_{0.7}Zr_{0.1}Y_{0.1}Yb_{0.1}O_{3-\delta}$	NiO - $BaCe_{0.7}Zr_{0.1}Y_{0.1}Yb_{0.1}O_{3-\delta}$	$Sm_{0.5}Sr_{0.5}Fe_{0.8}Cu_{0.2}O_{3-\delta}$ – $Ce_{0.8}Sm_{0.2}O_{2-\delta}$	289	600	[92]
$BaCe_{0.4}Zr_{0.4}Y_{0.2}O_{3-\delta}$	NiO – $BaZr_{0.85}Y_{0.15}O_{3-\delta}$	$Pr_2NiO_{4+\delta}$	243	700	[105]
$BaZr_{0.8}Y_{0.2}O_{3-\delta}$	NiO – $BaZr_{0.84}Y_{0.16}O_{2-\delta}$	$La_{0.6}Sr_{0.4}Co_{0.2}Fe_{0.8}O_{3-\delta}$ – $Gd_{0.1}Ce_{0.9}O_{2-\delta}$	176	700	[106]
$BaZr_{0.8}Y_{0.2}O_{3-\delta}$	NiO – $BaCe_{0.7}Zr_{0.2}Y_{0.1}O_{3-\delta}$	$Sm_{0.5}Sr_{0.5}CoO_{3-\delta}$-$Ce_{0.8}Sm_{0.2}O_{2-\delta}$	170	700	[107]

2.3 Cathode

The cathode is where the oxygen reduction reaction (ORR) takes places within a PCCFC (2.7).

$$\frac{1}{2}O_2 + 2H^+ + 2e^- \rightarrow H_2O \qquad (2.7)$$

The reverse of this occurs on the same electrode with an electrolyser, however in this case the cathode is defined as the anode. The cathode must be porous so that O_2 is able to diffuse through and interact with the dense electrolyte. It must also be a good electrical and ionic conductor, having high catalytic activity towards the ORR. The cathode should be chemically stable in humid atmosphere as H_2O will be present when operating as both the fuel cell and electrolyser. Cathodes can be classified into three main types (Figure 2.1) known as pure electronic conductors (such as platinum), mixed ionic electronic conductors (MIEC), and triple conductors. (TC).

Triple phase boundaries (TPBs) are key for cathodes that have been sintered onto an electrolyte. TPB are the active sites between an electrode and an electrolyte, which allow the interaction between the reactant gases, conducted ions, and conducted electrons.

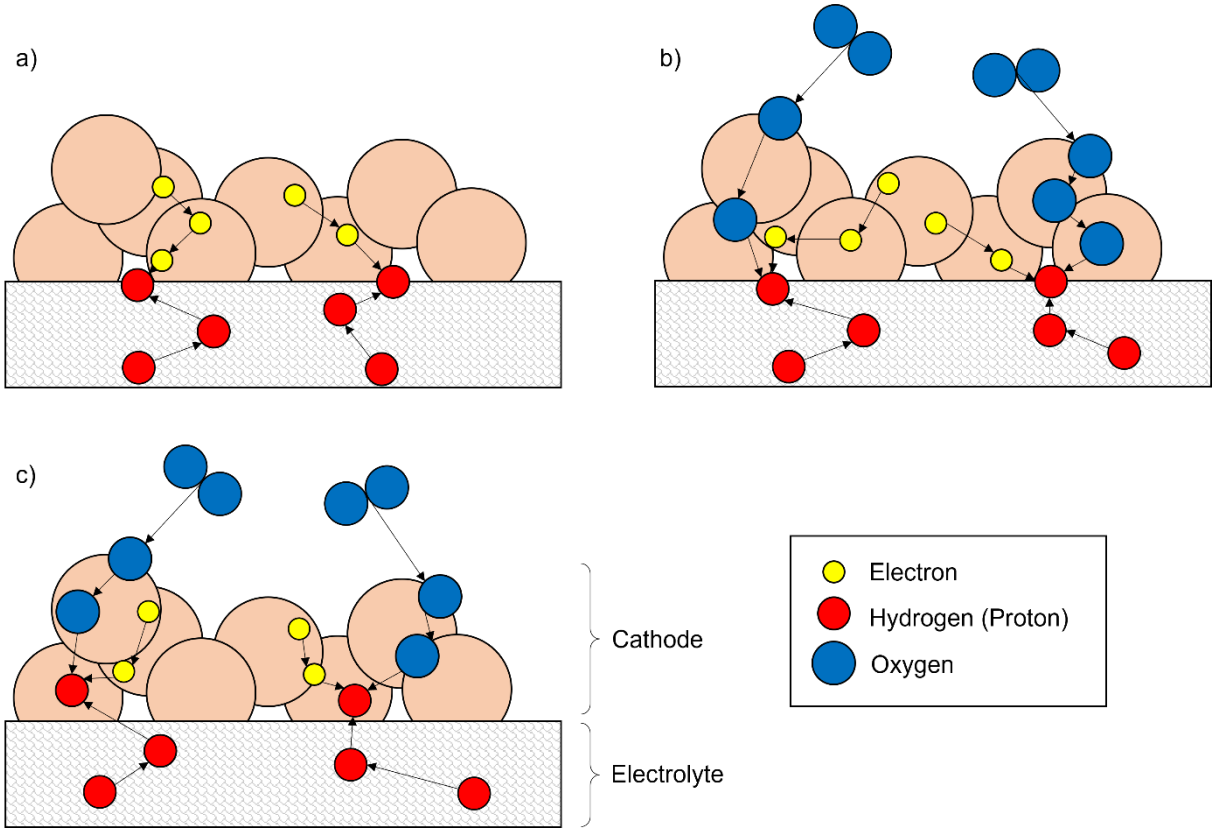


Figure 2.1: Figure showing various cathodes types a) pure electronic conductor b) mixed ionic electronic conductor, and c) triple conductor

2.3.1 Mixed Ionic Electronic Conductors

MIEC are able to conduct both ions and electrons and have been heavily researched for OC-SOCs. These materials have then been translated to the PCCC field for use as electrode, suggesting that as long as the electrolyte is a proton conductor, the electrode does not need to be [108]. However, the reverse does not hold true. Sozal *et al.* [109] showed that by performing symmetrical cell measurements using an oxide conducting electrolyte with a proton conducting electrode there will be no difference in resistivity between humid and dry air.

When applying MIECs to PCCCs, oxygen gas diffuses into the pores in the cathode, where it is dissociated and reduced. Protons are transferred across the anode and electrolyte, where they then interact with the oxygen ions to form H_2O [110]. In the case of pure MIECs, the TPB has a limited area as it only occurs on the surface of the electrolyte where the electrolyte and cathode come into contact.

Research in this area is sparse, as composite MIECs are preferred (Table 2.2). Recently there have been some noteworthy compositions which have been used in high performing cells such as $Ba_{0.5}Sr_{0.5}Co_{0.8}Fe_{0.2}O_{3-\delta}$ which was used in a cell that achieved 1300 $mWcm^{-2}$ (at 600°C), a $La_{0.6}Sr_{0.4}Co_{0.2}Fe_{0.8}O_{3-\delta}$ which achieved 753 $mWcm^{-2}$ (at 700°C) and $La_{0.6}Sr_{0.4}CoO_{3-\delta}$ cathode which achieved 1100 $mWcm^{-2}$ (at 600°C) [90, 91, 111].

Table 2.2: Table showing various cells that used MIECs. Cells split in terms of cathode used, followed by power density.

Electrolyte	Anode	Cathode	Power Density ($mW\ cm^{-2}$)	Temperature (°C)	Ref
$BaCe_{0.7}Zr_{0.1}Y_{0.2}O_{3-\delta}$	NiO - $BaCe_{0.7}Zr_{0.1}Y_{0.2}O_{3-\delta}$	$Sm_{0.5}Sr_{0.5}CoO_{3-\delta}$ – $BaCe_{0.7}Zr_{0.1}Y_{0.2}O_{3-\delta}$	780	700	[99]
$BaCe_{0.7}Zr_{0.1}Y_{0.2}O_{3-\delta}$	NiO - $BaCe_{0.7}Zr_{0.1}Y_{0.2}O_{3-\delta}$	$Sm_{0.5}Sr_{0.5}CoO_{3-\delta}$ – $BaCe_{0.7}Zr_{0.1}Y_{0.2}O_{3-\delta}$	725	700	[112]
$BaCe_{0.7}Zr_{0.1}Y_{0.2}O_{3-\delta}$	NiO - $BaCe_{0.7}Zr_{0.1}Y_{0.2}O_{3-\delta}$	$Sm_{0.5}Sr_{0.5}CoO_{3-\delta}$ – $BaCe_{0.7}Zr_{0.1}Y_{0.2}O_{3-\delta}$	580	700	[113]
$BaCe_{0.8}Zr_{0.1}Y_{0.1}O_{3-\delta}$	NiO - $BaCe_{0.8}Zr_{0.1}Y_{0.1}O_{3-\delta}$	$Sm_{0.5}Sr_{0.5}CoO_{3-\delta}$ – $BaCe_{0.8}Zr_{0.1}Y_{0.1}O_{3-\delta}$	530	700	[114]
$BaZr_{0.1}Ce_{0.66}Ni_{0.04}Y_{0.2}O_{3-\delta}$	NiO - $BaZr_{0.1}Ce_{0.66}Ni_{0.04}Y_{0.2}O_{3-\delta}$	$Sm_{0.5}Sr_{0.5}CoO_{3-\delta}$ – $BaZr_{0.1}Ce_{0.66}Ni_{0.04}Y_{0.2}O_{3-\delta}$	477	700	[115]
$BaCe_{0.7}Zr_{0.1}Y_{0.2}O_{3-\delta}$	NiO - $BaCe_{0.7}Zr_{0.1}Y_{0.2}O_{3-\delta}$	$Sm_{0.5}Sr_{0.5}CoO_{3-\delta}$ – $BaCe_{0.7}Zr_{0.1}Y_{0.2}O_{3-\delta}$	300	600	[116]
$BaZr_{0.8}Y_{0.2}O_{3-\delta}$	NiO - $BaZr_{0.8}Y_{0.2}O_{3-\delta}$	$Sm_{0.5}Sr_{0.5}CoO_{3-\delta}$ – $BaZr_{0.8}Y_{0.2}O_{3-\delta}$	132	600	[116]
$BaCe_{0.7}Zr_{0.1}Y_{0.2}O_{3-\delta}$	NiO - $BaCe_{0.7}Zr_{0.1}Y_{0.2}O_{3-\delta}$	$Sm_{0.5}Sr_{0.5}CoO_{3-\delta}$ – $Ce_{0.8}Sm_{0.2}O_{2-\delta}$	665	700	[117]
$BaZr_{0.8}Y_{0.05}In_{0.15}O_{3-\delta}$	NiO - $BaZr_{0.8}Y_{0.05}In_{0.15}O_{3-\delta}$	$Sm_{0.5}Sr_{0.5}CoO_{3-\delta}$ – $Ce_{0.8}Sm_{0.2}O_{2-\delta}$	379	700	[80]
$BaZr_{0.7}Sn_{0.1}Y_{0.2}O_{3-\delta}$	NiO - $BaZr_{0.7}Sn_{0.1}Y_{0.2}O_{3-\delta}$	$Sm_{0.5}Sr_{0.5}CoO_{3-\delta}$ – $Ce_{0.8}Sm_{0.2}O_{2-\delta}$	360	700	[83]
$BaZr_{0.7}Pr_{0.1}Y_{0.2}O_{3-\delta}$	NiO - $BaZr_{0.8}Y_{0.1}O_{3-\delta}$	$La_{0.6}Sr_{0.4}Co_{0.2}Fe_{0.8}O_{3-\delta}$- $BaZr_{0.7}Pr_{0.1}Y_{0.2}O_{3-\delta}$	163	600	[118]
$BaZr_{0.8}Y_{0.1}O_{3-\delta}$	NiO - $BaZr_{0.8}Y_{0.1}O_{3-\delta}$	$La_{0.6}Sr_{0.4}Co_{0.2}Fe_{0.8}O_{3-\delta}$ – $BaCe_{0.9}Yb_{0.1}O_{3-\delta}$	110	600	[119]

2.3.1.1 Mixed Electronic Ionic Conductors as Composite Cathodes

An alternative approach to using MIECs is to combine them with a PCC, creating a composite of an oxide conductor and a proton conductor, thus having conductivity characteristics similar to a TC. By mixing the two together the reactive area is increased, and thus the amount of TPBs allowing the electrochemical reaction to occur across the complete volume of the cathode. Composites can also improve the compatibility between the electrolyte and the cathode if the composite consists of the same material as the electrolyte.

A common composite that has been explored is $Sm_{0.5}Sr_{0.5}CoO_{3\delta}$. The presence of Co allows it to have high ionic conductivities. Mixing this with a PCC, commonly $BaCe_{0.7}Zr_{0.1}Y_{0.2}O_{3-\delta}$, is able to produce high power outputs [99, 112, 113]. The variable in these methods tends to be the way in which the cell has been manufactured, with co-pressing and co-sintering achieving the highest power output [99].

Yang *et al.* [99] were able to produce a $Sm_{0.5}Sr_{0.5}CoO_{3\delta}$ composite cathode, with a $BaCe_{0.7}Y_{0.2}Zr_{0.1}O_{3-\delta}$ electrolyte, that produced a peak power density of 780 $mWcm^{-2}$, by co-pressing and co-firing the cell. Liu *et al.* [113] used the same cell components however, attempted an alternative approach by creating an electrolyte suspension and co-sintering at 1400°C. Both papers achieved the same thickness of their electrolyte, 20 μm, but saw variations in their power outputs at 700°C and sintered the cathode at 1000°C for 3 h [99, 113]. Alternatively Dai *et al.* [116] co-sintered but varied the cathode composite. Instead of using the same electrolyte ($BaCe_{0.7}Zr_{0.1}Y_{0.2}O_{3-\delta}$) in the composite, they opted to use $BaZr_{0.8}Y_{0.2}O_{3-\delta}$ stopping the formation of CeO_2 and $BaCoO_3$ impurities. However this saw a decrease in power output.

$Sm_{0.5}Sr_{0.5}Fe_{0.8}Cu_{0.2}O_{3-\delta}$-$Ce_{0.8}Sm_{0.2}O_{2-\delta}$ composites have been explored with $BaZr_{0.7}Sn_{0.1}Y_{0.2}O_{3-\delta}$, and $BaZr_{0.8}Y_{0.15}In_{0.05}O_{3-\delta}$, although they have not shown to give as high power densities such as with $BaCe_{0.7}Zr_{0.1}Y_{0.2}O_{3-\delta}$ [80, 83]. Using a $BaCe_{0.7}Zr_{0.1}Y_{0.2}O_{3-\delta}$ electrolyte with a $Sm_{0.5}Sr_{0.5}Fe_{0.8}Cu_{0.2}O_{3-\delta}$-$Ce_{0.8}Sm_{0.2}O_{2-\delta}$ cathode gave a power density of 665 $mWcm^{-2}$ [117]. However, a composite cathode of $Sm_{0.5}Sr_{0.5}Fe_{0.8}Cu_{0.2}O_{3-\delta}$-$Ce_{0.8}Sm_{0.2}O_{2-\delta}$ produces lower power densities then a composite cathode of $Sm_{0.5}Sr_{0.5}Fe_{0.8}Cu_{0.2}O_{3-\delta}$–electrolyte material.

$La_xSr_{1-x}Co_yFe_{1-y}O_{3-\delta}$ materials are another set of MIECs which have been commonly used with OC-SOCs, have been shown to have good ionic and electronic conductivity in the 600°C to 700°C temperature range. When studying them for use in proton conducting ceramics cells (PCCCs) a lower power density is seen, compared to using $Sm_{0.5}Sr_{0.5}CoO_{3\delta}$, possibly due to the poor ionic conductivity of the $BaZr_{0.8}Y_{0.2}O_{3-\delta}$ electrolyte [118, 119]. As previously mentioned, barium zirconates are dwarfed in their ionic conductivity compared to barium cerates. Therefore, the cells which utilise $BaZr_{1-x}Y_xO_{3-\delta}$ as part of the composite will most likely have lower power outputs compared to ones that utilise barium cerates.

2.3.1.2 Cobalt Free

Cathodes that contain cobalt often face the problem of incompatible thermal expansion coefficients compared to the electrolyte, therefore alternatives are often sought. Li *et al.* [120] showed that $Sr_2Fe_{1.5}Mo_{0.5}O_{6-\delta}$ could be used as a composite cathode and showed that varying the sintering temperature would cause a change in the cells performance. A sintering temperature of 1000°C was found to give the highest peak power density of 396 $mWcm^{-2}$ using a $BaCe_{0.7}Y_{0.1}Zr_{0.2}O_{3-\delta}$ electrolyte at 800°C [120]. Mao *et al.* [121] achieved a greater power density with $NdBaFe_{1.9}Mn_{0.1}O_{5+\delta}$ cathode and a $BaCe_{0.7}Y_{0.1}Zr_{0.2}O_{3-\delta}$ electrolyte to obtain a power density of 453 $mWcm^{-2}$. $NdBaFe_{2-x}Mn_xO_{5+\delta}$ where x = 0, 0.1, 0.2 and 0.3 were also explored in terms of conductivity, with $NdBaFeMnO_{5+\delta}$ showing the highest value [121]. Bi *et al.* [122] sought to maintain a $BaCe_{0.8}Sm_{0.2}O_{3-\delta}$ electrolyte layer of 16 μm with, whilst $La_{0.7}Sr_{0.3}FeO_{3-\delta}$-$BaCe_{0.8}Sm_{0.2}O_{3-\delta}$ composite cathode and was able to achieve a power density of 352 $mWcm^{-2}$. $Ba_{0.95}La_{0.05}FeO_{3-\delta}$ has been explored as a cobalt free cathode, however has an incompatible thermal expansion coefficient to that of $BaCe_{0.7}Y_{0.2}Z_{0.1}O_{3-\delta}$, to overcome this, a composite of the two was created, which was able to produce a maximum power density of 325 $mWcm^{-2}$[123].

2.3.2 Triple Conductor

TC cathode materials are able to conduct protons, oxygen and electrons, unlike MIEC which cannot conduct protons. These materials can be barium cerium or barium zirconate doped with either a transition metal or multivalent element [103, 124-126]. One such example is Co and Fe co-doping into barium zirconate, $BaCo_{0.4}Fe_{0.4}Zr_{0.2}O_{3-\delta}$, which has shown to improve electrical conductivity. The cell was tested with a $BaCe_{0.7}Zr_{0.1}Y_{0.1}Yb_{0.1}O_{3-\delta}$ electrolyte, with pure H_2 flowing to the anode, peak power density of 225 mW cm^{-2} was achieved at 600°C [124].

Further doping with Y to give the composition $BaCo_{0.4}Fe_{0.4}Zr_{0.1}Y_{0.1}O_{3-\delta}$, has showed power outputs of 405 $mWcm^{-2}$ at 500°C, a $BaCe_{0.7}Zr_{0.1}Y_{0.1}Yb_{0.1}O_{3-\delta}$ electrolyte was used once again with pure H_2 fed to the anode [103]. Between the publication of these two compositions, the cell manufacturing method was also refined, contributing to the increase it power output. Further improvements were made by combing the cathode with $BaCe_{0.6}Zr_{0.3}Y_{0.1}O_{3-\delta}$. A composite cathode was formed that was able to reach a peak power of 455 $mWcm^{-2}$, under the same conditions as previously stated [103].

A-doped barium ferrites ($BaFeO_{3-\delta}$) such as $Ba_{1-x}La_xFeO_{3-\delta}$ (x= 0.1 – 0.4), specifically $Ba_{0.9}La_{0.1}FeO_{3-\delta}$ showed an area specific resistance of 0.37Ω cm^{-2} at 700°C as a symmetrical cell [127]. Further doping proved to be possible with $Ba_{0.95}La_{0.05}Fe_{0.8}Zr_{0.1}Y_{0.1}O_{3-\delta}$ achieving 305 $mWcm^{-2}$, at 600°C, the electrolyte used was $BaCe_{0.7}Y_{0.2}Zr_{0.1}O_{3-\delta}$ [128]. Lanthanum (La) was introduced to improve CO_2 tolerance, Zr to aid in proton uptake, and Y to improve conductivity and stabilise the cubic structure [66, 128-130]. Another $BaFeO_{3-\delta}$ to show good conductivities is $BaFe_{0.8}Ce_{0.1}Y_{0.1}O_{3-\delta}$ which showed a value of 1.55 Scm^{-1}, then when mixed with $BaCe_{0.8}Fe_{0.1}O_{3-\delta}$, formed a composite with which cathode 750 $mWcm^{-2}$ with $BaCe_{0.7}Zr_{0.1}Y_{0.2}O_{3-\delta}$ electrolyte [131]. The most promising of the cobalt free $BaFeO_{3-\delta}$ is $BaFe_{0.5}Sn_{0.2}Bi_{0.3}O_{3-\delta}$, achieving 1277 $mWcm^{-2}$ again using $BaCe_{0.7}Zr_{0.1}Y_{0.2}O_{3-\delta}$ as the electrolyte [97]. Xia *et al.* found that incorporating Bi in $BaFe_{0.5}Sn_{0.5}O_{3-\delta}$ improved the hydration ability of the sample, with $BaFe_{0.5}Sn_{0.2}Bi_{0.3}O_{3-\delta}$ which had been hydrated showing a 5.53% weight loss during thermogravimetric analysis (TGA) [97].

Choi *et al*. [132] and Ma *et al*. [133] observed that introducing Pr into a sample improved its hydration ability. Ma *et al*. [133] explored using $BaCe_{0.7}Zr_{0.1}Y_{0.1}O_{3-\delta}$ electrolyte with various Pr doped $La_{0.5}Sr_{0.5}FeO_{3-\delta}$ cathodes, using pure H_2. $La_{0.25}Pr_{0.25}Sr_{0.5}FeO_{3-\delta}$ showed a peak power density of 616 $mWcm^{-2}$. Although complete substitution of La with Pr to give $Pr_{0.5}Sr_{0.5}FeO_{3-\delta}$ showed the highest H_2O incorporation, it did not show the highest power density, which is thought to be due to Pr^{4+} forming and suppressing the valence state of Fe thereby, increasing oxygen vacancy formation, thus OH^- incorporation [133].

While Choi *et al.* [132] observed the proton uptake of $PrBa_{0.5}Sr_{0.5}Co_{1.5}FeO_{5+\delta}$ through performing TGA in humid and dry air and compared the humid and dry data. From this it was determined that there was 3.5 mol% and 1.7 mol% of H_2O incorporation at 200°C and 600°C, respectively. Fuel cell testing, with a $Ba_4Ce_{0.4}Zr_{0.}Y_{0.1}Yb_{0.1}O_{3-\delta}$ electrolyte, was then performed where a maximum of 1096 $mWcm^{-2}$ at 600°C was achieved [132].

2.3.2.1 Ruddlesden Popper Nickelates

Ruddlesden-Popper nickelates have the formula $A_{n+1}Ni_nO_{3n+1}$ where A is a cation generally La, neodymium (Nd), praseodymium (Pr), or strontium (Sr) and n is the number of perovskite layers that separate the rock salt layers in the structure (Figure 2.2) [134]. These materials have been previously utilised as electrodes in OC-SOC. For this application, they have been shown to have adequate electrical conductivity and thermal stability between 500°C and 700°C , therefore they have been considered for use in PCCC, which operate in the same temperature range [135]. Further supporting this $Pr_2NiO_{4+\delta}$ has been previously shown to be able to incorporate OH^- and successfully used in a PCFCs as a TC cathode [136, 137]. Further studies into Ruddlesden-Popper nickelates, where La or Nd is on the A-site, have shown them to be viable TC cathodes [102, 138, 139].

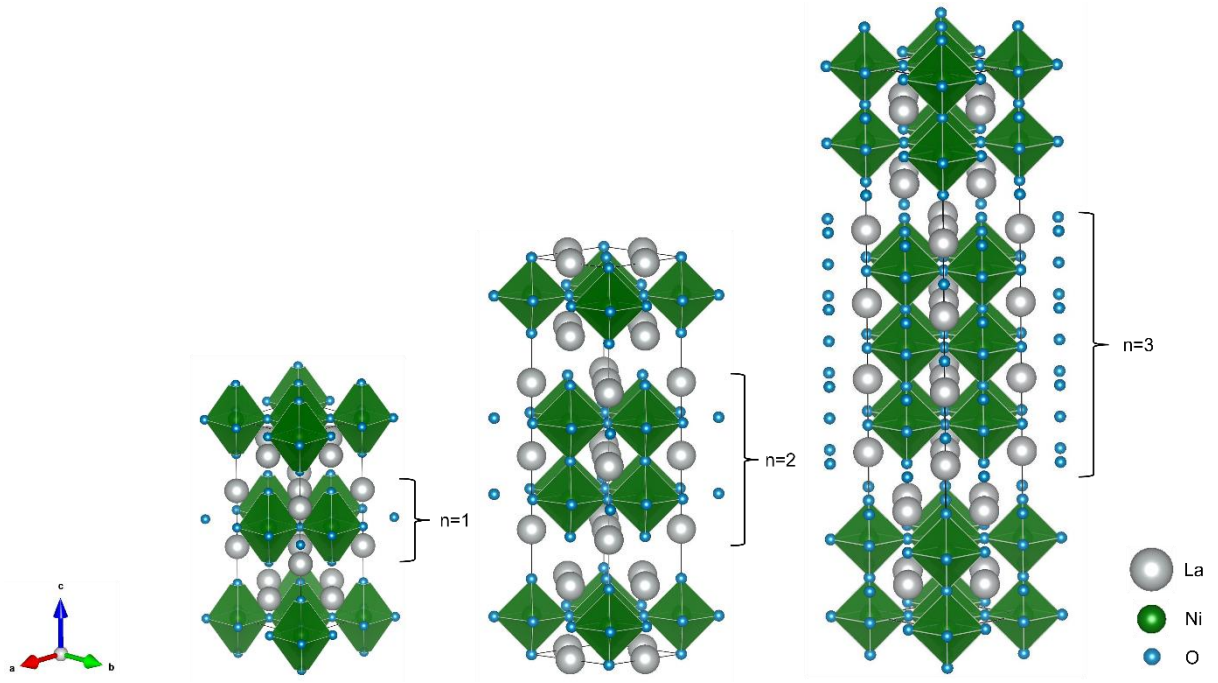


Figure 2.2: Figure showing lanthanum nickelate Ruddlesden-Popper structure. Showing $La_2NiO_{4+\delta}$ on the left, $La_3Ni_2O_{7-\delta}$ in the middle and $La_4Ni_3O_{10-\delta}$ on the right.

Symmetrical cell tests have been performed on all $Ln_2NiO_{3-\delta}$ using a $BaCe_{0.9}Y_{0.1}O_{3-\delta}$ electrolyte [140]. From these compositions $Pr_2NiO_{4+\delta}$ showed the lowest area specific resistance (ASR), therefore cell testing with a $BaCe_{0.9}Y_{0.1}O_{3-\delta}$ was performed and 180 $mWcm^{-2}$ was achieved at 600°C [137]. Future testing using $Pr_2NiO_{4+\delta}$ used a different electrolyte ($BaCe_{0.55}Zr_{0.3}Y_{0.15}O_{3-\delta}$) and was able to achieve a power output of 850 $mWcm^{-2}$ and 560 $mWcm^{-2}$ at 650°C and 600°C, respectively [137]. $Nd_2NiO_{4+\delta}$ was also explored with a $BaCe_{0.9}Y_{0.1}O_{3-\delta}$ electrolyte but a power density of 60 $mWcm^{-2}$ only, was achieved at 600°C [138].

Composite cathodes of $La_2NiO_{4+\delta}$ and $LaNi_{0.6}Fe_{0.4}O_{3-\delta}$ achieved a maximum power density of 708 $mWcm^{-2}$ [102, 139]. The high power density is possibly due to using $BaCe_{0.7}Zr_{0.1}Y_{0.2}O_{3-\delta}$ being used as an electrolyte and also through the use of an anode functional layer consisting of NiO and $BaCe_{0.7}Zr_{0.1}Y_{0.2}O_{3-\delta}$ in a 6:1 ratio [102]. The functional layer was been the electrolyte and anode, the anode also being a mixture of NiO and $BaCe_{0.7}Zr_{0.1}Y_{0.2}O_{3-\delta}$, but in a 65:35 ratio [102]. The $La_2NiO_{4+\delta}$-$LaNi_{0.6}Fe_{0.4}O_{3-\delta}$ composite was found to have a lower polarisation resistance (R_p) compared to

$Sm_{0.2}Ce_{0.8}O_{2-\delta}$-$LaNi_{0.6}Fe_{0.4}O_{3-\delta}$. Suggesting that $La_2NiO_{4+\delta}$-$LaNi_{0.6}Fe_{0.4}O_{3-\delta}$ had a better composite formulation, possibly due to the oxygen interstitial sites present in the $La_2NiO_{4+\delta}$ structure [102].

2.4 Anode

The anode of a PC-SOFC should be a good electrical conductor while also being porous. The porosity allows the gaseous reactants to travel through the electrode and interact with the triple phase boundary, through the layer. Often the anode is a mixture of the electrolyte material used along with NiO [70, 90, 91, 138]. As NiO forms a dense layer when heated, often other compounds, such as starch, are added to ensure the anode is porous. The majority of the literature will use some ratio variation of the electrolyte material and NiO, with at least 60% NiO in the material mix [92, 99, 106, 107, 138].

The same electrolyte material does not always need to be used, although is often preferred so that there is good adhesion between the anode and electrolyte. Sun *et al.* [107] have shown that a $BaZr_{0.8}Y_{0.1}O_{3-\delta}$ electrolyte can be used with an anode consisting of $BaCe_{0.7}Zr_{0.3}Y_{0.1}O_{3-\delta}$ and NiO and still achieve good adhesion between the anode and electrolyte. $BaZr_{0.8}Y_{0.1}O_{3-\delta}$ was chosen as an electrolyte due to its better chemical stability.

2.5 Fabrication

Currently PCCC cannot be commercially purchased, therefore if cells are desired then both material synthesis and cell fabrication are required. The synthesis of PCC, in large quantities can be difficult on a laboratory scale. Thus, fabrication methods that use a small quantity of powders are often preferred. The fabrication of cells also requires high sintering temperatures to create a dense electrolyte, especially when using a barium zirconate-based electrolyte. These high temperatures are not always accessible, due to furnace limitations Therefore if using the conventional method of sintering in a furnace, a sintering aid is often required to achieve a dense electrolyte at a lower temperatures. Alternatively sintering methods that do not require a high temperature furnace are often explored.

2.5.1 Synthesis

Within the literature the common synthesis method of choice is often through solid state synthesis, which consists of mixing the oxides together with intermittent grinding and heating to break the bonds between the precursors and form new ones. The process can be quite slow as diffusion through the solid is limited and only produces small batches of material [141]. Solid state reactive sintering (SSSR) uses the principle of solid state synthesis to form dense pellets [142].

Solid state synthesis cannot often be used to produce more complex compositions, instead the alternative method of sol-gel is used to produce various PCCs [63, 85, 87, 88, 143, 144]. Sol-gel is a wet chemical technique that produces a gel, as the precursors break down and water evaporates. The gel is then heated to decompose the unwanted precursors and leave a solid, which will then be heated to higher temperature. It also has the advantage of being able to produce larger batches [141]. It is thereby possible to synthesise the same material but at a lower temperature compared to solid state process. This was shown by Sawant who was unable to produce $BaCe_{0.6}Zr_{0.2}Y_{0.2}O_{3-\delta}$, $BaCe_{0.4}Zr_{0.4}Y_{0.2}O_{3-\delta}$ and $BaCe_{0.2}Zr_{0.6}Y_{0.2}O_{3-\delta}$ by solid state, but could through sol-gel [63].

2.5.2 Sintering Aids

Sintering aids are used to improve the density of an electrolyte while not requiring as high a temperature as would normally be used (Table 2.3). Creating a dense electrolyte is often difficult with $BaZr_{1-x}B_xO_{3-\delta}$ compositions in particular, but can also be an issue for $Ba(Ce/Zr)_{1-x}B_xO_{3-\delta}$, temperature often exceeding 1600°C [145-147].

A lot of the early research focused on improving the sintering ability of barium zirconates. One of the earliest pieces of work was performed by Babilo *et al.* [146] (Figure 2.3) who looked at using scandium oxide, titanium oxide, vanadium oxide, chromium oxide, manganese oxide, iron (III) oxide, cobalt oxide, copper oxide, nickel oxide and zinc oxide. Nickel oxide (NiO) was seen to give the densest pellet. However, Babilo *et al.* [146] did not further explore the use of NiO as a sintering aid as it improved the electrical conductivity of the sample, which is not what is wanted from an electrolyte.

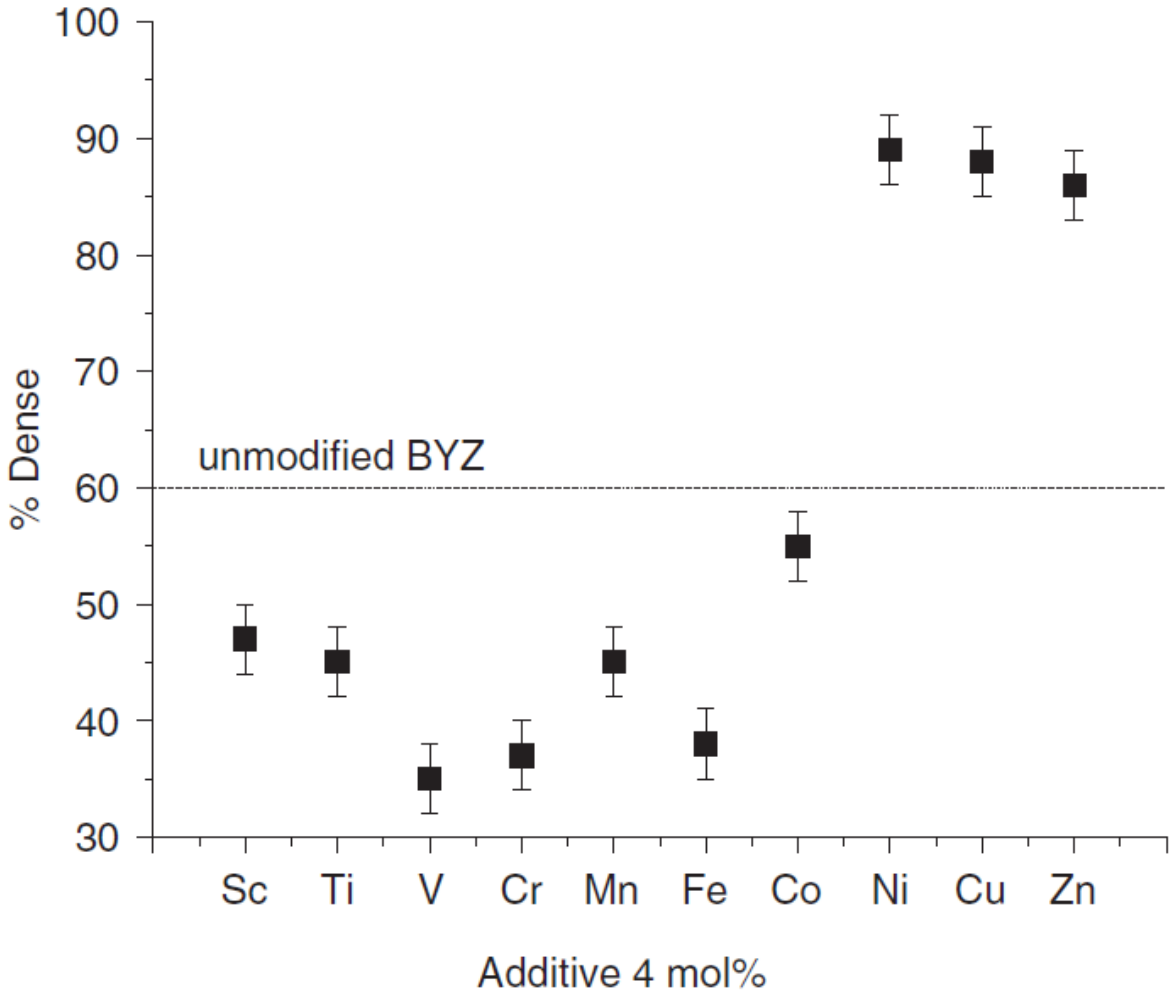


Figure 2.3: Impact of the various sintering aids employed by Babilo *et al.* [146]. Reproduced from [146] with permission from John Wiley and Sons.

Table 2.3: Table showing the sintering aids used with various electrolytes. The sintering aids with no density given belong samples where the electrolyte was part of a cell, so no density was given.

Sintering Aid	Electrolyte	Quantity of Sintering Aid (%)	Sintering Temperature (°C)	Sintered Time (h)	Density (%)	Ref
NiO	$BaZr_{0.8}Y_{0.2}O_{3-\delta}$	2 wt	1350	10	95	[148]
CaO	$BaZr_{0.8}Y_{0.2}O_{3-\delta}$	4 mol	1500	6	92.7	[149]
CaO	$BaZr_{0.8}Y_{0.2}O_{3-\delta}$	4 mol	1600	6	97.5	[149]
$LiNO_3$	$BaZr_{0.8}Y_{0.2}O_{3-\delta}$	-	1600	6	96.5	[150]
CuO	$BaZr_{0.84}Y_{0.15}Cu_{0.1}O_{3-\delta}$	1 mol	1500	3	-	[151]
ZnO	$BaZr_{0.8}Y_{0.2}O_{3-\delta}$	4 mol	1300	4	93	[146]
NiO	$BaCe_{0.7}Zr_{0.1}Y_{0.1}Yb_{0.1}O_{3-\delta}$	1 wt	1400	18	-	[70]

Sintered samples using zinc oxide (ZnO) were shown to form dense pellets at 1300°C that remained chemically stable in CO_2, however, a decrease in ionic conductivity was observed [146]. Further studies have continued to explore ZnO as a sintering aid [147, 152-154]. Tao *et al.* [154] has shown the applied ZnO as a sintering aid to $BaCe_{0.8}Y_{0.2}O_{3-\delta}$ and $BaCe_{0.5}Zr_{0.3}Y_{0.2}O_{3-\delta}$ to reduce the sintering temperature to 1500°C for 10 h, however a decrease in ionic conductivity was observed. Alternatively, Zn was incorporated into the crystal structure to give the composition $BaCe_{0.5}Zr_{0.3}Y_{0.16}Zn_{0.04}O_{3-\delta}$, which was found to have a conductivity on par with other cerium samples [154]. In the case of $BaCe_{0.5}Zr_{0.3}Y_{0.16}Zn_{0.04}O_{3-\delta}$ a dense pellet could be achieved at 1325°C in 10 h.

Further studies have been made inspecting the hydration ability of $BaZr_{0.8}Y_{0.2}O_{3-\delta}$ when paired with a sintering aid. It has been shown that the using copper oxide (CuO), NiO or ZnO will reduce the proton conductivity of the sample [155]. Other sintering aids have been explored with varying degrees of

success, some of which have improved the electrochemical properties of the material, as denser pellets can be produced [149, 150].

NiO has been used as a common sintering aid with many PCCC's [70, 77]. It has been seen that the Ni occupies an interstitial position in the lattice, specifically the (1/2, 0, 0) position in $BaZr_{0.8}Y_{0.1}O_{3-\delta}$ [156]. It may suppress the ability of the electrolyte to become hydrated while also reducing electrical conductivity [156, 157]. It has also been observed that 2 wt% of NiO with $BaZr_{0.8}Y_{0.1}O_{3-\delta}$ can cause the formation of BaY_2NiO_5, aiding in densification and grain growth [148].

An interesting approach to producing cells with a dense electrolyte has been taken by Tong *et al.* [142] who attempted a method known as solid-state reactive sintering (SSRS) to produce $BaZr_{.8}Y_{0.2}O_{3-\delta}$ pellets. They mixed all precursors for the electrolyte with the sintering aid and sintered them. Various sintering aids were employed for this method such as LiF, Al_2O_3, SnO_2 and NiO. However Al_2O_3 and SnO_2 did not improve the density of the pellet. When 1 wt% LiF and 2 wt% LiF were applied, 40% and 50% of the theoretical density was achieved respectively. The ideal sintering aid was found to be NiO which achieved over 95% after sintering at 1400°C for 24 h. This method has been further used with $BaCe_{0.7}Zr_{0.1}Y_{0.1}Yb_{0.1}O_{3-\delta}$ electrolyte powders to develop a cell that achieved a power output of 405 $mWcm^{-2}$ [103]. A similar method has been used with 1.4 wt% CuO producing a power density of 268 $mWcm^{-2}$ [103]. Both these measurements were taken at 600°C with a $BaCo_{0.4}Fe_{0.4}Zr_{0.1}Y_{0.1}O_{3-\delta}$ cathode.

Furthering this work, Duan *et al.* [70] applied the SSRS method to proton conducting ceramic electrolysers (PCCEs), using NiO as a sintering aid. A $BaCe_{0.7}Zr_{0.1}Y_{0.1}Yb_{0.1}O_{3-\delta}$ electrolyte was used, the fuel electrode consisted of 40 wt% $BaCe_{0.7}Zr_{0.1}Y_{0.1}Yb_{0.1}O_{3-\delta}$ and 60 wt% NiO and the steam electrode was $BaCo_{0.4}Fe_{0.4}Zr_{0.1}Y_{0.1}O_{3-\delta}$ [70]. A current density of approximately 1500 $mAcm^{-2}$ with 10% H_2O at 500°C. Tests were also performed at 550°C and 600°C, with similar results achieved.

It has been shown that Ni is able to diffuse across from the anode to the electrolyte and affect the morphology of the electrolyte (Figure 2.4) [155, 158]. Co-sintering of an anode and electrolyte at

1300°C showed 1.3 wt% of Ni in the electrolyte layer near the electrolyte/anode interface. Increasing the sintering temperature to 1400°C showed 2.8 wt% of Ni within the electrolyte layer [158]. The presence of the Ni can be seen to have a positive effect, as the cell co-sintered at 1350°C showed a power density of 377 $mWcm^{-2}$ [158] When increasing the sintering temperature further to 1400°C, though, the Ni has a negative effect, reducing the power density to 360 $mWcm^{-2}$ [158]. These measurements were taken using $BaCe_{0.7}Zr_{0.1}Y_{0.1}Yb_{0.1}O_{3-\delta}$ as an electrolyte.

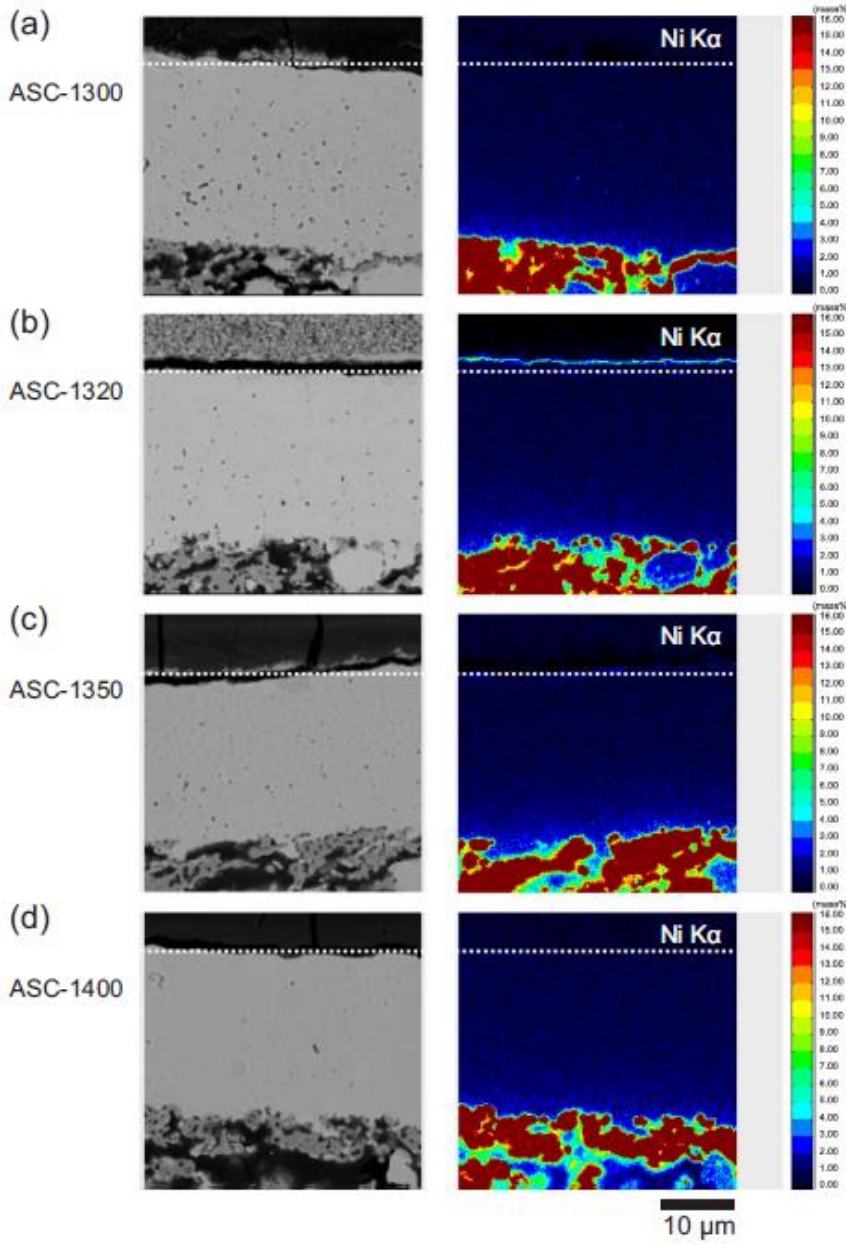


Figure 2.4: Field emission electron probe microanalysis showing the cross section of the cells sintered at a) 1300°C, b)1320°C c) 1350°C and d) 1400°C. Dotted lines indicate the electrolyte surface. The images show low quantities of nickel (blue) are present throughout the pellet. Reproduced from [158] with permission from Elsevier.

2.5.3 Electrolyte and Anode Manufacturing

Co-pressing and co-sintering appears to be a common method of manufacturing PCCC and gives consistent results [70, 74, 75, 93, 99, 102, 116, 133, 137, 158]. Pressing an anode pellet, then sprinkling on the electrolyte power and pressing again is the common procedure. Once both components have been

pressed the half cell is sintered. Alternative methods have been attempted in developing cells, with various methods applied to ensure a thin electrolyte (Table 2.4) [67]. Often despite the method used, the OCV of the cell is generally lower than expected possibly due to electronic leakage, with papers generally citing an OCV between 0.9 V and 0.98 V at 700°C [101, 105, 106, 141, 149, 150, 159].

Table 2.4: Table showing various methods of applying the electrolyte layer, along with sintering temperature and layer thickness.

Electrolyte	Film Fabrication Method	Sintering Temperature (°C)	Film Thickness (µm)	Ref
$BaZr_{0.8}Y_{0.1}O_{3-\delta}$	Pulsed laser deposition	600	4	[119]
$BaZr_{0.8}Y_{0.1}O_{3-\delta}$	Dip coating	1450	20	[101]
$BaZr_{0.8}Y_{0.1}O_{3-\delta}$	Aerosol deposition	1200	5	[106]
$Ba_{0.98}Ce_{0.6}Zr_{0.3}Y_{0.2}O_{3-\delta}$	Wet powder spraying	1400	10 - 15	[86]
$BaZr_{0.8}Y_{0.2}O_{3-\delta}$	Tape casting	1500	74.2	[141]
$BaCe_{0.8}Zr_{0.1}Y_{0.1}O_{3-\delta}$	Wet powder spraying	1400	9	[114]
$BaZr_{0.8}Y_{0.16}Zn_{0.04}O_{3-\delta}$	Spin coating	1450	10	[160]
$BaZr_{0.8}Y_{0.16}Zn_{0.04}O_{3-\delta}$	Spin coating	1450	15	[160]
$BaZr_{0.8}Y_{0.16}Zn_{0.04}O_{3-\delta}$	Spin coating	1450	20	[160]

2.5.3.1 Tape-casting

Tape-casting can be a difficult method of manufacturing a PCCC, due to requiring a large amount of electrolyte powder, Ma *et al.* [141] overcame the issue of synthesising large amounts of electrolyte material by combining SSRS with tape-casting. Two electrolyte slurries for tape-casting were made,

with the electrolyte being $BaZr_{0.8}Y_{0.2}O_{3-\delta}$. The first slurry consisted of 123.75 g of precursor powder, NiO and graphite to make a porous electrolyte layer. The second slurry consisted of 161.70 g of precursor power and 2 wt% NiO was used to make a dense electrolyte layer, the difference between the two compositions being the additional quantity of NiO added as a sintering aid. The two layers were then hot pressed together at 50°C and sintered. The anode was impregnated onto the porous electrode and the cathode coated onto the dense electrolyte. The final cell had an OCV of 0.92 V at 700°C and a power density of 318 $mWcm^{-2}$ [141].

Alternatively, Dailly *et al.* [114] used tape-casting to produce the anode support for their cell and then used wet powder spraying to apply the $BaCe_{0.8}Zr_{0.1}Y_{0.1}O_{3-\delta}$ electrolyte. Through this method a cell with dimensions of 3 × 3 cm^2 was produced. The cell had a power output of 530 $mWcm^{-2}$.

2.5.3.2 Hot Pressing

Hot pressing of $BaZrO_3$ and $BaZr_{0.9}Y_{0.1}O_{3-\delta}$ has been shown to achieve 98% dense pellets when sintered at 1500°C and 1550°C, respectively [67]. However, in this instance Y was seen to accumulate at the grain boundaries, possibly due to Ba evaporation which occurs at high temperature. It was speculated that the Ba evaporation was a result of the carbon from the pressing die reacting with the powder, (2.8) and (2.9) [67].

$$BaZrO_3 + C \rightarrow ZrO_2 + CO + Ba \quad (2.8)$$

$$BaZrO_3 + CO \rightarrow ZrO_2 + CO_2 + Ba \quad (2.9)$$

If the reaction with the carbon tape was taken into account with the suspected Ba evaporation occurring, then hot pressing would result in a heavily Ba deficient surface. Despite this, it was stated that the bulk conductivities achieved aligned with those of previously published literature regarding yttrium doped barium zirconates [66, 67, 79].

2.5.3.3 Microwave Sintering

Microwave sintering has been utilised as a cost effective method of sintering, as sintering can occur at lower temperatures and for shorter periods [161]. An et al. [91] sintered the cathode in two steps. The first was sintering at 800°C for 1 min to create good adhesion between the electrolyte and cathode. The second sintering step occurred at 700°C for 1 min, with the aim to create a porous cathode. Xu *et al.* [98] used microwave sintering to co-sinter the $BaCe_{0.7}Zr_{0.1}Y_{0.2}O_{3-\delta}$ electrolyte and anode at 1200°C for 2 h after co-pressing. Xu *et al.* [98] used a composite cathode consisting of the $BaCe_{0.7}Zr_{0.1}Y_{0.2}O_{3-\delta}$ and lanthanum-strontium ferrite, however a composition was not given. The microwaved cell was then compared to one that had been conventionally sintered. The microwaved cell showed a peak power density of 838 $mWcm^{-2}$, while the conventionally sintered cell had a peak power density of 645 $mWcm^{-2}$ [98]. The difference between the two sintering temperature and times is due to An *et al.* [91] sintering a cathode and Xu *et al.* [98] co-sintering an anode and an electrolyte.

2.5.3.4 Pulsed Laser Deposition

Pulsed laser deposition can be used to create a dense thin film [119, 132]. Choi *et al.* [132] used two methods of applying the $PrBa_{0.5}Sr_{0.5}Co_{1.5}Fe_{0.5}O_{5+\delta}$ cathode onto a $BaCe_{0.4}Zr_{0.4}Y_{0.1}Yb_{0.1}O_{3-\delta}$ electrolyte. One cell had the cathode painted, the second cell had the cathode applied using pulsed laser deposition and then painted, with the aim of improving the contact between the electrolyte and cathode. The cell made by the conventional method showed a peak power density of 800 $mWcm^{-2}$, while the cell that had the pulsed laser deposited layer reached a power density of 1098 $mWcm^{-2}$, due to the improved contact between the electrolyte and cathode [132].

2.5.3.5 Dip Coating

Dip coating is often used for the manufacture of tubular cells and is not common with planar cells [81, 101, 162]. Using dip coating, a thin $BaZr_{0.8}Y_{0.2}O_{3-\delta}$ electrolyte cell with $Sm_{0.5}Sr_{0.5}CoO_{3-\delta}$-$Ce_{0.8}Sm_{0.2}O_{2-\delta}$ cathode was produced by Xia *et al.* [101]. They obtained an electrolyte layer with a thickness of 25 μm and achieved a power density of 70 $mWcm^{-2}$ at 650°C. As such a low power density was achieved,

research into dip coating has not been further pursued for PCCC, although it is possible that the poor performance was due to the morphology of the anode, which was described as 'sponge' like.

2.5.3.6 Spin Coating

Luisetto *et al.* [160] showed it was possible to spin coat a $BaZr_{0.8}Y_{0.16}Zn_{0.04}O_{3-\delta}$ electrolyte on an anode supported cell and platinum was used as the cathode. 3, 4 and 6 layers were spin coated at 6000 rpm for 30 s to achieve a thickness of 10 μm, 15μm and 20 μm respectively. Dense electrolyte layers were produced to obtain a peak power density of 75 $mWcm^{-2}$, possibly due to BaY_2NiO_5 impurities present after sintering [160]. Nasani *et al.* [105] also attempted spin coating of a $BaCe_{0.4}Zr_{0.4}Y_{0.2}O_{3-\delta}$ electrolyte and achieved better results. Two layers of the electrolyte slurry were spin coated and co-sintered with the anode to achieve a 5 μm, dense electrolyte layer. The $Pr_2NiO_{4+\delta}$ cathode mixed with ink vehicle and brushed on. An OCV of 0.96 was achieved at 700°C along with a power density of 234 $mWcm^{-2}$.

Better results were obtained by Shimada *et al.* [163] by spin coating a dense electrolyte layer followed by a porous electrolyte layer, and then a $La_{0.6}Ba_{0.4}CoO_{3-\delta}$- $BaCe_{0.7}Zr_{0.1}Y_{0.1}Yb_{0.1}O_{3-\delta}$ composite cathode (Figure 2.5). The dense layer of $BaCe_{0.7}Zr_{0.1}Y_{0.1}Yb_{0.1}O_{3-\delta}$ was first spin coated at 500 rpm on to a NiO-$BaCe_{0.7}Zr_{0.1}Y_{0.1}Yb_{0.1}O_{3-\delta}$ pre-sintered anode. The two were co-sintered at 1300°C for 3 h to form a dense layer of $BaCe_{0.7}Zr_{0.1}Y_{0.1}Yb_{0.1}O_{3-\delta}$. Another layer of $BaCe_{0.7}Zr_{0.1}Y_{0.1}Yb_{0.1}O_{3-\delta}$ was spin coated at 1000 rpm and sintered at 1300°C for 1 h. The second layer was porous, as the sintering time was shorter. Through this method they was able to achieve a power density of 243 $mWcm^{-2}$ at 600°C and nearly 584 $mWcm^{-2}$ at 700°C [163].

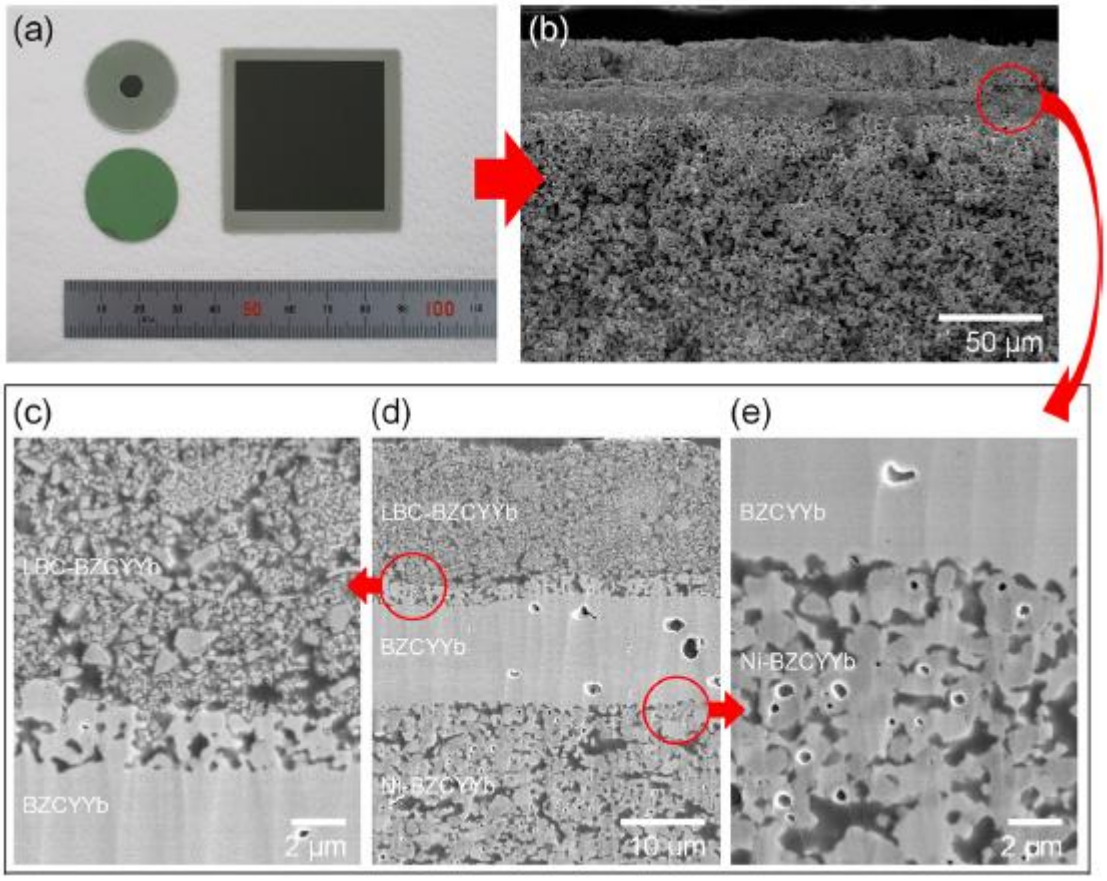


Figure 2.5: Reproduced from [163] with permission from American Ceramic Society. a) shows the anode supported cells, b)shows the cross-sectional images of the PCCFC after testing, c) shows cross-section image of the cell but focused on the various layers, where the cathode, the porous and dense electrolytes can be seen, d) shows all four layers and e) shows the interface between the anode and dense electrolyte.

Li *et al.* [164] also explored using spin coating to make PCCEs, spin speeds were not given however two electrolyte layers were spin coated to insure sufficient packing. The electrolyte used was $BaCe_{0.6}Zr_{0.2}Y_{0.1}O_{3-\delta}$, the fuel electrode consisted of the electrolyte and NiO in a 1:1 ratio and the steam electrode was $Pr_2NiO_{4+\delta}$. With this cell configuration 40% and 60% H_2O in air at 600°C was tested, both H_2O contents achieving similar a similar current density of 977 $mAcm^{-2}$

2.5.3.7 Aerosol deposition

A unique method creating a dense thin film has been shown by Bae *et al.* [106] who used aerosol deposition to apply the electrolyte. Through this method, Bae *et al*. [106] was able to create a 5 µm $BaZr_{0.8}Y_{0.1}O_{3-\delta}$ layer that was sintered at 1200°C for 5 h, followed by $La_{0.6}Sr_{0.4}Co_{0.2}Fe_{0.8}O_{3-\delta}$-

$Gd_{0.1}Ce_{0.9}O_{2-\delta}$ cathode screen-printed onto the electrolyte surface. The final cell had a performance of 180 $mWcm^{-2}$, although since its publication no further advancements have been reported on aerosol deposition [106].

2.5.3.8 Spark Plasma Sintering

Spark plasma sintering has been previously attempted to create dense electrolytes, in part to mitigate the use of a sintering aid which, as previously mentioned, may have an adverse effect on the cell performance. $BaCe_{0.9}Y_{0.1}O_{3-\delta}$, $BaZr_{0.8}Y_{0.1}O_{3-\delta}$ and $BaZr_{0.7}Ce_{0.2}Y_{0.1}O_{3-\delta}$ have all been used to create dense layers using spark plasma sintering, with no additional phases formed [165-168]. $BaCe_{0.9}Y_{0.1}O_{3-\delta}$ was sintered at 1600°C for 3 h, $BaZr_{0.8}Y_{0.1}O_{3-\delta}$ created a dense layer at 1700°C in 5 min and $BaZr_{0.7}Ce_{0.2}Y_{0.1}O_{3-\delta}$ 1550°C in 5 min [165-168]. All samples reached approximately 99% density. Despite the short sintering times, spark plasma sintering has not yet been implemented to manufacture a complete cell.

2.6 Steam Electrolysis

Proton conducting ceramic electrolysers (PCCE) have been explored, to varying degrees of success [164, 169-174]. They are beneficial as they are able to produce dry H_2 at the Ni containing electrode, unlike with oxide conducting electrolyte solid oxide electrolysers, where O_2 is produced on the Ni containing electrode which is therefore prone to oxidation at high operating temperatures, thus creating issues with long term stability [70]. However, they do come with limitations in particular requiring materials that are able to withstand a high H_2O concentration during operation and poor Faradaic efficiencies, where Faradaic efficiency is defined by the following equation (2.10) [164, 175, 176].

$$\eta_F = \frac{2FJ_{H_2}}{i} \qquad (2.10)$$

Where F is the Faraday constant, J_{H2} is the net hydrogen molar flux per cell area, *i* is the current density. Let *at al.* [164] explored the use of a $BaZr_{0.8}Y_{0.2}O_{3-\delta}$ electrolyte and $Sr_2Fe_{1.5}Mo_{0.5}O_{3-\delta}$ steam electrode, exposing them both to 20% H_2O and air mixture for 50 h at 600°C. XRD patterns of the samples before and after operation showed no changes. Current densities of 210 $mAcm^{-2}$ were achieved when operating

in electrolysis mode at 600°C, with a Faradic efficiency of 63.6% [164]. Gan *et al.* [170] was able to achieve a PCCE with 80% Faradic efficiency, the cell consisted of a $BaCe_{0.5}Zr_{0.3}Y_{0.16}Zn_{0.04}O_{3-\delta}$ electrolyte and $La_{0.8}Sr_{0.2}Mn_{0.05}Sc_{0.05}O_{3-\delta}$ steam electrode. However, a current density of 75.07 mA cm^{-2} was achieved at 700°C using 5% H_2O and air as the feed for the steam electrode [170]. $Pr_2NiO_{4+\delta}$ and $BaCe_{0.6}Zr_{0.2}Y_{0.2}O_{3-\delta}$ composite has also been explored as a steam electrode, and $BaCe_{0.6}Zr_{0.2}Y_{0.2}O_{3-\delta}$ as the electrolyte, with the cell achieving 977 $mAcm^{-2}$ at 700°C. The steam electrode feed was 40% H_2O and 60% air and pure H_2 as the feed stream for the fuel electrode. By using a thin film electrolyte at 95% Faradaic efficiency obtained [171].

Duan *et al.* [70] explored increasing Faradaic efficiencies, in particular noting that at higher current densities, when the Faradaic efficiency decreases, this was thought to be due to a drop in H_2O partial pressures and an increase in O_2 partial pressures. It was then suggested that increasing H_2O partial pressures at low temperatures would reduce electronic leakage and thus increase the Faradaic efficiency [70].

Bi *et al.* [172] showed the stability of $BaZr_{0.8}Y_{0.1}O_{3-\delta}$ in humid atmosphere for 24 h. They discussed using $BaCe_{0.5}Zr_{0.3}Y_{0.2}O_{3-\delta}$ as it would give a higher current density, however, they did not believe it to be chemically stable under the current operating conditions [172]. The final cell consisted of $La_{0.6}Sr_{0.4}Co_{0.2}Fe_{0.8}O_{3-\delta}$-$BaZr_{0.8}Y_{0.1}O_{3-\delta}$ as a composite steam electrode, with a 3% H_2O and 97% air feed The fuel electrode consisted of NiO and $BaZr_{0.8}Y_{0.1}O_{3-\delta}$ with 4% H_2 and 96% argon (Ar) feed. Despite using a $BaZr_{0.8}Y_{0.1}O_{3-\delta}$, Bi *et al.* [172] were still able to achieve a current density of 437 $mAcm^{-2}$ at 700°C [172].

He *et al.* [173] have shown to be able to achieve 830 $mAcm^{-2}$ using $BaCe_{0.5}Zr_{0.3}Y_{0.2}O_{3-\delta}$ at 700°C. He *et al.* [173] also used a larger quantity of H_2O (50%) , entering the $Sm_{0.5}Sr_{0.5}CoO_{3-\delta}$-$BaCe_{0.5}Zr_{0.3}Y_{0.2}O_{3-\delta}$ steam electrode. Alternatively $BaCe_{0.7}Zr_{0.1}Y_{0.2-x}Yb_xO_{3-\delta}$ has been used as an electrolyte with a $PrBa_{0.5}Sr_{0.5}Co_{2-x}Fe_xO_{3-\delta}$ steam electrode and NiO and $BaCe_{0.7}Zr_{0.1}Y_{0.2-x}Yb_xO_{3-\delta}$ as the fuel electrode [174]. A current density of 1330 $mAcm^{-2}$ at 600°C was achieved, despite using only 3% H_2O in the

steam electrode feed [174]. Although no study was performed on the chemical stability of the materials and molar quantities for Y, Yb, Co and Fe were not given [174].

2.7 Conclusion

Proton conducting electrolytes have been heavily researched, with a variation of $BaCe_{1-x-y}Zr_xY_yO_{3-\delta}$ being the most suitable candidate, due to being able to remain chemically stable in humid atmospheres, whilst still maintaining good conductivity. Sintering aids have been explored to create a dense electrolyte layer, the most commonly used appearing to be either ZnO or NiO.

Various cathodes have been extensively studied, in particular composite cathode materials have been extensively studied, the basis of which are materials that have been previously used in OC-SOCs. The most common composites consist of $Sm_{0.5}Sr_{0.5}CoO_{3-\delta}$ and $Ce_{0.8}Sm_{0.2}O_{2-\delta}$. In comparison, little research has been explored in regard to other viable electrode materials. Especially when considering there are a plethora of other other OC-SOC cathodes that could in fact be TC, similar to $Pr_2NiO_{4+\delta}$. With even less research looking at their chemical stability, the research of the chemical stability of electrolyte materials is often favoured.

To fabricate a cell, co-pressing appears to be the most favourable method, as it can be done using small quantities of material. Cathodes are then applied, with analysis predominantly favouring fuel cell testing. Symmetrical cell testing is occasionally performed, a systematic approach would be to first test cathodes as symmetrical cells and then as a fuel cell. Electrolyser tests are also an option, with the advantage of PCCEs being they are able to produce dry H_2, which is not the case for oxide conducting solid oxide electrolysers (OC-SOEs), however, PCCE studies are sparse.

2.8 Project Objectives

The objectives of the project were to:

1. Synthesise a selection of promising materials and assess the effect of heating them in various atmospheres, in particular the effect on the lattice parameters. Whether these materials were chemically stable in humid N_2 was of further interest. The investigation was furthered by looking into the potential of H_2O incorporation.
2. Select a viable electrolyte composition that was able to withstand humid conditions and produce a dense pellet, through the use of a sintering aid, that could be used for fabricating cells for testing.
3. Perform symmetrical cell testing using the dense pellet from a selection of viable electrode materials.
4. Select a single electrode material in order to develop a functioning PCCC.
5. Test the functioning PCCC as a fuel cell and in electrolyser mode.

Chapter 3: Experimental Techniques

This chapter outlines the methods of material synthesis. Followed by the characterisation techniques used, the theory and practise behind them. Finishing off with details of symmetrical cell, fuel cell and electrolyser testing.

3.1 Material Synthesis

3.1.1 Solid State

Solid state synthesis is a simple and established synthesis route. Precursor materials, such as oxides or carbonates, were weighed in stoichiometric ratios and then mixed together. If barium carbonate ($BaCO_3$, VWR, 99.8%) is utilised as a precursor, excess $BaCO_3$ is often required to compensate for barium evaporating at higher temperatures. A list of all chemicals used for solid state synthesis is given in Table 3.1.

Table 3.1: List of chemicals used for solid state synthesis, as well as their purities.

Chemical Name	Chemical Formula	Purity (%)	Source of Reagents
Barium carbonate	$BaCO_3$	99.8	VWR
Bismuth (III) oxide	Bi_2O_3	99.99	Sigma-Aldrich
Cerium (IV) oxide	CeO_2	≥99.0	Sigma-Aldrich
Hexane	$CH_3(CH_2)_4CH_3$	≥95.0	Sigma-Aldrich
Iron (III) oxide	Fe_2O_3	≥99.0	Sigma-Aldrich
Lanthanum (III) oxide	La_2O_3	≥99.9	Sigma-Aldrich
Nickel (II) oxide	NiO	99.0	Sigma-Aldrich
Niobium (V) oxide	Nb_2O_5	99.99	Sigma-Aldrich
Strontium carbonate	$SrCO_3$	≥99.9	Sigma-Aldrich
Yttrium (III) oxide	Y_2O_3	99.99	Sigma-Aldrich

Mixing first occurred using a pestle and mortar. With compounds that are harder to synthesise also being ball milled. For ball milling a 3 mL of hexane (Sigma-Aldrich, ≥95.0) was added to aid in mixing. Ball milling occurred at 500 rpm, 4 repetitions, 15 min each using a Fritsch Pulverisette 7 Planetary Micro Mill, 12 mL pots and four 10 mm zirconium oxide (ZrO_2) balls. Once completed, the sample was dried in the atmosphere until all the solvent had evaporated.

The dry mixture was then placed within an alumina crucible with a lid placed on top to prevent contamination. The crucible and lid are placed within a Carbolite Gero Ltd. CWF 13/13 muffle furnace, heated to 900°C, for 12 h. This step is known as calcination, with many of the bonds in the compounds breaking and reforming, eliminating unwanted carbonates from the sample. The material was then ground allowing fresh reagent sites to be available, for the second heating step. A higher temperature was observed, variable to the material ranging between 1000°C to 1400°C, these values will be given in chapters respective to their material. The sample was then reground, so that it is a uniform powder suitable for X-ray diffraction (XRD). XRD was performed after the sintering step to ensure correct phase composition.

As previously stated, solid state synthesis is a simple and established synthesis route, although it is not always effective, with more complex methods being needed depending on the material. The issue arises from the prolonged heating times due to limitations with solid state diffusion and a great deal of energy being needed to break the bonds of the precursors.

3.1.2 Sol-Gel Synthesis

For sol-gel synthesis, metal nitrates were measured in stoichiometric ratios and then mixed together in deionised water. Ethylene glycol (VWR, ≥99.0%) and citric acid (Sigma-Aldrich, 99.0%) are added, to stimulate the generation of organic-metallic polymers. Ethylene glycol was added to a 1:1 ratio of moles of product to moles of ethylene glycol and citric acid was also added with a 4:1 ratio, of citric acid to ethylene glycol.

During this process the mixture is heated, to evaporate water, forming a gel. A list of chemicals used for sol-gel is given in Table 3.2.

Table 3.2: List of chemicals used for sol-gel synthesis, as well as their purities.

Chemical Name	Chemical Formula	Purity (%)	Source of Reagents
Barium nitrate	$Ba(NO_3)_2$	≥99.0	Alfa Aesar
Cerium (III) nitrate hexahydrate	$Ce(NO_3)_3.6H_2O$	99.0	Sigma-Aldrich
Citric acid	$HOC(CO_2H)(CH_2CO_2H)_2$	99.0	Sigma-Aldrich
Ethylene glycol	$HOCH_2CH_2OH$	≥99.0	VWR
Lanthanum (III) nitrate hexahydrate	$La(NO_3)_3.6H_2O$	99.99	Sigma-Aldrich
Nickel (II) nitrate hexahydrate	$Ni(NO_3)_2.6H_2O$	99.99	Alfa Aesar
Praseodymium (III) nitrate hexahydrate	$Pr(NO_3)_3.6H_2O$	99.9	Sigma-Aldrich
Yttrium (III) nitrate hexahydrate	$Y(NO_3)_3.6H_2O$	99.8	Sigma-Aldrich
Zirconium (IV) oxynitrate hydrate	$ZrO(NO_3)_2.xH_2O$	99.0	Sigma-Aldrich

The gel was then transferred to a Carbolite Gero Ltd. LHT 6/60 oven with a target temperature of 300°C (for electrolyte materials) and 350°C (for electrode materials) for 1h, the aim of this being to eliminate organic materials and evaporate any water in the sample. The ramp rate was set to slow (0.5°Cmin^{-1}, so as not to evaporate the water too quickly, causing rapid thermal expansion resulting in overflowing. The sample was then ground, placed in a crucible and then calcined for 12 h at 700°C to remove any unwanted carbonates. Following this it was ground again and sintered at a higher temperature, once again for 12 h. XRD was then performed to ensure correct phase composition.

Although sol-gel can be a more labour-intensive method, compared to that of solid-state synthesis, the main advantage is that the formation of the material occurs at lower temperatures. The powders synthesised often have a smaller particle size.

3.1.3 Pellet Pressing

Pellets were pressed for use in several characterisation experiments. These were for used for 4-probe, symmetrical cell, fuel cell or electrolyser testing. For the manufacturing of the pellets a manual hydraulic pellet press was used, the pellet press was obtained from Doreth Engineering Co. Ltd. The powders were transferred into a die a 10 mm Specac die was used for 4-probe and a 30 mm Pellet Press Die Sets die was used for all other processes. The pressure applied to the powders, is dependent on the material with factors such as material adhesion, moisture levels and particle size having an affecting it.

When preparing pellet for 4-prove the pellet is sintered at the temperature at which it was synthesised at. Pellets are sintered to allow the formation of bonds between the single particles, increasing the density, grain size and mechanical strength of the sample.

3.2 Characterisation

3.2.1 X-ray Diffraction

3.2.1.1 Crystal Structure

To be able to understand X-ray diffraction (XRD), an understanding of solid structures is needed. There are two types of solids: these are amorphous and crystalline. Amorphous solids lack long-range order of their atoms while crystalline solids have a regular arrangement of atoms/ions, which develop their lattice structure. The smallest arrangements of the atoms/ions in the lattice, which can be repeated by translation, is known as the unit cell.

The dimensions of a unit cell are represented by constants denoted by a, b and c, the angle between these are represented by α, β and γ. Variations in the magnitude of these constants can lead to variations in the crystal structure which are described through seven crystal systems, shown in Table 3.3.

Table 3.3: Showing various crystal systems and the conditions defining them.

Crystal System	Lattice Constants	Bond Angles
Cubic	$a = b = c$	$\alpha = \beta = \gamma = 90°$
Hexagonal	$a = b \neq c$	$\alpha = \beta = 90° \ \gamma = 120°$
Orthorhombic	$a \neq b \neq c$	$\alpha = \beta = \gamma = 90°$
Monoclinic	$a \neq b \neq c$	$\beta \neq \alpha = \gamma = 90°$
Tetragonal	$a = b \neq c$	$\alpha = \beta = \gamma = 90°$
Triclinic	$a \neq b \neq c$	$\alpha \neq \beta \neq \gamma \neq 90°$
Trigonal/rhombohedral	$a = b = c$	$\alpha = \beta = \gamma \neq 90°$

The crystal systems can be further segregated into base centred, body centred, face centred and primitive, leading to fourteen crystalline arrangements, known as the Bravais lattices. Crystal structures can be further classified through the use of space groups, which describe the symmetry of the structure.

3.2.1.2 Miller Indices

Crystal structures can be further analysed to give the positions of the atom and lattice planes. These are represented by fractional coordinates and Miller indices, respectively. Fractional coordinates are given in the format (*a*, *b*, *c*), where each value represents a direction in their respective axis. The fractional coordinates are dimensionless values, therefore can be used for a direct comparison of positions between different unit cells. Miller indices are used to indicate the orientation of a plane in the form (*hkl*), the values are reciprocals of the point at which the plane crosses the *a*, *b* and *c* axis. *h* relates to the *a* axis, *k* to the *b* axis and *l* to the *c*.

3.2.1.3 Theory

XRD utilises monochromatic X-rays, they are generated by a potential difference being applied to a tungsten filament (cathode), generating electrons. The generated electrons are used to bombard a metal (anode) such as cobalt (Co) or copper (Cu). The charged electrons from the tungsten excite other

electrons in the anode, ejecting them from their shells. Often the K shell (1s orbital), leaving an electron hole. An electron from a higher energy shell, either the L shell (2p orbital) or M shell (3p orbital) drops to the lower energy shell, while also producing electromagnetic radiation known as X-rays. The shell which the electron originated from effects the wavelength of the X-ray.

If the electron originated from the L or M shell then K_α or K_β radiation is produced, respectively. The K_α and K_β radiation can be further divided into $K_{\alpha1}$, $K_{\alpha2}$, $K_{\beta1}$ and $K_{\beta2}$ radiation which is a result of the varying spin states of the electrons. Bremsstrahlung radiation (braking radiation) is also produced, a result of the cathode electrons being attracted to the positive charge of the anodes nucleus, resulting in the loss of energy as an X-ray photon.

As a single wavelength of X-rays are required filters are used to remove unnecessary wavelengths, nickel (Ni) foil is commonly used for Cu source radiation. Crystal monochromators can also be used, these are aligned to diffract the unwanted wavelengths, these tend to be germanium based. The result is the removal of the Bremsstrahlung radiation and the K_β radiation. The $K_{\alpha2}$ can be difficult to separate from the $K_{\alpha1}$ radiation as the two share similar wavelengths. Therefore, an average of wavelengths in taken for Cu and Co radiation these being 1.54 Å and 1.79 Å respectively.

A crystalline sample is illuminated with a beam of X-rays, with scattering occurring due to the electrons and regular arrangement of atoms. Constructive interference is able to occur at specific angles. This is also known as diffraction and the angle it occurs at are the diffractive angles (Figure 3.1). These are represented by Bragg's law, (3.1).

$$n\lambda = 2dsin\theta \qquad (3.1)$$

Where *n* is an integer, *d* is the crystal plane spacing, λ is the wavelength of the X-ray and θ is the angle of the X-rays in relation to the plane.

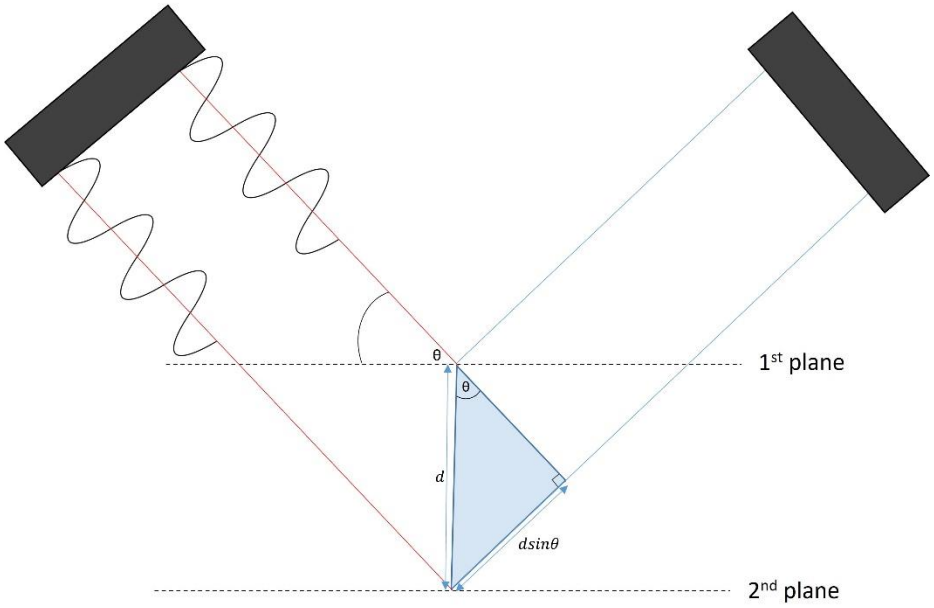


Figure 3.1: Relationship between crystal planes and the angles of incident/diffraction x-rays.

For constructive interference to occur, the phase of the wavelength being diffracted from the first plane must be the same phase of the wavelength being diffracted from the second plane. Therefore the extra distance travelled by the X-ray between the planes must be a whole number of wavelengths. The constructive interference is represented as peaks on a diffraction pattern.

The diffraction scan produced represents the crystal structure of the sample. The data can be compared to other XRD scans, which can be retrieved from a crystallography database. A comparison of the data can aid in determining the unit cell parameters and phase purity.

XRD was performed using several instruments depending on availability. Either the Bruker D8 diffractometer, Panlaytical Empyrean diffractometer or Bruker D2 diffractometer was used. The D8 and Panalytical used Cu Kα radiation, while the Bruker D2 used a Co Kα radiation. By varying the source of the radiation, the wavelength of the X-rays can vary, thus XRD performed on the same sample using two different radiation sources will have a change in peak positions. For a few selected samples variable temperature X-ray diffraction (VT-XRD) was performed, using a Bruker D8 diffractometer, with a variable temperature stage. The sample was heated between 25°C and 775°C at varying temperature

ranges, to see the change in crystal structure and unit cell with respect to temperature and also to observe any difference in cell parameters when H_2O/CO_2 release is expected.

To prepare a sample for both XRD and VT-XRD, an adequate amount of powder was placed into the powder specimen holder. When preparing the sample, the powder was evenly spread evenly and packed well using a glass slide. This would ensure correct sample height, with any deviations in the sample height resulting in shifts in the 2θ values of the observed peaks. For XRD the powder specimen holder was then placed into the instrument holder and then attached to the instrument. While for VT-XRD the powder specimen holder was placed onto an Anton Parr heating stage, which was then attached to the instrument.

3.2.1.4 Rietveld refinement

Rietveld refinement is utilised to interpret XRD data. This is done by refining a theoretical (calculated) profile against an experimental (observed) profile, using a least squares regression, to as close a fit as possible. The theoretical profile contains a baseline of information, such as the space group, unit cell parameters, atom positions and fractional occupancy. Various parameters are refined, while also trying to reduce the sum of squared error for all data points, represented by (1.1).

$$S_y = \sum_{i=1}^{n} w_i \left(Y_i^{obs} - Y_i^{calc}\right)^2 \qquad (3.2)$$

Where Y_i^{obs} is the intensity of the observed data at a point *i*, w_i is the statistical weight and Y_i^{calc} is the intensity of the calculated data at point *i*.

To determine the quality of a fit, several numerical values can be calculated and compared. These are known as R factors and are as follows: the R-pattern (R_p), the R-weighted pattern (R_{wp}) and the R-expected (R_{exp}). The R_p compares all data points for the observed and calculated patterns and is shown by (3.3).

$$R_p = \frac{\sum \left|Y_i^{obs} - Y_i^{calc}\right|}{Y_i^{obs}} \times 100\% \qquad (3.3)$$

The R_{wp} also follows a similar formula however, takes into account the statistical weight and can be calculated through (3.4).

$$R_{wp} = \left[\frac{\sum w_i\left(Y_i^{obs} - Y_i^{calc}\right)^2}{w_i\left(Y_i^{obs}\right)^2}\right] \times 100\% \quad (3.4)$$

Finally the R_{exp} ((3.5)) is the ideal R value that can be achieved assuming a perfect refinement.

$$R_{exp} = \left(\frac{N - P - C}{\sum w_i\left(Y_i^{obs}\right)^2}\right) \times 100\% \quad (3.5)$$

Where N is the number of observations, P is the number of refined parameters and C is the number of constraints.

These numerical values are an indication of the quantity of the fit. Lower R values theoretically suggest a better fit. However it should be noted that by reducing the sum of squared error for all data points and incorrect calculated profile can be developed. Thus a visual observation of the calculated profile and difference profile should be regularly performed, to ensure that no unrealistic parameters are set.

3.2.2 Heating in Various Gases

Successfully synthesised samples were heated within a Carbolite Gero Ltd. CTF 12/75 tube furnace to observe the effect of different heat treatments on the crystal structure. Samples were placed in the centre of the tube furnace, located near the thermocouple (Figure 3.2). The samples were heated to 700°C with ramp rate of 4°Cmin^{-1}, held for 12 h and cooled down to room temperature at 0.8°Cmin^{-1}. A carrier gas, either nitrogen (N_2) or oxygen (O_2) was passed through the tube furnace. By utilising N_2 as a carrier gas, low oxygen partial pressures were imitated.

The carrier gas enters and exits a bubbler containing either deionised water (H_2O) or concentrated sulfuric acid (H_2SO_4). In the case of H_2O, the carrier gas would uptake some (3%) H_2O, thus the gas is stated as being humid. The exposed sample is able to interact with hydroxide ions (OH^-), through oxygen vacancies. Initially N_2 is used as a carrier gas for the H_2O, following this O_2 is used. In the case of using O_2 as a carrier gas, some of the oxygen vacancies in the sample can also be occupied by O_2 altering

oxygen stoichiometry. A comparison of XRD pattern of both samples exposed to both carrier gases and Rietveld refinement was done after the heat treatment.

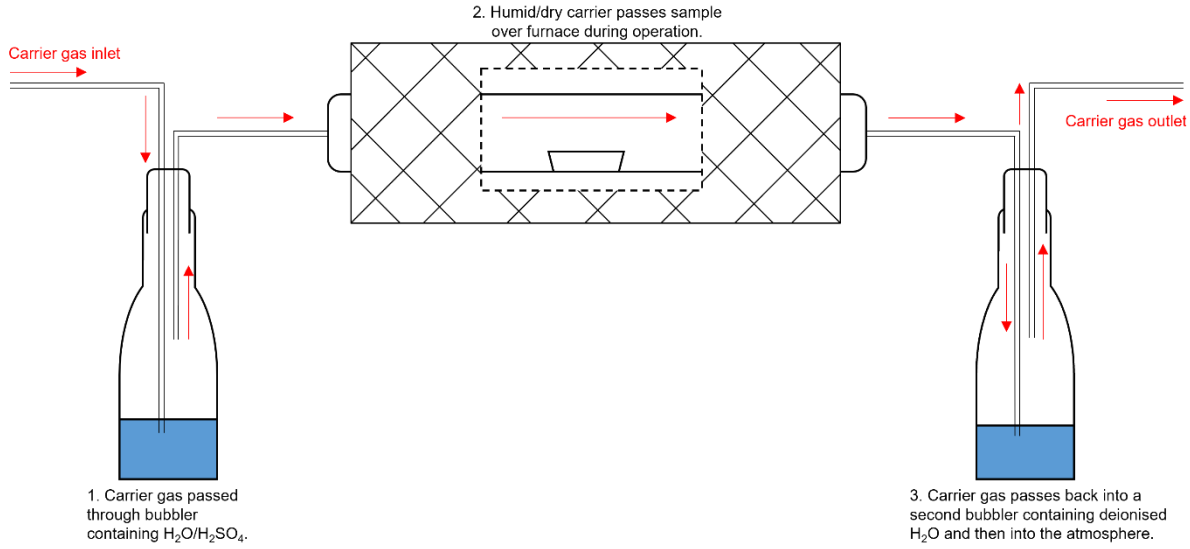


Figure 3.2: Setup used for heating samples in humid N_2, dry N_2 and humid O_2.

By using H_2SO_4 within the bubbler the carrier gas, N_2, was stripped of any moisture that it may contain. Therefore, was referred to as being dry. In this instance, no H_2O is present in the carrier gas to interact with the sample, therefore no H_2O incorporation would occur. Instead, there is the possibility of the oxidation state of the transition metal in the compound decreasing due to the low oxygen partial pressures, this would then vary the lattice parameters of the sample.

Comparing the samples heated in humid N_2, dry N_2 and humid O_2 can give an indication of the process occurring. An increase in lattice parameters of both N_2 samples can indicate a reduction of the sample. While comparing the humid N_2 and humid O_2 sample, both showing an increase in lattice parameters, can give an indication of H_2O incorporation.

3.2.3 Thermogravimetric Analysis

Thermogravimetric analysis (TGA) observes the difference in mass of a sample with respect to temperature. As the sample is heated, gaseous products are often expelled from the sample, causing the mass to decrease. A carrier gas is set at a constant flow rate, to aid in transport of any expelled gases. Examples of gases used can be used are air, H_2, O_2, or N_2.

To fully maximise data from a TGA, it can be coupled with mass spectrometry (MS), which is able to record the relative atomic mass of the gaseous products. Allowing for an assessment of what the gaseous products could have been that led to the weight loss. If a single product is released an approximation of the molar quantity can be determined through a comparison of relative atomic mass and weight before and after mass loss has occurred. TGA was carried out using N_2 as a carrier gas at a flowrate of 50 $mLmin^{-1}$, with H_2O, O_2 and CO_2 being detected by the MS. The TGA instrument used was a Netzsch STA 449 F1 Jupiter Thermal Analyser and the MS instrument used was a Netzsch MS 403C Aëolos Mass Spectrometer.

3.2.4 Scanning Electron Microscopy and Energy Dispersive X-Ray Spectroscopy Analysis

A Hitachi Tabletop Microscope TM3030 Plus scanning electron microscopy (SEM) was used for the investigation of the surface morphology of $BaCe_{0.6}Zr_{0.3}Y_{0.1}O_{3-\delta}$ pellets. SEM uses an electron gun to generate electrons. Three types of electron emitters can be used which are tungsten filaments, solid-state hexaboride crystals and field emission guns. In the case of the TM3030 Plus a tungsten filament is used.

The electrons are then focused using various condenser lenses, followed by an objective lens. The objective lens is the final lens and is used to focus the electron beam onto the surface of the sample. Once the beam is focused it is passed through a scanning coil. Allowing the beam to be deflected along the x and y axis so that the complete surface of the sample can be scanned.

Secondary electron detector (SEDs) are used for inelastic scattering of electron, which occurs due to electrons from the electron beam exciting other electrons in the sample, also resulting in some loss in energy. The excited electron transfers through the sample, until it is ejected. It is then detected by the SED and forms an image. As these electrons come from the surface of the sample, the resolution of the image produced is better than from back-scattered electrons (BSEs).

Back scattered electron detectors (BSEDs) are used for the detection of elastically scattered electrons. These are electrons which have been reflected from the electron beam and have greater energy then

those detected by SED. The electrons originate from below the surface of the sample, so can help to identify any pores in the sample.

Samples were prepared by first placing carbon tape on the aluminium SEM sample holder, followed by the sample. Non-conductive samples are often coated with conductive material such as platinum or gold, through a process known as sputter coating. In this case, the samples were already conductive and gave clear images so sputter coating was not needed.

Energy dispersive X-ray spectroscopy (EDXS) was used, with SEM, to provide elemental mapping. During interactions of the atoms with the electron beam, electrons from an low energy shell are ejected leaving a vacancy which is then filled by an electron from a higher energy shell. This movement results in the loss of a photon, the energy loss is characteristic of the element. This is able to provide an elemental composition of the sample.

3.2.5 4 Probe Direct Current (DC) Conductivity

4 probe direct current (DC) conductivity was employed for the measuring of electrical resistance of material using a Keithley 6220 Precision Current Source and Keithley 2182A Nanovoltmeter. The materials examined had a low resistivity, being electrode material. Four metal probes are painted onto a sintered pellet, the metal used varies on the maximum experimental temperature these are shown in Table 3.4. Wires are then attached to the probes, which are of the same material. The pellets are then placed within a furnace, set to the drying temperature, to evaporate all the solvent from the metal paint.

Table 3.4: Metal paint, maximum experimental temperature and drying temperature.

Metal	Maximum Experimental Temperature (°C)	Drying Temperature (°C)
Silver (Ag)	700	600
Gold (Au)	900	800
Platinum (Pt)	1000	900

3.2.5.1 Theory

For analysis the pellet is placed within a furnace and the four wires attached, shown in Figure 3.3. As the temperature is increased/decreased a current is applied to the two outer wires, 1 and 4. A difference in voltage is measured across the two inner wires, 2 and 3. With the current and voltage the resistance at the set temperature can be calculated using Ohm's law, through (3.6). From the resistance, the conductivity of the sample can be calculated through the inverse of the resistance. Followed by the conductivity specific to the area, represented by (3.7).

$$R = \frac{V}{I} \tag{3.6}$$

$$\sigma = \frac{L}{A} \times \frac{1}{R} \tag{3.7}$$

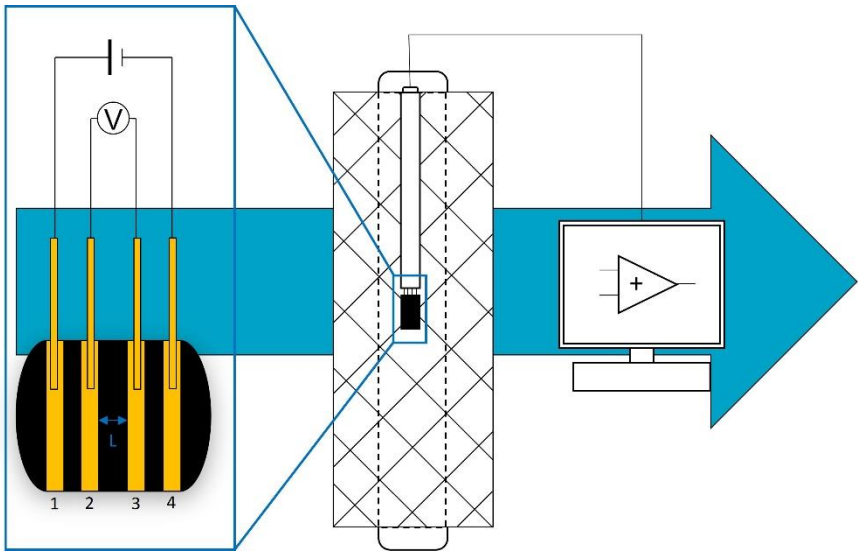


Figure 3.3: Pellet setup for 4-probe and the rig it is placed in. On the left is enlarged image of the pellet with the 4 electrodes connected. The pellet is then connected to a Keithley 6220 Precision Current Source and Keithley 2182A Nanovoltmeter and placed in a vertical furnace. A LabVIEW program is used to collect experimental data.

3.3 Cell Manufacturing

3.3.1 Electrolyte Sintering

Successful symmetrical cells and full cells were made using an electrolyte as a support. The electrolyte support consisted of $BaCe_{0.6}Zr_{0.3}Y_{0.1}O_{3-\delta}$, 20% excess $BaCO_3$, to account for barium evaporation, along with 1 wt% NiO, which acted as a sintering aid. All powders were ball milled with 3 mL hexane (Sigma-Aldrich, ≥95.0%) to act as a lubricant. Ball milling was done initially at 300 rpm and then at 500 rpm, to ensure all powders were sufficiently crushed and mixed.

A 30 mm pellet die was lubricated with GT85 lubricating polytetrafluoroethylene spray to aid in removing the pellet, without cracking from the die. 1.5 g of electrolyte mixture was measured and poured into the pellet die. The plunger was applied and the die pressed using an isostatic press, with a weight of 10 tons for 10 min. Pellets were then carefully removed from the pellet die. Once removed they were left for 24 h in ambient conditions, so to evaporate any excess lubricant.

Afterwards the pellets were placed on a 2 g bed of $BaCe_{0.6}Zr_{0.3}Y_{0.1}O_{3-\delta}$, which itself was on an alumina plate. A further 2 g of $BaCe_{0.6}Zr_{0.3}Y_{0.1}O_{3-\delta}$ was placed on top of the electrolyte pellet and an alumina disk with holes, to allow for any evaporation of solvents, was gently placed on top. The alumina disk applied a set weight to the pellet to prevent it from deforming on heating.

The $BaCe_{0.6}Zr_{0.3}Y_{0.1}O_{3-\delta}$ powders surrounding the pellet played two key roles. The first was to further reduce barium evaporation and the second was to prevent the alumina from the plate and disk reacting with the pellet during heating. This was then all covered with an alumina crucible to ensure that no impurities fell on the sample within the furnace during heating. Dense pellets were found to be successful when heated to a temperature of 1500°C for 10 h, the heating profile can be seen in Figure 3.4. The furnace used was a Vecstar Ltd. VF2 muffle furnace.

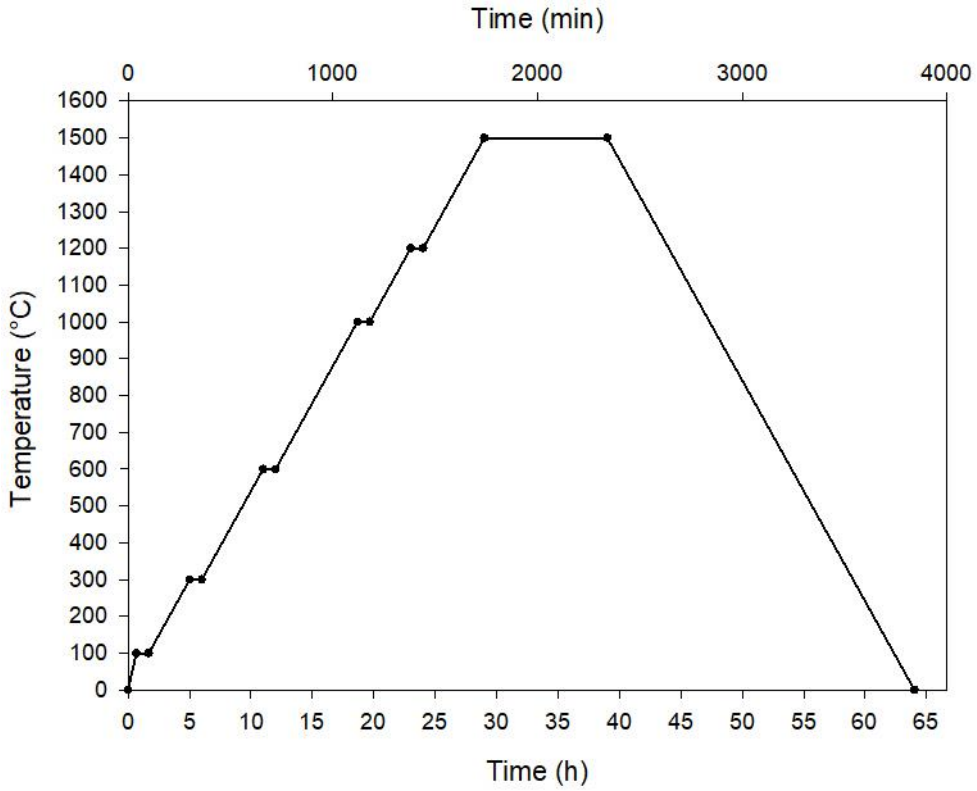


Figure 3.4: Program used for the sintering of $BaCe_{0.6}Zr_{0.3}Y_{0.1}O_{3-\delta}$ pellets.

Once the heat treatment was completed the samples were carefully taken out of the furnace, the crucible removed, and the sacrificial powder delicately removed from the sample. The final pellet was now ready for further processing to either a symmetrical cell or a complete cell.

3.3.2 Symmetrical Cells

Electrode inks were made using Terpineol-based ink vehicle (Fuel Cell Materials) and the synthesised electrode powders. The electrode powers were mixed with the ink vehicle in a 2:1 ratio. The two were mixed until a homogeneous mixture formed. The mixture were then passed through a EXAKT 35 three roll mill and collected in a sample jar.

Sintered electrolyte pellets were painted on either side with the electrode inks. Each side was done one at a time, once one side was done the pellets were placed into an oven to dry at 70°C for 4 h to ensure that all the ink vehicle had evaporated. The pellets were then placed on to a previously made $BaCe_{0.6}Zr_{0.3}Y_{0.1}O_{3-\delta}$ pellet, which was being used as a support, and then placed onto an alumina plate.

This time an alumina disk was not placed on top of the pellet as the pellet were not expected to deform during the sintering of the electrode. Again, an alumina crucible was used to cover the pellet during heating. The sample was heated to 1000°C for 4h, as seen by the heating profile in Figure 3.5. After completing the heat treatment, the symmetrical cells were ready for testing.

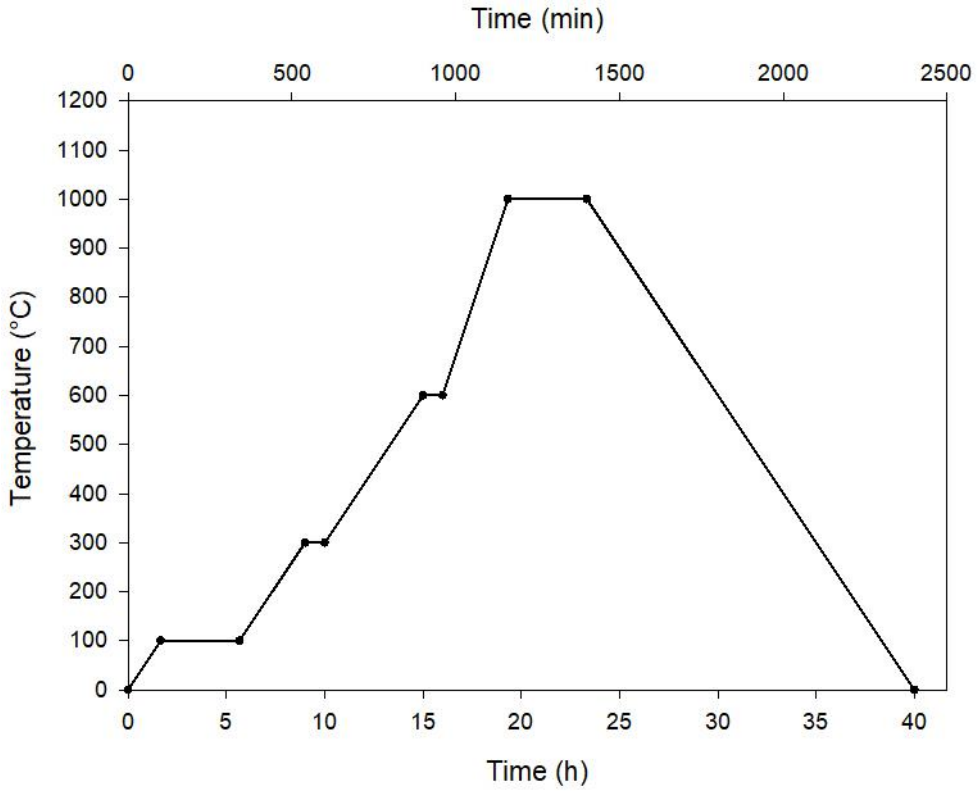


Figure 3.5: Program used for the sintering of cathodes for $BaCe_{0.6}Zr_{0.3}Y_{0.1}O_{3-\delta}$ symmetrical cells.

3.3.3 Full Cell Fabrication

For the manufacturing of a full cell, nickel-based powders had to initially be produced. The nickel-based powders make the anode electrode when the cell is operated in fuel cell mode and the cathode electrode when operated in electrolysis mode. To make the powder NiO (Sigma-Aldrich, 99.0%), $BaCe_{0.6}Zr_{0.3}Y_{0.1}O_{3-\delta}$ and tapioca starch (used as a pore former) were mixed in a ball mill. 3 mL hexane (Sigma-Aldrich, ≥95.0%) was added as a lubricant, the powders and solvent were initially mixed at 300 rpm and then at 500 rpm for 15 min, 4 repetitions using a Fritsch Pulverisette 7 Planetary Micro Mill, 12 mL pots and four 10 mm zirconium oxide (ZrO_2) balls. The powders were then removed from the ball mill and left in ambient air for 12 h so any residual hexane was able to evaporate.

The nickel-based mixture was then mixed with Terpineol-based ink vehicle (Fuel Cell Materials) in a 2:1 ratio, to produce an ink. Which was then further combined using a triple roll mill. The ink was collected in a sample vial. To apply the ink onto the electrolyte pellet spin coating method was used, using a Ossila L2001A3 spin coater. Two layers were spin coated onto the electrolyte, with intermittent drying at 40°C

The pellet was placed in a spin coating sample holder and an adhesive mask with a 20 mm diameter was placed on top. 175 µL of nickel-based ink was pipetted onto the pellet and evenly distributed. The holder and pellet were then placed into the spin coater, which was set at 100 rpm for 15 s, to ensure even distribution of the ink. Followed by 2500 rpm for 25 s, removing any excess ink from the surface. The mask was removed, and the pellet placed into an oven under extraction for at 40°C for 4 h.

A second ink layer was added, once the current layer was dry. A similar preparation procedure was applied, however in this case 125 µL of nickel-based ink was used. Again, the sample was left to dry in an oven for 4 h at 40°C. Once the second layer was dry the pellet was placed onto a 1 g bed of $BaCe_{0.6}Zr_{0.3}Y_{0.1}O_{3-\delta}$ powder, which itself was on an alumina plate. The sample was then covered further with $BaCe_{0.6}Zr_{0.3}Y_{0.1}O_{3-\delta}$ powder, then with an alumina crucible heated to 1300°C for 6 h, following a similar heating profile as shown previously in Figure 3.5. The furnace used was a Carbolite Furnaces Ltd. CWF 13/13 muffle furnace.

After the nickel-based electrode had been sintered, the pellet was removed from the furnace. The alternative electrode was painted onto the other side of the pellet following the same procedure previously described for manufacture of a symmetrical cell. Following these procedures completed the fabrication of a cell.

3.4 Cell Testing

3.4.1 Symmetrical Cell Testing

Symmetrical cell testing was performed in a custom-built rig with Bronkhurst air mass flow controllers, shown in Figure 3.6. The rig used a Vecstar Ltd. VQF vertical tube furnace which contained two alumina

tubes. One of which had a cell holder made from Macor. Along with two gold current collectors (Fiaxell) which would then be connected to a Solartron 1470E and 1455 FRA analyser.

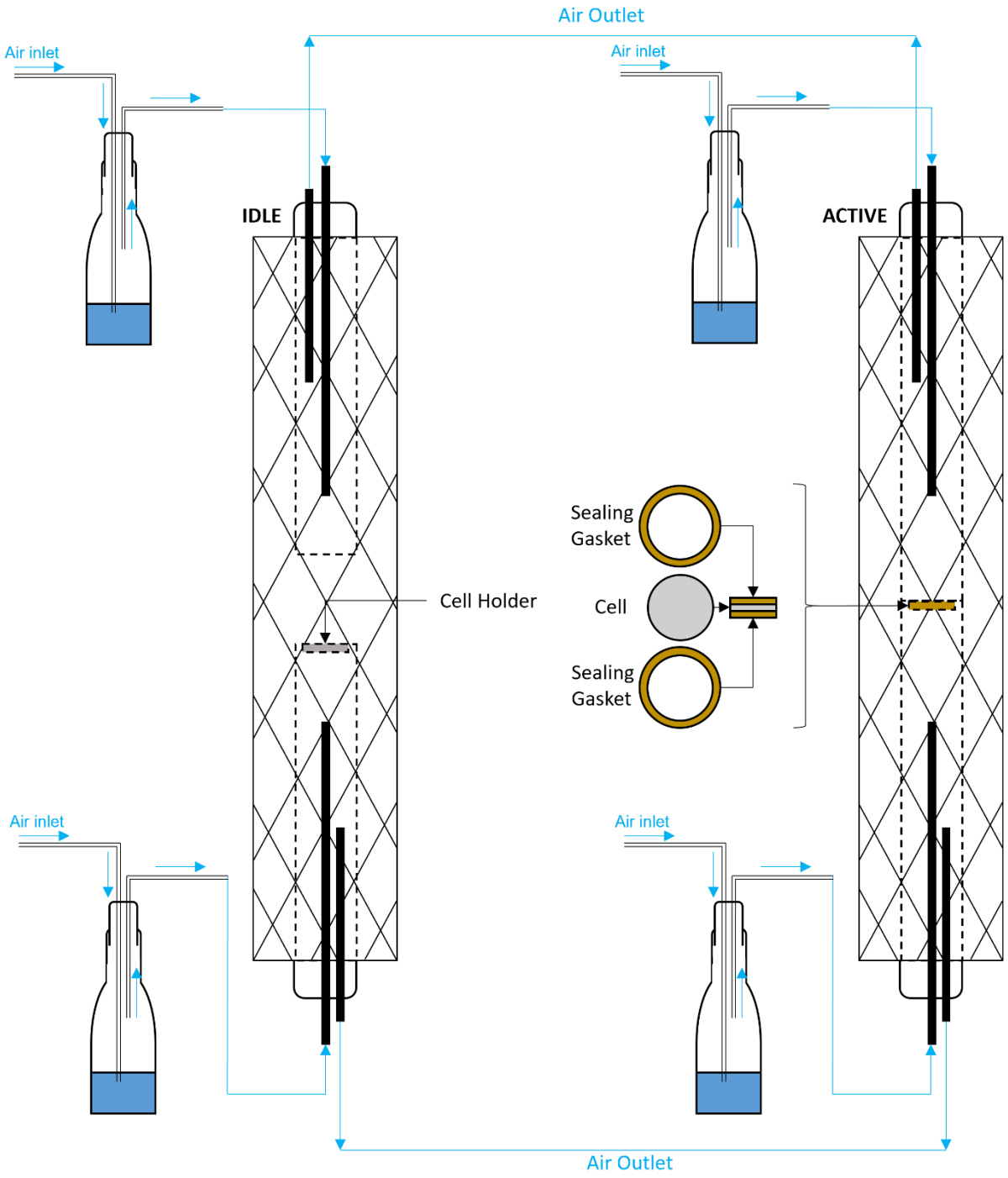


Figure 3.6: Diagrams of rig for symmetrical cell testing. Left, is a diagram when the rig is not in use notice the separation of the two tubes. Right, is a diagram when the rig is in use, notice the two tubes have come together.

For testing the manufactured symmetrical cell was first painted with gold ink (70% solid loading, Fuel Cell Materials) to improve contact between the cell and the gold current collectors used. Each side of the cell was painted one at a time and left to drive in the oven at 70°C. Once both sides had dried it was ready for testing.

Before placing the symmetrical cell into the rig, Thermiculite® 870 gaskets were put into the cell holder, to reduce leakage between either side of the cell. One side of the rig was spring loaded to apply pressure onto the gaskets and cell to further improve sealing, therefore the Thermiculite® 870 gaskets were preferred for use. The alternative gasket for use is the Thermiculite® 866 however these do not compress when pressure is applied. Instead, if using Thermiculite® 866 gaskets the top of the cell holder must be firmly in place to ensure no gas leakage, although this risks applying too much pressure onto the cell causing it to crack.

A gold current collector connect to gold wires was then placed on top of the gasket, followed by the cell, then another gold current collector and a final gasket. The other side of the cell holder was then placed on top, ensuring the weighted spring was firmly in place.

Once completely set-up, air was flown into the rig at 40 mL min^{-1} and impedance measurements taken between 400°C and 700°C at 50°C increments. Electrochemical impedance spectroscopy (EIS) measurements were taken between 0.01 and 10^5 Hz at an amplitude of 10 mV. After all measurements were completed, EIS was performed again at the same temperature points, however air was flown through bubblers containing deionised water.

3.4.1.1 Electrochemical Impedance Spectroscopy (EIS)

Electrochemical impedance spectroscopy (EIS) is a non-destructive technique for the investigation of the electrical properties, with relation to chemical properties, for a material or combination of materials. A small periodic stimulus is applied, while measuring the response. A small stimulus, either in terms of voltage or current, is applied resulting in a pseudo-linear response in the alternative property. The stimulus is a sinusoidal wave, ranging from high to low frequency. The voltage can be represented by (2.2).

$$V(t) = V_0 \cos(\omega t) \quad (3.8)$$

Where V_0 is the voltage magnitude (V) and ω is the frequency (Hz). The voltage can also be represented in terms of sin, as both sin and cosine are sinusoidal waves with a difference of $\frac{\pi}{2}$rad or 90°. The response from the electrochemical system is a sinusoidal wave, with the same input frequency however is out of phase, represented by the addition of φ. It is represented by current in (3.9).

$$I(t) = I_0 \cos(\omega t - \varphi) \quad (3.9)$$

Where I_0 is the current magnitude (**A**). The response can give an indication of the electrochemical properties of the system, namely the impedance. Impedance as per Ohm's law is the ratio between voltage and current, as a function of frequency shown by equation (3.10).

$$Z = \frac{V(t)}{I(t)} \quad (3.10)$$

Input of the sinusoidal stimulus and response will result in the following substitution, (3.11).

$$Z = \frac{V(t)}{I(t)} = \frac{V_0 \cos(\omega t)}{I_0 \cos(\omega t - \varphi)} = Z_0 \frac{\cos(\omega t)}{\cos(\omega t - \varphi)} \quad (3.11)$$

Where Z_0 is the magnitude of the impedance.

The response of the varying frequencies can give an indication of the electrochemical properties of the system, namely the impedance.

Taking into consideration Euler's relationship (3.12).

$$e^{j\varphi} = \cos(\varphi) + j \sin(\varphi) \quad (3.12)$$

$$where\ j = \sqrt{-1}$$

Voltage and current can be represented as a complex number, (3.13) and (3.14)

$$V(t) = V_0 \cos(\omega t) = V_0 e^{j\omega t} \quad (3.13)$$

$$I(t) = I_0 \cos(\omega t - \varphi) = I_0 e^{j\omega t - j\varphi} \quad (3.14)$$

Therefore, substituting these new expression for voltage and current into equation (3.10) a new expression for impedance can be developed, (3.15). Allowing impedance to be defined as a complex number.

$$Z = \frac{V(t)}{I(t)} = \frac{V_0 e^{j\omega t}}{I_0 e^{j\omega t - j\varphi}} = Z_0 e^{j\varphi} \qquad (3.15)$$

$$= Z_0(\cos(\varphi) + j\sin(\varphi))$$

This allows the impedance to be expressed in a real and imaginary component where $Z_{Real}=Z_0.\cos(\varphi)=Z'$ and $Z_{Imaginary}=Z_0.j.\sin(\varphi)= jZ''$. The real and imaginary impedance values can then be plotted as a graph on the x and y axis respectively, known as a Nyquist plot.

3.4.1.1.1 Electrical Components in an Equivalent Circuit

EIS data is often compared to a hypothetical equivalent circuit, which models the electrochemical properties of the system using various components. Components which are often utilised are resistors, capacitors, and inductors. The equations to determine the voltage of each of the electrical components can in Table 3.4, where V is voltage, I is current, R is resistance, C is capacitance, L is inductance and t is time.

Table 3.5: Electrical components and their respective equations for voltage.

Electrical Component	Voltage
Resistor	IR
Capacitor	$\frac{1}{C}\int Idt$
Inductor	$L\frac{dI}{dt}$

To determine the impedance of these elements Fourier transformation must be performed on the formulas given in Table 3.5. Leading to the Equations shown in Table 3.6which represent the impedance (Z) of the elements. The impedance for the resistor and capacitor in parallel was included as these two components produce an impedance arc which is key when determining equivalent circuit.

Table 3.6: Impedance equations for the electrical components shown in Table 3.5.

Electrical Component	Impedance
Resistor	R
Capacitor	$\frac{1}{j\omega C}$
Resistor and Capacitor in Parallel	$\frac{R}{1+(\omega RC)^2} - j\frac{\omega R^2 C}{1+(\omega RC)^2}$
Inductor	$j\omega L$

When plotting the impedance for the electrical components onto a Nyquist plot, each component has a plot, which can be seen in Figure 3.7. Plotting a Nyquist plot for a singular resistor will result in a single point in real axis, as the impedance term for a resistor does not consist of any imaginary components. While the term for a single capacitor or inductor, does not contain any real components, therefore all these points will be plotted along the imaginary axis of the Nyquist plot. The plot for the impedance of the capacitor (Z_C) can be determined by the following limits (3.16) and (3.17).

$$\lim_{\omega \to 0}(Z_c) \to -j\infty \tag{3.16}$$

$$\lim_{\omega \to \infty}(Z_c) = 0 \tag{3.17}$$

Therefore, as the frequency decreases to 0 the impedance will be negative of the imaginary value. While as the frequency increases to ∞ the impedance becomes 0. Similarly, limits can also be used to describe the impedance for the inductor (Z_L) (3.18) and (3.19).

$$\lim_{\omega \to 0}(Z_L) = 0 \tag{3.18}$$

$$\lim_{\omega \to \infty}(Z_L) \to j\infty \tag{3.19}$$

The expression of the inductor is the inverse of the capacitor, thus the opposite plot is to be expected. As can be seen by the limits, as the frequency reaches 0 the impedance also reaches 0. While as the frequency reaches ∞ the impedance also reaches ∞, however unlike the capacitor this occurs in the positive direction.

Having a resistor and capacitor in parallel, in a circuit produces an impedance arc. Following similar limits as previous ((3.20) and (3.21)) as well as expressing frequency as $\omega = (RC)^{-1}$ (3.22), the impedance for a resistor and capacitor in parallel (Z_{RC}) can be expressed as a real and imaginary term, resulting in the distinctive arc shape.

$$\lim_{\omega \to 0}(Z_{RC}) = R \tag{3.20}$$

$$as\ Z_{RC} = \frac{R}{1 + (\omega RC)^2} - j\frac{\omega R^2 C}{1 + (\omega RC)^2} = R - j(0) = R$$

$$\lim_{\omega \to \infty}(Z_{RC}) = 0 \tag{3.21}$$

$$as\ Z_{RC} = \frac{R}{1 + (\omega RC)^2} - j\frac{\omega R^2 C}{1 + (\omega RC)^2} = 0 - j(0) = 0$$

$$for\ \omega = (RC)^{-1};$$

$$Z_{RC} = \frac{R}{1 + (\omega RC)^2} - j\frac{\omega R^2 C}{1 + (\omega RC)^2} = \frac{R}{2} - j\frac{R}{2} \tag{3.22}$$

Another component which is often considered when modelling equivalent circuits is a constant phase element (CPE), which in essence does not have a real life component. The formula to simulate a CPE is represented by equation (3.23).

$$Z_{CPE} = \frac{1}{Q(j\omega)^{\alpha}} \tag{3.23}$$

Where Q is the non-ideal capacitance and α is the order. The value of α is between 0 and 1. By applying these α they can be represented in two statements (3.24) and (3.25).

$$\lim_{\alpha \to 0}(Z_{CPE}) = \frac{1}{Q} = Q^{-1} \tag{3.24}$$

Resulting in Z_{CPE} not being a function of frequency, thus being similar to a resistor. Another limit can be applied to α.

$$\lim_{\alpha \to 1}(Z_{CPE}) = \frac{1}{Qi\omega} \tag{3.25}$$

Which is similar to the equation to represent a capacitor. Therefore plotting a Nqyuist plot for a CPE is similar to that of a capacitor at an angle which is dependent on α.

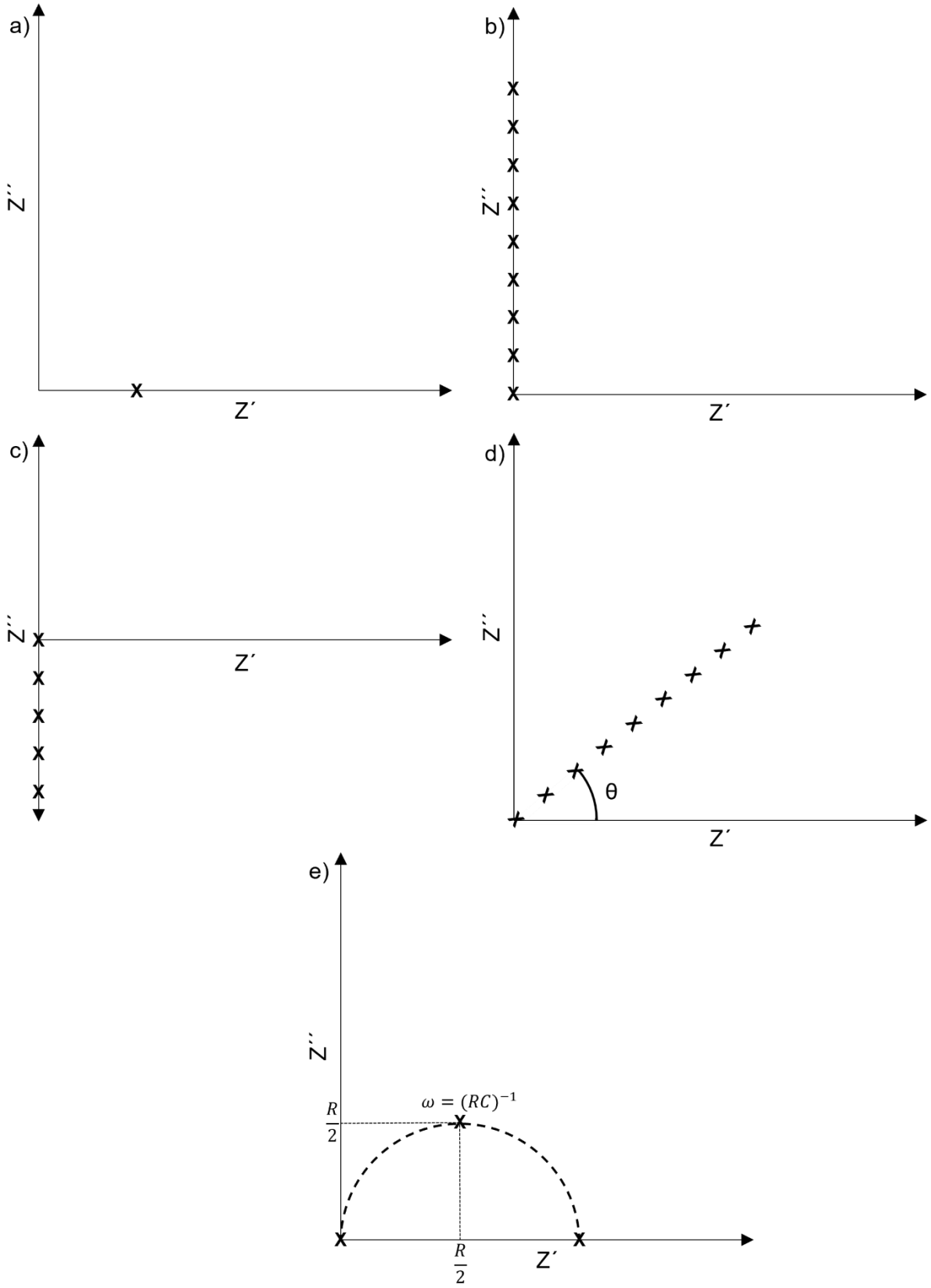


Figure 3.7: Nyquist plots for a) a single resistor, b) a single capacitor, c) a single inductor, d) a CPE and e) a resistor and capacitor in parallel.

As previously mentioned, an equivalent circuit can be used to represent the impedance of an electrochemical system. Certain phenomena are responsible for the response (Table 3.7)[177]. Figure 3.8 shows an example of a Nyquist plot for a fuel cell and its corresponding circuit. The inductor (L_{Sys}) mimics the data points of the positive imaginary value. The positive imaginary values can be attributed to the instrumental noise. The x axis intercept is the ohmic resistance (R_O) of the whole system (electrolyte and electrodes) and is represented solely by the resistor, as it does not have an imaginary value.

Table 3.7: Capacitance values and their respective phenomenon [177].

Capacitance (F)	Phenomenon Responsible
10^{-12}	Bulk
10^{-11}	Minor, second phase
$10^{-11} – 10^{-8}$	Grain boundary
$10^{-10} – 10^{-9}$	Bulk ferroelectric
$10^{-9} – 10^{-7}$	Surface layer
$10^{-7} – 10^{-5}$	Sample-electrode interface
10^{-4}	Electrochemical reaction

The two semicircles, the first at higher frequency and the second at lower frequencies, are each represented by a resistor and a capacitor in parallel. The high frequency semicircle is a result of the anode activation loss (R_{An} and C_{An}) while the low frequency semicircle represents the cathode activation loss (R_{Cat} and C_{Cat}). For each semicircle the resistor represents the kinetic resistance, larger diameters indicating sluggish reaction kinetics. While the capacitor is used to describe the charge separation at the electrode/electrolyte interface. The sum of all the semicircle diameters gives the resistance of the complete cell also known as the polarisation resistance (R_{pol}). When testing a symmetrical cell, the R_{pol} is divided by two to account for the two electrodes on either side of the electrolyte, giving the R_{pol} for a single electrode.

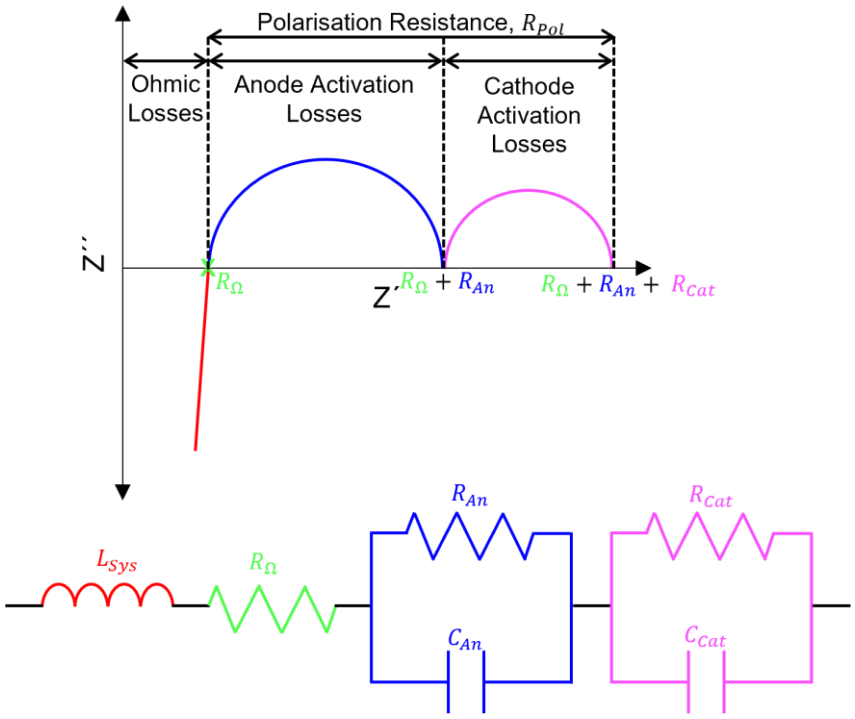


Figure 3.8: Example of a Nyquist plot and the equivalent circuit associated with it.

3.4.2 Fuel Cell/Electrolyser Testing

Fuel cell testing was performed on a separate rig from the symmetrical cell testing rig, again it was custom-built (Figure 3.9). A similar setup is followed to that of the symmetrical cell in regard to the gold ink, gold current collectors and gaskets. The fuel cell rig consisted of a H_2, N_2 and air Bronkhurst mass flow controller. For electrolysis, a Bronkhurst controlled evaporator mixer (CEM) was used.

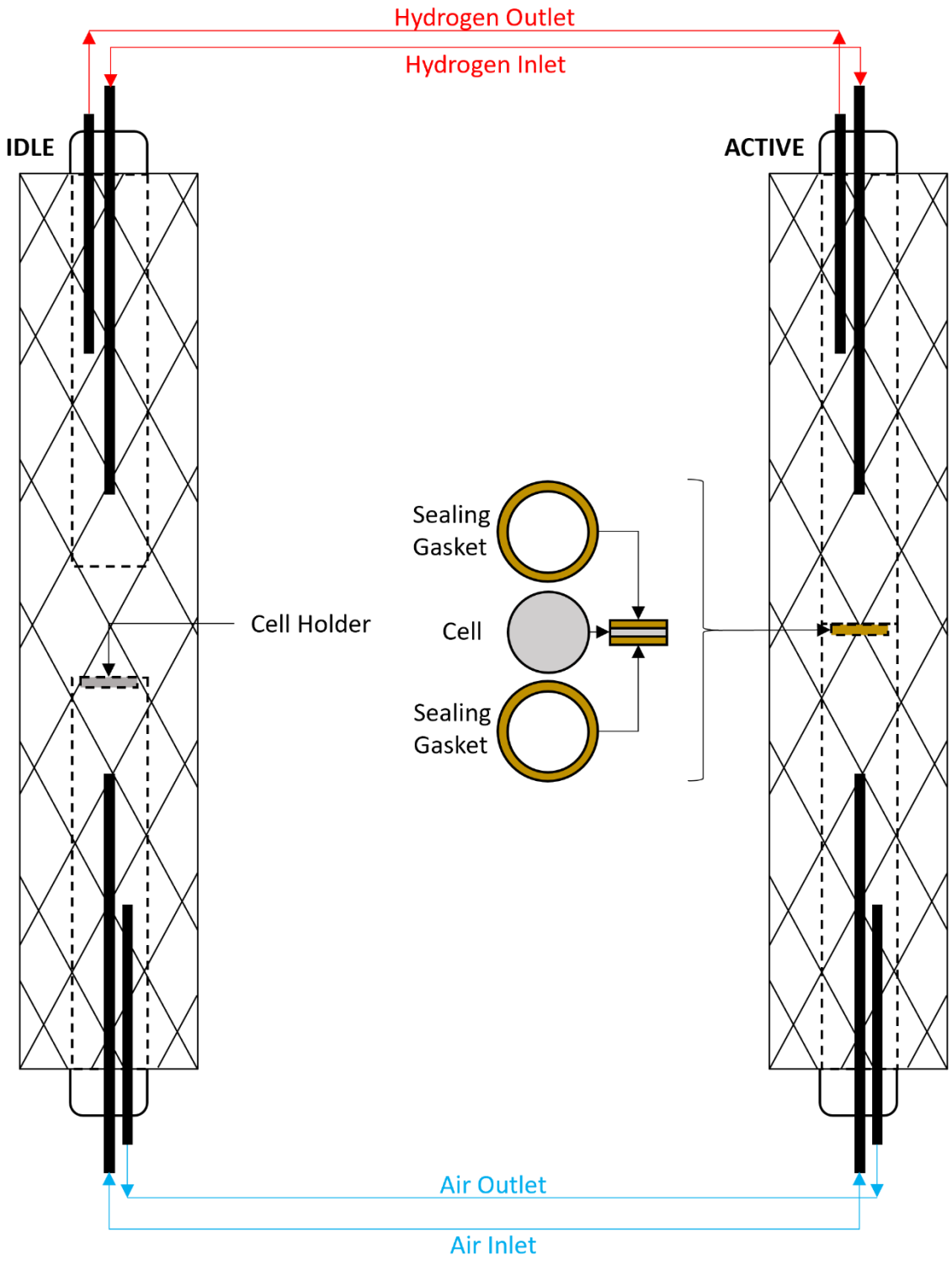


Figure 3.9: Diagrams of rig for fuel cell and electrolyser testing. Left, is a diagram when the rig is not in use notice the separation of the two tubes. Right, is a diagram when the rig is in use, notice the two tubes have come together.

A cell was placed inside the cell holder with Thermiculite® 870 gaskets. The rig was sealed, and the furnace set to ramp to 450°C at 2°Cmin^{-1}. When a temperature of 350°C was reached, N_2 was flowed into the anode, through a bubbler containing deionised water, at a flow rate of 40 mLmin^{-1}, while air was flowed into the cathode at 40 mLmin^{-1}. This was to purge the anode side of any air, so that the hydrogen and oxygen would not react with one another at higher temperatures. At 400°C, 40 mLmin^{-1} of H_2 was introduced into the anode side of the rig. While the flow rate of air was increased to 80 mLmin^{-1}. By introducing the H_2 at 400°C it creates a H_2 rich environment before the reduction of nickel oxide (NiO) is expected to occur. The rig continued to ramp to 450°C. Where it dwells for 1 h, to allow the NiO to start reducing. The rig then ramps to 700°C for at 1°Cmin^{-1}. Once 700°C was reached, the nitrogen flow rate was reduced to 0 mLmin^{-1} and the air flowrate reduced to 40 mLmin^{-1}. The cell was left to anneal for 12 h, before measurements were taken.

To achieve a baseline for fuel cell testing using the custom-built rig, cell testing was originally performed against a commercial cell. A commercial proton conducting ceramic cell (PCCC) could not be obtained therefore a commercial oxide conducting solid oxide cell (OC-SOC) was used. The cell was purchased from Ningbo SOFCMAN Energy Technology Co. Ltd. and consisted of a lanthanum strontium ferrite doped with cobalt (LSCF) and gadolinium-doped cerium (GDC) cathode, a 8 mol% yttrium stabilised zirconium (8YSZ) electrolyte and an anode consisting of 50:50 wt% of NiO:8YSZ. Using the commercial OC-SOC, at 700°C, a maximum power density of 89.5 mWcm^{-2} was achieved and a maximum current density of 302 mAcm^{-2} was achieved (Figure 3.10). The OCV achieved was 1.04 V, with 1.1 V being ideal, suggesting adequate sealing and very little gas crossover.

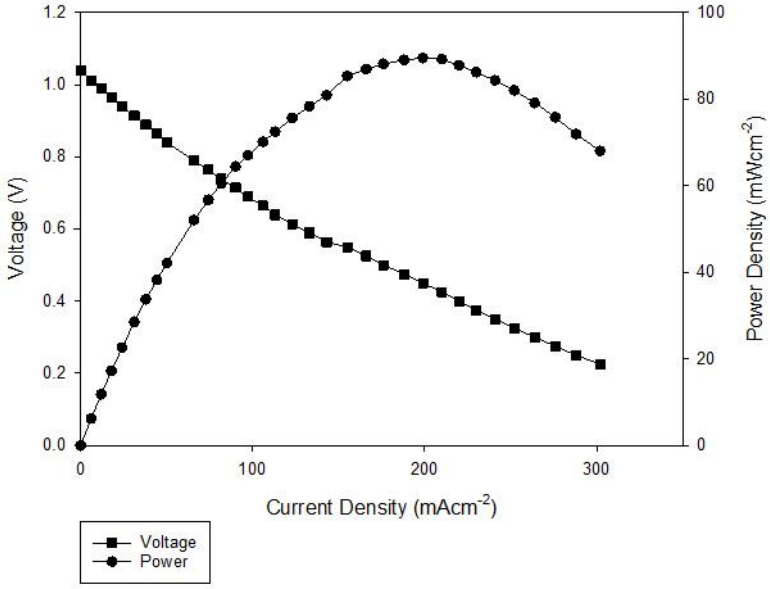


Figure 3.10: Voltage (square) and power density (circle) verses current density of commercial OC-SOC, measurements taken at 700°C. OC-SOC consisted of LSCF and GDC cathode, 8YSZ electrolyte and 50:50 wt% of NiO:8YSZ anode.

For electrolysis measurements the flow rate of air was 52 $mLmin^{-1}$ and water was 0.82 gh^{-1}, air would travel through a Bronkhurst CEM and was heated to 70°C. The pipeline connecting the Bronkhurst CEM and rig was wrapped in heating tape, wrapped in three layers of Superwool flame retardant insulation (from RS Components) to maintain 70°C. Air/H_2O entered through the bottom of the vertical furnace, so that any reacted H_2O would feed down and out of the rig. If the air/H_2O outlet was at the top of vertical furnace then any unreacted H_2O would condense in the outlet pipe and feed back into the rig. The H_2 flow rate was set at 52 $mLmin^{-2}$ to match the flowrate of air. Air would travel through a Bronkhurst CEM was heated to 70°C.

3.4.2.1 Chemical Thermodynamics

The enthalpy (H) of a reaction is the difference between the total empathy of the products minus the total enthalpy of the reactants. For an exothermic reaction the enthalpy change is negative, as the energy for forming the bonds in the product/s is greater than the energy required to break the bonds of the reactants, therefore energy is removed from the system. If the enthalpy is positive, the reaction is

endothermic, so more energy is required to break the bonds of the reactants then produced by forming new bonds.

Entropy (S), in early concepts, can be described as the dispersal of energy. The higher the energy dispersal, the higher the entropy value. Therefore, in a closed system entropy is always increasing, as per the second law of thermodynamics. Often, it is now described as the disorder of a system. It can be it can be represented in terms of heat transfer (Q) and temperature (T), as shown by (3.26).

$$\Delta S = \frac{\Delta Q}{T} \tag{3.26}$$

Gibbs free energy is a measure of how readily a chemical reaction will occur on its own. A negative value of Gibbs free energy indicates a spontaneous reaction while a positive value means that it is not. A value of zero, implies that the reaction is at equilibrium. Gibbs free energy can be represented by the following (3.27).

$$\Delta G = \Delta H - T\Delta S \tag{3.27}$$

Where H is the enthalpy, T is the temperature and S is entropy. The enthalpy and entropy of a reaction largely determine the value of the Gibbs free energy as can be seen in Figure 3.11.

	ΔH<0	**ΔH>0**
ΔS>0	ΔG<0. The reaction will be spontaneous for all temperatures.	At high temperatures when TΔS>ΔH, ΔG<0 Therefore the reaction will be spontaneous.
ΔS<0	At low temperatures so that the equality ΔH<TΔS is satisfied, ΔG<0. The reaction will be spontaneous.	ΔG>0. The reaction will not be spontaneous at any temperature, as Gibbs free energy is always positive.

Figure 3.11: The expected outcome with varying vales of enthalpy, entropy and Gibbs free energy.

The Gibbs free energy can also be applied to electrochemical reactions, where it can be defined as the maximum work performed during the electrochemical process. This can be seen in equation (3.28).

$$\Delta G = -nFE^0 \qquad (3.28)$$

Where n is the number of electrons, F is the Faraday constant (96485 C mol^{-1}) and E^0 is the reversible cell potential also known as the standard potential, which is the minimum potential required for a reaction to occur [46].

These thermodynamic properties can be applied to the water splitting electrolysis reaction (Figure 3.12). When water is a liquid, under standard conditions, the reaction has an enthalpy value of 285.83 $kJmol^{-1}$ and Gibbs free energy of 237.14 $kJmol^{-1}$. When temperature increases and a change in phase, from liquid to gas occurs a drop in the enthalpy and Gibbs free energy occurs, at 400 K these are 242.845 $kJmol^{-1}$ and 219.05 $kJmol^{-1}$ respectively. The enthalpy gradually increases between 400 K and 1500 K, while remaining positive. The heat demand also increases, although at a greater rate [56]. Therefore the Gibbs free energy decreases as temperature increases. Relating this to (3.28) means that the Nernest potential also decreases with temperature. Consequently, less electricity is required for the water splitting reaction. Solid oxide cells (SOC's) operate between 500°C and 800°C, hence can take advantage of the thermodynamics of the reaction.

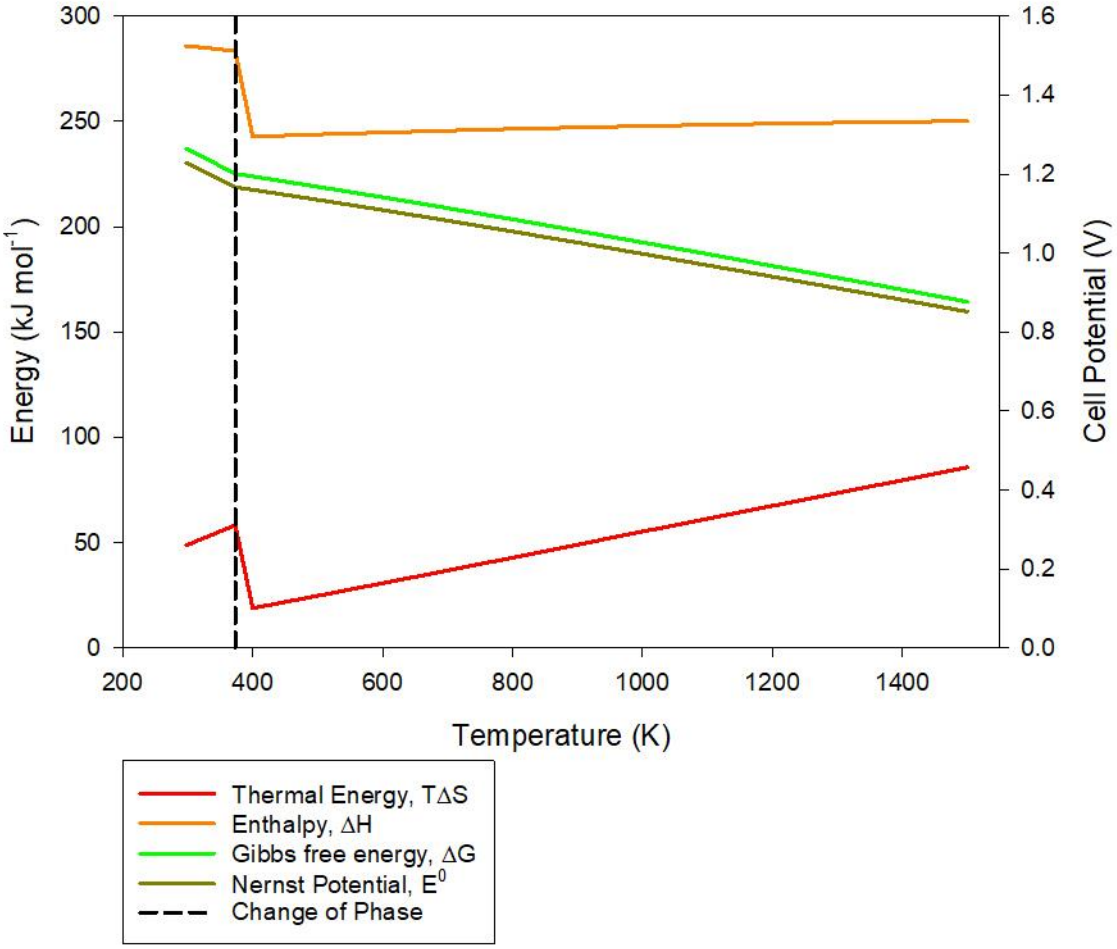


Figure 3.12: Graph showing the relationship between Gibbs free energy/enthalpy and temperature [178, 179]

3.4.2.2 Polarisation Curve

The Nernst potential is the theoretical maximum possible potential that can be achieved. The potential considers the temperature and pressure of the various species involved. The theoretical value is difficult to achieve within a fuel cell due to irreversible losses such as to species crossover, electronic leakage, and contaminants. Low temperature fuel cells such as proton exchange membrane cells (PEMCs) are more susceptible to irreversible losses compared high temperature fuel cells such as SOCs. This is a result of the characteristics of PEMCs. The potential can be described through the Nernst equation given by equation (3.29).

$$E = E^0 + \frac{RT}{2F}\ln\left(\frac{pO_2{}^{\frac{1}{2}} \times pH_2}{pH_2O}\right) \quad (3.29)$$

Where R is the ideal gas constant 8.314 J K^{-1} mol^{-1}, F is Faraday's constant 96,500 C mol^{-1}, pO_2, pH_2 and pH_2O are the partial pressures for O_2, H_2 and H_2O respectively. E^0 is the reversible cell potential also known as the standard potential, as previously shown with relation to Gibbs free energy.

Open circuit voltage (OCV) of a cell is the potential difference between two electrodes, without the pressure of a load. It is also the same value as the Nernst potential. Applying an overpotential, will either result in anodic polarisation (potential is greater than the OCV) or cathodic polarisation (potential less than the OCV). Anodic polarisation results in electrolysis reactions taking place, thus a decrease in current while cathodic polarisation results in the reverse. The latter is the operation of a fuel cell. The relationship between the applied potential and the current produces a polarisation, also known as an IV curve (Figure 3.13).

A polarisation curve can be segmented into three distinct regions, depending on the main characteristic shown by the polarisation curve. The first region (indicated by I on Figure 3.13) is attribute to activation losses induced by sluggish kinetics and electrode reactions. These losses are insignificant for SOCs due to high operating temperature resulting in fast kinetics. PEMCs operate at lower temperatures, so have slower kinetics, therefore this region is clearly visible. Initially there is a steep drop in voltage due to the high concentration of reactants.

The second region (indicated by II on Figure 3.13) is characterised by a negative linear correlation, the result of which is due to ohmic losses. Electronic and ionic resistance occurs throughout the complete cell, whether it be the electrode, electrolyte, or current collectors. The characteristic is governed by Ohm's law hence the linear correlation. Temperature can influence the conductivity, the effect of which will vary depending in the composition of the cell. PEMCs have relatively low ohmic losses as the polymer electrolyte is highly conductive. However, SOCs are dominated by ohmic losses due to the ceramic nature of the cell.

The final region (indicated by III on Figure 3.13) pertains to concentration losses, also known as mass transport losses. Attributed to a lack of reactants or lack of reactant sites, inhibiting the reaction. Both high temperature and low temperature cells show similar trends in this region. When considering all these losses the voltage can be calculated through the following equation (3.30)

$$V = E - \eta_{act} - \eta_{ohm} - \eta_{conc} \tag{3.30}$$

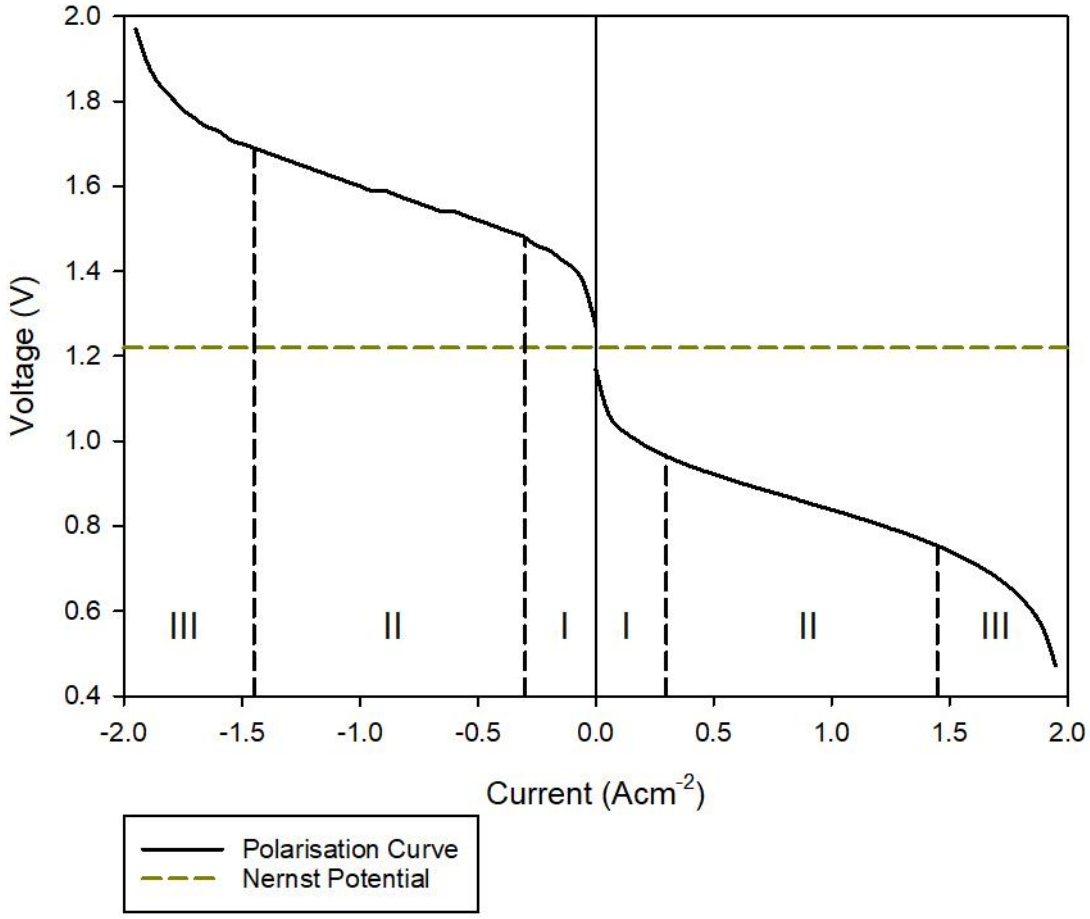


Figure 3.13: Polarisation curve for a PEMCs. The three distinct regions can be clearly seen for PEMCs, unlike with an SOC where the activation loss is negligible due to the high operating temperature.

Chapter 4: Bi and Nb Doping in $BaFeO_{3-\delta}$

4.1 Introduction

Cobalt (Co) containing perovskites are often used as electrodes in solid oxide cells (SOCs), although they have several issues such as: cost and availability of cobalt, poor chemical stability and high reactivity with zirconium-based materials [180-182]. Suitable Co – free electrode materials, that can operate within the intermediate temperature range (500°C to 700°C) are currently being explored. One alternative is to use iron (Fe) based materials, with prior work suggesting that these electrode materials have better compatibility with the electrolyte [183, 184]. However, one key issue is that they tend to have lower catalytic activity and lifetime [183].

$BaFeO_{3-\delta}$, a perovskite with the general formula ABO_3 (Figure 4.1), can have various crystal structures depending on the oxygen deficiency, relating to the fact that the oxygen content can be varied through altering the temperature or oxygen partial pressure during heat treatment [185, 186]. This allows the formation of the cubic, triclinic, rhombohedral, tetragonal, and hexagonal structures reported within the literature [185, 186]. Further study into $BaFeO_{3-\delta}$ has shown that hydration, through incorporation of H_2O into oxygen vacancies forming hydroxide ions (OH^-), can be achieved, facilitating proton conductivity [187]. Therefore $BaFeO_{3-\delta}$ could be seen as a possible electrode material for proton conducting ceramic cells (PCCC). The large ionic radius of the barium (Ba) ion creates a large free volume in the lattice which allows for potential rapid ion migration, while the presence of oxygen vacancies subsequently allows for hydration [188].

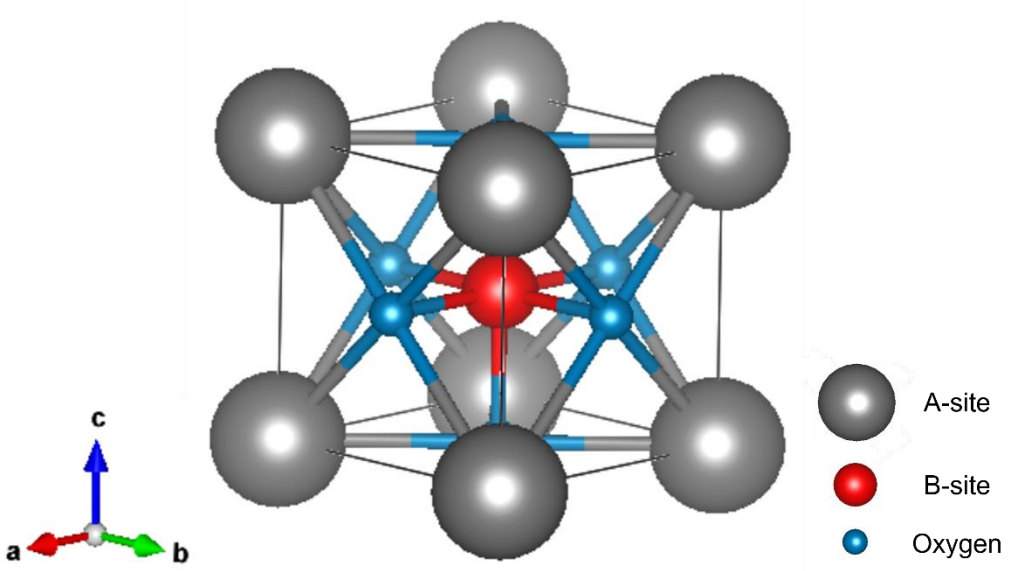


Figure 4.1: Example of a cubic *Pm*-3*m* space group perovskite, with the general formula ABO_3. Where the grey orbs represent the A-site, the red orbs represent the B-site and the blue orbs represent oxygen atoms.

A challenge of undoped $BaFeO_{3-\delta}$ is its instability due to the large oxygen deficiencies possibly which can lead to significant structural changes and result in large volume changes. Consequently, there is a lot of interest in finding strategies to stabilise the structure. Past research has shown that doping with bismuth (Bi), cerium (Ce), gadolinium (Gd), lanthanum (La), nickel (Ni), niobium (Nb), samarium (Sm) and zirconium (Zr) leads to compounds better suited for SOC applications [184, 189-192]

In particular Bi and Nb have been shown previously to occupy the B site of perovskites [189-191, 193, 194]. Bi is a common dopant regarding PCCC electrodes, previously being shown to improve the performance [183, 195, 196]. While Bi doping in Co-containing perovskites has been explored, the chemical stability of these samples are often overlooked [188, 197].

Nb doping often focuses on electrodes for intermediate oxide conducting solid oxide cells (OC-SOC), improving chemical stability [184, 190, 198, 199]. Using Nb creates larger unit cells, leading to easier incorporation of oxide ion vacancies and better conductivity [199]. A similar concept can be applied to PCCC, as proton transport is thought to be facilitated through OH^- incorporation [200]. Less than 20 mol% of Nb doped on the B site has previously been explored [188, 190, 198]. Nb was shown to improve

the oxygen reduction reaction (ORR) at temperatures below 625°C [201]. However more than 20 mol% of Nb doping has not been fully explored for the use in PCCCs.

Doping $BaFeO_{3-\delta}$ with either Bi or Nb, is expected to occur on the B-site of the perovskite. In both cases Fe^{3+} would be substituted with either Bi^{5+} or Nb^{5+}. Increasing the quantity of Bi^{5+} or Nb^{5+} is expected to increase the unit cell parameters, as the higher charge of the dopant would shift the oxidation state of Fe^{4+} to Fe^{3+}. The shift of Fe^{4+} to Fe^{3+} would result in a reduction in oxygen vacancies, therefore possibly reducing the quantity of hydroxide ions, thus water, that can be incorporated. Electrical conductivity will be expected to decrease with increasing Bi and Nb, once again as a result in the change in oxidation state of Fe. The shift in Fe results in a decrease in electrical charge carriers [202]. Despite this Bi or Nb doping is expected to stabilise the crystal structure to form a cubic phase, which has improved chemical stability, as previously seen [184, 190, 198, 199].

Consequently, within this chapter Bi and Nb doped $BaFeO_{3-\delta}$ samples will be reported. Samples were synthesized and lattice parameters determined, including analysis of lattice parameter after exposure to humid and dry nitrogen (N_2) conditions while heating. Finally, conductivity measurements were performed, as a preliminary ex-situ measure of possible application as a PCCC electrode.

4.2 Experimental

$BaCO_3$ (VWR, 99.8%), Fe_2O_3 (Sigma-Aldrich, ≥99.0%), Bi_2O_3 (Sigma-Aldrich, 99.99%) and Nb_2O_5 (Sigma-Aldrich, 99.99%) were used to synthesise $BaFe_{1-x}Bi_xO_{3-\delta}$ and $BaFe_{1-x}Nb_xO_{3-\delta}$. All compounds were prepared with the relevant stoichiometric ratios of starting materials. The powders were ground using a pestle and mortar, then heated in a Carbolite Gero Ltd. CWF 13/13 muffle furnace to 900°C for 12 h, followed by further grinding and then heating to higher temperatures see Table 4.1.

X-ray diffraction (XRD) analysis was performed using the Bruker D8 diffractometer with Cu K_α radiation, to determine phase purity and structures formed. Structural refinement was performed through Rietveld refinement, using the GSAS-II suite of programmes [203]. In order to determine the potential for water incorporation, samples were heated within a Carbolite Gero Ltd. CTF 13/13 tube furnace in

the presence of humid N_2. XRD analysis was the performed to observe any phase change on hydration. Thermogravimetric analysis (TGA) with mass spectrometry (MS), using a Netzsch STA 449 F1 Jupiter Thermal Analyser attached to a Netzsch MS 403C Aëolos Mass Spectrometer, was performed to determine the resultant content. Using MS it was possible to differentiate between mass losses due to water (H_2O) and other gases, such as oxygen (O_2) and carbon dioxide (CO_2). The as-prepared sample was also heated in dry N_2 and the XRD pattern compared to the humid N_2 sample.

For electrical conductivity measurements, pellets were formed by pressing powders in a 10 mm Specac die, under 5 tons and sintering them at the temperature they were synthesised at. The pellet press was obtained from Doreth Engineering Co. Ltd. Four gold wires were then attached using gold paste heated to 800°C for 1h. 4 probe measurements were performed, up to 700°C on the pellets in air, to determine the electrical conductivity of the doped $BaFeO_{3-\delta}$ samples.

Table 4.1: Samples synthesised at Synthesis temperature used.

Composition	**Temperature (°C)**
$\mathbf{BaFe_{0.925}Bi_{0.075}O_{3-\delta}}$	1100
$\mathbf{BaFe_{0.9}Bi_{0.1}O_{3-\delta}}$	1100
$\mathbf{BaFe_{0.85}Bi_{0.15}O_{3-\delta}}$	1100
$\mathbf{BaFe_{0.6}Nb_{0.4}O_{3-\delta}}$	1200
$\mathbf{BaFe_{0.55}Nb_{0.45}O_{3-\delta}}$	1200
$\mathbf{BaFe_{0.5}Nb_{0.5}O_{3-\delta}}$	1150

4.3 Bismuth Doped Systems $BaFe_{1-x}Bi_xO_{3-\delta}$

XRD data showed the successful synthesis of $BaFe_{1-x}Bi_xO_{3-\delta}$ where x = 0.075, 0.1 and 0.15 (Figure 4.2). All samples were first refined using the cubic *Pm*-3*m* space group followed by a tetragonal *P*4/*mmm* space group as described by [189, 193]. Calculated cell parameters are given in Table 4.2 and Table 4.3, both cubic and tetragonal models were explored. However tetragonal splitting was negligible as similar

R-weight pattern (R_{wp}) potential were seen. Therefore, the higher symmetry cubic phase was selected as the ideal fit. An example of the Rietveld refinement profile is shown in Figure 4.3.

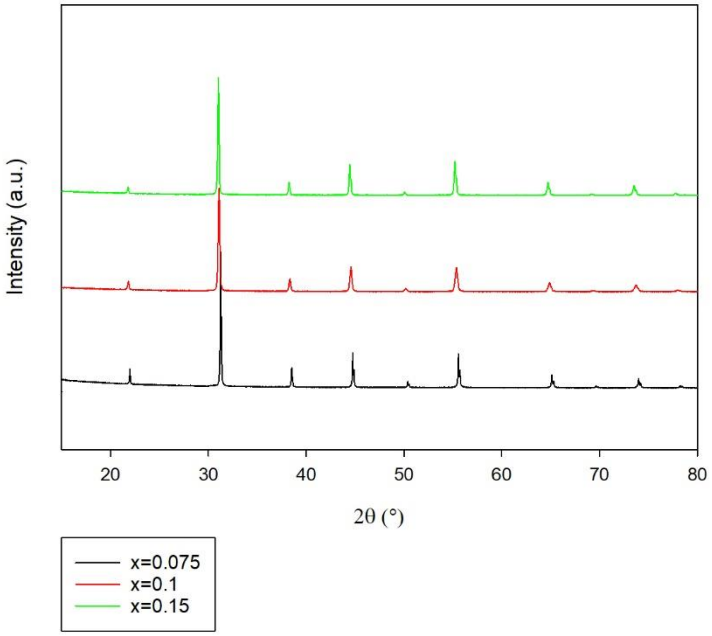


Figure 4.2: XRD of $BaFe_{1-x}Bi_xO_{3-\delta}$ where x = 0.075, 0.1 and 0.15.

Table 4.2: Unit cell parameters for $BaFe_{1-x}Bi_xO_{3-\delta}$ where x = 0.075, 0.1 and 0.15. The structure presented was refined against a cubic *Pm*-3*m* space group.

	Unit Cell Parameters (Å)			
Composition	a	**Unit Cell Volume (Å^3)**	**R_{wp}(%)**	**R_{exp}(%)**
$BaFe_{0.925}Bi_{0.075}O_{3-\delta}$	4.0490(1)	66.38(0)	6.26	3.33
$BaFe_{0.9}Bi_{0.1}O_{3-\delta}$	4.0593(0)	66.89(0)	4.21	2.60
$BaFe_{0.85}Bi_{0.15}O_{3-\delta}$	4.0679(0)	67.32(0)	5.29	2.72

Table 4.3: Unit cell parameters for $BaFe_{1-x}Bi_xO_{3-\delta}$ where x = 0.075, 0.1 and 0.15. The structure presented was refined against a tetragonal space group *P*4/*mmm* space group.

Composition	Unit Cell Parameters (Å)		Unit Cell Volume (Å^3)	R_{wp}(%)	R_{exp}(%)
	a	c			
$BaFe_{0.925}Bi_{0.075}O_{3-\delta}$	4.0488(3)	4.0492(5)	66.38(0)	6.29	3.33
$BaFe_{0.9}Bi_{0.1}O_{3-\delta}$	4.0569(1)	4.0653(1)	66.91(0)	3.97	2.60
$BaFe_{0.85}Bi_{0.15}O_{3-\delta}$	4.0665(1)	4.0720(1)	67.33(0)	5.07	2.72

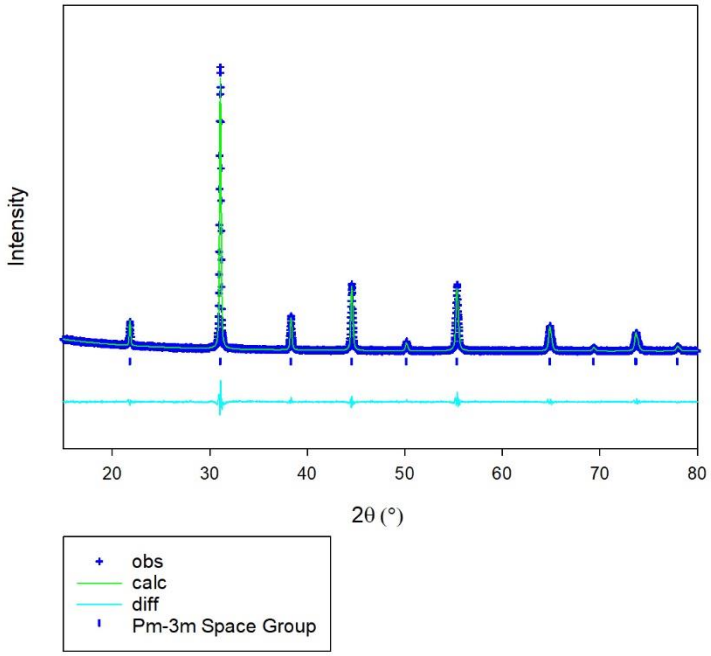


Figure 4.3: Example of observed (blue cross), calculated (green) and difference (cyan) profiles for Rietveld refinement performed (cubic *Pm*-3*m* space group, R_w=4.21%).

Inspection of Figure 4.2 shows increasing mol% of Bi results in peaks shifting to lower 2θ angles, indicating an increase in lattice parameters. This is further confirmed from refinement data, shown in Table 4.2 and Table 4.3. $BaFe_{0.925}Bi_{0.075}O_{3-\delta}$ has the smallest parameters of the three samples, and $BaFe_{0.85}Bi_{0.15}O_{3-\delta}$ has the largest unit cell. The increase in the cell parameters can be explained by the higher charged Bi doping increasing the Fe^{3+} content, Fe^{3+} has a larger ionic radius than Fe^{4+}.

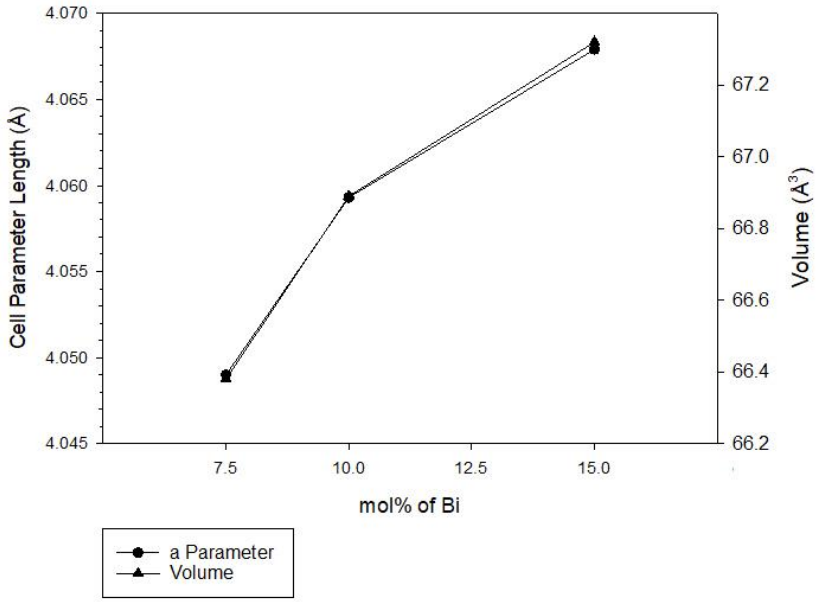


Figure 4.4: Variation of cell parameter of $BaFe_{1-x}Bi_xO_{3-\delta}$ with Bi content. Samples were refined against a cubic *Pm*-3*m* space group. Circle indicates *a* parameter. Triangle indicates the volume of the unit cell.

4.3.1 Investigation into the Effect of Heating Under Humid Nitrogen

The Bi doped samples were then heated in humid N_2 to examine potential H_2O incorporation. The XRD patterns of the samples after this heat treatment (Figure 4.5) showed no change in structure. Therefore all samples were shown to be chemically stable in humid conditions, a requirement for PCCC [204]. A peak shift towards lower angles was however observed for the hydrated sample (Figure 4.6). The peak shift is due the lattice size increasing, suggesting either reduction of Fe^{4+} to Fe^{3+}, H_2O incorporation into the crystal lattice or a combination of both effects. The lattice parameter, from performing a Rietveld refinement (Table 4.4, Figure 4.7 and Figure 4.8) show that the lattice parameters for all samples have increased. After humidification of the samples, TGA/MS analysis was performed to observe whether mass loss was observed and whether it correlated with H_2O incorporation.

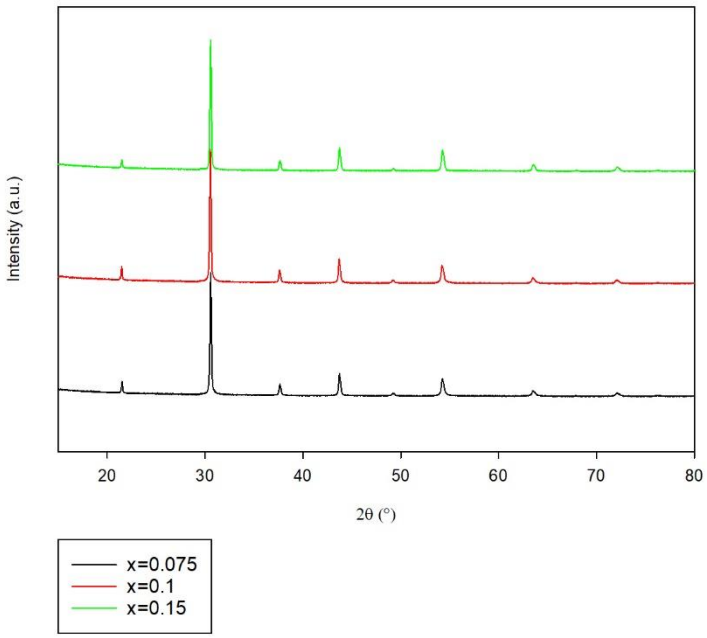


Figure 4.5: XRD of $BaFe_{1-x}Bi_xO_{3-\delta}$ where x = 0.075, 0.1 and 0.1, after samples were exposed to humid N_2.

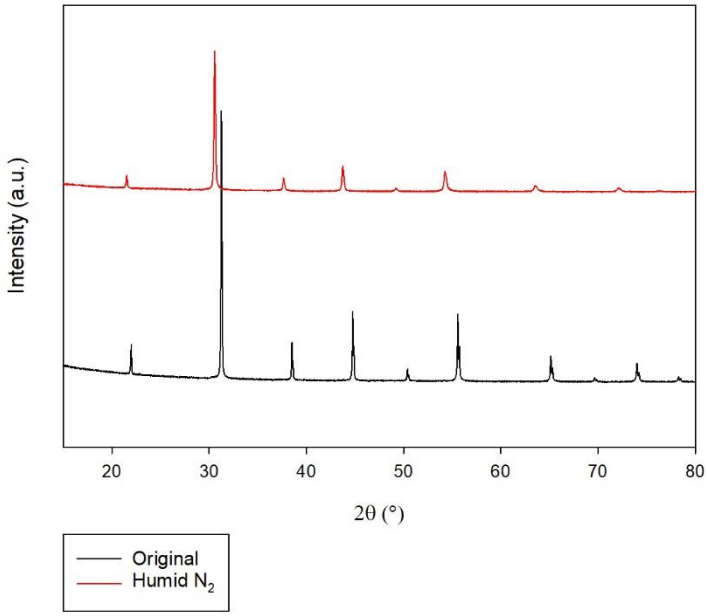


Figure 4.6: XRD of $BaFe_{0.925}Bi_{0.075}O_{3-\delta}$ before (bottom) and after humid N_2 (top).

Table 4.4: Unit cell parameters for $BaFe_{1-x}Bi_xO_{3-\delta}$ samples heated in humid N_2; where x = 0.075, 0.1 and 0.15. (cubic *Pm*-3*m* space group).

Composition	Unit Cell Parameters (Å)	
	a	Unit Cell Volume (Å^3)
$BaFe_{0.925}Bi_{0.075}O_{3-\delta}$	4.1422(1)	71.07(1)
$BaFe_{0.9}Bi_{0.1}O_{3-\delta}$	4.1421(0)	71.07(0)
$BaFe_{0.85}Bi_{0.15}O_{3-\delta}$	4.1404(1)	70.98(0)

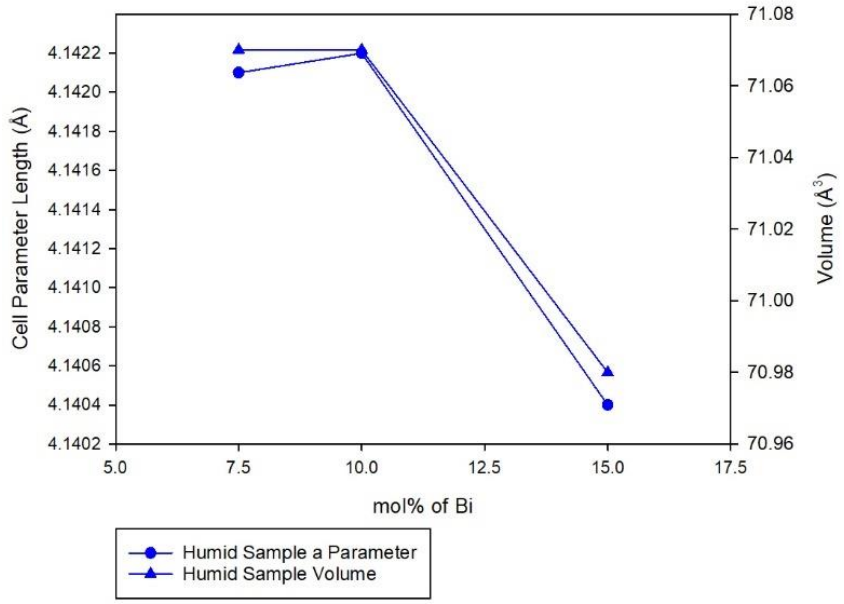


Figure 4.7: Lattice parameter (cubic *Pm-3m*) of $BaFe_{1-x}Bi_xO_{3-\delta}$ doped samples. Circles indicate the *a* parameters and triangles indicate the volume of the cell.

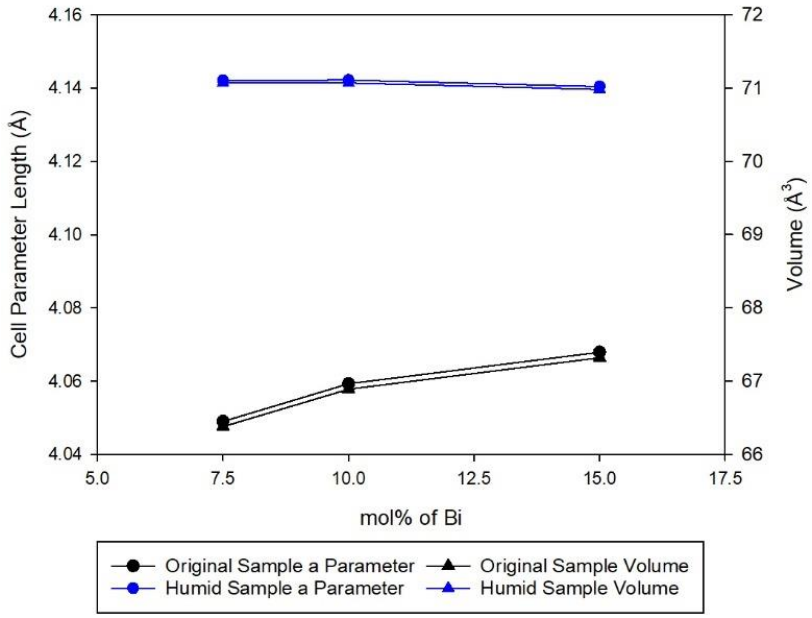


Figure 4.8: Lattice parameter (cubic *Pm*-3*m*) of $BaFe_{1-x}Bi_xO_{3-\delta}$ doped samples. Circles indicate the a parameters and triangles indicate the volume of the cell. Black indicated original samples, blue indicated sample heated in humid N_2

TGA studies showed that all samples lost H_2O above 100°C (Figure 4.9 to Figure 4.11). MS detected a singular H_2O peak for $BaFe_{0.85}Bi_{0.15}O_{3-\delta}$, indicating H_2O loss for the sample. Decreasing the Bi content led to H_2O release occurring in two stages instead of one. This can most clearly be seen in $BaFe_{0.925}Bi_{0.075}O_{3-\delta}$, the first stage of H_2O loss occurred between 40°C and 250°C, the second stage of H_2O loss occurs between 250°C and 400°C. The humidified $BaFe_{0.9}Bi_{0.1}O_{3-\delta}$ sample also showed a two-stage mass loss, although not as distinct as $BaFe_{0.925}Bi_{0.075}O_{3-\delta}$. For all samples, H_2O loss below 100°C can be attributed to H_2O loss from the surface of the sample, as mass loss begins from low temperatures. Above 100°C, H_2O loss is from the bulk of the sample. TGA/MS also showed O_2 release at the same time as H_2O for $BaFe_{0.925}Bi_{0.075}O_{3-\delta}$ and $BaFe_{0.9}Bi_{0.1}O_{3-\delta}$. The O_2 loss was not seen for $BaFe_{0.85}Bi_{0.15}O_{3-\delta}$.

The moles of H_2O incorporated were determined with respect to the mass loss and the oxygen content in the sample and are shown in Table 4.5. $BaFe_{0.925}Bi_{0.075}O_{3-\delta}$ showed the most significant H_2O loss correlating with the lower oxygen content, therefore greater oxygen vacancies. Increasing the Bi content led to a decrease in H_2O loss and an increase in oxygen content, leading to less oxygen vacancies present

for OH^- ions to occupy on hydration, as per Equation (3.1) [200]. These results correlate with previous studies which have shown that increasing Bi content can cause a decrease in proton conductivity [205].

$$H_2O + V_O^{\bullet\bullet} + O_O^{\times} \leftrightarrow 2OH_O^{\bullet} \quad (4.1)$$

Above 700°C, further mass loss is observed and O_2 is detected. O_2 loss occurs at high temperatures for all samples, this is due to the Fe and Bi reducing in the N_2 atmosphere.

Table 4.5: $BaFe_{1-x}Bi_xO_{3-\delta}$ oxygen content determined by Rietveld refinement and moles of H_2O incorporated into the Bi doped samples, obtained from TGA data analysis.

Composition	Oxygen Content	Moles of H_2O per Formula Unit (mol)
$BaFe_{0.925}Bi_{0.075}O_{3-\delta}$	2.5620	0.0813
$BaFe_{0.9}Bi_{0.1}O_{3-\delta}$	2.7201	0.0785
$BaFe_{0.85}Bi_{0.15}O_{3-\delta}$	2.7423	0.0297

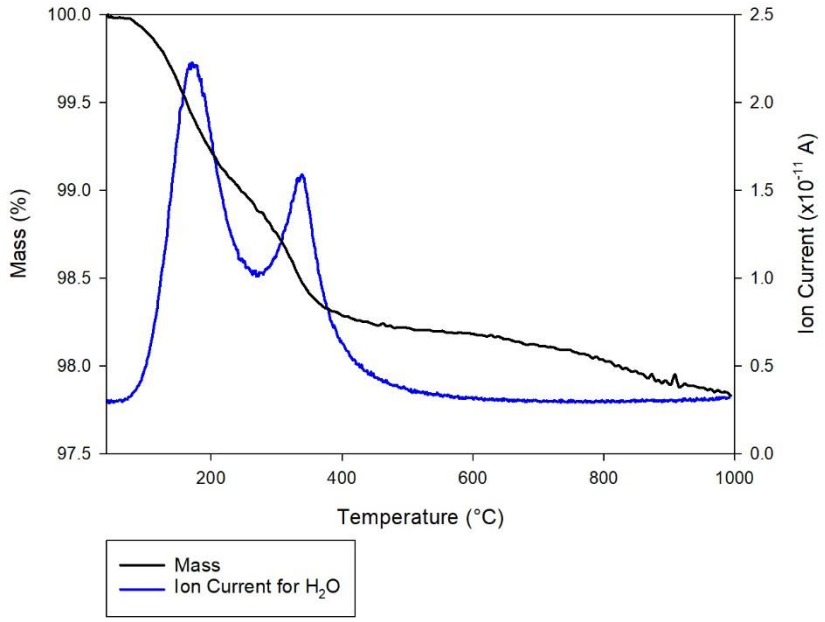


Figure 4.9: TGA and MS data for humidified $BaFe_{0.925}Bi_{0.075}O_{3-\delta}$ when heated to 1000°C showing mass loss (black) and H_2O loss (blue).

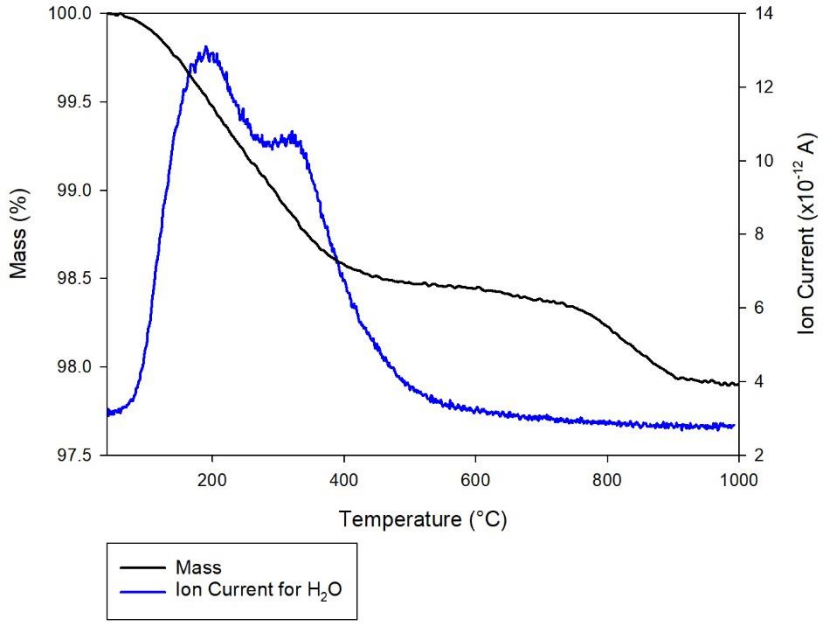


Figure 4.10: TGA and MS data for humidified $BaFe_{0.9}Bi_{0.1}O_{3-\delta}$ of sample when heated to 1000°C showing mass loss (black) and H_2O loss (blue).

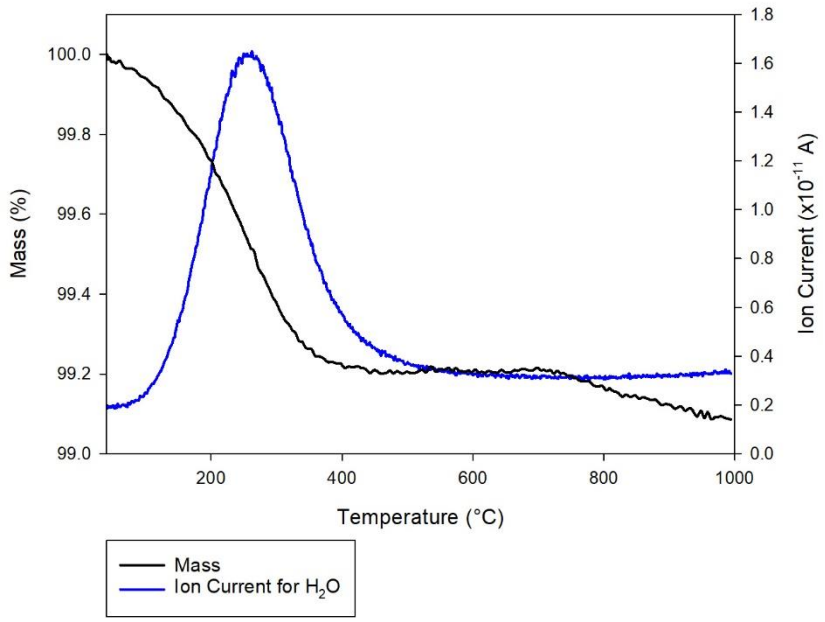


Figure 4.11: TGA and MS data for humidified $BaFe_{0.85}Bi_{0.15}O_{3-\delta}$ of sample when heated to 1000°C showing mass loss (black) and H_2O loss (blue).

4.3.2 Investigation into the Effect of Heating under Dry Nitrogen

In order to provide further information and to correlate what changes were due to the presence of H_2O and what were due to the N_2 treatment, Bi doped samples were also heated in dry N_2 (Figure 4.12). XRD patterns after heating for x = 0.075 and 0.15 show peak shoulders, while x = 0.1 showed peak broadening. The presence of shoulders suggests the presence of a second phase, therefore two-phase Rietveld refinement was performed using two cubic *Pm*-3*m* space groups (Table 4.6 and Figure 4.13). Phase fractions were also refined to determine the quantity of both phases.

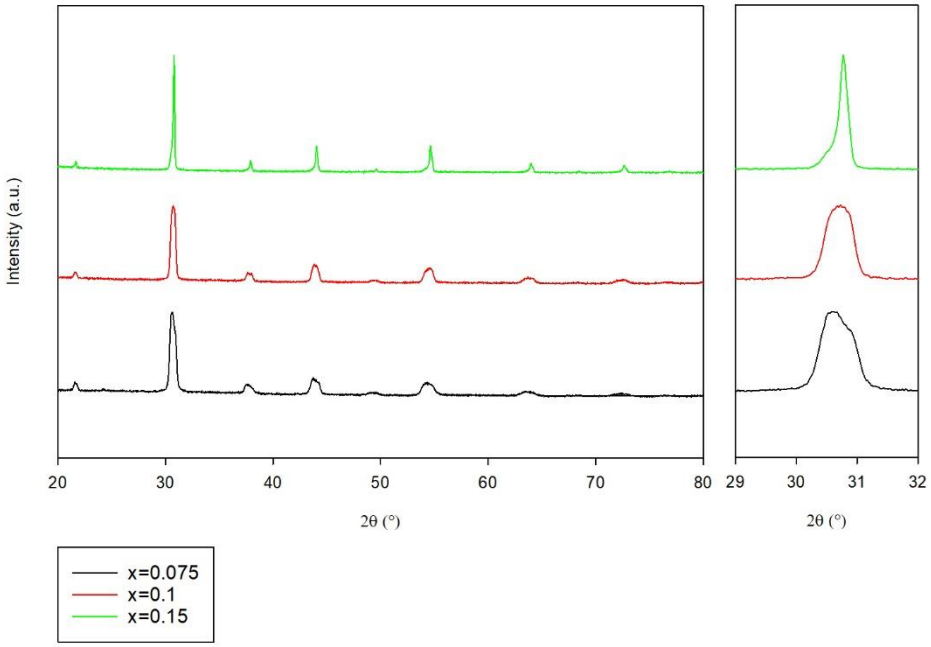


Figure 4.12: XRD pattern of $BaFe_{1-x}Bi_xO_{3-\delta}$ where x = 0.075, 0.1 and 0.15 after heating in dry N_2. Left shows the shoulders on the 110 reflection.

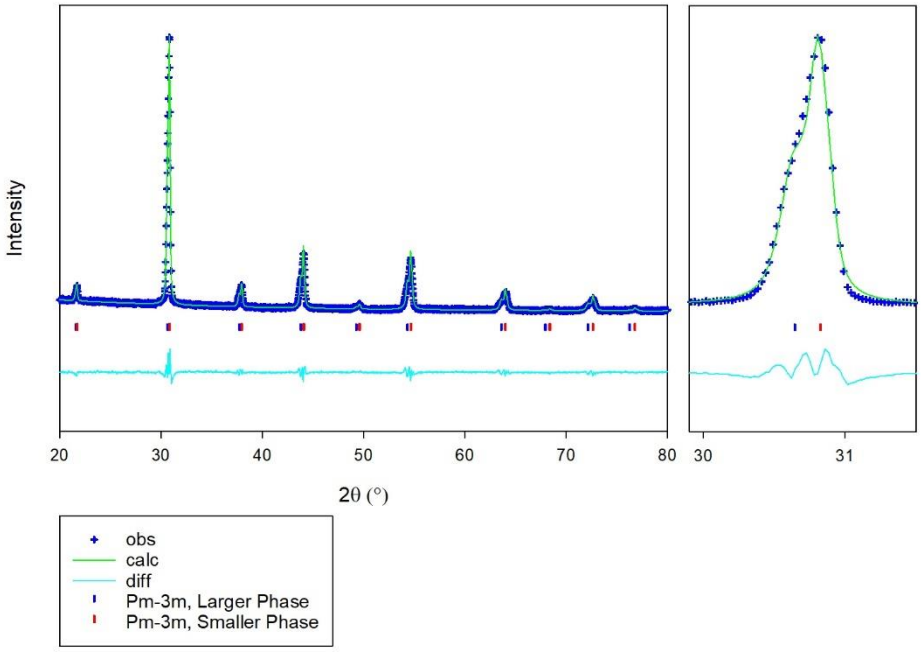


Figure 4.13: Example of observed (blue cross), calculated (green) and difference (cyan) profiles for Rietveld refinement performed (two cubic *Pm*-3*m* space group, R_w=4.67%).

Table 4.6: Unit cell parameters for $BaFe_{1-x}Bi_xO_{3-\delta}$ samples heated in dry N_2; where x = 0.075, 0.1 and 0.15. Data presented are for the larger unit cell (top) and smaller unit cell (bottom) and was the structure refined using a cubic *Pm*-3*m* space group.

Larger Unit Cell			
		Unit Cell Parameters (Å)	
Composition	**Phase Fraction**	a	**Unit Cell Volume (Å^3)**
$BaFe_{0.925}Bi_{0.075}O_{3-\delta}$	0.5712	4.1570(6)	71.84(3)
$BaFe_{0.9}Bi_{0.1}O_{3-\delta}$	0.5126	4.1517(3)	71.56(1)
$BaFe_{0.85}Bi_{0.15}O_{3-\delta}$	0.4114	4.1432(2)	71.12(1)
Smaller Unit Cell			
		Unit Cell Parameters (Å)	
Composition	**Fraction**	a	**Unit Cell Volume (Å^3)**
$BaFe_{0.925}Bi_{0.075}O_{3-\delta}$	0.4288	4.1176(6)	69.81(3)
$BaFe_{0.9}Bi_{0.1}O_{3-\delta}$	0.4874	4.1206(3)	69.96(1)
$BaFe_{0.85}Bi_{0.15}O_{3-\delta}$	0.5886	4.1192(1)	69.89(1)

A comparison of the lattice parameters of the original and dry N_2 samples (Figure 4.14 and Figure 4.15), shows both phases in the dry N_2 samples have larger lattice parameters then the original. This is due to the reduction of Fe^{4+} to Fe^{3+}. The presence of two phases maybe due to the outer layer being more heavily reduced when heated. The inner sample remains less reduced therefore has a smaller unit cell. This would suggest slow kinetics for the reduction process.

The XRD patterns of the previously mentioned humid samples did not show any obvious signs of containing two phases. Interestingly the humid N_2 samples appear uniform on heating with only a single phase observed suggesting the presence of H_2O would have aided in this process. It has already been observed through the dry N_2 samples that the outer surface Fe^{4+} ions are reduced to Fe^{3+}. OH^- from H_2O would bind to oxygen vacancies present in the sample. The binding of OH^- would supply protons which

would result in the reduction of Fe^{4+} to Fe^{3+} below the surface layer of the sample. Thus, resulting in the complete samples being reduced in humid conditions.

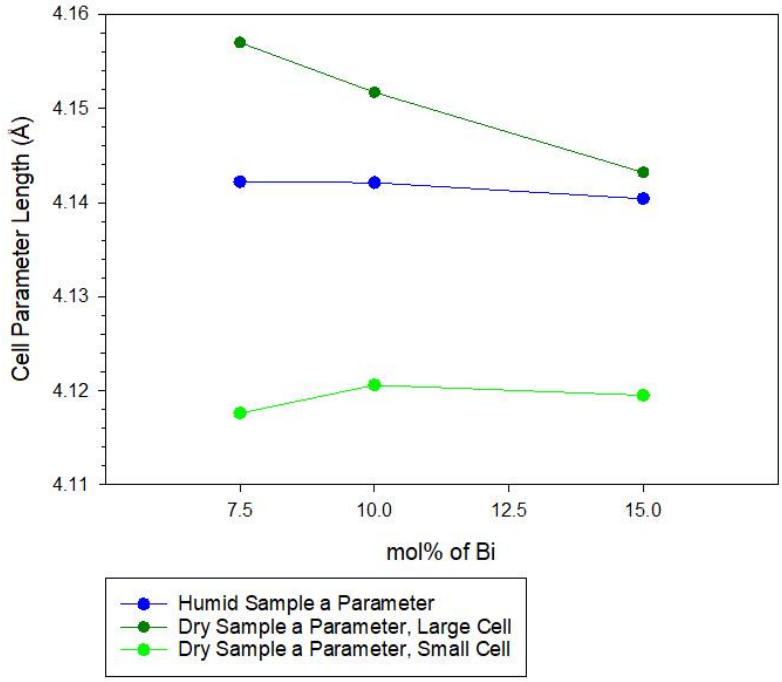


Figure 4.14: Lattice parameters for $BaFe_{1-x}Bi_xO_{3-\delta}$ doped samples. Samples were refined against a cubic *Pm*-3*m* space group. Blue shows the sample heated in humid N_2. Dark green shows the sample heated in dry N_2 and is the larger cell. Green shows the sample heated in dry N_2 and is the smaller cell.

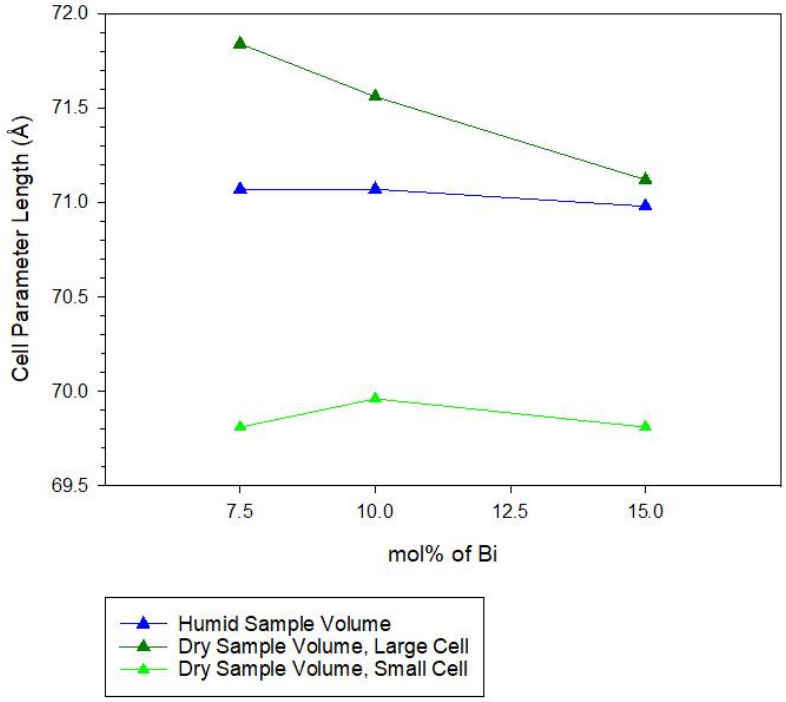


Figure 4.15: Volume for $BaFe_{1-x}Bi_xO_{3-\delta}$ doped samples. Samples were refined against a cubic *Pm*-3*m* space group. Blue shows the sample heated in humid N_2. Dark green shows the sample heated in dry N_2 and is the larger cell. Green shows the sample heated in dry N_2 and is the smaller cell.

4.3.3 Conductivity data

Electrical conductivity measurements for all samples showed the same general trend (Figure 4.16). On heating, the conductivity of the samples would increase, with all samples reaching a maximum conductivity at 487°C (Table 4.7), with the 7.5 mol% Bi having the highest conductivity of 7.54 Scm^{-1}. Further heating past 487°C to 700°C, led to a decrease in conductivity. This latter decrease can be explained by oxygen loss at higher temperatures reducing the oxidation state of Fe, similar to results for related system in the literature [206].

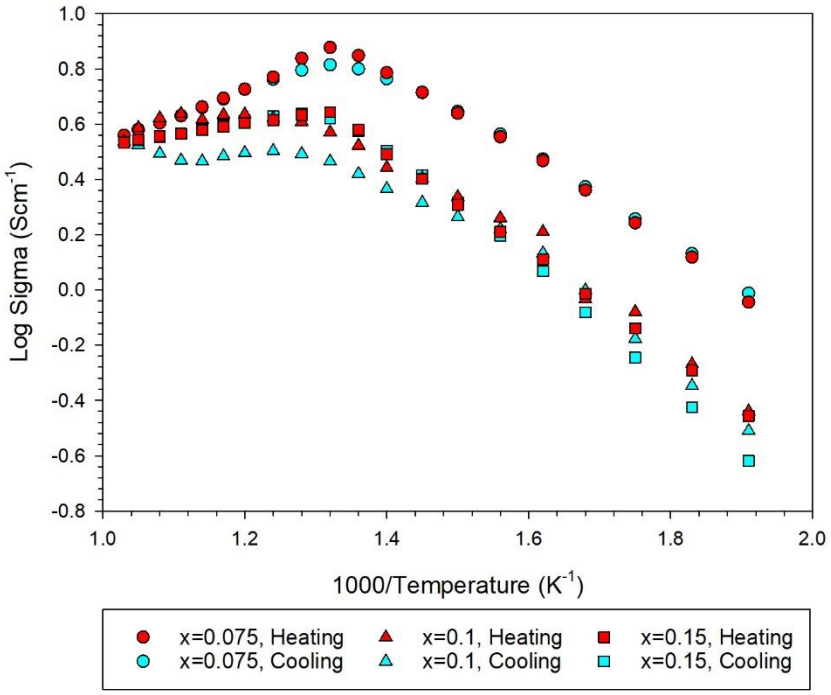


Figure 4.16: Conductivity results of $BaFe_{1-x}Bi_xO_{3-\delta}$ samples dependent of temperature. Red fill indicates heating and cyan fill indicates cooling; data shown between 250°C to 700°C. Measurements taken in air.

Table 4.7: $BaFe_{1-x}Bi_xO_{3-\delta}$ where x = 0.075, 0.1 and 0.15, conductivity at 487°C, 629°C and 700°C.

	Conductivity (Scm^{-1})		
Composition	487°C (1.32 K^{-1})	629°C (1.11 K^{-1})	700°C (1.03 K^{-1})
$BaFe_{0.925}Bi_{0.075}$	7.54	4.27	3.62
$BaFe_{0.9}Bi_{0.1}O_{3-\delta}$	3.72	4.34	3.44
$BaFe_{0.85}Bi_{0.15}O_{3-\delta}$	4.40	3.68	3.42

4.4 Niobium Doped Systems $BaFe_{1-x}Nb_xO_{3-\delta}$

XRD data showed the successful synthesis of single phase $BaFe_{1-x}Nb_xO_{3-\delta}$ where x = 0.4, 0.45 and 0.5 (Figure 4.17). Rietveld refinement was performed using a cubic *Pm*-3*m* space group (Table 4.8). The cell parameters show a general increasing trend with increased Nb doping (Figure 4.17). The increase is due to Fe^{4+} reducing to Fe^{3+}, which has a larger ionic radius. The reduction is a result of the greater charge of Nb^{5+}.

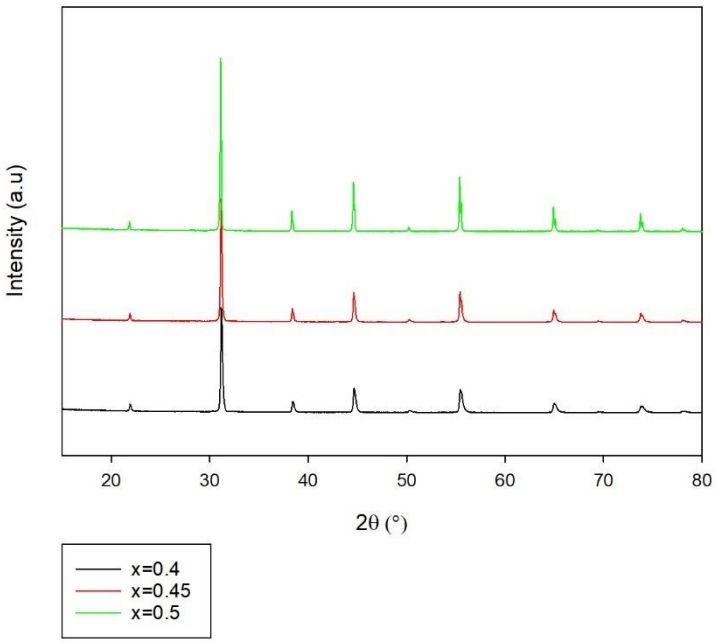


Figure 4.17: XRD of $BaFe_{1-x}Nb_xO_{3-\delta}$ where x = 0.4, 0.45 and 0.5.

Table 4.8: Unit cell parameters for $BaFe_{1-x}Nb_xO_{3-\delta}$ where x = 0.4, 0.45 and 0.5, (cubic *Pm*-3*m* space group).

Composition	**Unit Cell Parameters (Å)** a	**Unit Cell Volume (Å)**
$BaFe_{0.6}Nb_{0.4}O_{3-\delta}$	4.0545 (1)	66.65(1)
$BaFe_{0.55}Nb_{0.45}O_{3-\delta}$	4.0561(1)	66.73(0)
$BaFe_{0.5}Nb_{0.5}O_{3-\delta}$	4.0564(0)	66.75(0)

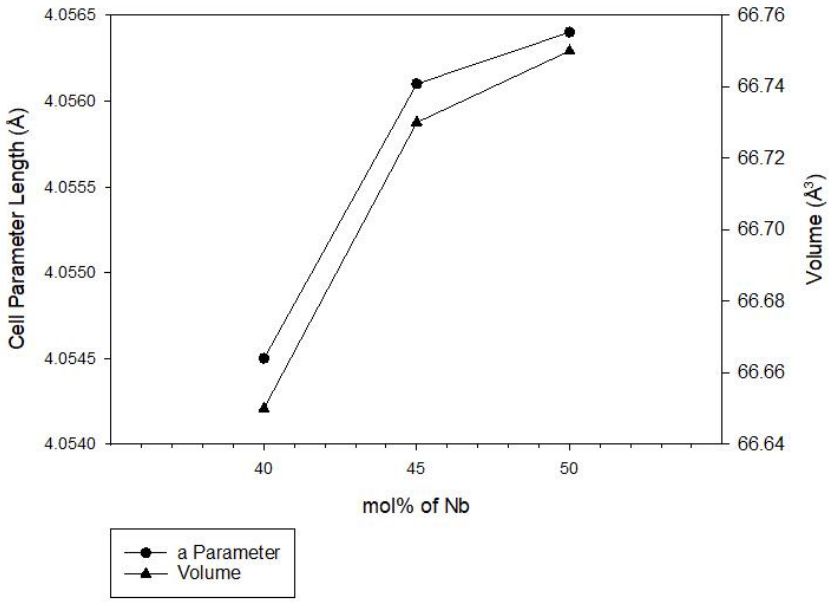


Figure 4.18: Lattice parameter of $BaFe_{1-x}Nb_xO_{3-\delta}$ doped samples, (*Pm*-3*m* space group). Circles indicate the a parameters and triangles indicate the volume of the cell.

4.4.1 Investigation into the Effect of Heating under Humid Nitrogen

The Nb doped samples were heated in humid N_2 to examine H_2O incorporation. The XRD patterns of the samples after humidification can be seen in Figure 4.19. Samples were shown to maintain their original phase. Lattice parameters are larger than the original sample (Table 4.9, Figure 4.20 and Figure 4.21). $BaFe_{0.6}Nb_{0.4}O_{3-\delta}$ showed the greatest increase, suggesting the greatest H_2O incorporation associated with reduction of Fe^{4+} to Fe^{3+}, providing vacancies for H_2O incorporation, TGA/MS were performed on all samples.

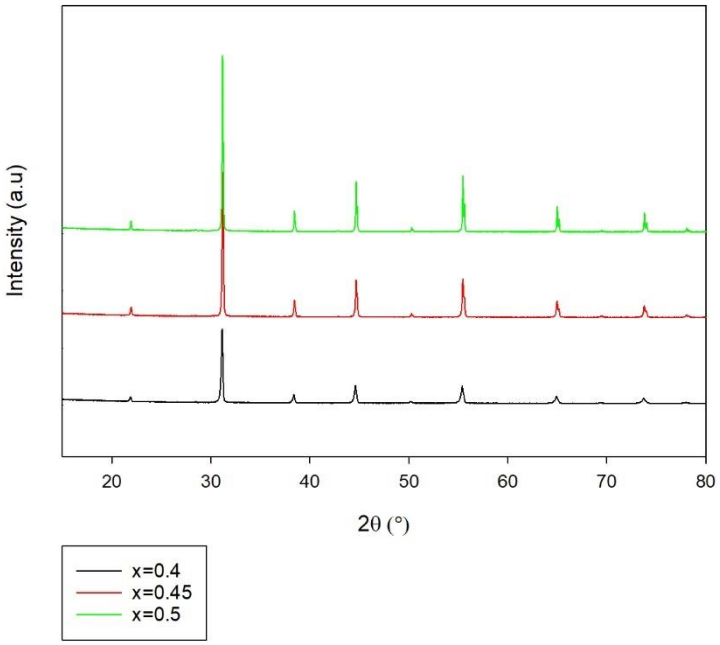


Figure 4.19: XRD of $BaFe_{1-x}Nb_xO_{3-\delta}$ where x = 0.4, 0.45 and 0.5, after samples were exposed to humid N_2.

Table 4.9: Unit cell parameters for $BaFe_{1-x}Nb_xO_{3-\delta}$ samples heated in humid N_2; where x = 0.4, 0.45 and 0.5 (cubic *Pm*-3*m* space group).

Composition	Unit Cell Parameters (Å)	
	a	Unit Cell Volume (Å)
$BaFe_{0.6}Nb_{0.4}O_{3-\delta}$	4.0627(1)	67.06(1)
$BaFe_{0.55}Nb_{0.45}O_{3-\delta}$	4.0595(1)	66.90(0)
$BaFe_{0.5}Nb_{0.5}O_{3-\delta}$	4.0571(0)	66.78(0)

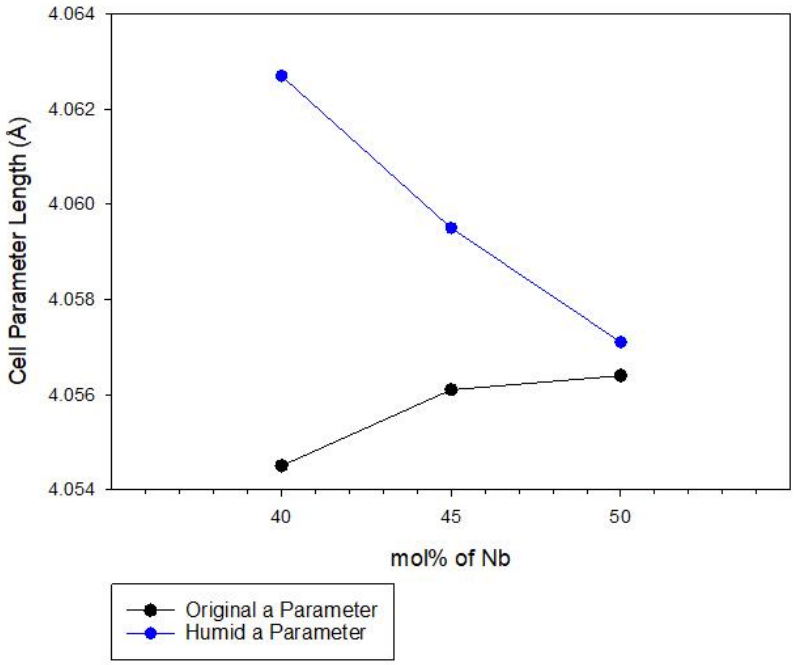


Figure 4.20: Lattice parameter of $BaFe_{1-x}Nb_xO_{3-\delta}$ doped samples (cubic *Pm*-3*m* space group). Black indicates the parent sample, blue indicates the sample heated in humid N_2.

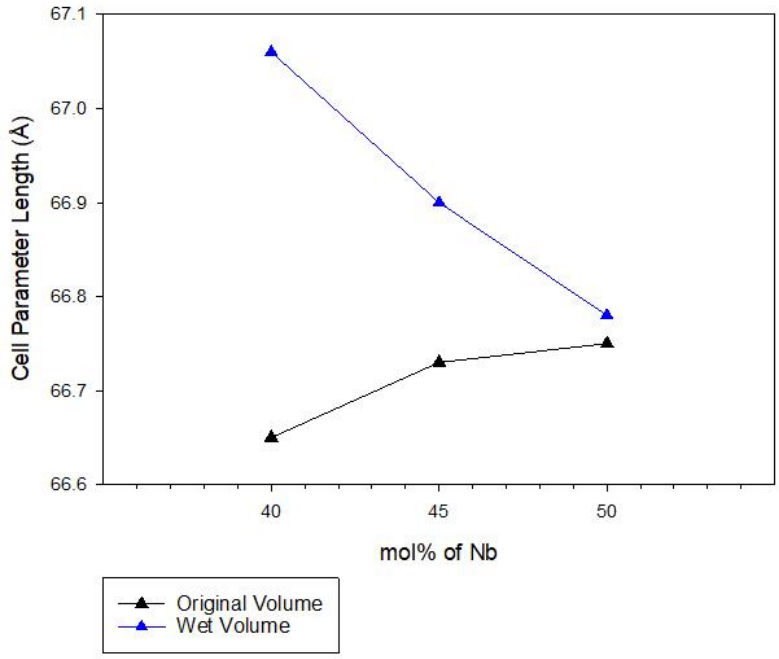


Figure 4.21: Volume of $BaFe_{1-x}Nb_xO_{3-\delta}$ doped samples (cubic *Pm*-3*m* space group). Black indicates the parent sample, blue indicates the sample heated in humid N_2.

TGA/MS data showed H_2O loss for all samples (Figure 4.22 and Figure 4.23). The H_2O and mass loss occurred between ca. 40°C to 300°C for $BaFe_{0.6}Nb_{0.4}O_{3-\delta}$ and $BaFe_{0.55}Nb_{0.45}O_{3-\delta}$. The H_2O content was determined to be 0.17 mol and 0.018 mol respectively. H_2O loss occurring below 100°C is suggested to be surface H_2O, while above 100°C is suggested to be bulk H_2O. For $BaFe_{0.5}Nb_{0.5}O_{3-\delta}$ negligible H_2O incorporation was seen consistent with no oxygen vacancies in this sample, as all the Fe ions being Fe^{3+}.

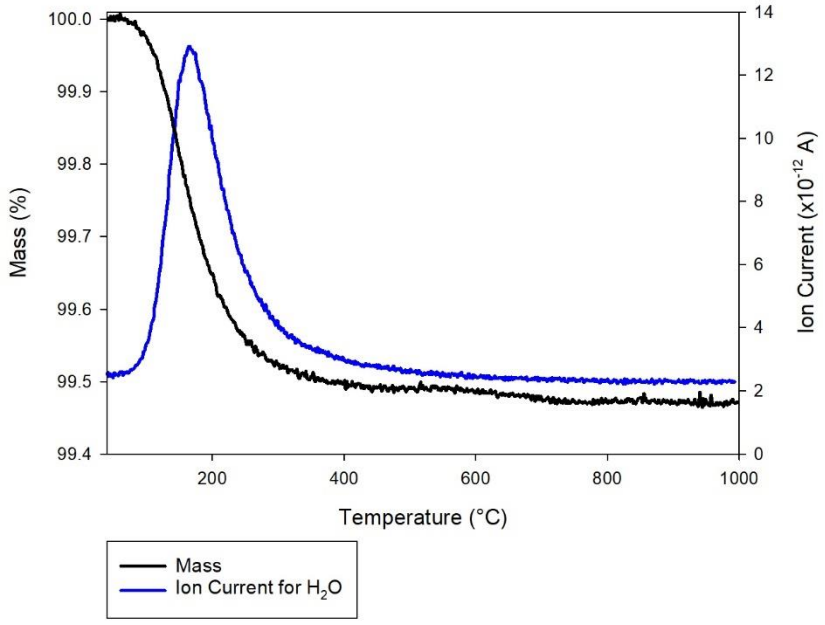


Figure 4.22: TGA and MS of humidified $BaFe_{0.6}Nb_{0.4}O_{3-\delta}$ when heated to 1000°C. Mass loss (black) and H_2O loss (blue).

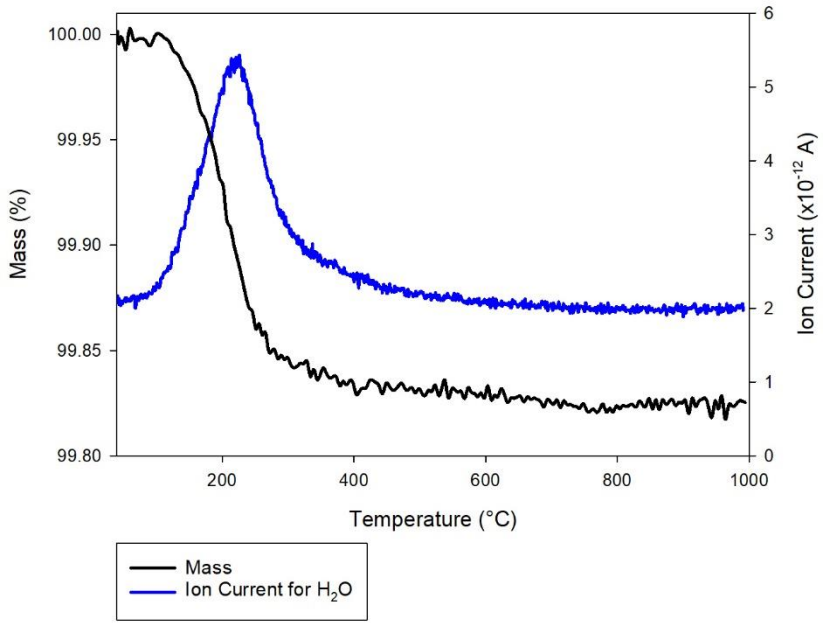


Figure 4.23: TGA and MS of humidified $BaFe_{0.55}Nb_{0.45}O_{3-\delta}$ when heated to 1000°C. Mass loss (black) and H_2O loss (blue).

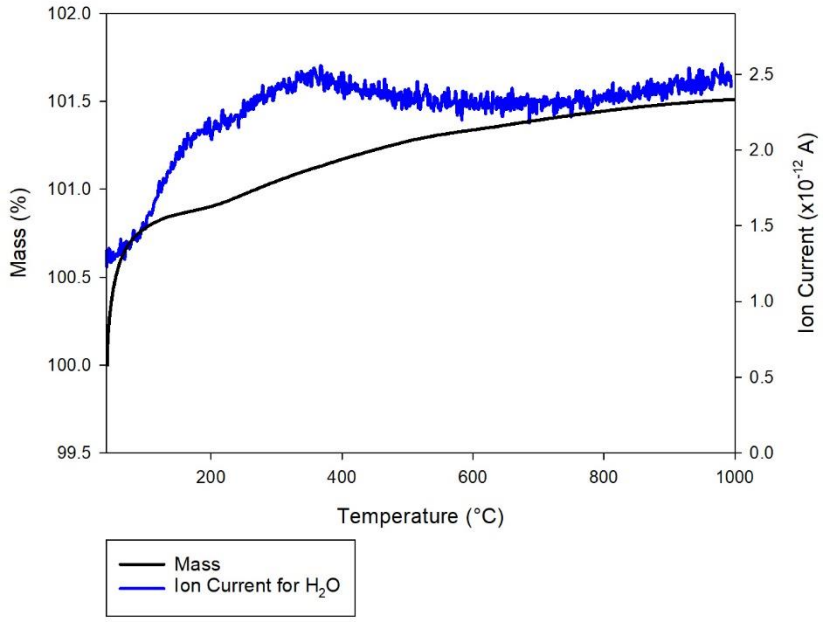


Figure 4.24: TGA and MS of humidified $BaFe_{0.5}Nb_{0.5}O_{3-\delta}$ when heated to 1000°C. Mass loss (black) and H_2O loss (blue).

4.4.2 Investigation into the Effect of Heating under Dry N_2

The $BaFe_{1-x}Nb_xO_{3-\delta}$ samples were then heated in dry N_2, to compare with the samples heated in humid N_2. The XRD patterns showed no change in the symmetry (Figure 4.25), however an increase in the 2θ values of the peaks can be seen. Rietveld refinement shows that the cell parameters of the dry N_2 samples were larger than the parent sample (Table 4.10). The larger size is due to the reduction of Fe^{4+} to Fe^{3+}.

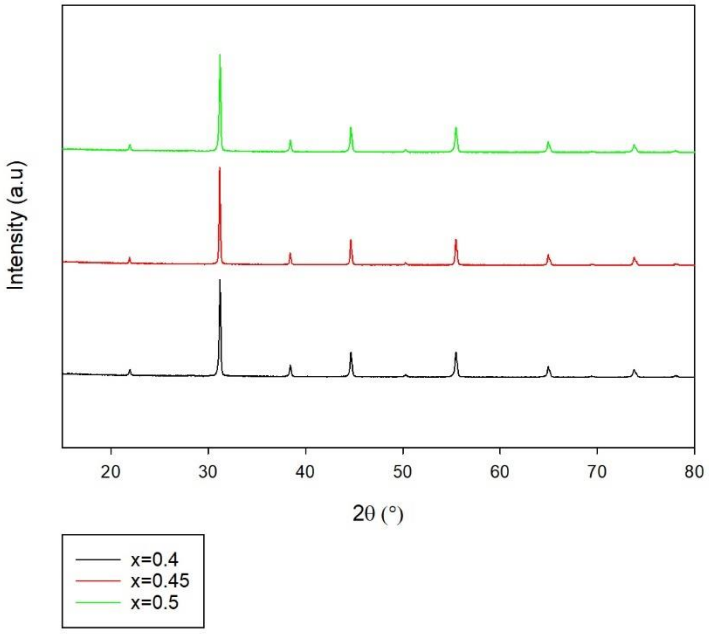


Figure 4.25: XRD of $BaFe_{1-x}Nb_xO_{3-\delta}$ where x = 0.4, 0.45 and 0.5, after samples were exposed to dry N_2.

A comparison between the dry N_2 and humid N_2 samples can aid in determining whether H_2O incorporation occurs (Figure 4.26 and Figure 4.27). The 40 mol% and 45 mol% humidified samples, have a larger volume then dry N_2 samples, indicating that some bulk H_2O incorporation occurred. The 50 mol% humid N_2 sample had smaller lattice parameters than the dry N_2 sample. In this case no bulk H_2O incorporation is thought to have occurred and any increase in lattice parameters is due to the reduction of Fe^{3+}. This correlates to the TGA/MS data, which showed very little mass change correlating to H_2O loss.

Table 4.10: Unit cell parameters for $BaFe_{1-x}Nb_xO_{3-\delta}$ samples heated in dry N_2; where x = 0.4, 0.45 and 0.5 (cubic *Pm*-3*m* space group).

Composition	Unit Cell Parameters (Å)	Unit Cell Volume (Å)
	a	
$BaFe_{0.6}Nb_{0.4}O_{3-\delta}$	4.0611(1)	66.98(1)
$BaFe_{0.55}Nb_{0.45}O_{3-\delta}$	4.0583(1)	66.84(0)
$BaFe_{0.5}Nb_{0.5}O_{3-\delta}$	4.0587(0)	66.86(0)

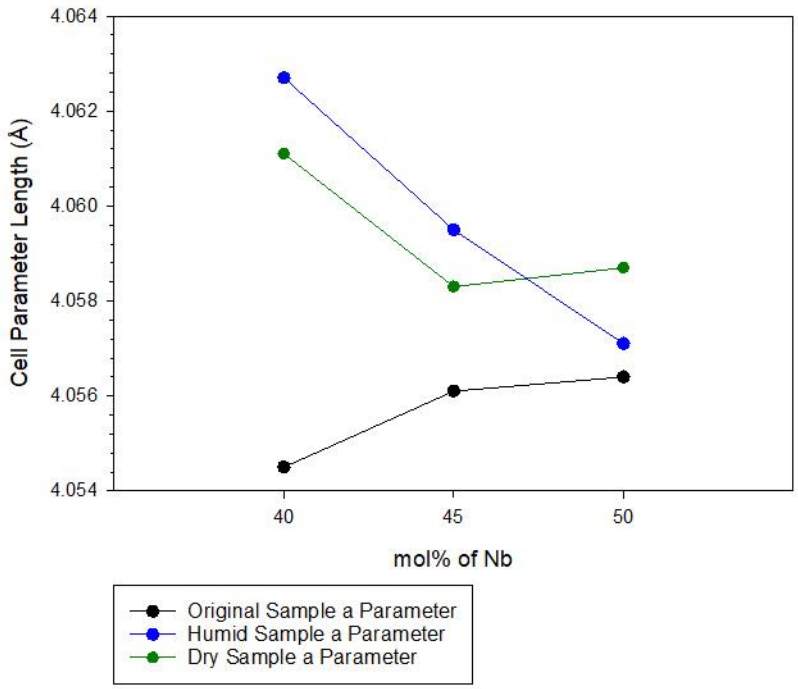


Figure 4.26: Lattice parameters for $BaFe_{1-x}Nb_xO_{3-\delta}$ doped samples (cubic *Pm*-3*m* space group). Blue shows the sample heated in humid N_2. Dark green shows the sample heated in dry N_2 and is the larger cell. Green shows the sample heated in dry N_2 and is the smaller cell.

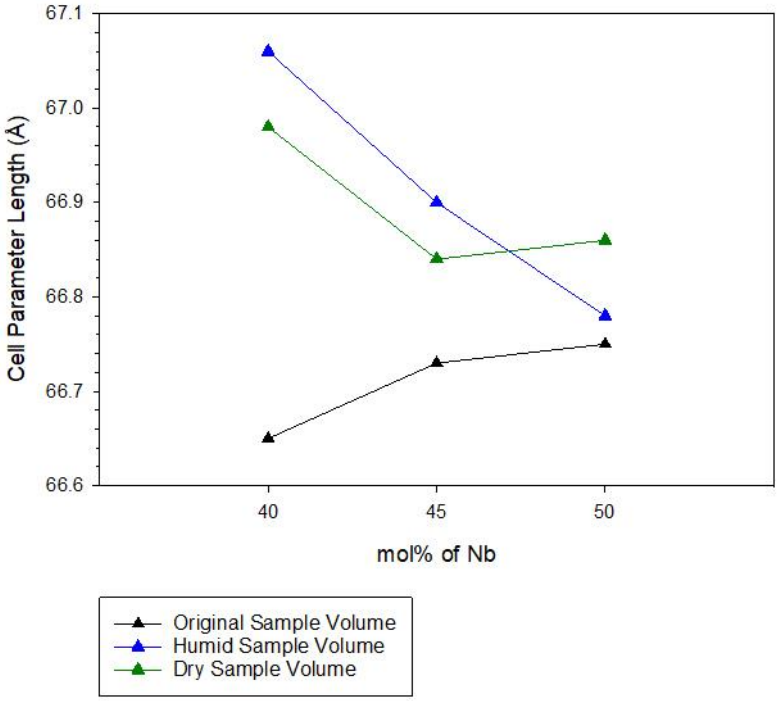


Figure 4.27: Volume of $BaFe_{1-x}Nb_xO_{3-\delta}$ doped samples (*Pm*-3*m* space group). Blue shows the sample heated in humid N_2. Dark green shows the sample heated in dry N_2 and is the larger cell. Green shows the sample heated in dry N_2 and is the smaller cell.

4.4.3 Conductivity Data

4 probe DC conductivity measurements, for the Nb doped samples are shown in Figure 4.28. 45 mol% and 40 mol% of Nb samples showed a similar overall trend in conductivity. An increase in conductivity was observed with increasing temperature for $BaFe_{0.55}Nb_{0.45}O_{3-\delta}$ and $BaFe_{0.6}Nb_{0.4}O_{3-\delta}$. $BaFe_{0.55}Nb_{0.45}O_{3-\delta}$ showed the highest conductivity of all samples, 15.01 Scm^{-1} (Table 4.11).

$BaFe_{0.5}Nb_{0.5}O_{3-\delta}$, at high temperatures, showed the lowest conductivity of all the samples, (5.03 Scm^{-1} at 700°C), while also showing a trend in conductivity that is unlike the other Nb doped samples. The conductivity decreases with increasing temperature, like that of a metal. Within a metal, the decrease is due to an increase in collisions between flowing electrons and fixed atoms in the lattice. Above 574°C, the electrical conductivity begins to increase. Further studies are required to determine the trend shown by $BaFe_{0.5}Nb_{0.5}O_{3-\delta}$, such as variable temperature XRD (VT-XRD), to determine whether there is a phase change at or above. Alternatively, it has been previously shown that increasing Nb^{5+} can lead to a

decrease in conductivity, as there is a decrease in the concentration of electronic charge carriers, due to reduction of Fe^{4+} to Fe^{3+} on Nb doping [202]. The 45 mol% of Nb appears to be the optimum concentration of Nb for the samples studied.

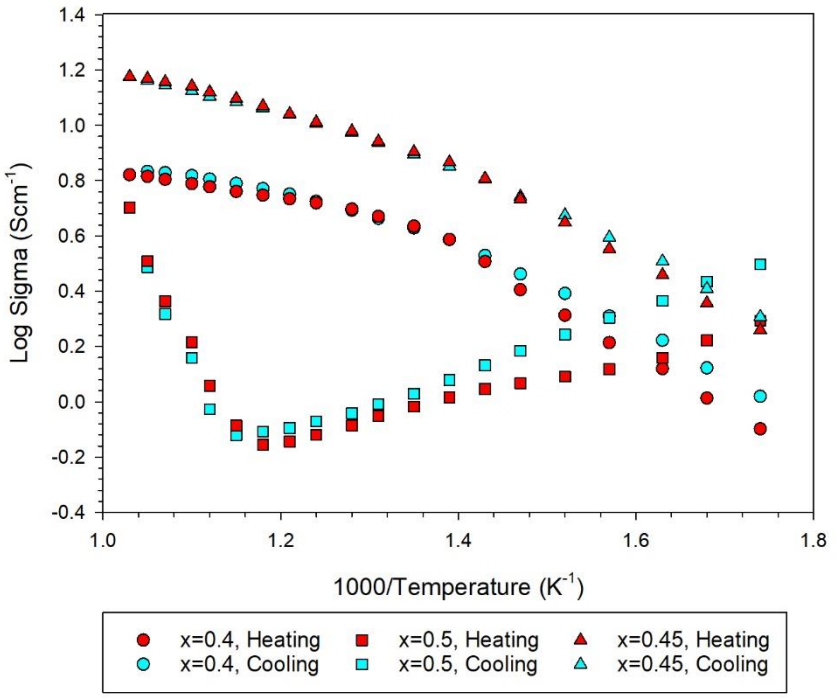


Figure 4.28: Conductivity results of $BaFe_{1-x}Nb_xO_{3-\delta}$ samples. Red fill indicates heating and cyan fill indicates cooling; data shown between 300°C to 700°C. Measurements taken in air.

Table 4.11: Conductivity at 300°C, 342°C and 700°C for $BaFe_{1-x}Nb_xO_{3-\delta}$.

Composition	**Conductivity (Scm^{-1})**		
	300°C (1.74 K^{-1})	342°C (1.63 K^{-1})	700°C (1.03 K^{-1})
$BaFe_{0.6}Nb_{0.4}O_{3-\delta}$	0.80	1.32	6.70
$BaFe_{0.55}Nb_{0.45}O_{3-\delta}$	1.82	2.88	15.01
$BaFe_{0.5}Nb_{0.5}O_{3-\delta}$	1.96	1.44	5.04

4.5 Conclusions

Bismuth and niobium where successfully doped onto the B site of $BaFeO_{3-\delta}$. Initial XRD patterns of Bi doping was shown to successfully form the cubic phase. Upon heating in dry N_2, the results implied that it was more plausible that this was a two-phase system. Similarly, Nb doping also formed a cubic phase. Nb doped samples maintained their parent phase when heated in N_2.

The current work shows that these samples can incorporate H_2O into the oxygen vacancies, thus suggesting they may have potential as electrodes for use in PCCC. $BaFe_{0.925}Bi_{0.075}O_{3-\delta}$ showed the greatest H_2O incorporation (0.081 mol), as well as the highest conductivity (7.54 Scm^{-1}) of the Bi doped samples. However, the overall conductivity of these samples was comparability low (<10 Scm^{-1}) which is unsuitable for electrodes. Of all the samples $BaFe_{0.55}Nb_{0.45}O_{3-\delta}$ showed the highest conductivity (15.01 Scm^{-1}), although H_2O incorporation was too low (0.017 mol).

Overall, a range of doped $BaFeO_{3-\delta}$ samples were prepared which showed evidence for H_2O incorporation. However, these phases had quite low electronic conduction which suggests that they cannot be used as an electrode material unless used in a composite with a good electrical conductor.

Chapter 5: Ba and Sr Doping in $La_2NiO_{4+\delta}$

5.1 Introduction

Ruddlesden-Popper phases have been explored as possible electrodes for intermediate temperature oxide conducting solid oxide cells (OC-SOCs) due to their ability to allow either oxygen vacancies or oxygen interstitial defects [134, 207-214]. In particular, $La_2NiO_{4+\delta}$ has been heavily explored as one such material and is a member of the lanthanum nickelate family, $La_{n+1}Ni_nO_{3n+1}$ [215, 216]. Similar materials with different rare earth metals have been investigated including $Pr_{n+1}Ni_nO_{3n+1}$ and $Nd_{n+1}Ni_nO_{3n+1}$ [209, 217, 218]. $La_{n+1}Ni_nO_{3n+1}$ are preferred as they have good thermal stability and conductivity within the intermediate temperature range (500°C to 700°C), and lanthanum is lower cost [135]

$La_2NiO_{4+\delta}$ has previously been shown to be a good oxide ion conductor, while the higher order phases; $La_3Ni_2O_{7-\delta}$ and $La_4Ni_3O_{10+\delta}$ have shown better conductivity as there is an increased quantity of NiO_6 octahedra's [135, 209, 213, 219]. Previous explorations of doping have mainly focused on $La_2NiO_{4+\delta}$ [220]. The alkali earth metals calcium (Ca), barium (Ba) and strontium (Sr) have been explored as dopants in small quantities [207, 221-225]. These dopants have been shown to improve the performance of the materials in terms of electrical and ionic conductivity [207, 224]. The focus of these materials has been to tailor them for oxide conduction.

Ba and Sr doping into $La_2NiO_{4+\delta}$ is expected to occur on the A-site of the Ruddlesden-Popper structure. Therefore La^{3+} will be substituted for either Ba^{2+} or Sr^{2+}. Ba^{2+} and Sr^{2+} both have larger ionic radiuses then La^{3+} therefore an increase in the volume of the unit cell is expected. The larger unit cell is expected to allow for better hydroxide ion incorporation. In terms of electrical conductivity, an improvement is expected similar to previously reported findings regarding Ba and Sr doping [207, 213, 226]. This is thought to be due to the difference in oxidation state of the dopant, forming electron holes within the structure.

This chapter will look at various dopants for lanthanum nickelate Ruddlesden-Popper phases and viability as electrodes for proton conducting ceramic cells (PCCCs). Sr and Ba were investigated as a dopant for $La_2NiO_{4+\delta}$. The chemical stability of the synthesised compositions was investigated by heating in nitrogen and oxygen. To conclude ex-situ electrical conductivity measurements were performed, to determine the potential of the materials as an electrode.

5.2 Experimental

$BaCO_3$ (VWR, 99.8%), La_2O_3 (Sigma-Aldrich, ≥99.9%), $SrCO_3$ (Sigma-Aldrich, ≥99.9%) and NiO (Sigma-Aldrich, 99.0%) were used for the synthesis of $La_{2-x}(Ba/Sr)_xNiO_{4+\delta}$ where x =0, 0.25 and 0.5. All compounds were prepared from the relevant stoichiometric ratios, followed by grinding using a pestle and mortar. The samples were then heated to a maximum temperature as stated in Table 5.1. The furnace used was a Carbolite Gero Ltd. CWF 13/13.

Table 5.1: Final heating temperatures for $La_{2-x}(Ba/Sr)_xNiO_{4+\delta}$.

Composition	Temperature (°C)
$\mathbf{La_2NiO_{4+\delta}}$	1000
$\mathbf{La_{1.75}Ba_{0.25}NiO_{4+\delta}}$	1200
$\mathbf{La_{1.5}Ba_{0.5}NiO_{4+\delta}}$	1200
$\mathbf{La_{1.75}Sr_{0.25}NiO_{4+\delta}}$	1200
$\mathbf{La_{1.5}Sr_{0.5}NiO_{4+\delta}}$	1200

X-ray diffraction (XRD) analysis was performed using a Panlaytical Empyrean diffractometer with Cu K_α radiation source. Structural refinement was performed through the Rietveld refinement, using the GSAS-II suite of programs [203]. Samples were then heated in a Carbolite Gero Ltd. CTF 12/75 tube furnace in humid nitrogen (N_2) , dry N_2 and humid oxygen (O_2), to investigate the chemical stability in different atmospheres. Thermogravimetric analysis (TGA) and mass spectrometry (MS), using a Netzsch STA 449 F1 Jupiter Thermal Analyser, were performed on samples heated in humid N_2 that

remained chemically stable. Water (H_2O), O_2, and carbon dioxide (CO_2) loss was monitored as temperature increased.

Variable temperature XRD (VT-XRD) was also performed, with flowing N_2, on samples that were shown to be stable in humid N_2. This was performed as to observe the change in lattice parameters and assess whether they correlated with the loss of the gaseous species. Sequential refinement was performed using data obtained from the VT-XRD measurements, through the use of GSAS-II software [203].

Electrical conductivity measurements were performed on the $La_{2-x}Sr_xNiO_{4+\delta}$. Pellets were formed from powders, using a 10 mm Specac die with a weight of 5 tons. The pellet press was obtained from Doreth Engineering Co. Ltd. The pellets were sintered at the temperatures stated in Table 5.1 . Four gold probes were painted using gold paint. Each probe was attached to its respective gold wire and heated to 800°C for 1 h. 4 probe DC conductivity measurements were performed between 200°C and 700°C, in air to determine the conductivity for each sample.

5.3 Ba Doped and Sr Doped $La_2NiO_{4+\delta}$; $La_{2-x}Ba_xNiO_{4+\delta}$ and $La_{2-x}Sr_xNiO_{4+\delta}$

XRD patterns (Figure 5.1) show the results from the synthesis of $La_{2-x}(Ba/Sr)_xNiO_{4+\delta}$ where x =0, 0.25 and 0.5. Rietveld refinement was performed on $La_2NiO_{4+\delta}$ (Figure 5.2) against an orthorhombic *Fmmm* space group [227, 228]. Other space groups have previously been investigated by Skinner [228], however, they were found to be unrealistic fits to the experimental data. Visibly, the XRD patterns for $La_{2-x}(Ba/Sr)_xNiO_{4+\delta}$ where x = 0.25, 0.5 appeared similar to $La_2NiO_{4+\delta}$, therefore Rietveld refinement was performed using the same space group (Table 5.2, Figure 5.3 and Figure 5.4). An R-weighted pattern (R_{wp}) of less than 10% was achieved so was considered an adequate fit.

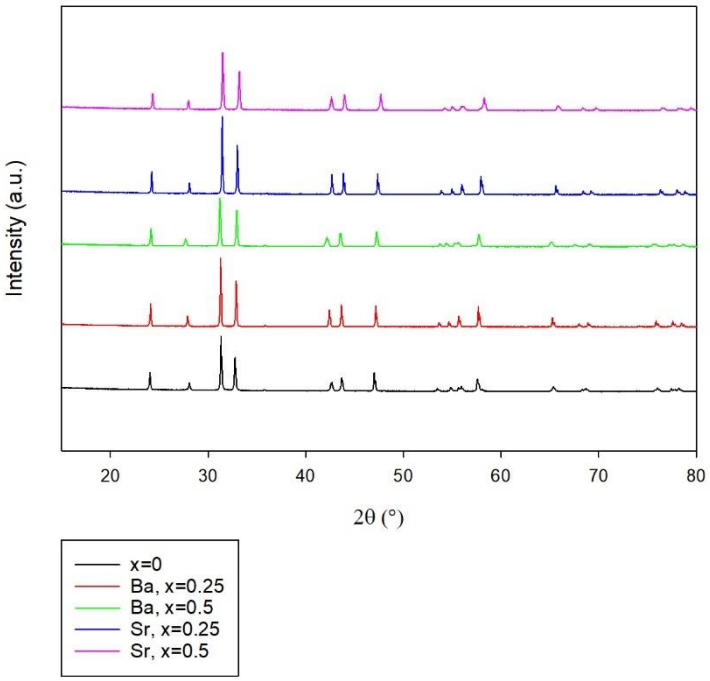


Figure 5.1: XRD pattens of $La_{2-x}Ba_xNiO_{4+\delta}$ and $La_{2-x}Sr_xNiO_{4+\delta}$ where x =0, 0.25 and 0.5. In ascending order $La_2NiO_{4+\delta}$ (black), $La_{1.75}Ba_{0.25}NiO_{4+\delta}$ (red), $La_{1.5}Ba_{0.5}NiO_{4+\delta}$ (green), $La_{1.75}Sr_{0.25}NiO_{4+\delta}$ (blue) and $La_{1.5}Sr_{0.5}NiO_{4+\delta}$ (pink).

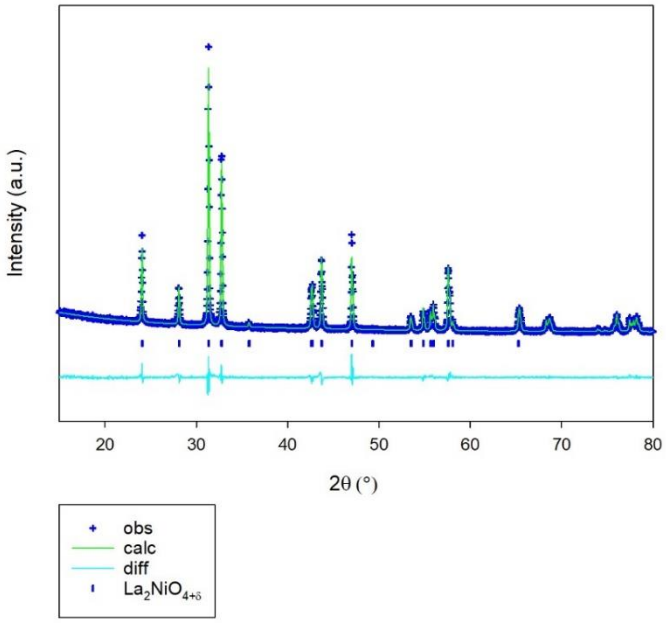


Figure 5.2: Example of observed (blue cross), calculated (green) and difference (cyan) profiles for Rietveld refinement performed on $La_2NiO_{4+\delta}$ (orthorhombic *Fmmm* space group, R_{wp}=5.83%).

Introduction of Sr or Ba into $La_2NiO_{4+\delta}$ causes a decrease in the *a* and *b* parameter (Figure 5.3 and Table 5.2) , and an increase in the *c* parameter (Figure 5.4) similar to previously reported literature [224, 225, 229]. The decrease in the *a* and *b* parameter is suggested to be due to the Ni^{2+} (ionic radius: 0.69 Å) oxidising to Ni^{3+} (ionic radius: 0.56 Å), to compensate for the lower (2+) charge of Sr/Ba in compensation to La (3+) [224, 225, 229].

Table 5.2: Lattice parameters (orthorhombic *Fmmm*) for Rietveld refinement performed on $La_{2-x}Ba_xNiO_{4+\delta}$ and $La_{2-x}Sr_xNiO_{4+\delta}$ (x =0, 0.25 and 0.5) samples

Composition	**Unit Cell Parameters (Å)**			**Unit Cell Volume (Å³)**	**R_{wp} (%)**
	a	b	c		
$La_2NiO_{4+\delta}$	5.4580(1)	5.4641(1)	12.6920(2)	378.51(1)	5.83
$La_{1.75}Ba_{0.25}NiO_{4+\delta}$	5.4460(3)	5.4443(3)	12.7797(2)	378.92(1)	8.54
$La_{1.5}Ba_{0.5}NiO_{4+\delta}$	5.4353(2)	5.4418(2)	12.8848(2)	381.10(1)	6.82
$La_{1.75}Sr_{0.25}NiO_{4+\delta}$	5.4236(1)	5.4266(1)	12.7034(2)	373.88(1)	5.87
$La_{1.5}Sr_{0.5}NiO_{4+\delta}$	5.3865(1)	5.3943(1)	12.7323(2)	369.96(1)	5.38

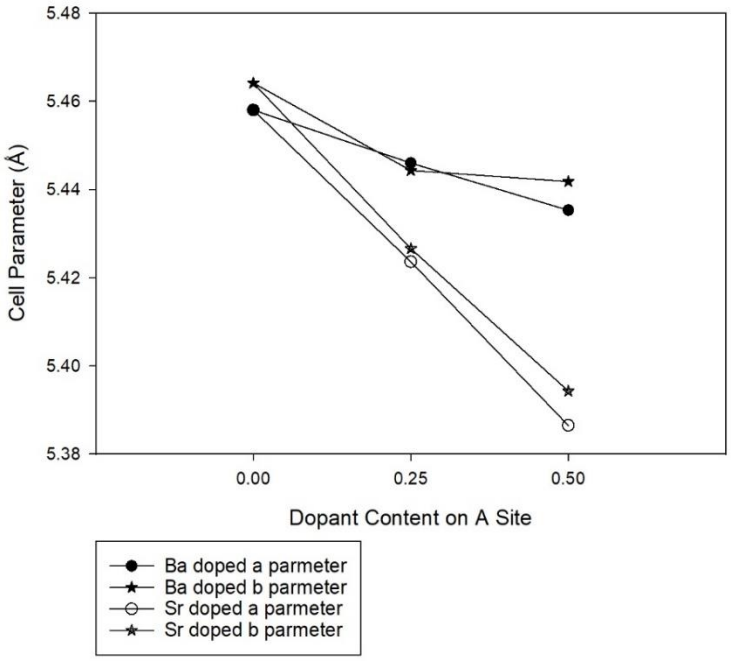


Figure 5.3: Variation of *a* and *b* lattice parameters for $La_{2-x}Ba_xNiO_{4+\delta}$ and $La_{2-x}Sr_xNiO_{4+\delta}$ with Ba/Sr content (x). Black circles indicates *a* parameter for Ba doped samples. Black stars indicates *b* parameter for Ba doped samples. Empty circle indicates *a* parameter for Sr doped samples. Empty star indicates *b* parameter for Sr doped samples.

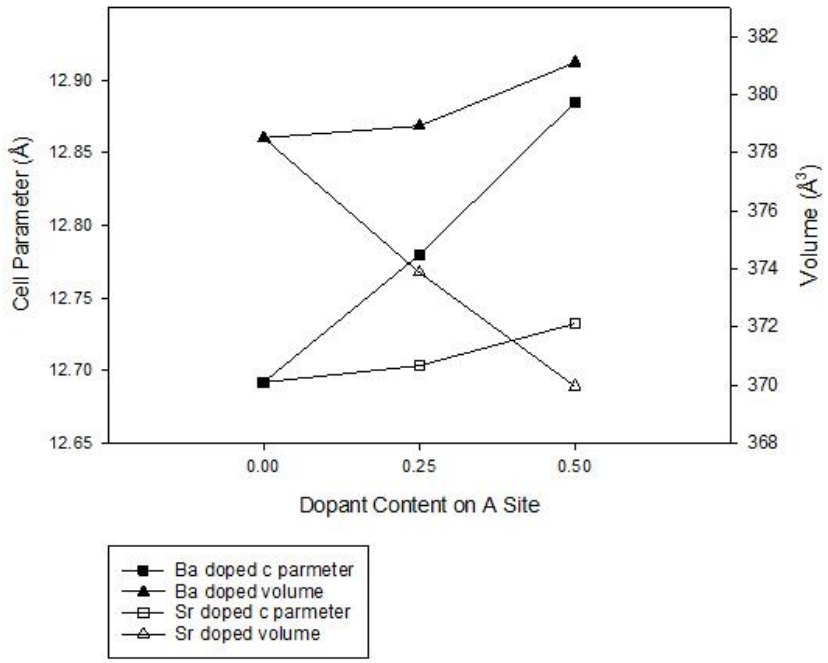


Figure 5.4: Variation of *c* lattice parameter and cell volume for $La_{2-x}Ba_xNiO_{4+\delta}$ and $La_{2-x}Sr_xNiO_{4+\delta}$ with Ba/Sr content (x). Black squares indicate *c* parameter for Ba doped samples. Black triangles indicates volume for Ba doped samples. Empty squares indicate *c* parameter for Sr doped samples. Empty triangles indicate volume for Sr doped samples.

The increase in the *c* parameter is due to the larger ionic radius of Sr^{2+} (1.31 Å) and Ba^{2+} (1.47 Å) substituting the smaller La^{3+} (1.216 Å) [224, 225]. Increasing the quantity of Ba dopant increases the volume of the cell (Figure 5.4). While the same is not seen for Sr doping. This is due to Ba having a greater ionic radius and thus a greater impact on the *c* parameter than Sr. Instead for the Sr doped samples the volume decreases as the *a*, *b* reduction outweighs the increase in the *c* parameter.

5.3.1 Investigation of Heating under Humid Nitrogen, Dry Nitrogen and Humid Oxygen

5.3.1.1 $La_2NiO_{4+\delta}$

$La_2NiO_{4+\delta}$ was heated in various atmospheres to determine the chemical stability in different conditions. The results of the XRD patterns indicated that the phase was stable in all the conditions studied (Figure 5.5). While the samples were stable, there were some changes in the cell parameters. An increase is observed in the *a* and *b* parameter of the samples heated in N_2, whether it be humid or dry (Table 5.3). In contrast a decrease in the *c* parameter is observed. This variation in lattice parameters can be

especially seen in the sample heated in humid N_2, which saw a larger difference in the lattice parameters. It has been previously observed that a small quantity of Ni^{3+} is present in $La_2NiO_{4+\delta}$, therefore the increase in the *a* and *b* parameters is caused by the reduction of Ni^{3+} to the larger Ni^{2+}, a result of the low oxygen partial pressures when heating [228].

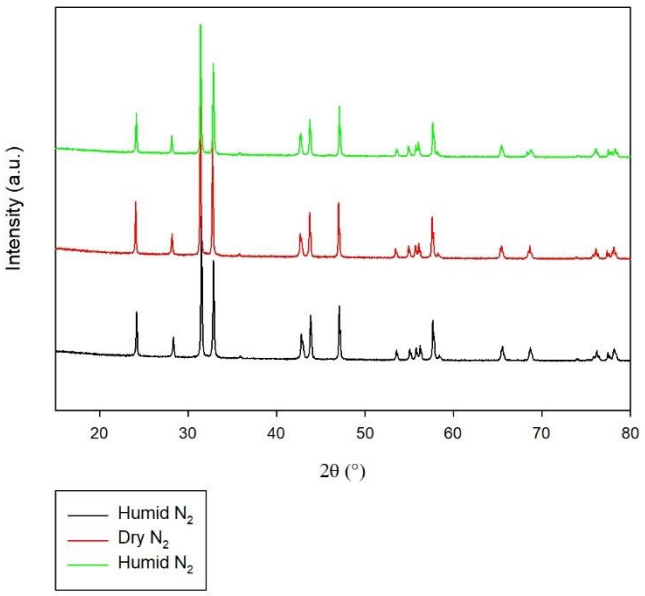


Figure 5.5: XRD patterns of $La_2NiO_{4+\delta}$ annealed in various conditions. In ascending order humid N_2 (black), dry N_2 (red) and humid O_2 (green).

Table 5.3: Lattice parameters (orthorhombic *Fmmm*) for Rietveld refinement performed on $La_2NiO_{4+\delta}$ heated in various conditions.

	Unit Cell Parameters (Å)			**Unit Cell Volume (Å³)**
	a	b	c	
Original	5.4580(1)	5.4641(1)	12.6920(2)	378.51(1)
Humid N_2	5.4669(2)	5.4707(2)	12.6531(2)	378.42(1)
Dry N_2	5.4652(2)	5.4687(2)	12.6661(2)	378.56(1)
Humid O_2	5.4582(2)	5.4582(2)	12.6940(2)	378.51(1)

Samples heated in humid O_2 also showed changes in the lattice parameter. In this instance the *b* parameter decreases, while the *a* parameter remains unchanged, leading to the *a* and *b* parameter being equal within errors, thus the lattice parameters are reminiscent of a tetragonal structure. Overall the volume of the humid O_2 sample remains the same as the original sample, because the *c* parameter increases compensating for the previously mentioned change.

TGA was performed on the sample heated in humid N_2 to determine whether there was any H_2O loss, thus H_2O incorporation. The sample showed H_2O loss from 40°C to ca. 400°C (Figure 5.6). This can be attributed to a mixture of surface and bulk H_2O. The loss that occurs from 40°C to 100°C, is surface H_2O, H_2O loss above 100°C is bulk H_2O. In addition to H_2O loss, CO_2 loss also occurs from 200°C to 600°C (Figure 5.7). Therefore, it is not possible to determine an accurate H_2O content within the sample, instead an estimation can be calculated. The estimation ignores CO_2 loss and assumes that all mass loss in the sample is due to H_2O. With this assumption it is determined that 0.0017 mol bulk H_2O was incorporated. O_2 loss also occurs from 400°C (Figure 5.6).

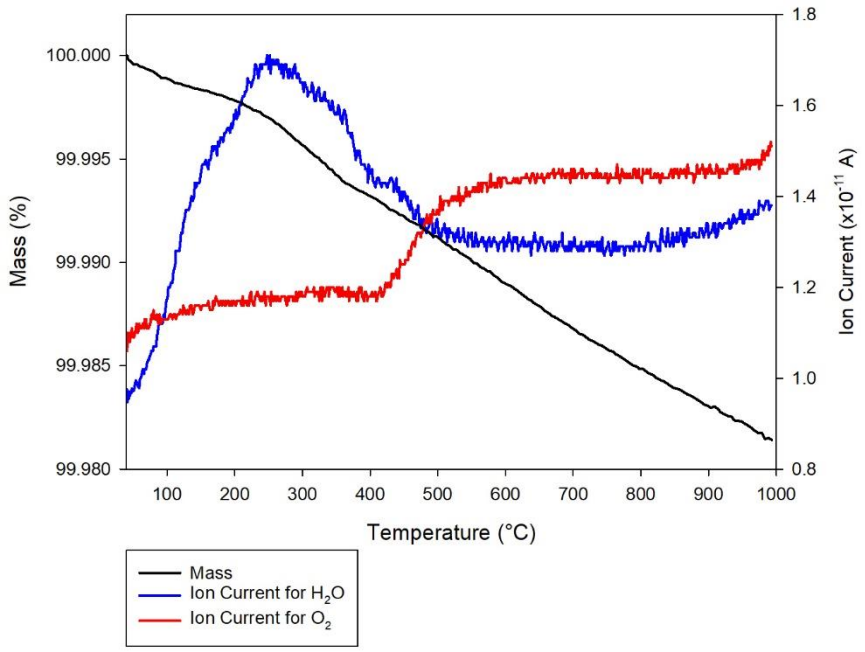


Figure 5.6: TGA and MS, up to a temperature of 1000°C, performed on $La_2NiO_{4+\delta}$ heated in humid N_2. Mass loss (black), H_2O loss (blue) and O_2 loss (red).

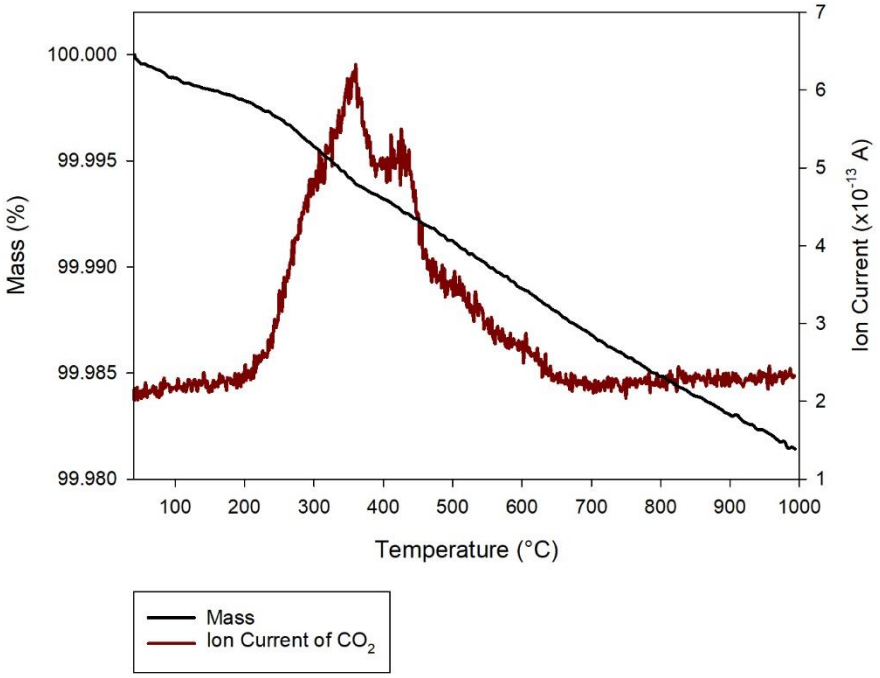


Figure 5.7: TGA and MS, up to a temperature of 1000°C, performed on $La_2NiO_{4+\delta}$ heated in humid N_2. Mass loss (black) and CO_2 loss (dark red).

CO_2 was initially assumed to be from $La_2O_2CO_3$ impurities. To assess this La_2O_3 was annealed in air for 24h and TGA/MS performed to identify the temperature at which CO_2 would be released. CO_2 was detected by the MS at temperatures exceeding 600°C (Figure 5.8). Therefore, the source of the CO_2 in $La_2NiO_{4-\delta}$ maybe from CO_3^{2-} binding to oxygen interstitial sites and vacancies [230]. Previous studies have shown that Ruddlesden-Popper phases are able to contain carbonate impurities, specifically the $Sr_4Fe_3O_{10}$ system [208]. It has been previously suggested that synthesis methods that utilise carbonate rich precursors are more prone to forming these impurities [208, 230].

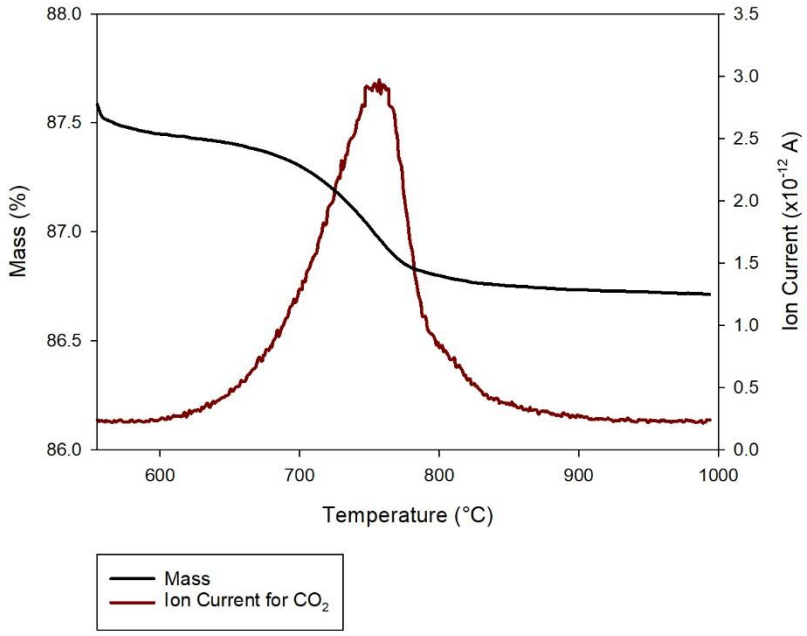


Figure 5.8: TGA and MS of La_2O_3 annealed in air, data profile for the temperature range between 550°C and 1000°C. Mass loss (black) and CO_2 loss (dark red).

5.3.1.2 $La_{2-x}Ba_xNiO_{4+\delta}$

Heating of $La_{2-x}Ba_xNiO_{4+\delta}$ samples in humid N_2 showed some degradation of the sample (Figure 5.9). The main Ruddlesden-Popper phase remained, while some impurities containing La, Ba and Ni formed. Degradation was thought to have occurred due to either the humid atmosphere, low oxygen partial pressures or both. Further studies showed that heating the sample in dry N_2 or humid O_2 did not show the same degradation. Therefore, it is suspected that a synergistic effect of the low oxygen partial pressure and the humidity, caused the degradation to occur. The lattice parameters of the samples heated in humid O_2 and dry N_2, resulted in a small increase in the volume (Table 5.4). For the dry N_2 samples it is suspected that this is related to Ni reduction causing the increase in volume. While for the humid O_2 sample it is postulated that there is some H_2O incorporation.

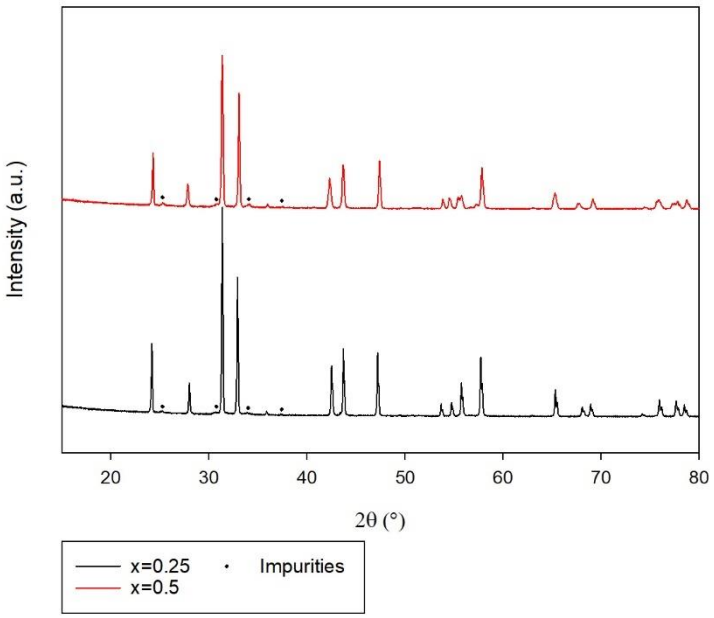


Figure 5.9: XRD pattern of $La_{2-x}Ba_xNiO_{4+\delta}$ where x=0.25 and 0.5, heated in humid N_2. In ascending order $La_{1.75}Ba_{0.25}NiO_{4+\delta}$ (black) and $La_{1.5}Ba_{0.5}NiO_{4+\delta}$ (red). Impurities are shown by circles.

Table 5.4: Lattice parameters (orthorhombic *Fmmm*) for Rietveld refinement performed on $La_{2-x}Ba_xNiO_{4+\delta}$ where x=0.25 and 0.5, annealed in various conditions.

	Unit Cell Parameters (Å)			**Unit Cell Volume (Å³)**
	a	b	c	
$La_{1.75}Ba_{0.25}NiO_{4+\delta}$				
Original	5.4440(2)	5.4462(2)	12.7797(2)	378.91(1)
Dry N_2	5.4515(1)	5.4477(1)	12.7714(1)	379.286(4)
Humid O_2	5.4462(1)	5.4492(1)	12.7866(1)	379.471(4)
$La_{1.5}Ba_{0.5}NiO_{4+\delta}$				
Original	5.4353(2)	5.4418(2)	12.8848(2)	381.10(1)
Dry N_2	5.4379(1)	5.4454(1)	12.8878(2)	381.63(1)
Humid O_2	5.4419(5)	5.4395(5)	12.8899(4)	381.56(3)

5.3.1.3 $La_{1.75}Sr_{0.25}NiO_{4+\delta}$

XRD patterns for $La_{1.75}Sr_{0.25}NiO_{4+\delta}$ heated in humid O_2 and dry N_2 showed no observable change in XRD patterns (Figure 5.10 and Table 5.5). Little change was seen in the sample heated in humid O_2, especially when considering experimental error, while heating in dry N_2 increased the *a* and *b* parameter, possibly attributed to the reduction of Ni^{3+} to Ni^{2+}. The increase in *a* and *b* was greater than the difference in the *c* parameter thus volume was increased overall.

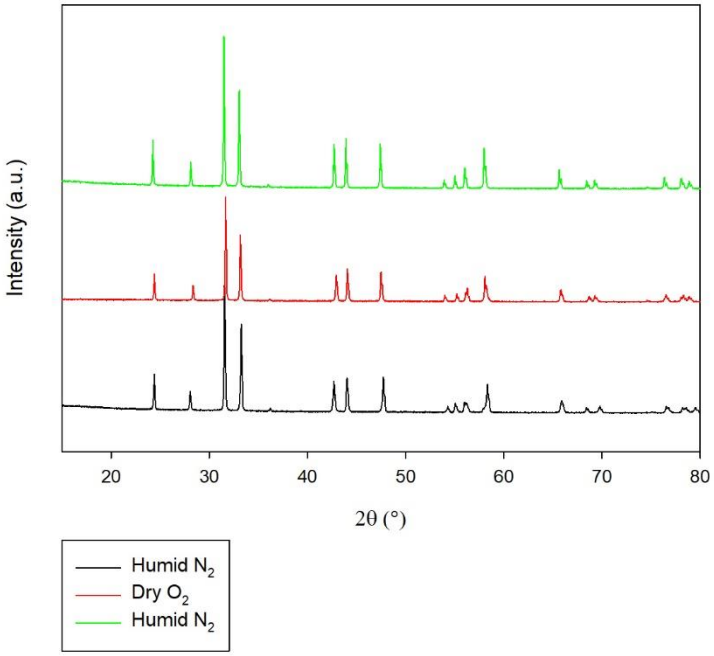


Figure 5.10: XRD patterns of $La_{1.75}Sr_{0.25}NiO_{4+\delta}$ annealed in various conditions. In ascending order humid N_2 (black), dry N_2 (red) and humid O_2 (green).

Table 5.5: Lattice parameters (orthorhombic *Fmmm*) for Rietveld refinement performed on $La_{1.75}Sr_{0.25}NiO_{4+\delta}$ heated in various conditions.

	Unit Cell Parameters (Å)			Unit Cell Volume (Å³)
	a	b	c	
Original	5.4236(1)	5.4266(1)	12.7034(2)	373.88(1)
Humid N_2	5.3868(1)	5.3944(1)	12.7318(3)	369.97(1)
Dry N_2	5.4299(1)	5.4350(1)	12.6757(2)	374.08(1)
Humid O_2	5.4235(1)	5.4269(1)	12.7040(1)	373.91(1)

$La_{1.75}Sr_{0.25}NiO_{4+\delta}$ heated in humid N_2 showed a decrease in the *a* and *b* cell parameters, in contrast to an increase in the *c* parameter. TGA/MS of this sample showed that H_2O loss occurred (Figure 5.11), with loss occurring from 40°C to 100°C, which is associated with surface H_2O. H_2O loss above 100°C was considered to be bulk H_2O and occurred from 100°C to ca. 400°C. 0.0120 mol of bulk H_2O was estimated to have been lost from the sample. There is a peak in H_2O loss which coincides with the start of CO_2 loss (Figure 5.12).

In regard to CO_2, there are two distinct periods in which CO_2 loss occurs. The first is between ca. 200°C and 500°C which is thought to be due to CO_3^{2-} impurities. The second is between ca. 500°C and 800°C, thought to be due to CO_2 loss from $La_2O_2CO_3$, as previously seen for La_2O_3 annealed in air. O_2 loss can be seen to occur above 800°C.

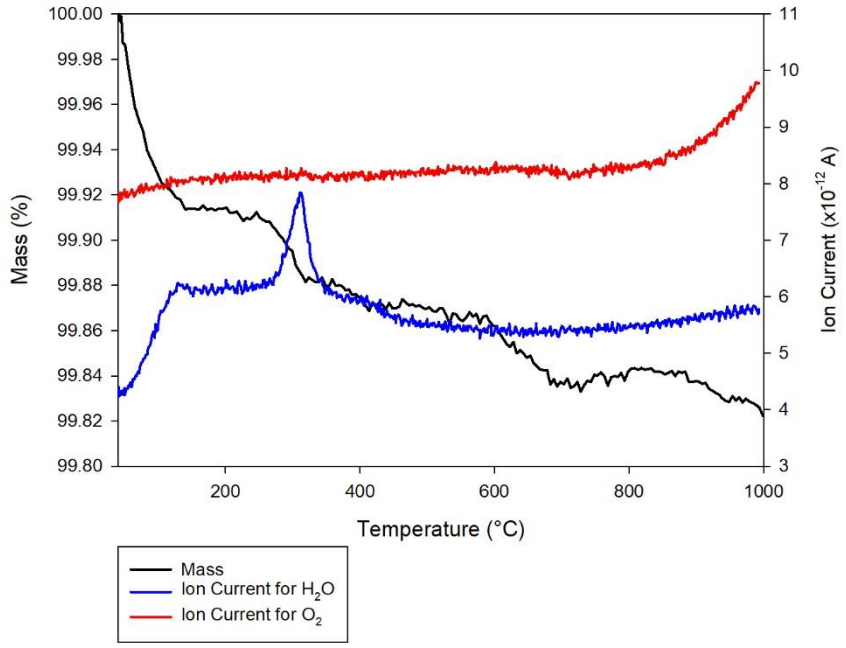


Figure 5.11: TGA and MS, up to a temperature of 1000°C, performed on $La_{1.75}Sr_{0.25}NiO_{4+\delta}$ heated in humid N_2. Mass loss (black), H_2O loss (blue) and O_2 loss (red).

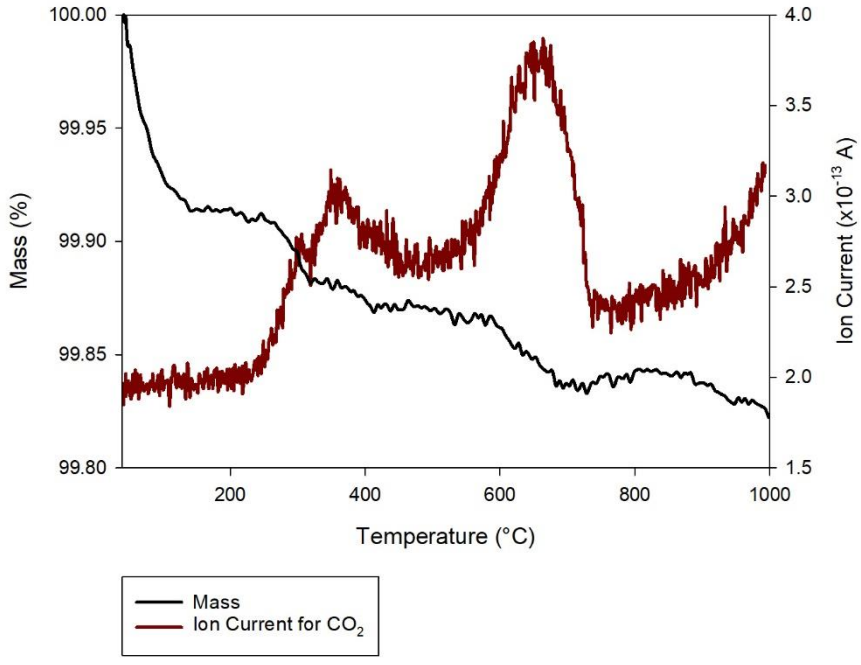


Figure 5.12: TGA and MS, up to a temperature of 1000°C, performed on $La_{1.75}Sr_{0.25}NiO_{4+\delta}$ heated in humid N_2. Mass loss (black) and CO_2 loss (dark red).

5.3.1.4 $La_{1.5}Sr_{0.5}NiO_{4+\delta}$

XRD was performed on all $La_{1.5}Sr_{0.5}NiO_{4+\delta}$ samples heated in humid N_2, dry N_2 and humid O_2 (Figure 5.13). Heating $La_{1.5}Sr_{0.5}NiO_{4+\delta}$ in the various conditions, showed that the samples remained chemically stable. Rietveld refinement performed on all samples, showed small changes in lattice parameters (Table 5.6).

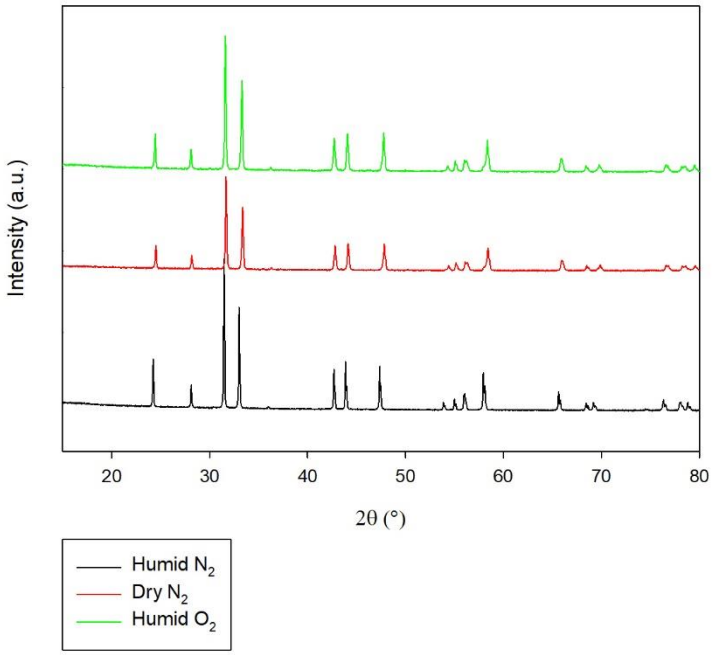


Figure 5.13: XRD patterns of $La_{1.5}Sr_{0.5}NiO_{4+\delta}$ annealed under various conditions. In ascending order humid N_2 (black), dry N_2 (red) and humid O_2 (green).

Table 5.6: Lattice parameters (orthorhombic *Fmmm*) for Rietveld refinement performed on $La_{1.5}Sr_{0.5}NiO_{4+\delta}$ annealed in various conditions.

	Unit Cell Parameters (Å)			Unit Cell Volume (Å³)
	a	b	c	
Original	5.3865(1)	5.3943(1)	12.7323(2)	369.96(1)
Humid N_2	5.4241(1)	5.4281(1)	12.6947(2)	373.77(1)
Dry N_2	5.3875(1)	5.3973(1)	12.7333(3)	370.26(1)
Humid O_2	5.3871(2)	5.3951(2)	12.7323(4)	370.05(3)

The sample heated in humid O_2 showed little change in lattice parameters (Table 5.6). Heating in dry N_2 showed an increase in the lattice parameters of the sample, which is thought to be due to the reduction of Ni^{3+} to Ni^{2+}, increasing the size of the unit cell. The sample heated in humid N_2 showed the largest increase compared to the other samples, possibly due to a mixture of H_2O incorporation and reduction of Ni^{3+}.

TGA performed on the humid $La_{1.5}Sr_{0.5}NiO_{4+\delta}$ showed H_2O loss (Figure 5.14) during the same temperature range as $La_2NiO_{4+\delta}$, estimated to be 0.0136 mol of bulk H_2O loss. The sample also showed CO_2 loss (Figure 5.15) starting at a similar temperature to the undoped parent sample. The initial CO_2 release occurring from 40°C to 600°C is thought to be from the crystal structure of the Ruddlesden Popper phase. However, CO_2 loss occurring past 600°C is attributed to the decomposition of $La_2O_2CO_3$.

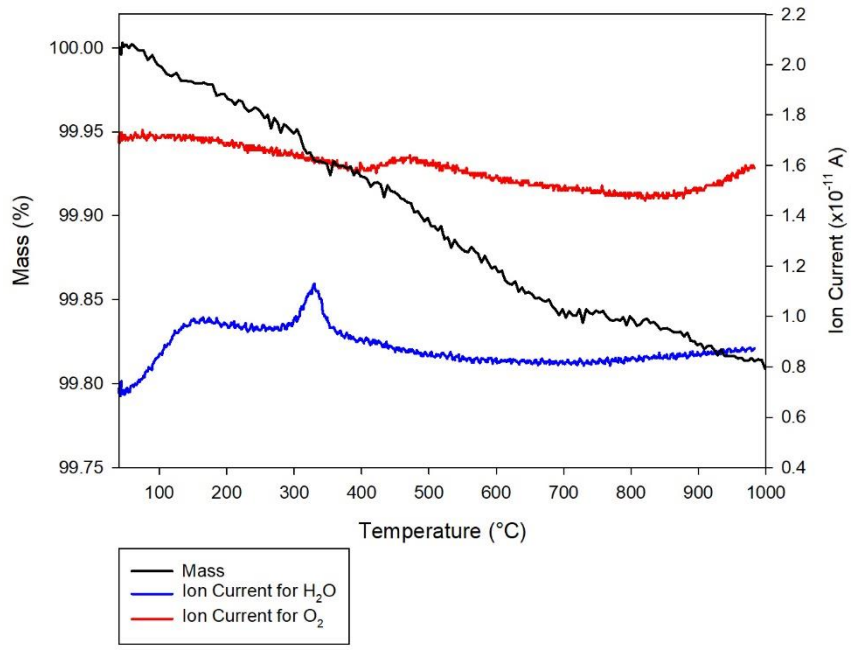


Figure 5.14: TGA and MS, up to a temperature of 1000°C, performed on $La_{1.5}Sr_{0.5}NiO_{4+\delta}$ heated in humid N_2. Mass loss (black), H_2O loss (blue) and O_2 loss (red).

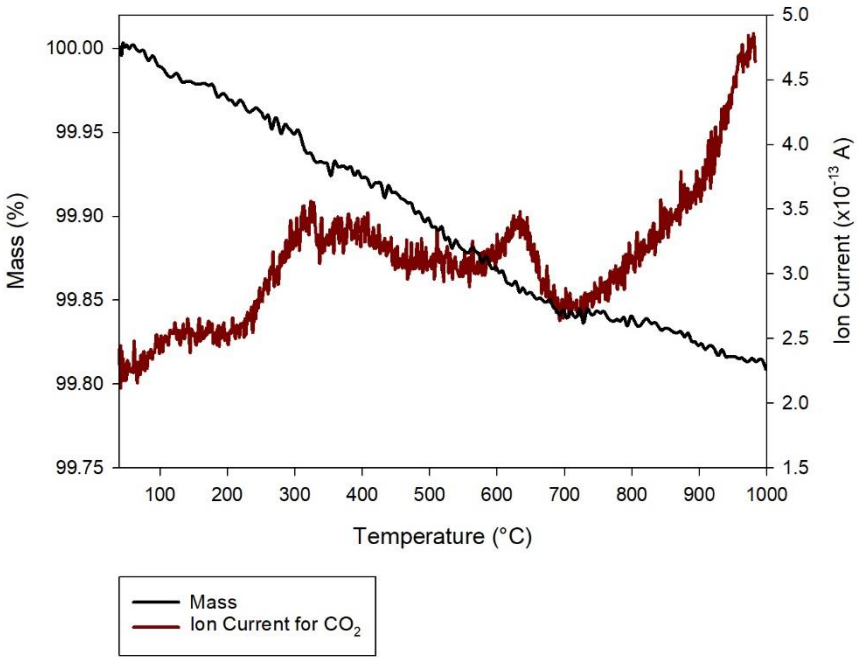


Figure 5.15: TGA and MS, up to a temperature of 1000°C, performed on $La_{1.5}Sr_{0.5}NiO_{4+\delta}$ heated in humid N_2. Mass loss (black) and CO_2 loss (dark red).

5.3.2 Analysis of Variable Temperature XRD on Samples treated in a Humid Atmosphere

5.3.2.1 $La_2NiO_{4+\delta}$

To further investigate the H_2O incorporation process, VT-XRD was performed, and the data compared to that of TGA/MS (Figure 5.17). An orthorhombic *Fmmm* space group was used for the refinement at 25°C and 125°C, as per literature [218, 228]. At 175°C the *a* and *b* parameter were seen to equate to one another, therefore sequential refinement for XRD patterns taken at 175°C and above was performed against a tetragonal *I4/mmm* space group. A similar change in symmetry has been seen by Song *et al.* [218]. The sample showed an increase in all lattice parameters on heating, as expected, due to thermal expansion (Figure 5.17 to Figure 5.19). There was a slight deviation in the *c* parameter between 225°C and 325°C (which has been highlighted in Figure 5.18) correlating to the temperatures at which bulk H_2O loss occurs. Regardless, the volume of the cell showed a linear increase, with no other deviations observed.

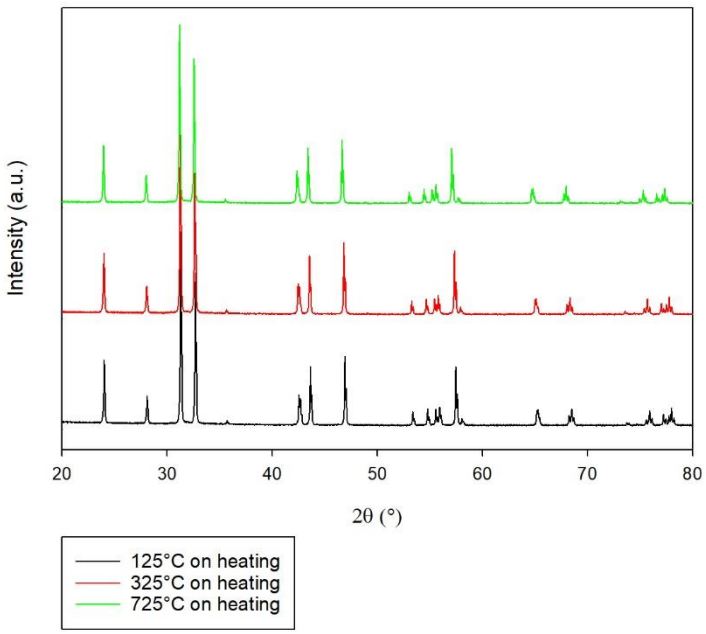


Figure 5.16: VT-XRD pattern of humidified $La_2NiO_{4+\delta}$ showing no change in XRD patterns during heating. In ascending order the temperatures 125°C (black), 325°C (red) and 725°C (green) are represented.

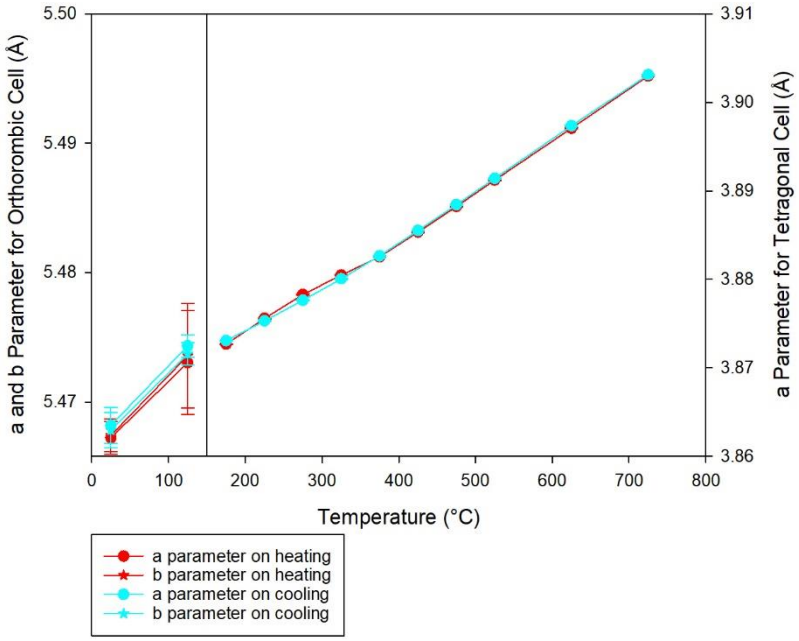


Figure 5.17: VT-XRD data showing the variation in *a* (circle) and *b* (star) parameter of humidified $La_2NiO_{4+\delta}$ versus temperature. The black line indicated the change in phase.

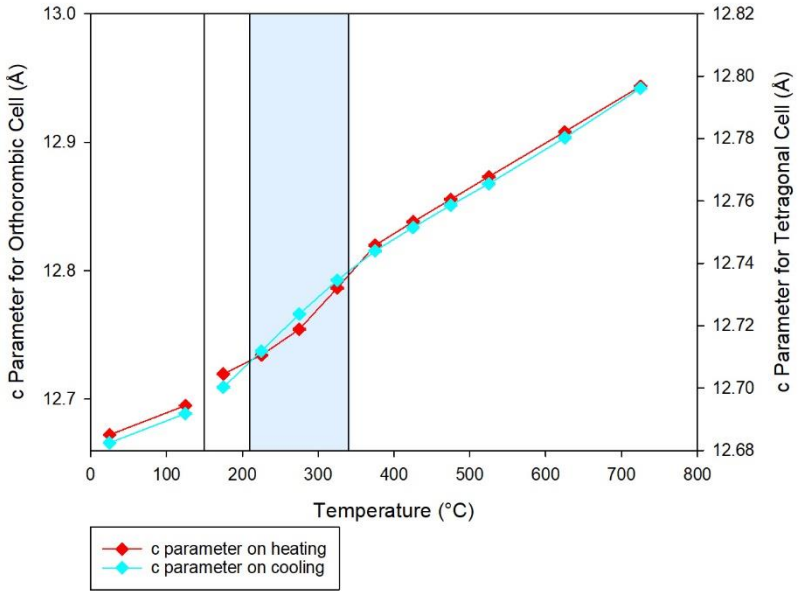


Figure 5.18: VT-XRD data showing the variation in *c* parameter of humidified $La_2NiO_{4+\delta}$ verses temperatures. Slight deviations in results are highlighted in blue. The black line showing the change in phase.

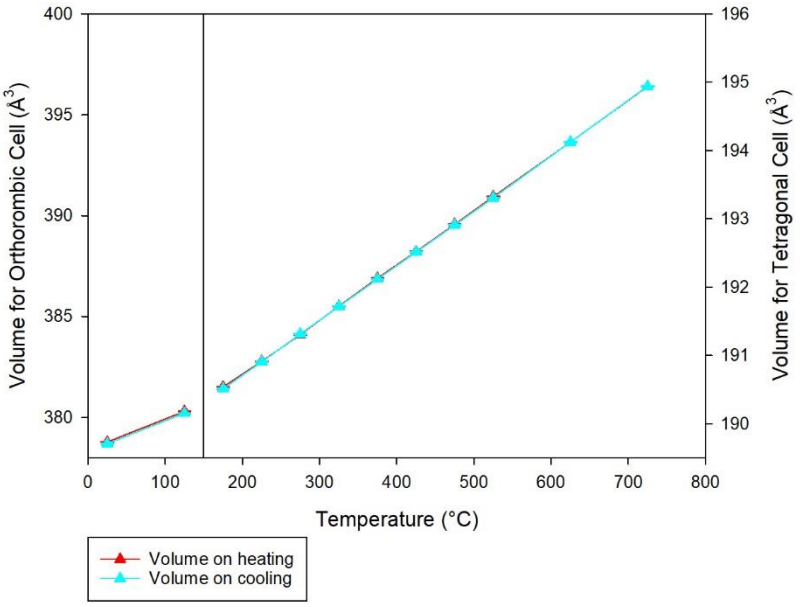


Figure 5.19: VT-XRD data showing the variation in cell volume of humidified $La_2NiO_{4+\delta}$ versus temperatures. The black line showing the change in phase.

5.3.2.2 $La_{1.75}Sr_{0.25}NiO_{4+\delta}$

VT-XRD was performed on humidified $La_{1.75}Sr_{0.25}NiO_{4+\delta}$, with sequential refinement performed against an orthorhombic *Fmmm* space group for all data sets, as there was no indication of a change in symmetry. During heating and cooling there was a linear increase and decrease respectively for all lattice parameters, with no deviations from the linear behaviour.

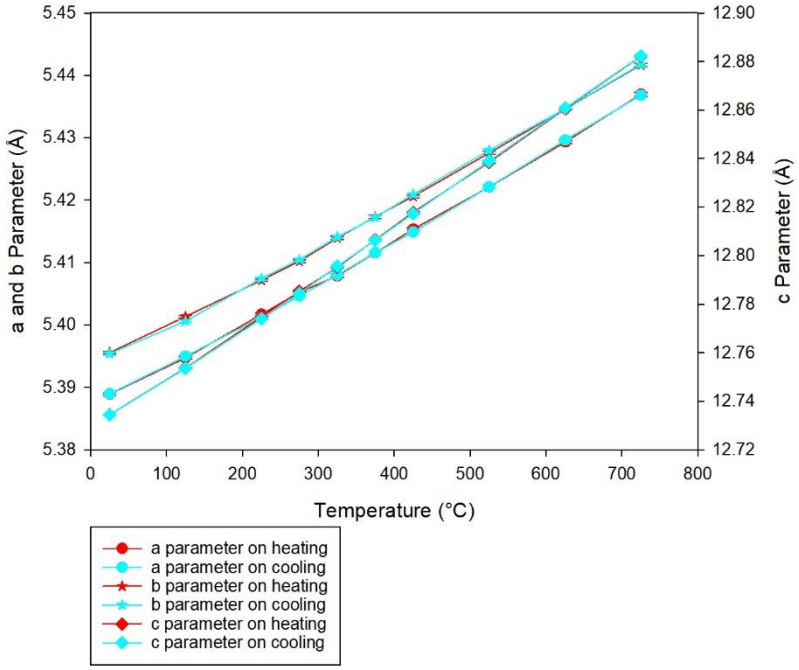


Figure 5.20: VT-XRD data showing the variation in lattice parameters of humidified $La_{1.75}Sr_{0.25}NiO_{4+\delta}$ versus temperature.

5.3.2.3 $La_{1.5}Sr_{0.5}NiO_{4+\delta}$

Performing VT-XRD on humidified $La_{1.5}Sr_{0.5}NiO_{4+\delta}$ revealed no visible change in XRD patterns (Figure 5.21) in the measured temperature range. A slight shoulder can be observed on the peak between 32° and 34° which indicates an orthorhombic symmetry. Therefore, sequential refinement was performed against an *Fmmm* space group.

There was a shift to higher 2θ angles when heating due to an increase in lattice parameters associated with thermal expansion, as expected on observation, supported by sequential refinement data (Figure 5.22 to Figure 5.25). The *a* parameter at 625°C showed a slight deviation from the linear trend during heating. This correlated with CO_2 release that occurred at ca. 600°C. Overall, there was a linear increase in the volume of the unit cell. A difference between the lattice parameters during cooling and heating was observed, which could be correlated with the gaseous species detected by TGA/MS, as they are not regained on cooling in the VT-XRD experiment.

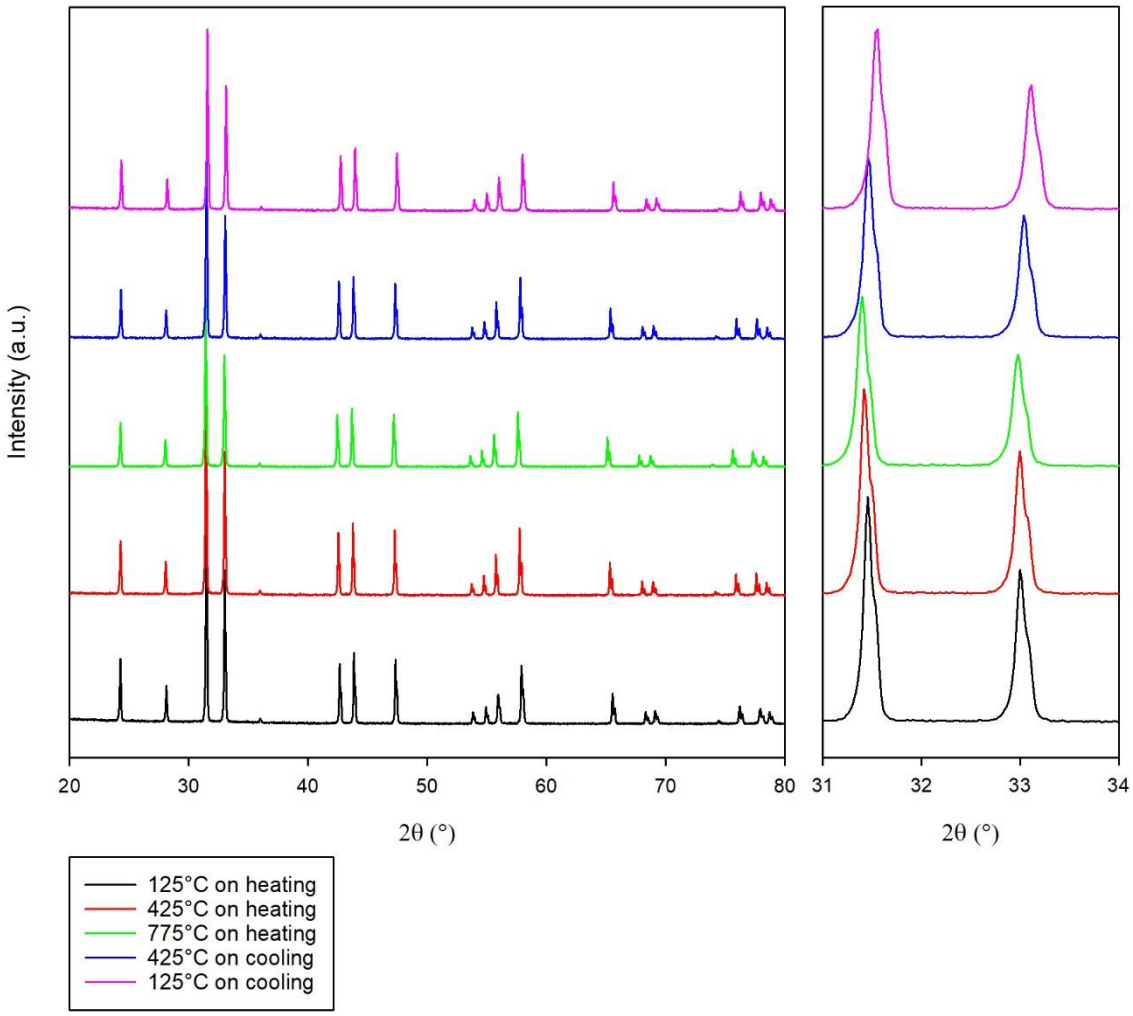


Figure 5.21: VT-XRD pattern of humidified $La_{1.5}Sr_{0.5}NiO_{4+\delta}$ showing no change in XRD patterns during heating. In ascending order the following temperatures 125°C on heating (black), 425°C on heating (red) and 775°C on heating (green), 425°C on cooling (blue) and 125°C on cooling (pink) are shown. Visible phase change in XRD patterns are not observed during heating or cooling. Specifically, between 31° and 34° shoulders are still present on peaks.

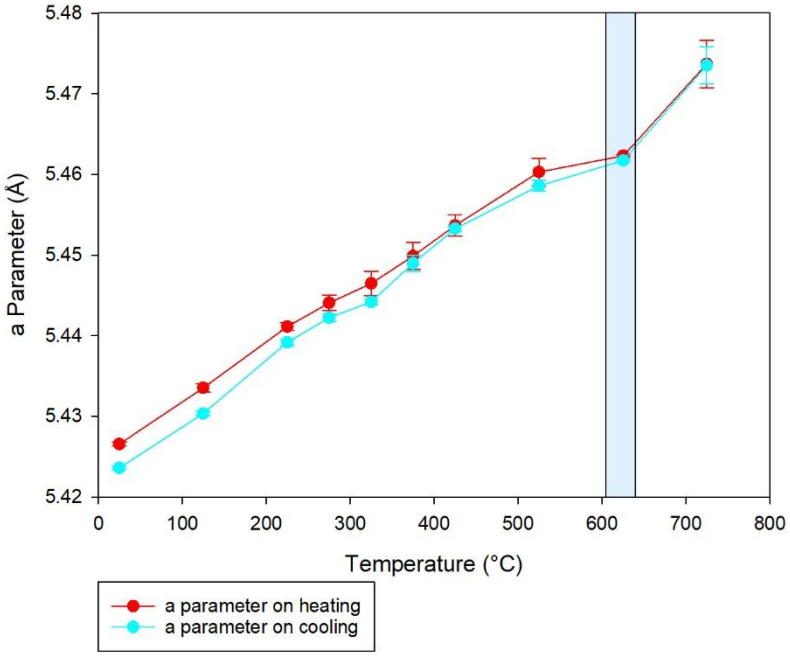


Figure 5.22: VT-XRD data showing the variation in a parameter of humidified $La_{1.5}Sr_{0.5}NiO_{4+\delta}$ versus temperature. Deviations from the linear trend are highlighted in blue.

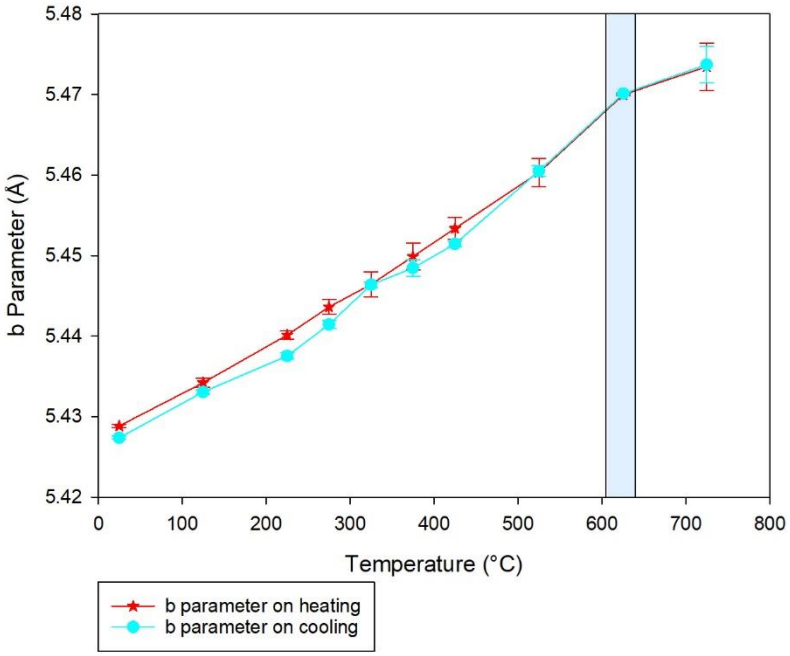


Figure 5.23: VT-XRD data showing the variation in *b* parameter of humidified $La_{1.5}Sr_{0.5}NiO_{4+\delta}$ versus temperature. Deviations from the linear trend are highlighted in blue.

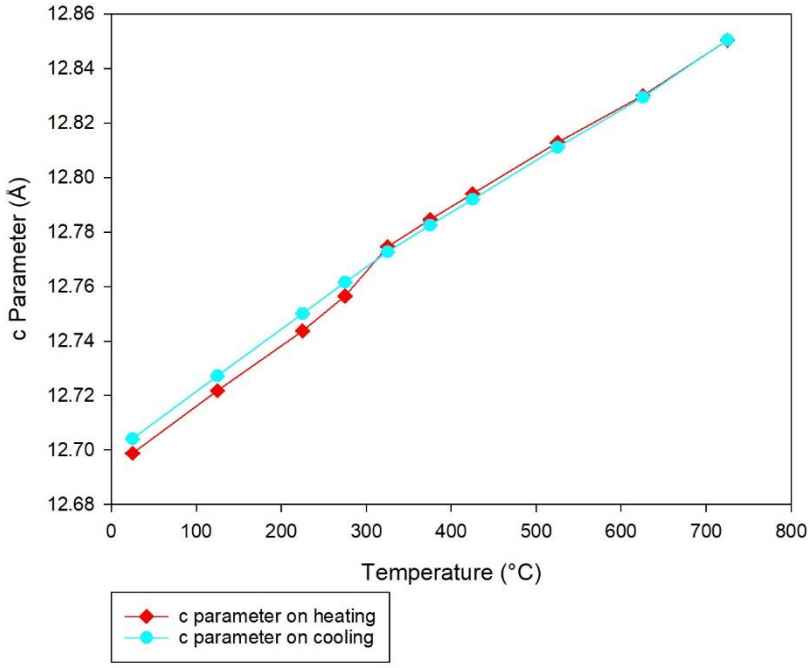


Figure 5.24: VT-XRD data showing the variation in *c* parameter of humidified $La_{1.5}Sr_{0.5}NiO_{4+\delta}$ versus temperature. Deviations from the linear trend are highlighted in blue.

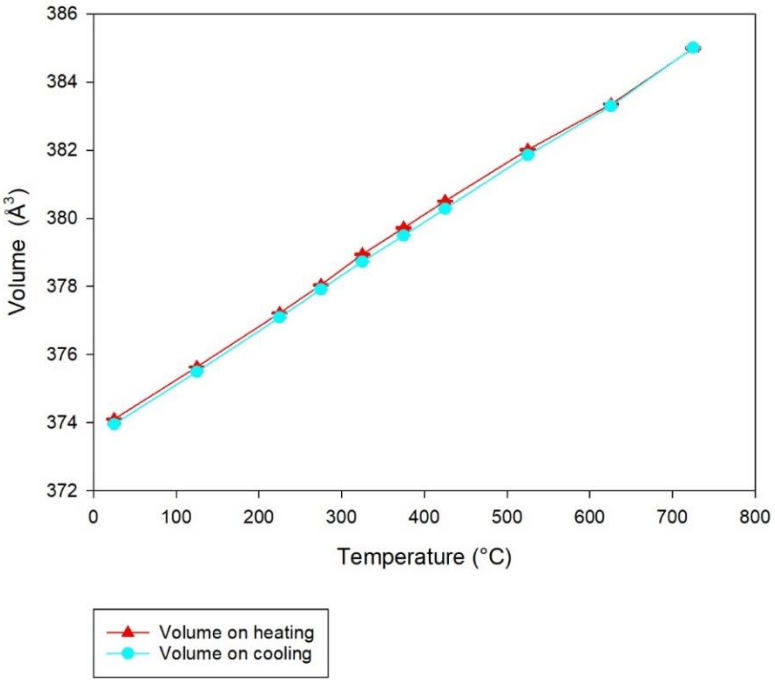


Figure 5.25: VT-XRD data showing the variation in cell volume parameter of humidified $La_{1.5}Sr_{0.5}NiO_{4+\delta}$ verses temperature. Deviations from the linear trend are highlighted in blue.

5.3.3 Conductivity Data

DC conductivity measurements for $La_{2-x}Sr_xNiO_{4+\delta}$ (x=0, 0.25 and 0.5) showed that Sr doping increased the electrical conductivity consistent with the greater Ni^{3+} content (Figure 5.26). $La_2NiO_{4+\delta}$ showed an initial increase in conductivity with temperature, up to a temperature of 475°C, where a conductivity of 13.49 Scm^{-1} was achieved (Table 5.7). Above this temperature the conductivity began to decrease, due to the loss of oxygen resulting in the reduction of Ni^{3+} to Ni^{2+}. The trend in conductivity was similar to that described by Takahashi *et al.* [213]. $La_2NiO_{4+\delta}$ and $La_{1.75}Sr_{0.25}NiO_{4+\delta}$ both saw the conductivity decrease post-475°C. For $La_{1.5}Sr_{0.5}NiO_{4+\delta}$ this transition occurred at a higher temperature, post-711°C, this sample also showing the highest conductivity.

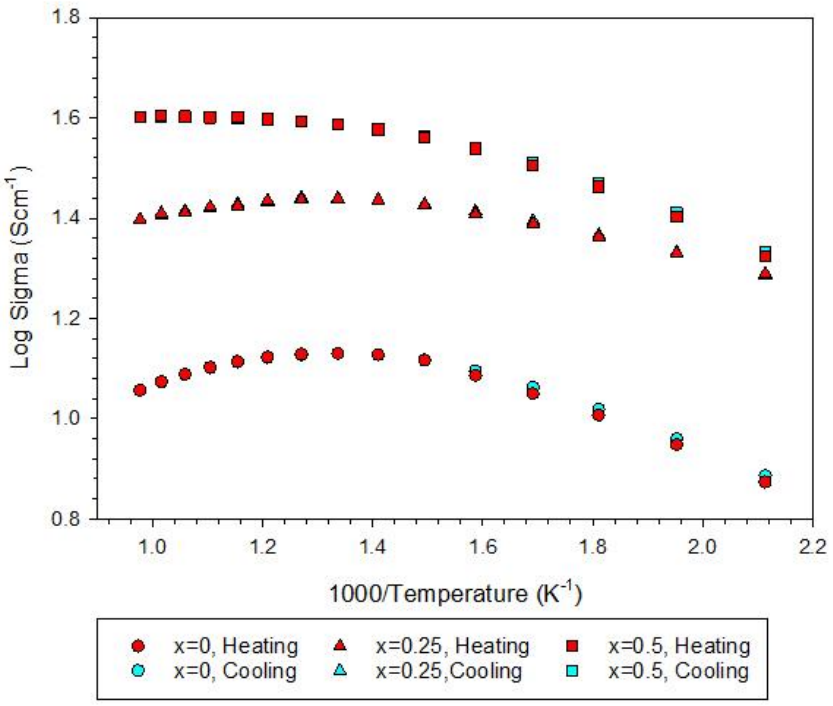


Figure 5.26: Conductivity data for $La_{2-x}Sr_xNiO_{4+\delta}$ where x=0 (circle) , 0.25 (triangle) and 0.5 (square). Red fill indicates heating and cyan fill indicates cooling; data shown between 200°C to 750°C. Measurements taken in air

Table 5.7: Conductivity of $La_{2-x}Sr_xNiO_{4+\delta}$ where x=0, 0.25 and 0.5, conductivity at 475°C, 711°C and 750°C.

Composition	Conductivity (Scm^{-1})		
	475°C (1.33 K^{-1})	711°C (1.02 K^{-1})	750°C (0.98 K^{-1})
$La_2NiO_{4+\delta}$	13.49	11.85	11.39
$La_{1.75}Sr_{0.25}NiO_{4+\delta}$	27.47	25.70	25.00
$La_{1.5}Sr_{0.5}NiO_{4+\delta}$	38.58	40.22	40.00

Introducing Sr into the crystal lattice increased the conductivity. As substitution of La^{3+} by an ion of a different oxidation state, Sr^{2+}, can lead to the formation of further electron holes in the Ni sites [207, 226]. $La_2NiO_{4+\delta}$ is a known p-type conductor, increasing electron holes increases the concentration of charge carriers [207, 218].

Increasing Sr content has been shown to further increase conductivity, in part due to the decrease in the *a* and *b* parameter, a result from shortening Ni-O bond lengths. The bond length for $La_2NiO_{4+\delta}$, $La_{1.5}Sr_{0.5}NiO_{4+\delta}$ and $La_{1.75}Sr_{0.25}NiO_{4+\delta}$ are 1.931 Å, 1.918 Å and 1.906 Å respectively. The main pathway for electrical conductivity utilises the Ni-O bonds in the NiO_6 octahedra [207, 213]. Therefore, decreasing the bond length has been speculated to lower activation energy for electron hole transport, as seen in conductivity data with increasing Sr content [207, 224, 231].

5.3.4 Conclusion

Ba and Sr were successfully doped into $La_2NiO_{4+\delta}$. XRD patterns of these samples showed that an orthorhombic phase had been achieved. Heating the Ba doped samples in humid N_2 showed some degradation of the samples. While heating in humid O_2 and dry N_2 showed the samples were able to maintain their original phase.

$La_{2-x}Sr_xNiO_{4+\delta}$ when heated in the various conditions remained stable, with all samples heated in humid N_2 showing some H_2O loss when TGA/MS was performed on the sample. An estimation of the H_2O content was established (Table 5.8). Increasing Sr content was shown to increase the quantity of H_2O

loss from the sample. VT-XRD was performed to further investigate H_2O loss. Only $La_2NiO_{4+\delta}$ showed a slight variation in lattice parameters when H_2O loss was expected. Conductivity measurements showed that doping with Sr increased the conductivity, with $La_{1.5}Sr_{0.5}NiO_{4+\delta}$ showing the highest conductivity (40.22 S cm^{-1}).

Table 5.8: Conductivity and H_2O loss from $La_{2-x}Sr_xNiO_{4+\delta}$ (x=0, 0.25 and 0.5).

Composition	Temperature of Maximum Conductivity (°C)	Maximum Conductivity (Scm^{-1})	Maximum H_2O loss from sample heated in humid N_2 (mol)
$La_2NiO_{4+\delta}$	475	13.49	0.0017
$La_{1.75}Sr_{0.25}NiO_{4+\delta}$	475	14.27	0.0120
$La_{1.5}Sr_{0.5}NiO_{4+\delta}$	711	40.22	0.0136

Chapter 6: Pr Doping in $La_{n+1}Ni_nO_{3n+1}$; n=2 and 3

6.1 Introduction

Higher order lanthanum nickelate Ruddlesden-Popper compounds ($La_3Ni_2O_{7-\delta}$ and $La_4Ni_3O_{10+\delta}$) have been shown to have better electronic conductivity as there is an increased quantity of Ni-O layers [135, 209, 213, 219]. These Ni-O layers, which relates to the number of perovskite layers the structure contains, consist of corner-linked NiO_6 octahedra. $La_4Ni_3O_{10-\delta}$ has three layers of corner-linked NiO_6 compared to $La_3Ni_2O_{7-\delta}$ which has two. This results in a higher electrical conductivity, as it is thought that these NiO_6 octahedral are predominantly responsible for charge transport [213].

Praseodymium (Pr) doping has been explored for $La_4Ni_3O_{10+\delta}$ in varying quantities for oxide conducting solid oxide cells (OC-SOC) application, with testing performed above 600°C [210-212]. Its variable oxidation state offers the potential to improve electrochemical performance. However, the viability in proton conducting ceramic cells (PCCCs) have not yet been explored, despite $Pr_2NiO_{4+\delta}$ having shown water (H_2O) incorporation into its crystal lattice and shown its viability as an anode in proton conducting ceramic electrolyser (PCCE) [136, 171]. It should be noted that $Pr_2NiO_{4+\delta}$ has been previously shown to have poor chemical stability, decomposing into $Pr_4Ni_3O_{10-\delta}$ and Pr_6O_{11} below 950°C [232].

Previously it has been reported that Pr is able to be doped into $La_4Ni_3O_{10-\delta}$. Pr is doped on the A-site, substituting La^{3+} for Pr^{3+} [210-212]. Due to Pr^{3+} having a smaller ionic radius then La^{3+} this is thought to reduce the volume of the unit cell. The smaller unit cell would imply smaller bond lengths between Ni-O, which would be expected to cause an increase in electrical conductivity. Pr doped samples are also expected to see an increase in water incorporation similar to previously Pr doped samples, which also showed an increase in oxygen vacancies and water incorporation [133].

Despite $La_3Ni_2O_{7-\delta}$ having been thoroughly structurally characterised, $La_3Ni_2O_{7-\delta}$ has not been as extensively explored as a viable electrode for solid oxide cells (SOCs) [135, 209, 213, 218, 220, 233]. This is mostly likely due to it not surpassing in either conductivity or stability, when compared to its counterparts. Therefore, published research of the doping of this phase is minimal. $La_3Ni_2O_{7-\delta}$ doped with Pr is expected to show a similar trend as $La_4Ni_3O_{10-\delta}$ doped with Pr. However, the electrical conductivity is expected to be lower for the $La_{3-x}Pr_xNi_2O_{7-\delta}$ samples, as $La_3Ni_2O_{7-\delta}$ has fewer Ni-O layers compared to $La_4Ni_3O_{10-\delta}$ [213, 218].

This chapter explores the effect of doping Pr into $La_4Ni_3O_{10-\delta}$, looking at doping a smaller amount of Pr and the effect this has on the performance. The viability of Pr doping into $La_3Ni_2O_{7-\delta}$ will be also explored. The chemical stability of the synthesised compositions heated in various conditions was investigated. To conclude ex-situ electrical conductivity measurements were performed, to determine the potential of the inspected materials as an electrode.

6.2 Experimental

Synthesis of $La_{3-x}Pr_xNi_2O_{7-\delta}$ and $La_{4-x}Pr_xNi_3O_{10-\delta}$ where x=0, 0.25, 0.5 and 1, was performed through a sol-gel approach. The precursor nitrates, $La(NO_3)_3.6H_2O$ (Sigma-Aldrich, 99.99%), $Ni(NO_3)_2.6H_2O$ (Alfa Aesar, 99.99%) and $Pr(NO_3)_3.6H_2O$ (Sigma-Aldrich, 99.9%) were dissolved in deionised H_2O. Ethylene glycol (VWR, ≥99.0%) and citric acid (Sigma-Aldrich, 99.0%) were then added. The solution was further mixed and then heated to 80°C until a gel formed. The gel was then heated in an oven to 350°C for 1 h. A final heat treatment was performed at the temperatures listed in Table 6.1 for the respective material. The furnace used was a Carbolite Gero Ltd. CWF 13/13 muffle furnace.

Table 6.1: Final heating temperatures for $La_{3-x}Pr_xNi_2O_{7-\delta}$ and $La_{4-x}Pr_xNi_3O_{10-\delta}$.

Composition	Temperature (°C)
$\mathbf{La_3Ni_2O_{7-\delta}}$	1150
$\mathbf{La_{2.75}Pr_{0.25}Ni_2O_{7-\delta}}$	1150
$\mathbf{La_{2.5}Pr_{0.5}Ni_2O_{7-\delta}}$	1150
$\mathbf{La_2PrNi_2O_{7-\delta}}$	1150
$\mathbf{La_4Ni_3O_{10+\delta}}$	1050
$\mathbf{La_{3.75}Pr_{0.25}Ni_3O_{10+\delta}}$	950
$\mathbf{La_{3.5}Pr_{0.5}Ni_3O_{10+\delta}}$	950
$\mathbf{La_3PrNi_3O_{10+\delta}}$	950

X-ray diffraction (XRD) analysis was performed using a Panlaytical Empyrean diffractometer with Cu K_α. The GSAS-II suite of programmes was used for structural Rietveld refinement [203]. To investigate the chemical stability of the samples, each was heated in humid nitrogen (N_2), dry and humid oxygen (O_2) using a Carbolite Gero Ltd. CTF 12/75 tube furnace. Thermogravimetric analysis (TGA) and mass spectrometry (MS) using a Netzsch STA 449 F1 Jupiter Thermal Analyser were performed on samples heated in humid N_2. H_2O, O_2 and carbon dioxide (CO_2) loss were observed and the estimated content of water and carbon dioxide determined.

Variable temperature XRD (VT-XRD), with flowing N_2, was then performed on the samples exposed to humid N_2 that remained chemically stable. The data were analysed using sequential refinement, through the use of GSAS-II [203]. The lattice parameters were then compared to TGA/MS data, specifically to determine water loss.

All praseodymium doped lanthanum nickelate powders were pressed into pellets using a pellet press from Doreth Engineering Co. Ltd, a 10 mm Specac die was used with a weight of 5 tons. The pellets were sintered at the temperatures at which they were synthesised. The sintered pellets were painted with

gold paint, 4 gold probes were attached and heated at 800°C for 1 h. 4 probe DC conductivity measurements were performed on the pellets between 200°C and 700°C, in air.

6.3 Pr doped $La_3Ni_2O_{7-\delta}$; $La_{3-x}Pr_xNi_2O_{7-\delta}$

Samples of $La_{3-x}Pr_xNi_2O_{7-\delta}$ (x=0, 0.25, 0.5 and 0.75) were synthesised, with XRD (Figure 6.1) collected and Rietveld refinement was performed, (Figure 6.2). Rietveld refinement was performed against an orthorhombic *Fmmm* space group for $La_3Ni_2O_{7-\delta}$, as per literature [135, 209, 234, 235]. Similar XRD patterns were observed when doping with Pr, therefore Rietveld refinement for subsequent samples was performed against the same *Fmmm* space group, Table 6.2, with the aim of achieving a good fit and an weighted pattern (R_{wp}) of 10% or less. In these Rietveld refinements, La was substituted by the appropriate amount of Pr on the A site.

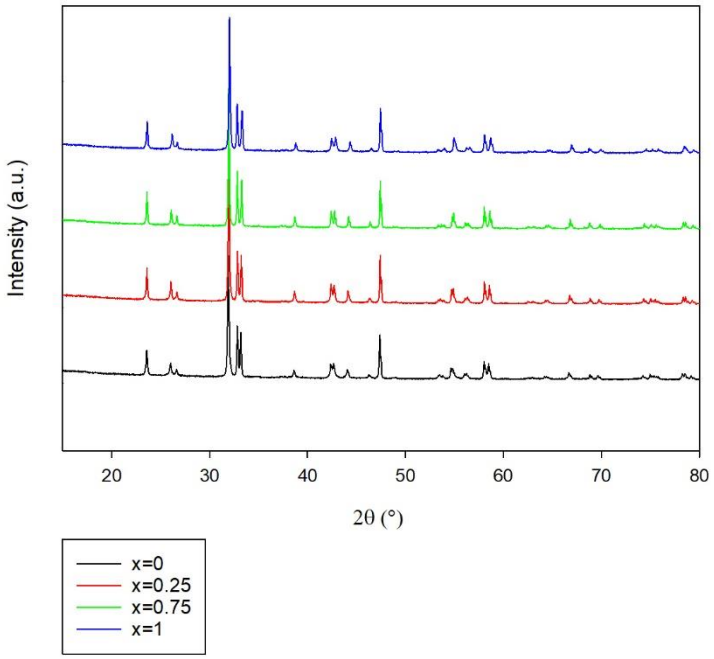


Figure 6.1: XRD patterns of $La_{3-x}Pr_xNi_2O_{7-\delta}$ samples where x =0, 0.5 and 0.75 and 1. In ascending order $La_3Ni_2O_{7-\delta}$ (black), $La_{2.75}Pr_{0.25}Ni_2O_{7-\delta}$ (red), $La_{2.5}Pr_{0.5}Ni_2O_{7-\delta}$ (green) and $La_2PrNi_2O_{7-\delta}$ (blue).

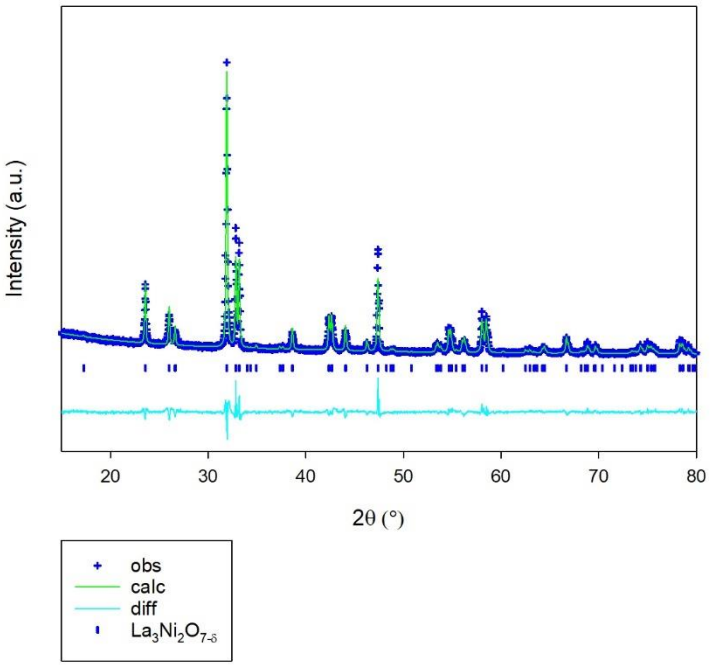


Figure 6.2: Example of observed, calculated and difference profiles for Rietveld refinement performed on $La_3Ni_2O_{7-\delta}$ (orthorhombic *Fmmm* space group, R_{wp}=7.44%).

An increase in Pr content showed a general decrease in the volume of the cell (Figure 6.4), due to the ionic radius of Pr^{3+} (1.179 Å) being smaller than the ionic radius of the replaced La^{3+} (1.216 Å). Closer inspection of the lattice parameters showed that the *a* and *c* parameter displayed the same trend (Figure 6.3 and Figure 6.4). However, the *b* parameter increased with Pr content with a similar observation having been made previously for $La_{4-x}Pr_xNi_3O_{10-\delta}$ [212]. The smaller ionic radius of Pr causes the difference between the *a* and *b* parameters to increase with Pr content [219].

Table 6.2: Lattice parameters (orthorhombic *Fmmm*) from Rietveld refinement performed for $La_{3-x}Pr_xNi_2O_{7-\delta}$ (x =0, 0.5 and 0.75 and 1) samples.

Composition	Unit Cell Parameters (Å)			Unit Cell Volume (Å^3)	R_{wp} (%)
	a	b	c		
$La_3Ni_2O_{7-\delta}$	5.3937(1)	5.4488(1)	20.5246(6)	603.20(2)	7.43
$La_{2.75}Pr_{0.25}Ni_2O_{7-\delta}$	5.3876(1)	5.4494(1)	20.4971(4)	601.78(1)	6.56
$La_{2.5}Pr_{0.5}Ni_2O_{7-\delta}$	5.3811(1)	5.4509(1)	20.4702(4)	600.43(1)	6.61
$La_2PrNi_2O_{7-\delta}$	5.3753(1)	5.4532(1)	20.4020(5)	598.04(2)	6.41

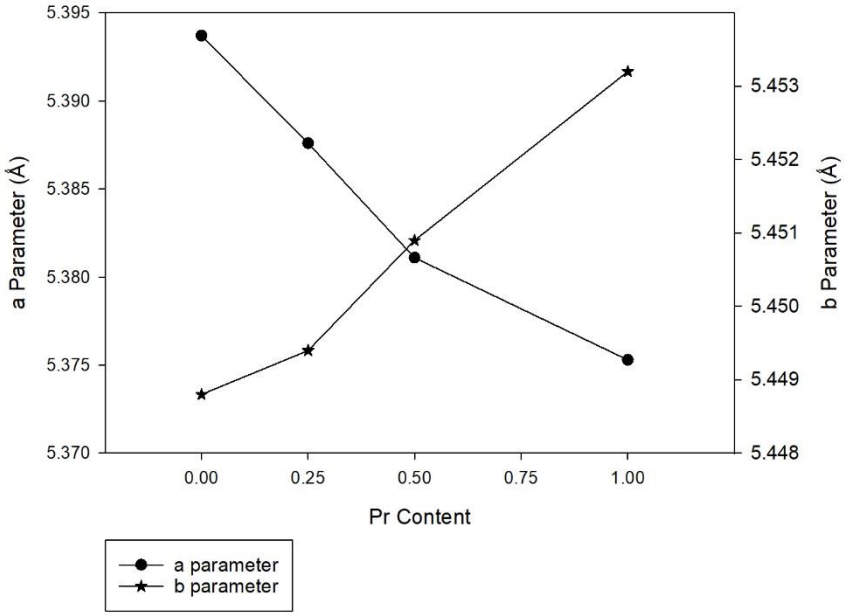


Figure 6.3: Variation of *a* and *b* lattice parameters for $La_{3-x}Pr_xNi_2O_{7-\delta}$ (x=0, 0.25, 0.5 and 1). Black circles indicate a parameter. Black stars indicate *b* parameter.

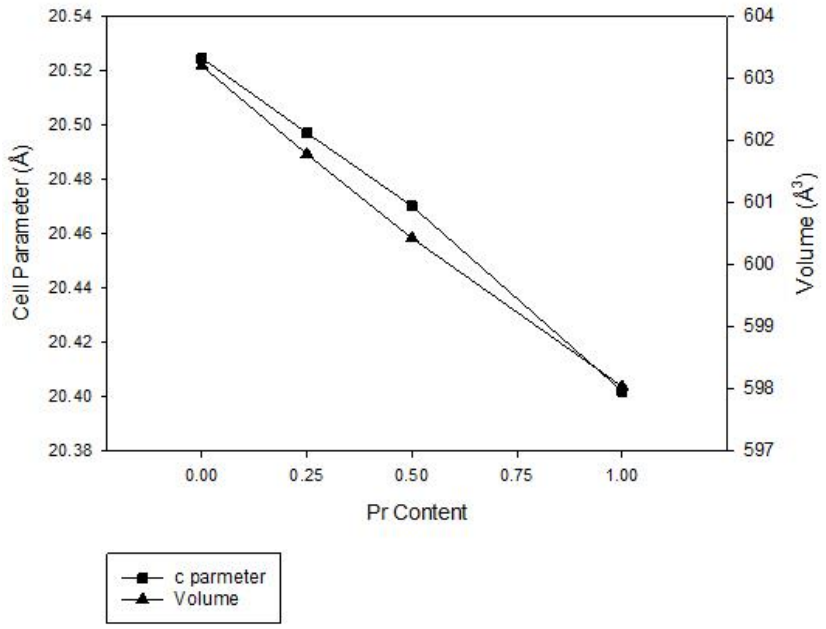


Figure 6.4: Variation of *c* lattice parameter and volume for $La_{3-x}Pr_xNi_2O_{7-\delta}$ (x=0, 0.25, 0.5 and 1). Black squares indicate *c* parameter. Black triangles indicate volume.

6.3.1 Investigation of Heating under Humid Nitrogen, Dry Nitrogen and Humid Oxygen

6.3.1.1 $La_3Ni_2O_{7-\delta}$

$La_3Ni_2O_{7-\delta}$ was heated in humid N_2, dry N_2 and humid O_2 and subsequently XRD analysis was performed (Figure 6.5). Heating $La_3Ni_2O_{7-\delta}$ in humid N_2 showed an increase in the *a* and *b* parameter, whilst there is a decrease in the *c* parameter (Table 6.3). Therefore, the overall volume of the unit cell shows little change. Despite this, TGA/MS analysis of the sample heated in humid N_2 shows H_2O loss from 40°C (Figure 6.6). During initial heating during TGA, H_2O loss from the surface of the sample occurred. H_2O loss continues between 100°C and 400°C, which is thought to be bulk H_2O. Above 700°C further H_2O loss was observed, along with a slight loss of O_2. CO_2 loss was observed between 200°C and 600°C (Figure 6.7), CO_2 loss has been previously observed for Ruddlesden-Popper system and is thought to be a result the synthesis method, due to using carbon rich precursors [236].

If a singular gaseous species was lost with mass loss, by comparing the relative molar mass before and after along with the mass before and after, a molar quantity of the lost gaseous species can be estimated.

In this case CO_2 loss coincides with H_2O it is difficult to achieve an accurate measurement of H_2O loss. Instead, an estimate can be obtained by assuming all mass loss is completely a result of H_2O loss. Therefore, it can be determined that the H_2O content loss between 100°C and 400°C was less than 0.032 mol. While above 700°C if O_2 loss is dismissed then the H_2O quantity is an additional 0.014 mol. A similar assumption can be made to determine CO_2 loss. An estimation for moles of CO_2 released was determined to be 0.036 mol, assuming all mass loss was a result of CO_2 released.

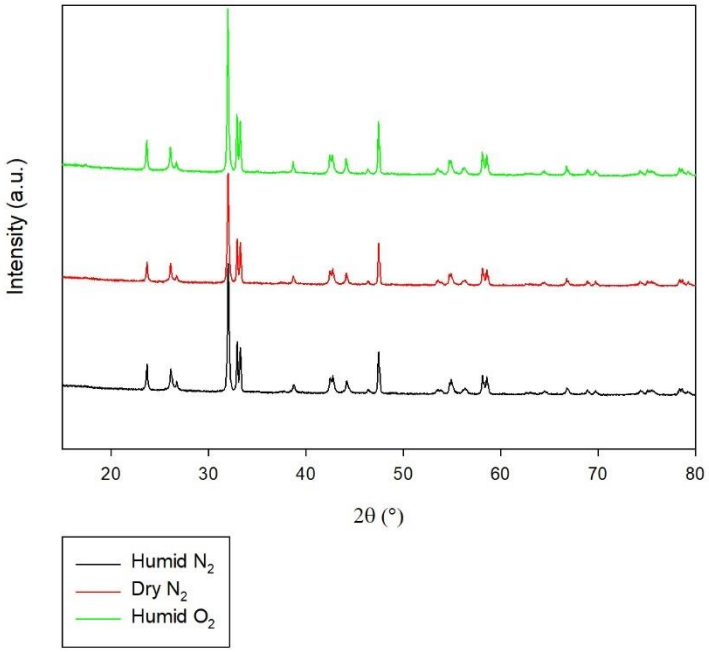


Figure 6.5: XRD patterns of $La_3Ni_2O_{7-\delta}$ heated in various conditions. In ascending order humid N_2 (black), dry N_2 (red) and humid O_2 (green).

Table 6.3: Lattice parameters (orthorhombic *Fmmm*) for Rietveld refinement performed on $La_3Ni_2O_{7-\delta}$ heated in various conditions.

	Unit Cell Parameters (Å)			Unit Cell Volume (Å^3)
	a	b	c	
Original	5.3937(1)	5.4488(1)	20.5246(6)	603.20(2)
Humid N_2	5.3967(2)	5.4510(2)	20.5050(9)	603.21(3)
Dry N_2	5.3939(2)	5.4498(2)	20.5237(7)	603.31(2)
Humid O_2	5.3945(2)	5.4483(2)	20.5238(10)	603.21(7)

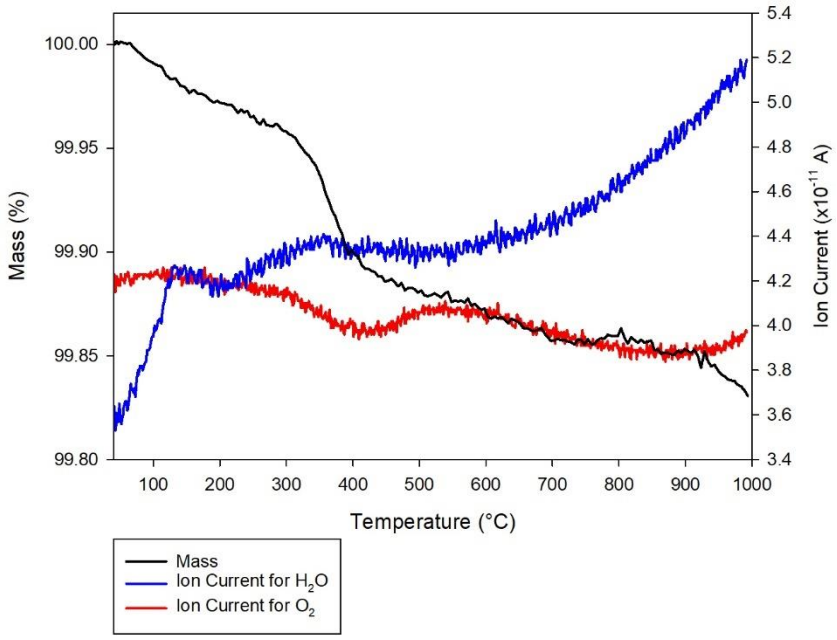


Figure 6.6: TGA and MS, up to a temperature of 1000°C, performed on $La_3Ni_2O_{7-\delta}$ heated in humid N_2. Mass loss (black), H_2O loss (blue) and O_2 loss (red).

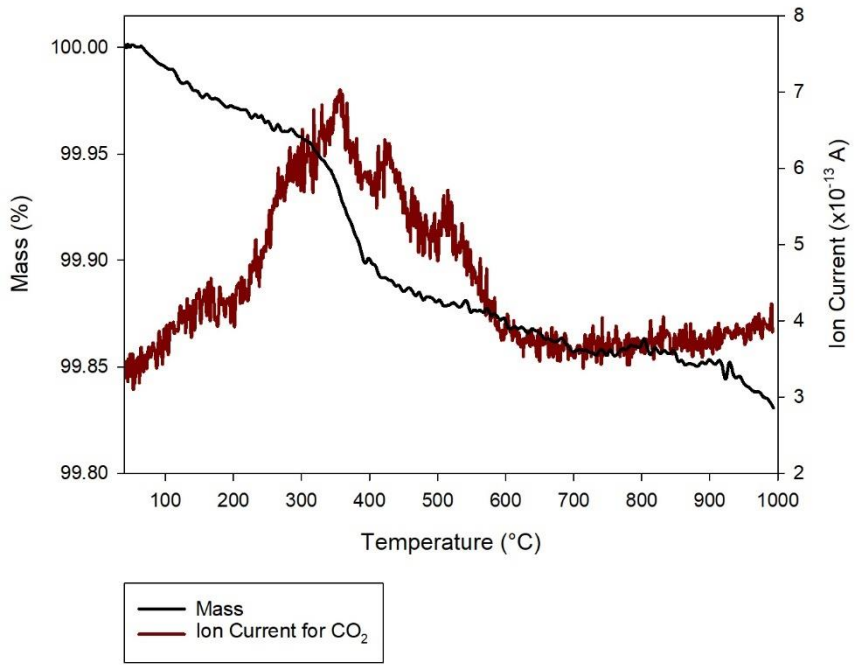


Figure 6.7: TGA and MS, up to a temperature of 1000°C, performed on $La_3Ni_2O_{7-\delta}$ heated in humid N_2. Mass loss (black) and CO_2 loss (dark red).

O_2 loss was also observed for $La_3Ni_2O_{7-\delta}$ heated in humid N_2, this occurs between 40°C and 350°C and then begins again from 400°C. The temperature range where O_2 loss does not occur is possibly due to O_2 being re-adsorbed by the sample. This is able to occur as H_2O has been released, allowing for re-incorporation of O_2.

A previous study had shown that annealing $La_3Ni_2O_{7-\delta}$ in O_2 for 24 h at 500°C, reduced the number of oxygen vacancies. The resulting stoichiometry was $La_3Ni_2O_{7.00}$; the annealing had minimal effect on lattice parameters [234]. Annealing in humid O_2 also appears to have little effect on lattice parameters.

$La_3Ni_2O_{7-\delta}$ has been previously shown to have an average oxygen content of 2.5 (δ=0) due to a mixture of Ni^{3+} and Ni^{2+} [233, 235, 237]. Heating in dry N_2 showed a minor increase in lattice parameters and an overall increase in volume, possibly due to the reduction of Ni^{3+} to Ni^{2+}. The increase in volume did not occur for the humid N_2 sample possibly due to oxygen vacancies produced being filled by H_2O, which counteracted the expansion.

6.3.1.2 $La_{2.75}Pr_{0.25}Ni_2O_{7-\delta}$

XRD patterns of $La_{2.75}Pr_{0.25}Ni_2O_{7-\delta}$ heated in humid N_2 and humid O_2 (Figure 6.8) showed an increase in intensity for peaks with the reflection (0 0 6), (0 0 10) and (0 0 12). As these reflections are parallel to the {00l} crystal plane, this was indicative of these samples having a preferred orientation parallel to this plane. Therefore, Rietveld refinement was performed considering the preferred orientation (Figure 6.9). As this occurred for both samples heated in humid conditions, it was thought the presence of H_2O influenced this change, along with the presence of Pr as the preferred orientation did not occur for the undoped sample ($La_3Ni_2O_{7-\delta}$). The presence of H_2O during heating possibly resulted in Pr within the lattice changing position, thus resulting in the preferred orientation. The cause for the preferred orientation would require further investigation.

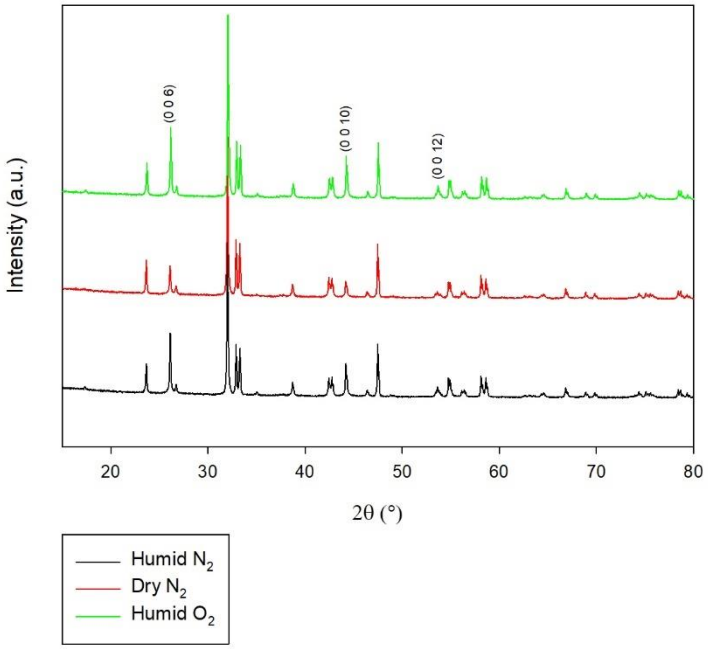


Figure 6.8: XRD patterns of $La_{2.75}Pr_{0.25}Ni_2O_{7-\delta}$ heated in various conditions. In ascending order humid N_2 (black), dry N_2 (red) and humid O_2 (green). (0 0 6), (0 0 10) and (0 0 12) reflections shown.

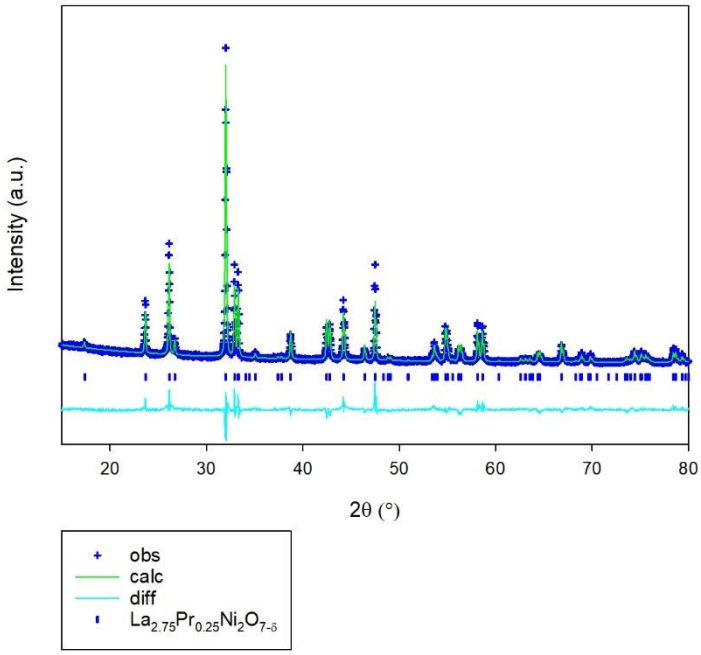


Figure 6.9: Example of observed (blue cross), calculated (green) and difference (cyan) profiles for Rietveld refinement performed on $La_{2.75}Pr_{0.25}Ni_2O_{7-\delta}$ (orthorhombic *Fmmm* space group, R_{wp}=8.11%).

Overall the difference in lattice parameters of the various heat treated samples were negligible (Table 6.4), more so when considering experimental errors, despite this TGA/MS of humid $La_{2.75}Pr_{0.25}Ni_2O_{7-\delta}$ showed H_2O loss (Figure 6.10) between 100°C and 400°C, which was estimated to be 0.044 mol. H_2O loss also occurred above 600°C (this equated to 0.2638 mol, ignoring potential occupying CO_2 and O_2 loss). The CO_2 loss (Figure 6.11) that occurred above 600°C was possibly due to $La_2O_2CO_3$ impurities within the sample, which was not identified within the XRD pattern. If CO_2 loss was only considered above 600°C, 0.097 mol was released.

Table 6.4: Lattice parameters (orthorhombic space group) for Rietveld refinement performed on $La_{2.75}Pr_{0.25}Ni_2O_{7-\delta}$ heating in various conditions.

	Unit Cell Parameters (Å)			Unit Cell Volume (Å^3)
	a	b	c	
Original	5.3876(1)	5.4494(1)	20.4971(4)	601.78(1)
Humid N_2	5.3876(1)	5.4500(1)	20.4965(6)	601.82(2)
Dry N_2	5.3874(1)	5.4496(1)	20.4974(5)	601.79(2)
Humid O_2	5.3879(1)	5.4495(1)	20.4950(6)	601.76(2)

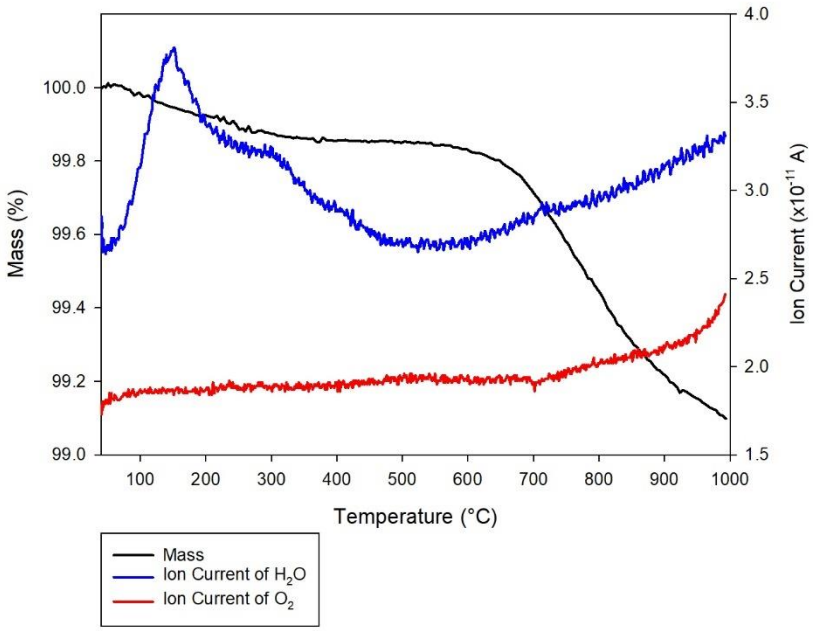


Figure 6.10: TGA and MS, up to a temperature of 1000°C, performed on $La_{2.75}Pr_{0.25}Ni_2O_{7-\delta}$ heated in humid N_2. Mass loss (black), H_2O loss (blue) and O_2 loss (red).

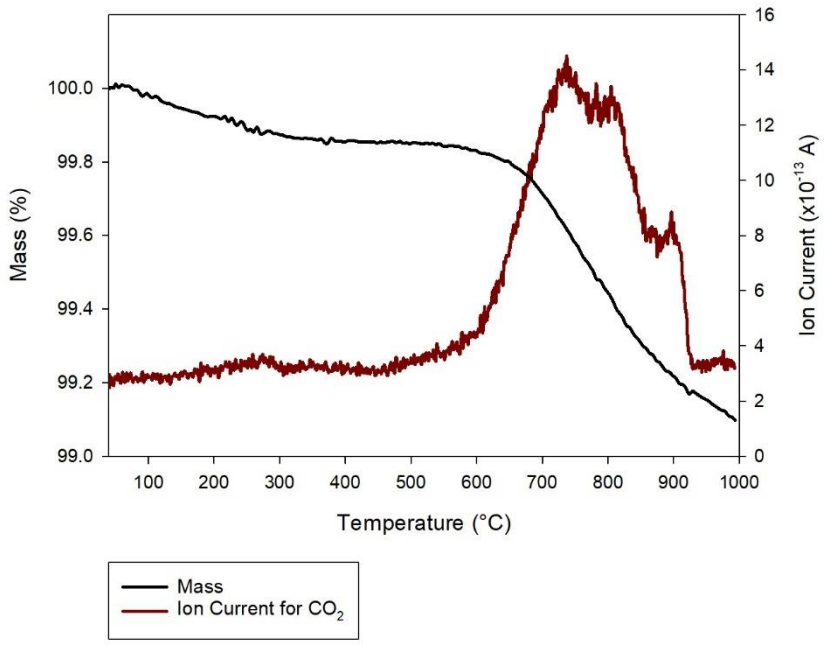


Figure 6.11: TGA and MS, up to a temperature of 1000°C, performed on $La_{2.75}Pr_{0.25}Ni_2O_{7-\delta}$ heated in humid N_2. Mass loss (black) and CO_2 loss (dark red).

6.3.1.3 $La_{2.5}Pr_{0.5}Ni_2O_{7-\delta}$

$La_{2.5}Pr_{0.5}Ni_2O_{7-\delta}$ was heated in humid N_2, dry N_2 and humid O_2 (Figure 6.12). The sample heated in dry N_2 degraded into lanthanum nickelate and praseodymium nickelate phases. Heating in humid O_2 caused the sample to have a greater preferred orientation along the {00l} plane and a decrease in the *c* parameter (Table 6.5). It is assumed that the preferred orientation is a result of the O_2 present within the sample, as this did not occur for the samples heated in humid N_2. It has been previously shown that $La_{4-x}Pr_xNi_3O_{10-\delta}$ contains mixed valency Pr which may also apply to $La_{3-x}Pr_xNi_2O_{7-\delta}$ [210]. Therefore the presence of O_2 may have caused the oxidation of some Pr^{3+} to Pr^{4+}, this may have then resulted Pr changing position in the lattice, resulting in the preferred orientation. Further work would be required to confirm this.

When heated in humid N_2 the sample remained chemically stable. It was assumed that the phase and random orientation was maintained due to a synergistic effect of the humid conditions and low oxygen partial pressures. Limited change was observed in lattice parameters (Table 6.5). TGA/MS analysis on

the sample, suggested that a maximum 0.032 mol of H_2O (Figure 6.13) was lost from the sample. However, this value is determined by not considering CO_2 loss (Figure 6.14) which occurs at a similar temperature range. In contrast by not consider H_2O loss, CO_2 can be estimated which was 0.017 mol. Unlike $La_{2.75}Pr_{0.25}Ni_2O_{7-\delta}$, CO_2 loss did occur above 600°C, so the CO_2 loss was not thought to be due to $La_2O_2CO_3$ impurities, but from CO_2 within the crystal structure.

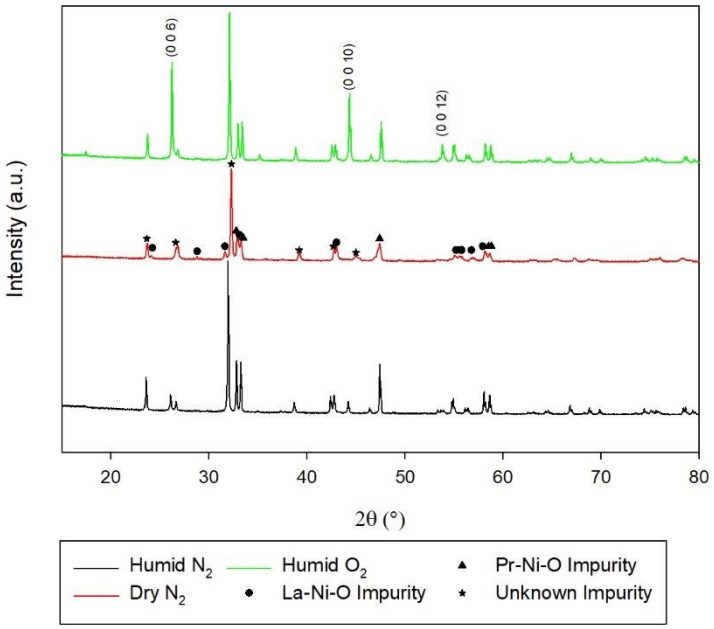


Figure 6.12: XRD patterns of $La_{2.5}Pr_{0.5}Ni_2O_{7-\delta}$ heated in various conditions. In ascending order humid N_2 (black), dry N_2 (red) and humid O_2 (green). (0 0 6), (0 0 10) and (0 0 12) reflections are shown.

Table 6.5: Lattice parameters (orthorhombic *Fmmm*) for Rietveld refinement performed on $La_{2.5}Pr_{0.5}Ni_2O_{7-\delta}$ heated in various conditions.

	Unit Cell Parameters (Å)			**Unit Cell Volume (Å³)**
	a	b	c	
Original	5.3811(1)	5.4509(1)	20.4702(4)	600.43(1)
Humid N_2	5.3810(1)	5.4511(1)	20.4702(4)	600.44(1)
Humid O_2	5.3815(2)	5.4511(2)	20.4682(4)	600.44(2)

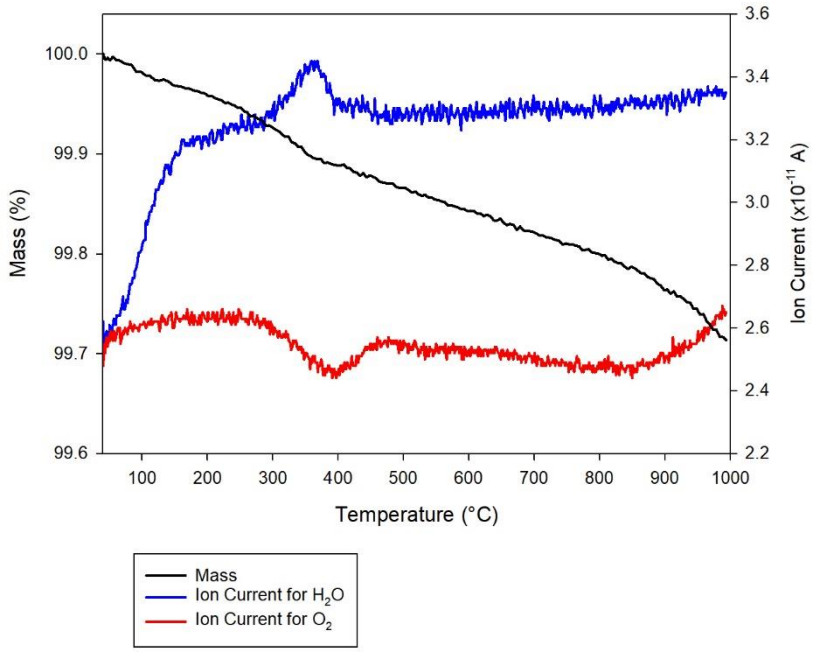


Figure 6.13: TGA and MS, up to a temperature of 1000°C, performed on $La_{2.5}Pr_{0.5}Ni_2O_{7-\delta}$ heated in humid. Mass loss (black), H_2O loss (blue) and O_2 loss (red).

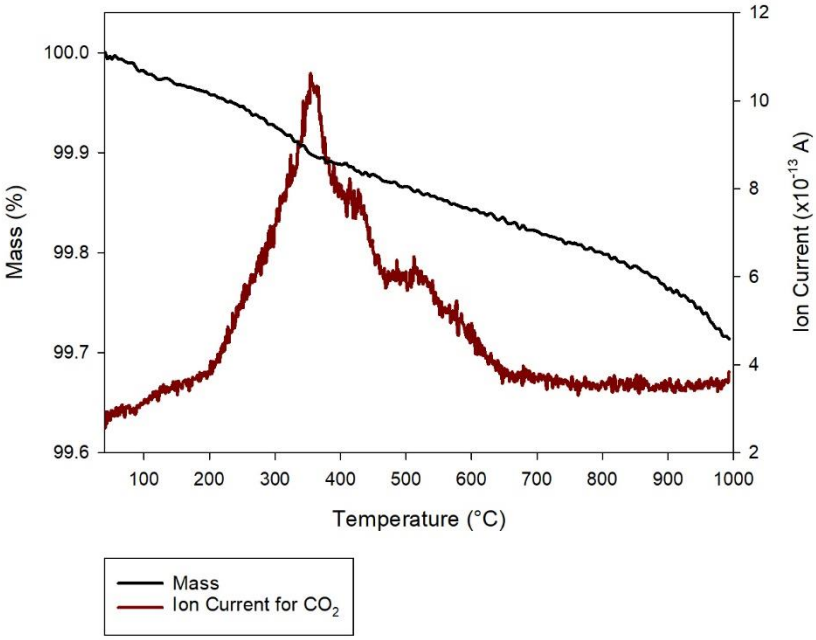


Figure 6.14: TGA and MS, up to a temperature of 1000°C, performed on $La_{2.5}Pr_{0.5}Ni_2O_{7-\delta}$ heated in humid N_2. Mass loss (black) and CO_2 loss (dark red).

Similar to $La_3Ni_2O_{7-\delta}$, $La_{2.5}Pr_{0.5}Ni_2O_{7-\delta}$ shows O_2 releases from 40°C to 350°C and then again above 400°C (Figure 6.13). This is possibly once again due to O_2 being readsorbed between 350°C and 400°C. As before the O_2 being readsorbed is possible due to H_2O being released at lower temperatures.

6.3.1.4 $La_2PrNi_2O_{7-\delta}$

XRD patterns of $La_2PrNi_2O_{7-\delta}$ showed no visible changed on heating in various conditions (Figure 6.15) Rietveld refinement of the $La_2PrNi_2O_{7-\delta}$ samples heated in dry N_2 showed no change in volume compared to the original sample, when considering experimental error. The sample heated in humid N_2 showed an increase in the volume of the unit cell, similarly the sample heated in humid O_2 showed a slight increase. TGA/MS performed on the humid N_2 sample showed H_2O loss (Figure 6.16). The ion current for H_2O can be seen in three sections. The first from 40°C to 100°C was from surface H_2O. The second exceeding 100°C was due to bulk H_2O incorporation and occurred up to 400°C, estimated to be a maximum 0.023 mol of H_2O. The final section of H_2O loss began at ca. 700°C, estimated to be 0.025 mol, although above 900°C O_2 loss does also occur. CO_2 loss was also observed H_2O loss occurring at ca. 200°C (Figure 6.17), and so the actual H_2O content will be lower than the above value.

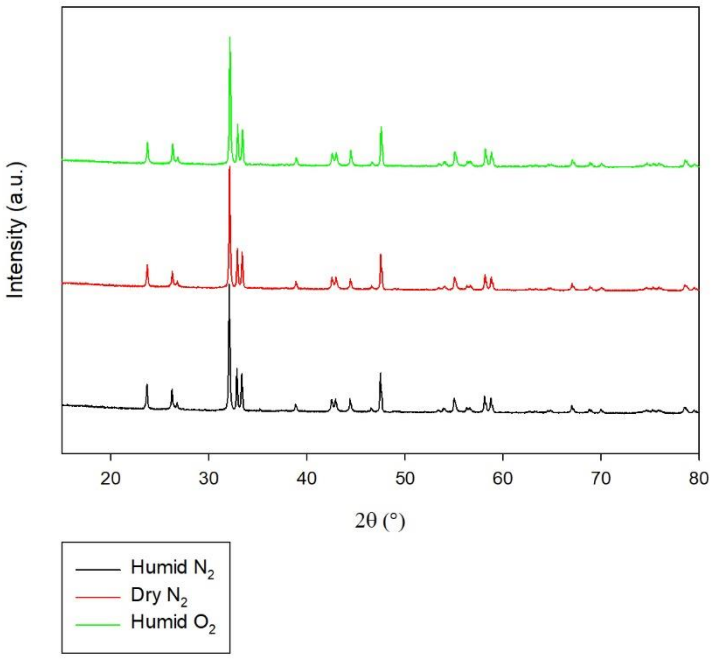


Figure 6.15: XRD patterns of $La_2PrNi_2O_{7-\delta}$ heated in various conditions. In ascending order humid N_2 (black), dry N_2 (red) and humid O_2 (green).

Table 6.6: Lattice parameters (orthorhombic *Fmmm*) for Rietveld refinement performed on $La_2PrNi_2O_{7-\delta}$ heated in various conditions.

	Unit Cell Parameters (Å)			**Unit Cell Volume (Å^3)**
	a	b	c	
Original	5.3753(1)	5.4532(1)	20.4020(5)	598.04(2)
Humid N_2	5.3752(1)	5.4543(1)	20.4025(5)	598.15(2)
Dry N_2	5.3752(1)	5.4538(1)	20.3988(6)	598.00(2)
Humid O_2	5.3759(1)	5.4539(1)	20.3999(6)	598.12(2)

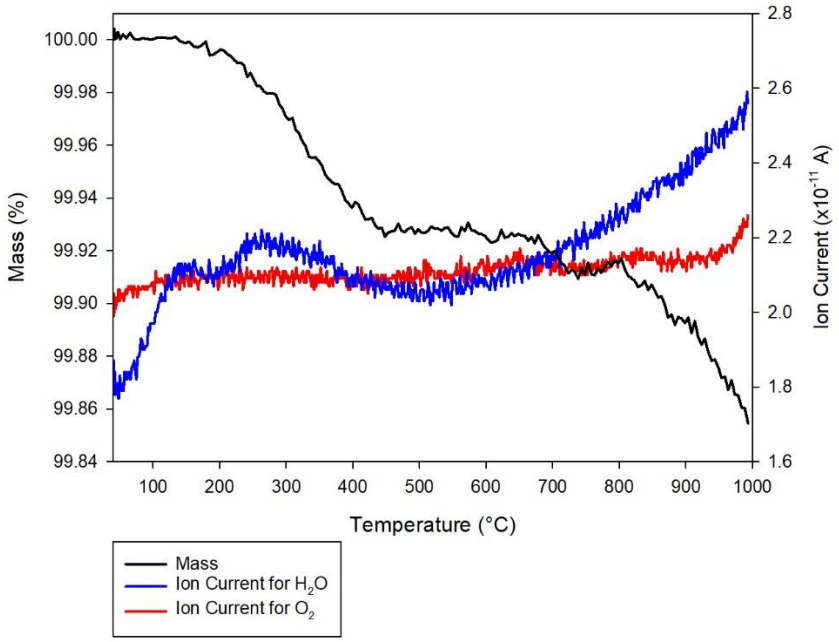


Figure 6.16: TGA and MS, up to a temperature of 1000°C, performed on $La_2PrNi_2O_{7-\delta}$ heated in humid N_2. Mass loss (black), H_2O loss (blue) and O_2 loss (red).

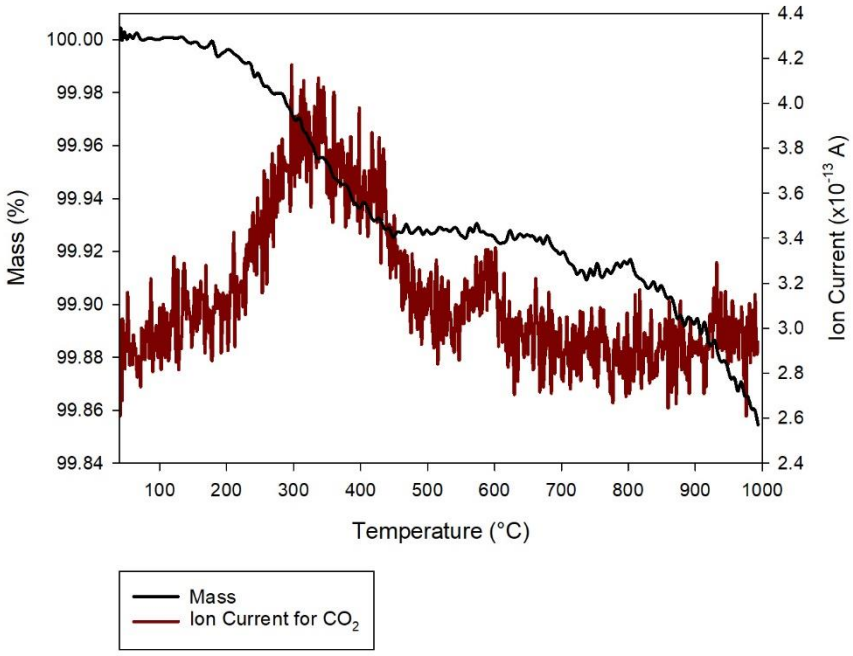


Figure 6.17: TGA and MS, up to a temperature of 1000°C, performed on $La_2PrNi_2O_{7-\delta}$ heated in humid N_2. Mass loss (black) and CO_2 loss (dark red).

Overall, heating $La_{3-x}Pr_xNi_2O_{7-\delta}$ in varying conditions gave varying results, the molar quantity of H_2O and CO_2 loss from the humidified samples can be seen in Table 6.7. $La_3Ni_2O_{7-\delta}$ heated in humid atmospheres took little impact on the overall volume of the unit cell, whether it be using N_2 or O_2 as a carrier gas [218, 234]. Introducing Pr as a dopant onto the A site influenced the chemical stability of the sample when heated in various gases. The results need further study to rationalise why low levels of Pr doping increased the preferred orientation when heated in various conditions.

Table 6.7: Maximum H_2O and CO_2 loss from TGA/MS of samples heated in humid N_2.

	Maximum H_2O loss of humid N_2 sample below 600°C (mol)	**Maximum CO_2 loss of humid N_2 sample below 600°C (mol)**
$La_3Ni_2O_{7-\delta}$	0.032	0.036
$La_{2.75}Pr_{0.25}Ni_2O_{7-\delta}$	0.044	0
$La_{2.5}Pr_{0.5}Ni_2O_{7-\delta}$	0.013	0.017
$La_2PrNi_2O_{7-\delta}$	0.023	0.025

6.3.2 Analysis of Variable Temperature XRD on Samples treated in a Humid Atmosphere

$La_3Ni_2O_{7-\delta}$, $La_{2.5}Pr_{0.5}Ni_2O_{7-\delta}$ and $La_2PrNi_2O_{7-\delta}$ samples heated in humid N_2 were characterised using VT-XRD. All samples showed a change from orthorhombic to tetragonal during heating. Previous studies have shown that after annealing, $La_3Ni_2O_{7-\delta}$ in 11% H_2/Ar and 11% H_2/N_2 can cause the oxygen stoichiometry to decrease to δ=0.65 and δ=0.16, respectively [234]. $La_3Ni_2O_{6.35}$ has been shown to have a tetragonal symmetry while $La_3Ni_2O_{6.84}$ has an orthorhombic symmetry. The symmetry for $La_3Ni_2O_{6.35}$ can be reverted to orthorhombic by re-annealing again at 450°C in O_2.

In these measurements, which were done with flowing N_2, $La_{2.5}Pr_{0.5}Ni_2O_{7-\delta}$ and $La_2PrNi_2O_{7-\delta}$ reverted to their orthorhombic structure during cooling, indicating that in this case the thermal expansion of the cell had a larger part to play in phase change then the oxygen stoichiometry.

6.3.2.1 $La_3Ni_2O_{7-\delta}$

VT-XRD patterns (Figure 6.18) showed that heating $La_3Ni_2O_{7-\delta}$ caused a shift in 2θ values towards lower angles, consistent with the observed thermal expansion, as expected. Initially $La_3Ni_2O_{7-\delta}$ has an orthorhombic structure, at 325°C it is seen to change to a tetragonal structure similar to that observed by Song *et al.* [218]. The cell symmetry change can be observed by the (020) and (200) reflections coalescing as the temperatures increases to a singular peak. Further heating of the tetragonal phase continues to see an increase in lattice parameters, as expected, due to thermal expansion (Figure 6.19 to Figure 6.21).

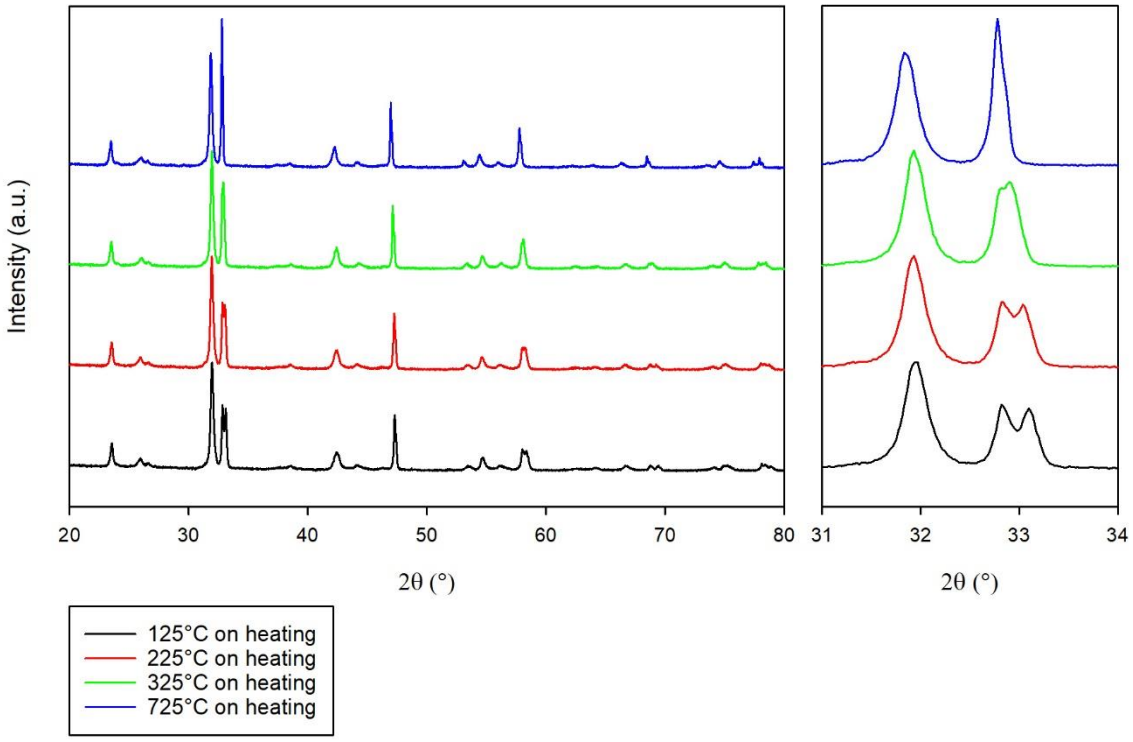


Figure 6.18: VT-XRD pattern of humid $La_3Ni_2O_{7-\delta}$ showing phase change, from orthorhombic to tetragonal, during heating. Specifically, peaks between 32.5° and 33.5° form a singular peak. In ascending order temperatures are 125°C on heating (black), 225°C on heating (red), 375°C on heating (green) and 725°C on heating (blue).

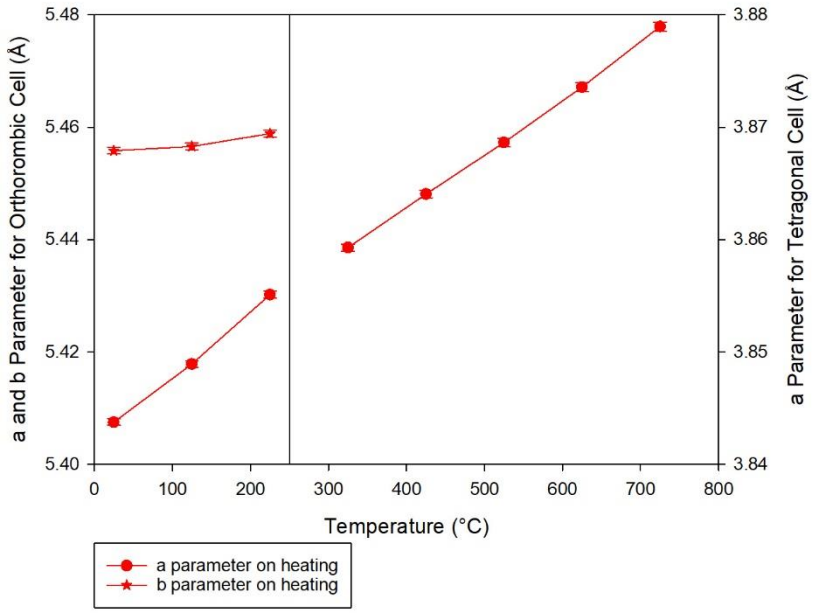


Figure 6.19: VT-XRD data showing the variation in a (circle) and b (star) parameter of humidifed $La_3Ni_2O_{7-\delta}$ versus temperature. At 325°C, the orthorhombic phase turns tetragonal. A black line is drawn to show this change in symmetry.

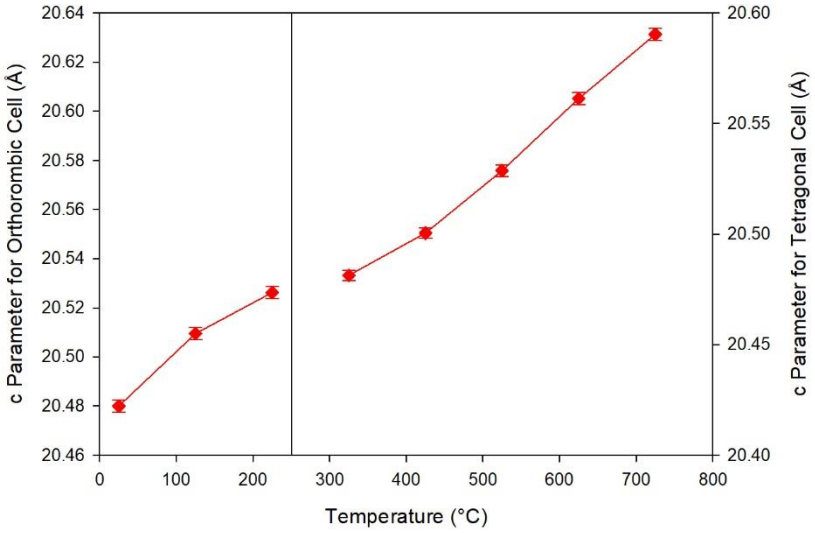


Figure 6.20: VT-XRD data showing the variation in c parameter (diamond) of humidified $La_3Ni_2O_{7-\delta}$ verses temperature. At 325°C, the orthorhombic phase turns tetragonal. A black line is drawn to show this change in symmetry.

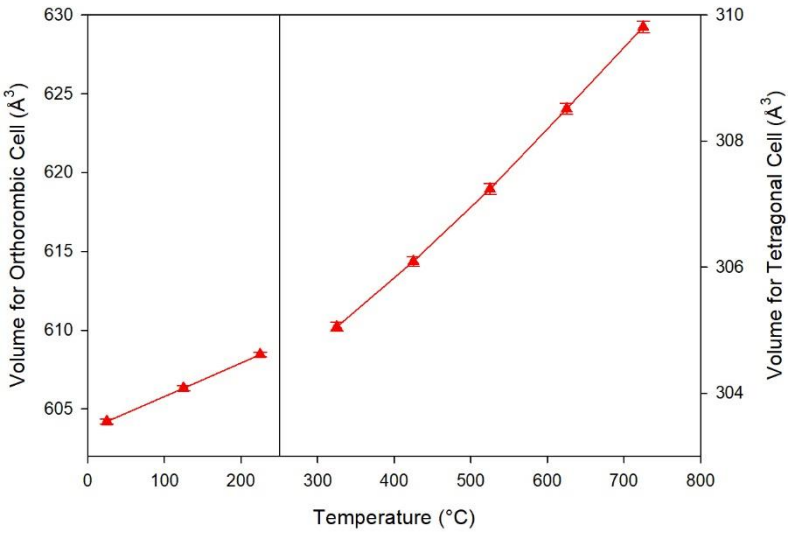


Figure 6.21: VT-XRD data showing the variation in volume (triangle) of humidifed $La_3Ni_2O_{7-\delta}$ versus temperature. At 325°C, the orthorhombic phase turns tetragonal. A black line is drawn to show this change in symmetry.

6.3.2.2 $La_{2.5}Pr_{0.5}Ni_2O_{7-\delta}$

Humid $La_{2.5}Pr_{0.5}Ni_2O_{7-\delta}$ has a similar orthorhombic *Fmmm* space group, to $La_3Ni_2O_{7-\delta}$. A cell symmetry change occurs at 675°C to a tetragonal *I4/mmm* space group (Figure 6.22). Heating causes the *a* and *b* parameter to increase (Figure 6.23), with a slight deviation in the trend at 275°C, when H_2O and CO_2 release are expected to occur as observed from TGA results. In contrast, the *c* parameter decreases after 225°C (Figure 6.24), only increasing again after 325°C. It is difficult to see this same trend in the volume (Figure 6.25), as the change in the *c* parameter is compensated by changes in the *a* and *b* parameters.

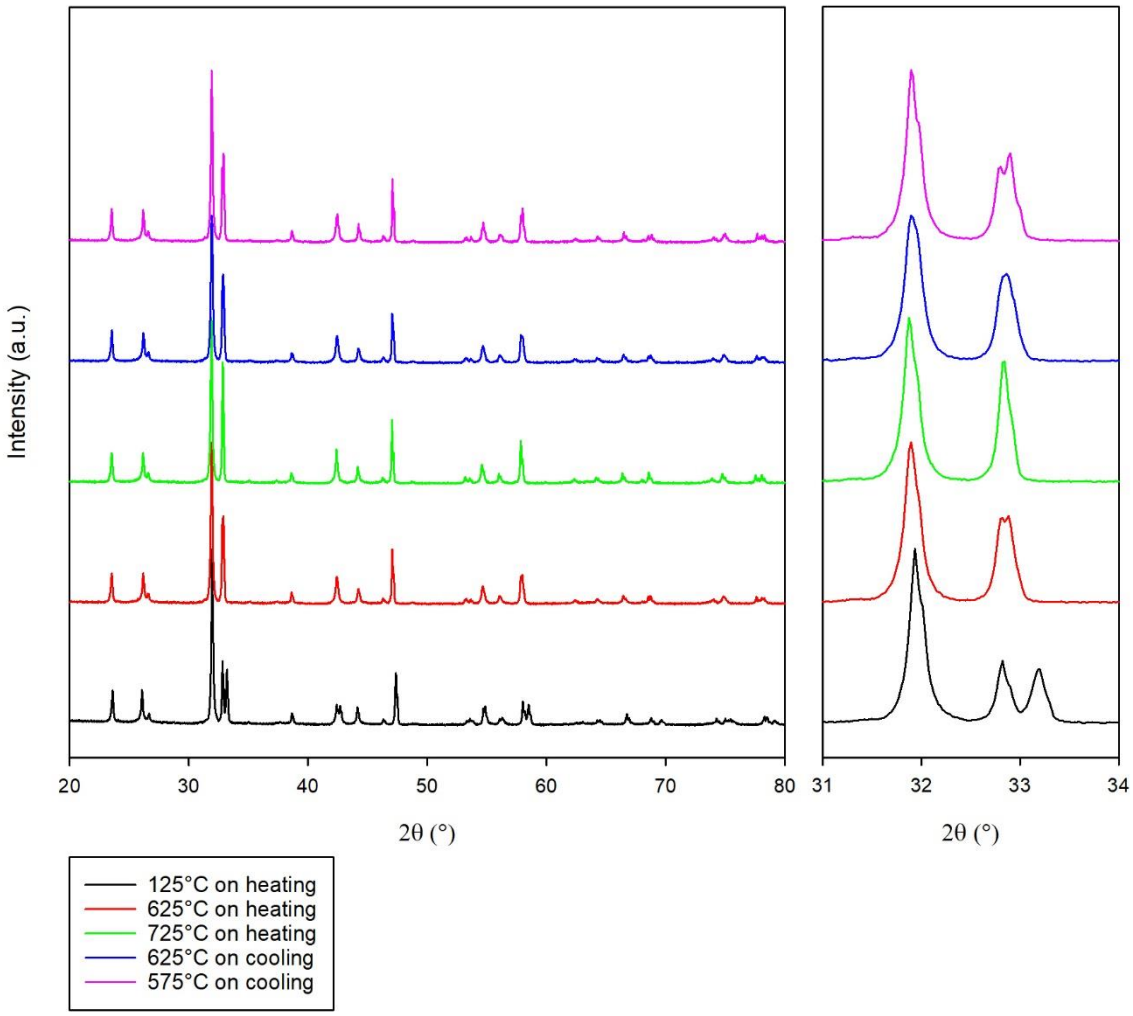


Figure 6.22: VT-XRD pattern of humid $La_{2.5}Pr_{0.5}Ni_2O_{7-\delta}$ showing phase change, from orthorhombic to tetragonal, during heating. Specifically, peaks between 32.5° and 33.5° form a singular peak. During cooling the tetragonal phase reverts to an orthorhombic structure. In ascending order, the temperatures are 125°C on heating (black), 625°C on heating (red), 725°C on heating (green), 625°C on cooling (blue) 575°C on cooling (pink).

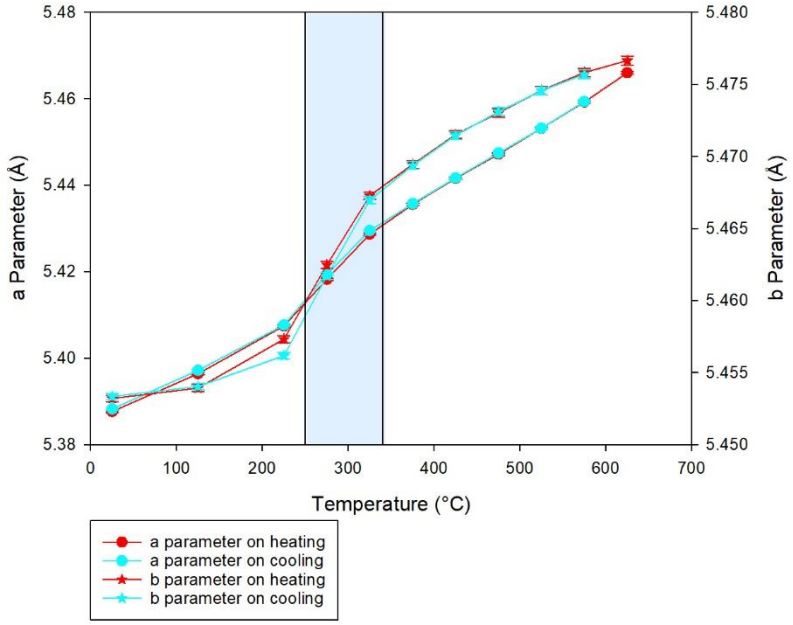


Figure 6.23: VT-XRD data showing the variation in *a* (circle) and *b* (star) parameter of humidified $La_{2.5}Pr_{0.5}Ni_2O_{7-\delta}$ versus temperature. Slight deviations in linearity are highlighted in blue.

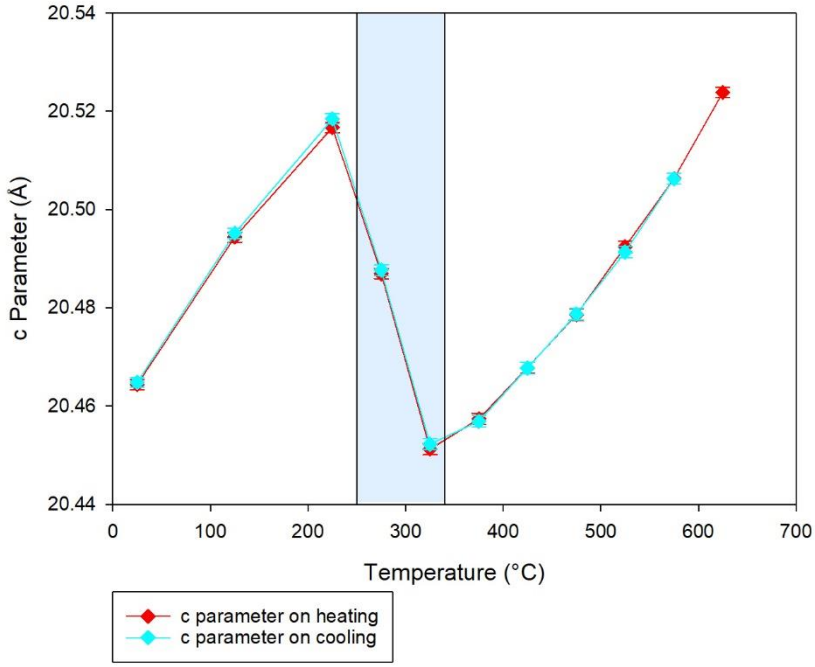


Figure 6.24: VT-XRD data showing the variantion in *c* parameter of humidified $La_{2.5}Pr_{0.5}Ni_2O_{7-\delta}$ against temperature. Deviations in results are highlighted. Deviations in linearity are highlighted in blue.

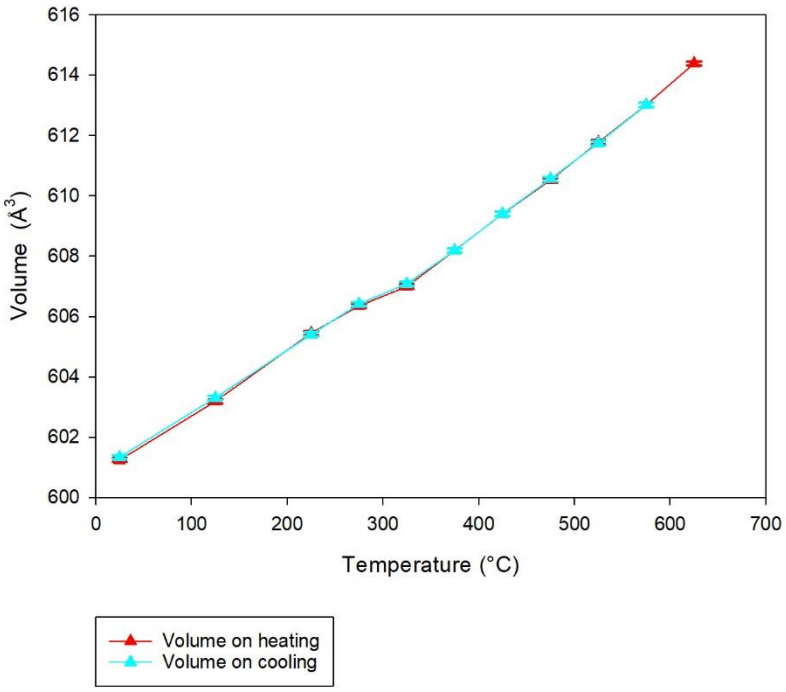


Figure 6.25: VT-XRD data showing the variation in volume of humidified $La_{2.5}Pr_{0.5}Ni_2O_{7-\delta}$ versus temperature.

On cooling, the cell symmetry changed back to the orthorhombic structure. Compared to the heating cycle this occurred at a slightly lower temperature of 575°C (Figure 6.22). Rietveld refinement of the VT-XRD patterns on cooling showed that the lattice parameters matched those when heating, for both the orthorhombic and tetragonal phase, even though H_2O and CO_2 release occurred below 600°, which may suggest that this has been negated on cooling.

6.3.2.3 $La_2PrNi_2O_{7-\delta}$

Increasing the quantity of Pr in $La_3Ni_2O_{7-\delta}$ showed the maintenance of the orthorhombic phase up to at least 775°C (Figure 6.26). While on heating the distance between the (020) and (200) peaks appears to decrease, indicating a reduction in orthorhombic splitting. The transition to a tetragonal cell is not seen within the temperatures studied. At 775°C there still appears to be a shoulder on the peak located between 32° and 33°, suggesting the sample is still orthorhombic.

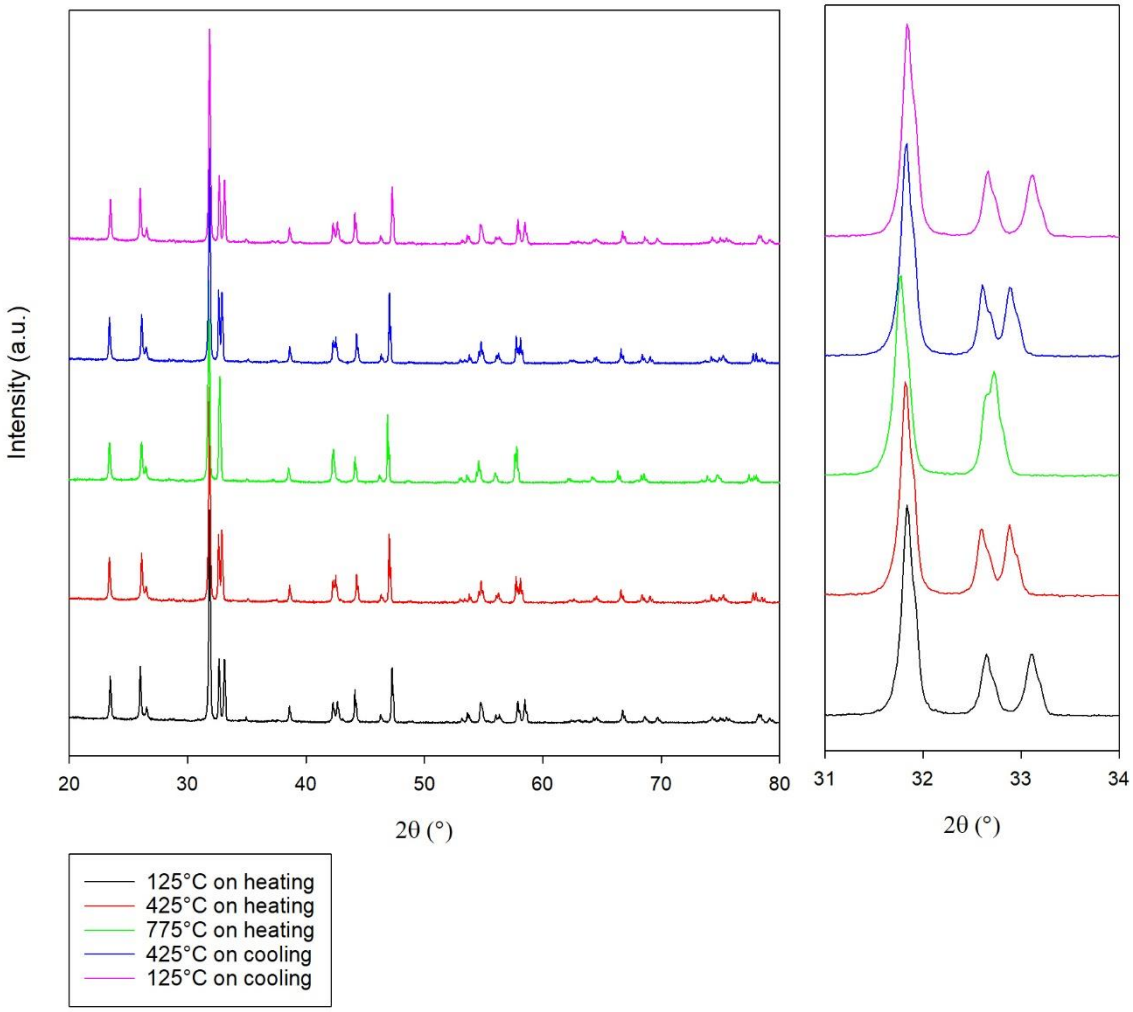


Figure 6.26: VT-XRD pattern of humid $La_2PrNi_2O_{7-\delta}$. Sample is orthorhombic at lower temperatures. During heating the distance between 32.5° and 33.5° peaks reduced. During cooling the previously mentioned peaks separated. In ascending order the temperatures are 125°C on heating (black), 425°C on heating (red), 775°C on heating (green), 425°C on cooling (blue) 125°C on cooling (pink).

Similar lattice parameter changes were observed for $La_{2.5}Pr_{0.5}Ni_2O_{7-\delta}$, which also aligns to H_2O and CO_2 loss seen in TGA/MS data. The *a* parameter during cooling was the same as when heating (Figure 6.27), although this was not the case for the *b* and *c* parameter (Figure 6.28). On cooling, these values were thought to be greater due to the loss of various gaseous species, as shown by TGA/MS data.

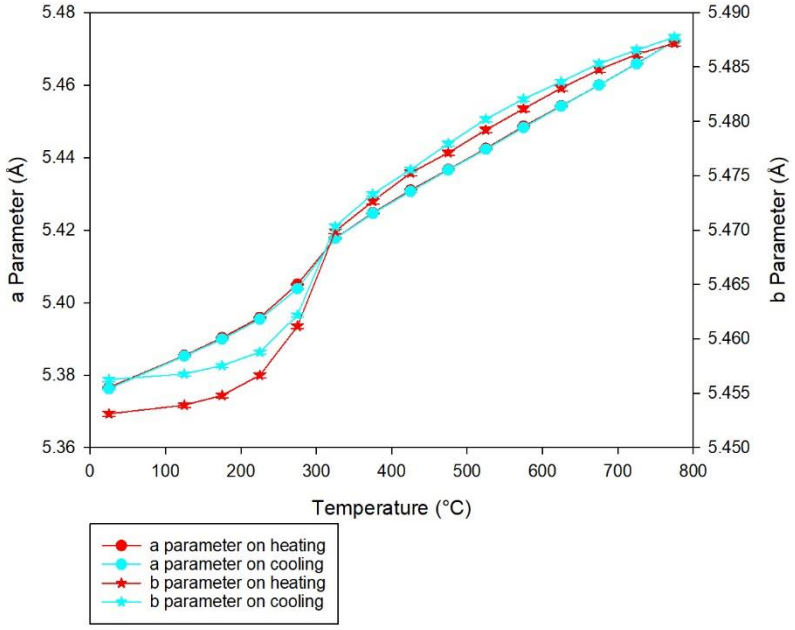


Figure 6.27: VT-XRD data showing the variation in *a* (circle) and *b* (star) parameters of humidified $La_2PrNi_2O_{7-\delta}$ versus temperature. Red fill indicates heating and cyan fill indicates cooling.

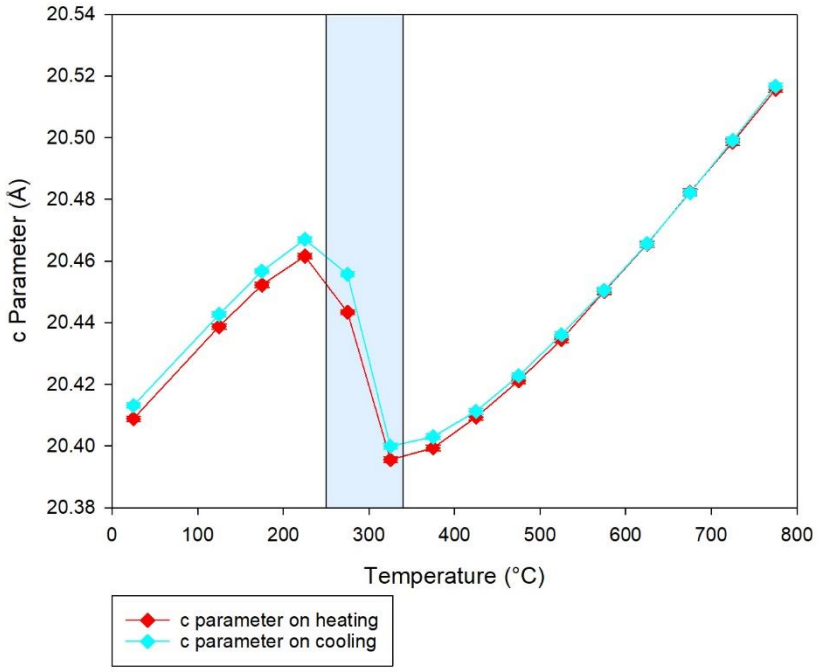


Figure 6.28: VT-XRD data showing the variantion in *c* parameter of humidified $La_2PrNi_2O_{7-\delta}$ versus temperature. Deviations in linearity of results are highlighted in blue.

It could be seen through VT-XRD, that the symmetry of $La_3Ni_2O_{7-\delta}$ changed at 325°C, to the increase Pr dopant on the A site increased the temperature at which this transition occured, Pr doped samples also saw the *c* parameter decrease between 275°C and 325°C, coinciding with H_2O and CO_2 loss. The same deviations are not observed in the unit volume (Figure 6.29).

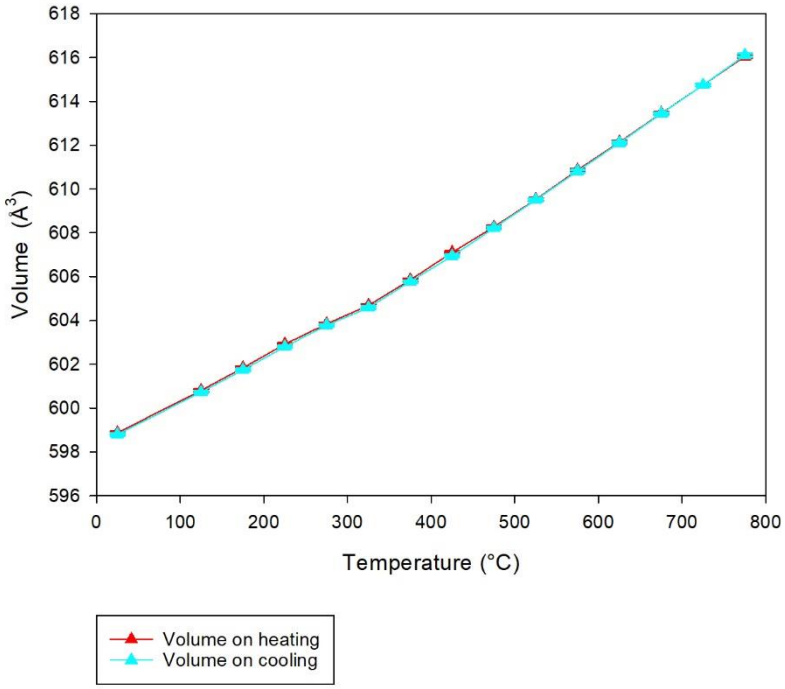


Figure 6.29: VT-XRD data showing the variation in volume of humidified $La_2PrNi_2O_{7-\delta}$ versus temperature.

6.3.3 Conductivity Data

$La_{3-x}Pr_xNi_2O_{7-\delta}$ (x=0, 0.25, 0.5 and 1) all showed a similar trend in conductivity with increasing temperature (Figure 6.30) which was consistent with results observed by Takahashi *et al.* [213]. Pr doping led to a decrease in conductivity at lower temperatures. Doping a Pr content of x=0.25 and 0.5 caused a small increase in conductivity at higher temperatures (Table 6.8). However, the increase was small, so could be a result of improved sintering with increasing Pr content. Further increasing Pr to form $La_2PrNi_2O_{7-\delta}$, gave the lowest conductivity of all samples. Some discrepancy was observed between the heating and cooling conductivity for the samples with the higher Pr content. As the biggest

variation could be seen for the $La_2PrNi_2O_{7-\delta}$ it was assumed that the doped Pr on the A-site was a contributing factor for the variation.

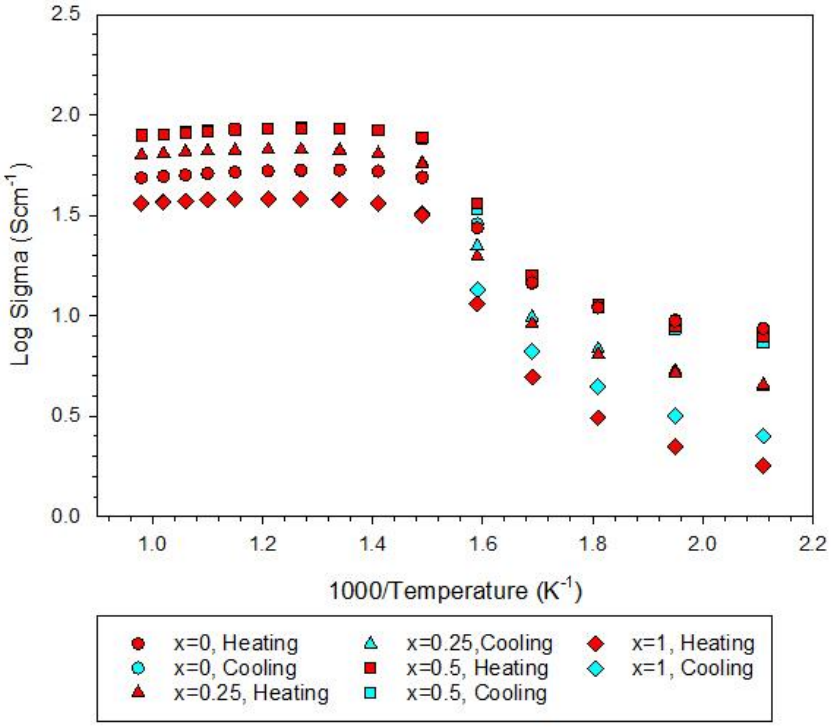


Figure 6.30: Conductivity data for $La_{3-x}Pr_xNi_2O_{7-\delta}$ where x=0 (circle), 0.25 (triangle) and 0.5 (square) and 1 (diamond). Red fill indicates heating and cyan fill indicates cooling, data shown between 200°C and 750°C.

Table 6.8: Conductivity for $La_{3-x}Pr_xNi_2O_{7-\delta}$ where x=0, 0.25, 0.5 and 1, conductivity at 200°C, 239°C, 554°C and 750°C.

Composition	**Conductivity (Scm^{-1})**			
	200°C (2.11K^{-1})	239°C (1.95 K^{-1})	554°C (1.21 K^{-1})	750°C (0.98 K^{-1})
$La_3Ni_2O_{7-\delta}$	8.63	9.41	52.67	48.67
$La_{2.75}Pr_{0.25}Ni_2O_{7-\delta}$	4.57	5.21	67.34	63.48
$La_{2.5}Pr_{0.5}Ni_2O_{7-\delta}$	7.84	8.93	85.59	79.50
$La_2PrNi_3O_{7-\delta}$	1.79	2.24	38.25	36.32

6.3.4 Conclusion

Pr was successfully doped onto the lanthanum site of $La_3Ni_2O_{7-\delta}$, with quantities of 0.25, 0.5 and 1. All samples showed an orthorhombic unit cell. When the samples were heated in various conditions, varying effects were observed, as shown in Table 6.9. VT-XRD was performed on $La_{3-x}Pr_xNi_2O_{7-\delta}$ where x = 0, 0.5 and 1 after they were heated in humid N_2. Increasing the quantity of La substituted by Pr caused the orthorhombic-tetragonal cell change to occur at higher temperatures. The doped samples also showed a decrease in the *c* parameter, during heating, which correlated to loss of H_2O and CO_2 detected by TGA/MS. $La_{2.5}Pr_{0.5}Ni_2O_{7-\delta}$ showed the highest electrical conductivity of all sample (85.59 S cm^{-1}).

Table 6.9: Summary of the effect of different heating conditions on $La_{3-x}Pr_xNi_2O_{7-\delta}$ (x=0, 0.25, 0.5 and 1) as well as H_2O loss (below 600°C) of humid samples and maximum electrical conductivity.

Composition	Effect of humid N_2	Effect of dry N_2	Effect of humid O_2	Maximum H_2O loss of humid N_2 sample below 600°C (mol)	Maximum Electrical Conductivity (Scm^{-1})
$La_3Ni_2O_{7-\delta}$	Chemically stable	Chemically stable	Chemically stable	0.032	52.67
$La_{2.75}Pr_{0.25}Ni_2O_{7-\delta}$	Preferred orientation along {00l} plane	Chemically stable	Preferred orientation along {00l} plane	0.044	67.34
$La_{2.5}Pr_{0.5}Ni_2O_{7-\delta}$	Chemically stable	Sample degraded	Preferred orientation along {00l} plane	0.013	85.59
$La_2PrNi_2O_{7-\delta}$	Chemically stable	Chemically stable	Chemically stable	0.023	38.25

6.4 Pr doped $La_4Ni_3O_{10-\delta}$; $La_{4-x}Pr_xNi_3O_{10-\delta}$

$La_{4-x}Pr_xNi_3O_{10-\delta}$ where x=0, 0.25, 0.5 and 0.75 were synthesised and XRD performed on all samples (Figure 6.31). Rietveld refinement of $La_4Ni_3O_{10-\delta}$ was performed against an orthorhombic *Fmmm* space group (Figure 6.32), similar to previously stated in literature [135, 209, 219, 233, 238], with an aim of achieving a good fit and an R_{wp} of 10% or less. Rietveld refinement, using the same space group, was

performed on all other samples. The stoichiometric quantity of La was substituted for Pr on the A site, during refinement, to account of Pr doping. Lattice parameters are shown in Table 6.10.

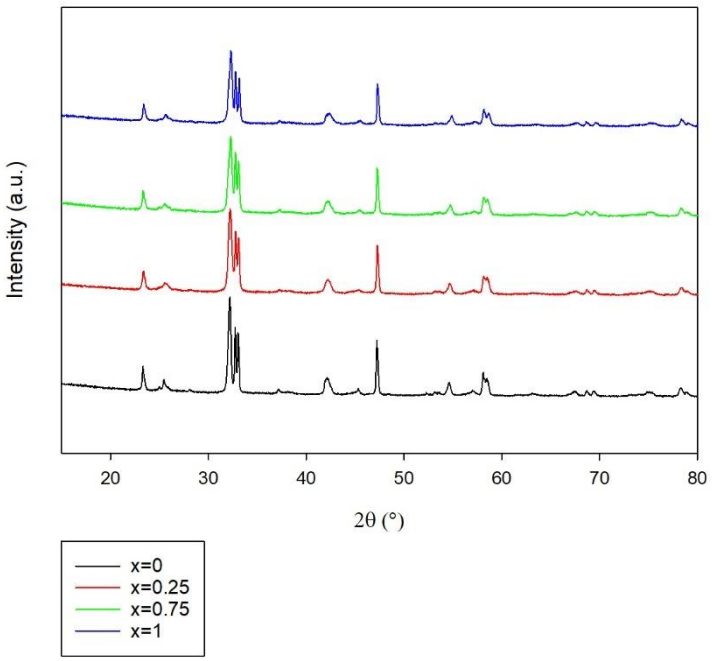


Figure 6.31: XRD pattens of $La_{4-x}Pr_xNi_3O_{10-\delta}$ samples where x =0, 0.5 and 0.75 and 1. In ascending order $La_4Ni_3O_{10-\delta}$ (black), $La_{3.75}Pr_{0.25}Ni_3O_{10-\delta}$ (red), $La_{3.5}Pr_{0.5}Ni_3O_{10-\delta}$ (green) and $La_3PrNi_3O_{10-\delta}$ (blue).

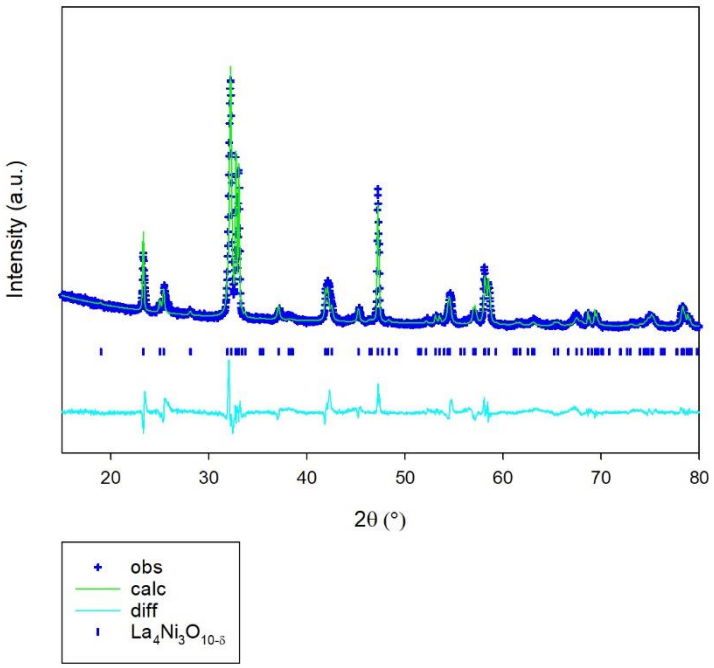


Figure 6.32: Example of observed (blue cross), calculated (green) and difference (cyan) profiles for Rietveld refinement performed on $La_4Ni_3O_{10-\delta}$ (orthorhombic *Fmmm* space group, R_{wp}=10.00%).

Introduction of a small quantity of Pr, x=0.25, showed a decrease in lattice parameters (Table 6.10), due to the smaller ionic radius of Pr^{3+} (1.179 Å) to that of La^{3+} (1.216 Å). Further increasing the quantity of Pr continued to show a decrease in the *a* and *c* parameter (Figure 6.33 and Figure 6.34), however, there was an increase in the *b* parameter. Zhang *et al.* [219] had previously noted that decreasing the ionic radius of the A site cation led to a greater difference between the a and b parameters, which was described as the orthorhombic strain (s), shown by equation (3.1).

$$s = 2\left(\frac{b-a}{b+a}\right) \qquad (6.1)$$

The value for orthorhombic strain for Ruddlesden-Popper phases can be represented as follows: $Nd_4Ni_3O_{10-\delta}$> $Pr_4Ni_3O_{10-\delta}$> $La_4Ni_3O_{10-\delta}$. Similarly, Pr doping on the A site of $La_4Ni_3O_{10-\delta}$ can be seen to increase the orthorhombic strain, (Table 6.10). Despite the increase in the *b* parameter the overall volume of the unit cell continued to decrease with an increase in Pr.

Table 6.10: Lattice parameters (orthorhombic *Fmmm*) from Rietveld refinement performed on $La_{4-x}Pr_xNi_3O_{10-\delta}$ (x =0, 0.5 and 0.75 and 1) samples.

Composition	Unit Cell Parameters (Å)			Orthorhombi c Strain, s	Unit Cell Volume (Å^3)
	a	b	c		
$La_4Ni_3O_{10-\delta}$	5.4143(2)	5.4623(2)	28.0328(22)	8.83 x 10^{-3}	829.06(7)
$La_{3.75}Pr_{0.25}Ni_3O_{10-\delta}$	5.4122(3)	5.4612(3)	28.0140(28)	9.01 x 10^{-3}	828.01(9)
$La_{3.5}Pr_{0.5}Ni_3O_{10-\delta}$	5.4096(2)	5.4615(2)	27.9732(30)	9.54 x 10^{-3}	826.46(9)
$La_3PrNi_3O_{10-\delta}$	5.4029(3)	5.4642(3)	27.9528(26)	1.12 x 10^{-2}	825.23(8)

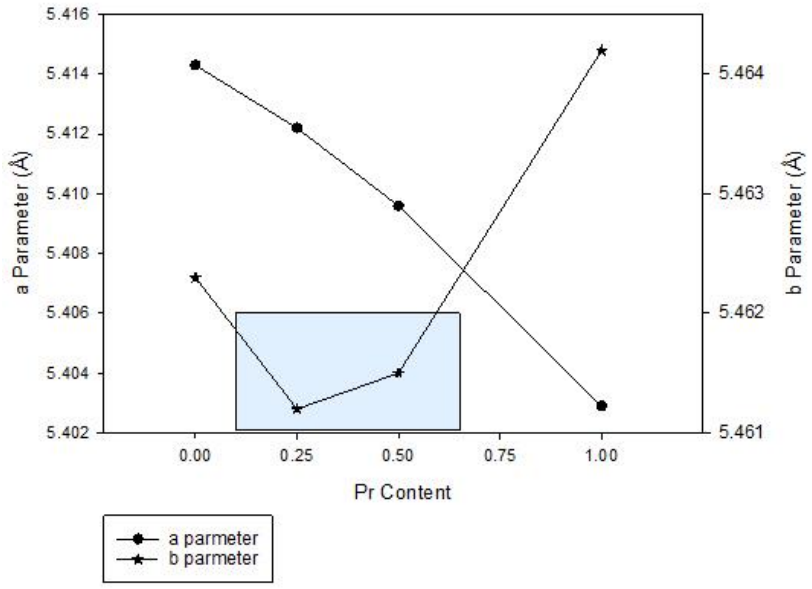


Figure 6.33: Variation of *a* (circle) and *b* (star) lattice parameters for $La_{4-x}Pr_xNi_3O_{10-\delta}$ (x=0, 0.25, 0.5 and 1). Black circles indicate a parameter. Black stars indicate *b* parameter. The highlighted region shows an initial decrease in the *b* parameter.

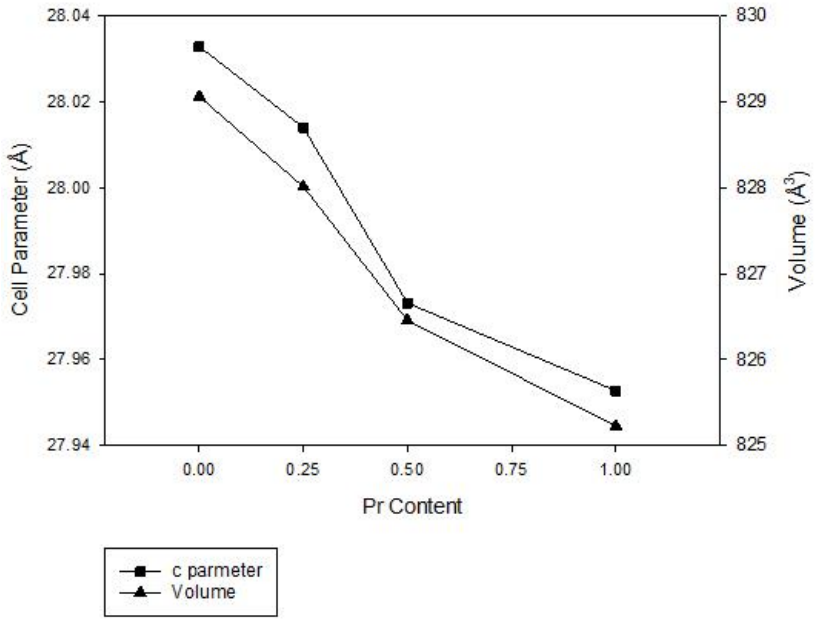


Figure 6.34: Variation of *c* lattice parameter and volume for $La_{4-x}Pr_xNi_3O_{10-\delta}$ (x=0, 0.25, 0.5 and 1). Black squares indicate *c* parameter. Black triangles indicate volume.

6.4.1 Investigation of Heating under Humid Nitrogen, Dry Nitrogen and Humid Oxygen

6.4.1.1 $La_4Ni_3O_{10-\delta}$

XRD analysis and Rietveld refinement were performed on $La_4Ni_3O_{10-\delta}$ samples heated in dry N_2, humid N_2 and O_2 (Figure 6.35 and Table 6.11). Heating the samples in humid conditions, regardless of whether they were heated in N_2 or O_2, led to a decrease in the cell volume of the samples. The change in volume exceeded the experimental error, from the Rietveld refinement. The decrease was assumed to be due to the presence of H_2O in the humid N_2, as heating in dry N_2 appeared to have the opposite effect. On heating in dry N_2, the volume has increased due to the reduction of Ni^{3+} to Ni^{2+} [237].

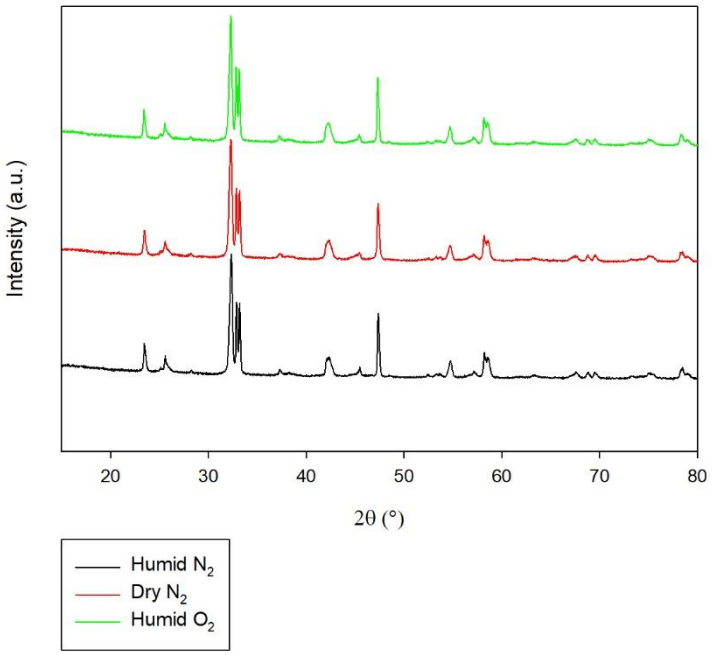


Figure 6.35: XRD patterns of $La_4Ni_3O_{10-\delta}$ heated in various conditions. In ascending order humid N_2 (black), dry N_2 (red) and humid O_2 (green).

Table 6.11: Lattice parameters (orthorhombic *Fmmm*) for Rietveld refinement performed on $La_4Ni_3O_{10-\delta}$ heated in various conditions.

	Unit Cell Parameters (Å)			**Unit Cell Volume (Å^3)**
	a	b	c	
Original	5.4143(2)	5.4623(2)	28.0328(22)	829.06(7)
Humid N_2	5.4126(2)	5.4611(2)	28.0174(25)	828.17(8)
Dry N_2	5.4115(3)	5.4616(3)	28.0720(28)	829.68(8)
Humid O_2	5.4127(2)	5.4612(2)	28.0300(25)	828.56(7)

TGA/MS conducted on the humid $La_4Ni_3O_{10-\delta}$ showed some H_2O loss from 40°C onwards (Figure 6.36). Initial loss was thought to be from the surface. Further H_2O loss, between 100°C and 400°C, was thought to be from the bulk of the sample. It was estimated that 0.037 mol of H_2O was lost from the sample if no CO_2 loss is considered. The ion current for H_2O was seen to increase again after reaching 700°C,

along with the ion current for O_2, implying loss of these species. If the loss of O_2 was disregarded, a maximum 0.055 mol H_2O was lost above 700°C.

CO_2 loss (Figure 6.37) occurred between 100°C and 600°C and was estimated to be a maximum of 0.014 mol, if not considering H_2O loss. Previously shown CO_2 loss, as a result of $La_2O_2CO_3$, is suspected to have occurred above 600°C. Therefore, it was assumed that CO_2 loss was a result of CO_3^{2-} incorporation between the Ni-O layers, resulting in the composition $La_4Ni_{3-x}C_xO_{10-\delta}$ where C is CO_3^{2-},similar to previously shown Ruddlesden-Popper $Sr_4Fe_2O_6CO_3$, where CO_3^{2-} is present between the Fe-O later [239]. CO_2 within the structure was assumed to be a result of the carbon rich precursors used during synthesis [236].

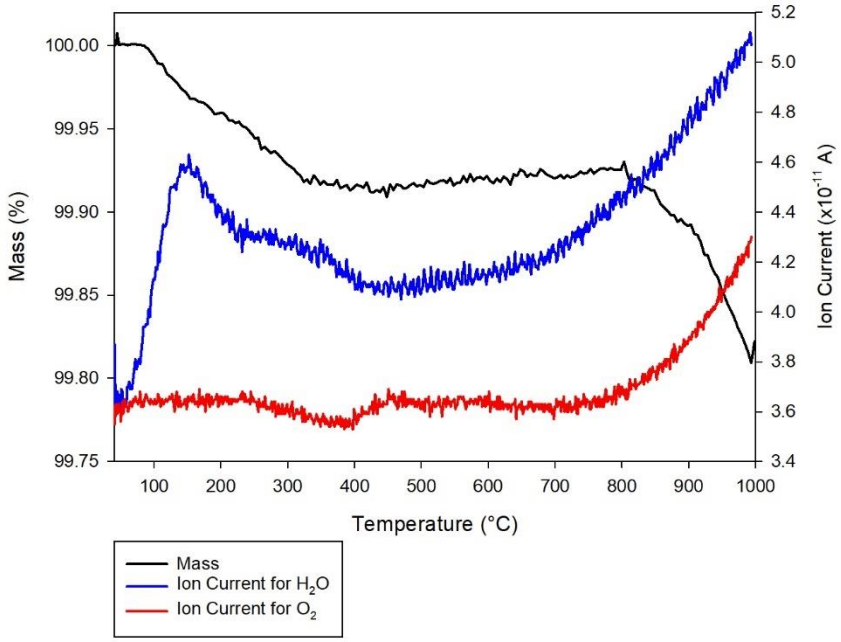


Figure 6.36: TGA and MS, up to a temperature of 1000°C, performed on $La_4Ni_3O_{10-\delta}$ heated in humid N_2. Mass loss (black), H_2O loss (blue) and O_2 loss (red).

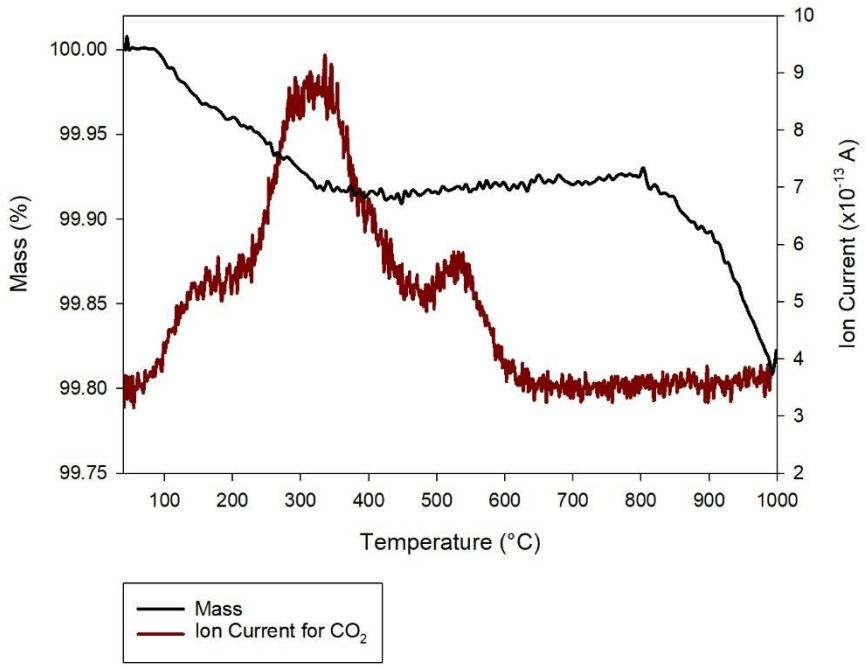


Figure 6.37: TGA and MS, up to a temperature of 1000°C, performed on $La_4Ni_3O_{10-\delta}$ heated in humid N_2. Mass loss (black) and CO_2 loss (dark red).

$La_4Ni_3O_{10-\delta}$ showed two stages of O_2 release, similar to $La_3Ni_2O_{7-\delta}$, this was between 40°C to 350°C and above 400°C. Again, O_2 is thought not to be released between 350°C and 400°C, due to O_2 being readsorbed as H_2O had been previously released.

6.4.1.2 $La_{3.75}Pr_{0.25}Ni_3O_{10-\delta}$

$La_{3.75}Pr_{0.25}Ni_3O_{10-\delta}$ samples heated in humid N_2, dry N_2 and humid O_2 (Figure 6.38) did not show any notable change in the volume of the unit cells, within experimental error (Table 6.12). However, all samples showed a decrease in the *a* and *b* parameters compared to the original sample, whilst *c* parameter increase was observed. As no increase in the overall volume was to be seen for the sample heated in dry N_2 it was assumed the ratio of Ni^{2+} and Ni^{3+} had remained unchanged.

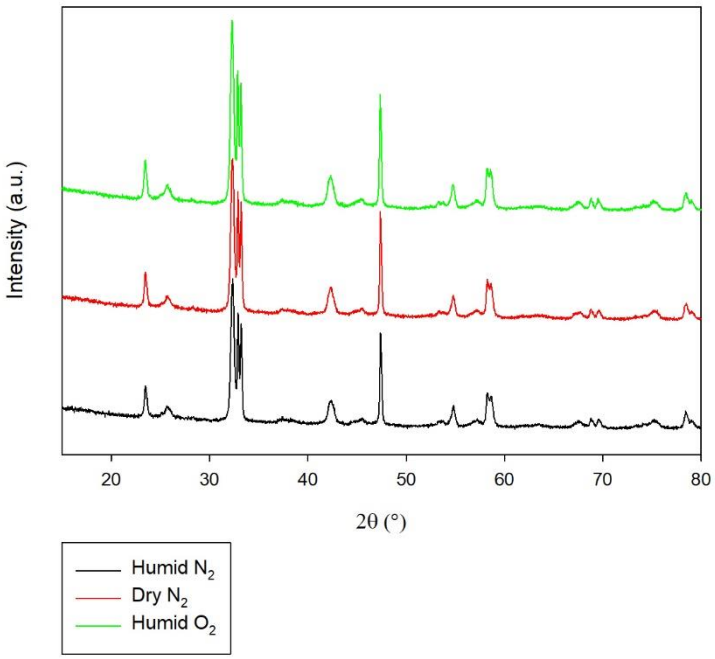


Figure 6.38: XRD patterns of $La_{3.75}Pr_{0.25}Ni_3O_{10-\delta}$ heated in various conditions. In ascending order humid N_2 (black), dry N_2 (red) and humid O_2 (green).

Table 6.12: Lattice parameters (orthorhombic *Fmmm*) for Rietveld refinement performed on $La_{3.75}Pr_{0.25}Ni_3O_{10-\delta}$ heated in various conditions.

	Unit Cell Parameters (Å)			**Unit Cell Volume (Å^3)**
	a	b	c	
Original	5.4122(3)	5.4612(3)	28.0140(28)	828.01(9)
Humid N_2	5.4109(3)	5.4610(3)	28.0226(30)	828.05(9)
Dry N_2	5.4106(3)	5.4608(3)	28.0241(29)	828.00(9)
Humid O_2	5.4107(3)	5.4607(3)	28.0193(30)	827.87(9)

Performing TGA/MS on the humid $La_{3.75}Pr_{0.25}Ni_3O_{10-\delta}$, showed the samples lose H_2O on heating (Figure 6.39). H_2O loss occurred between 40°C and 400°C, with 0.050 mol of H_2O was estimated to have been released between 100°C and 400°C. A further 0.1317 mol H_2O was estimated to be lost above 600°C, however O_2 loss also occurred at the same temperature range and therefore the actual H_2O loss value

will be lower than this estimated value. CO_2 loss (Figure 6.40) also occurred above 200°C, which was estimated to be a maximum of 0.020 mol. Similar to the previously studied $La_4Ni_3O_{10-\delta}$, CO_3^{2-} was expected to be located within the Ni-O layers and was thought to be a result of the carbon precursors used during synthesis causing carbonate impurities [236, 239].

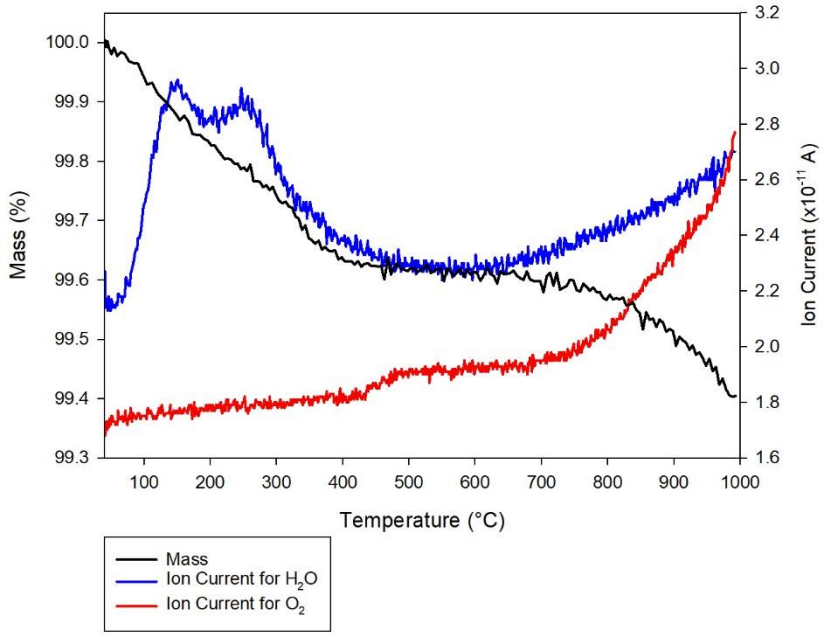


Figure 6.39: TGA and MS, up to a temperature of 1000°C, performed on $La_{3.75}Pr_{0.25}Ni_3O_{10-\delta}$ heated in humid N_2. Mass loss (black), H_2O loss (blue) and O_2 loss (red).

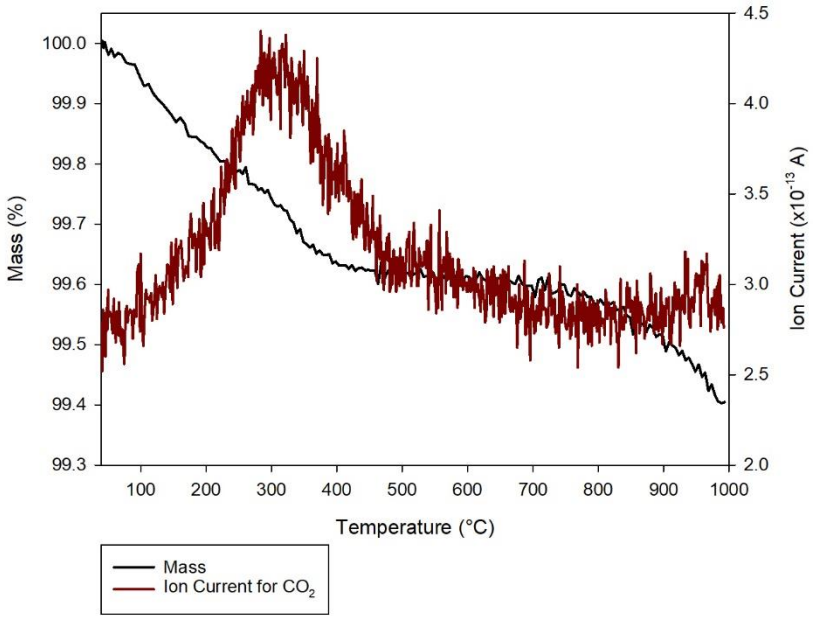


Figure 6.40: TGA and MS, up to a temperature of 1000°C, performed on $La_{3.75}Pr_{0.25}Ni_3O_{10-\delta}$ heated in humid N_2. Mass loss (black) and CO_2 loss (dark red).

6.4.1.3 $La_{3.5}Pr_{0.5}Ni_3O_{10-\delta}$

$La_{3.5}Pr_{0.5}Ni_3O_{10-\delta}$ samples heated in humid N_2 (Figure 6.41) were shown to degrade into $(La/Pr)_4Ni_3O_{10-\delta}$ and $(La/Pr)_2NiO_{4+\delta}$ (Figure 6.42). XRD patterns of the samples heated in humid O_2 and dry N_2 did not show this degradation. When heated in humid O_2 (Figure 6.41) the lattice parameters were the same as the original sample (Table 6.13). Heating $La_{3.5}Pr_{0.5}Ni_3O_{10-\delta}$ in dry N_2 (Figure 6.42) saw an increase in the volume of the cell, thought to be through the reduction of Ni^{3+} to Ni^{2+} as a result of low oxygen partial pressures [237]. The humid N_2 sample was thought to have degraded as a result of the slightly reducing conditions from the low oxygen partial pressures and the humidity.

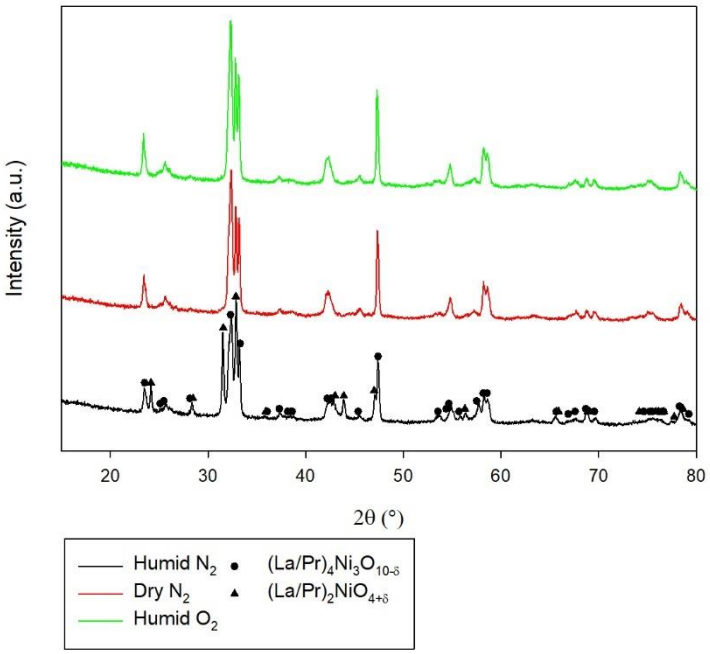


Figure 6.41: XRD patterns of $La_{3.5}Pr_{0.5}Ni_3O_{10-\delta}$ heated in various conditions. In ascending order humid N_2 (black), dry N_2 (red) and humid O_2 (green). $La_4Ni_3O_{10-\delta}$ phase shown by black circle, $Pr_2NiO_{4-\delta}$ shown by black triangle.

Table 6.13; Lattice parameters (orthorhombic *Fmmm*) for Rietveld refinement performed on $La_{3.5}Pr_{0.5}Ni_3O_{10-\delta}$ heated in various conditions.

	Unit Cell Parameters (Å)			**Unit Cell**
	a	b	c	**Volume (Å^3)**
Original	5.4096(2)	5.4615(2)	27.9732(30)	826.46(9)
Dry N_2	5.4095(2)	5.4626(2)	27.9796(32)	826.80(10)
Humid O_2	5.4097(2)	5.4616(2)	27.9737(30)	826.50(9)

6.4.1.4 $La_3PrNi_3O_{10-\delta}$

Heating of $La_3PrNi_3O_{10-\delta}$ in humid N_2, dry N_2 and humid O_2 saw little change in XRD patterns (Figure 6.42). The lattice parameters of the samples heated in the various conditions saw little change, especially when considering experimental errors. However, performing TGA/MS on the humid sample showed H_2O loss (Figure 6.43) between 100°C and 400°C, estimated to be a maximum of 0.089 mol, and H_2O loss above 700°C, estimated to be a maximum of 0.1099 mol. Once again loss of H_2O and CO_2 (Figure

6.43 and Figure 6.45) overlapped one another. CO_2 loss was determined to be less than 0.050 mol. CO_2 incorporation has possibly occurred due to the carbon rich precursors causing impurities [236].

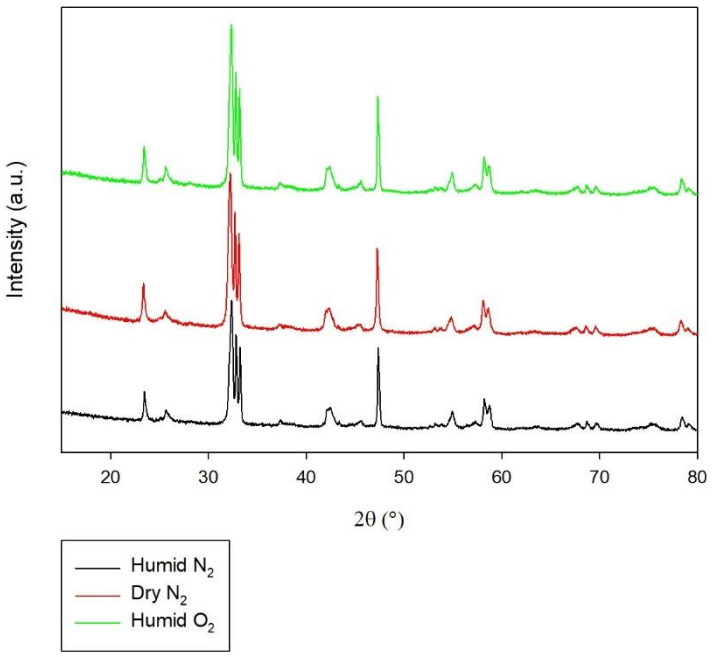


Figure 6.42: XRD patterns of $La_3PrNi_3O_{10-\delta}$ heated in various conditions. In ascending order humid N_2 (black), dry N_2 (red) and humid O_2 (green).

Table 6.14: Lattice parameters (orthorhombic *Fmmm*) for Rietveld refinement performed on $La_3PrNi_3O_{10-\delta}$ heated in various conditions.

	Unit Cell Parameters (Å)			**Unit Cell**
	a	b	c	**Volume (Å³)**
Original	5.4029(3)	5.4642(3)	27.9528(26)	825.23(8)
Humid N_2	5.4024(3)	5.4642(3)	27.9555(29)	825.24(9)
Dry N_2	5.4029(3)	5.4687(3)	28.0030(27)	827.40(9)
Humid O_2	5.4041(3)	5.4649(3)	27.9403(23)	825.15(8)

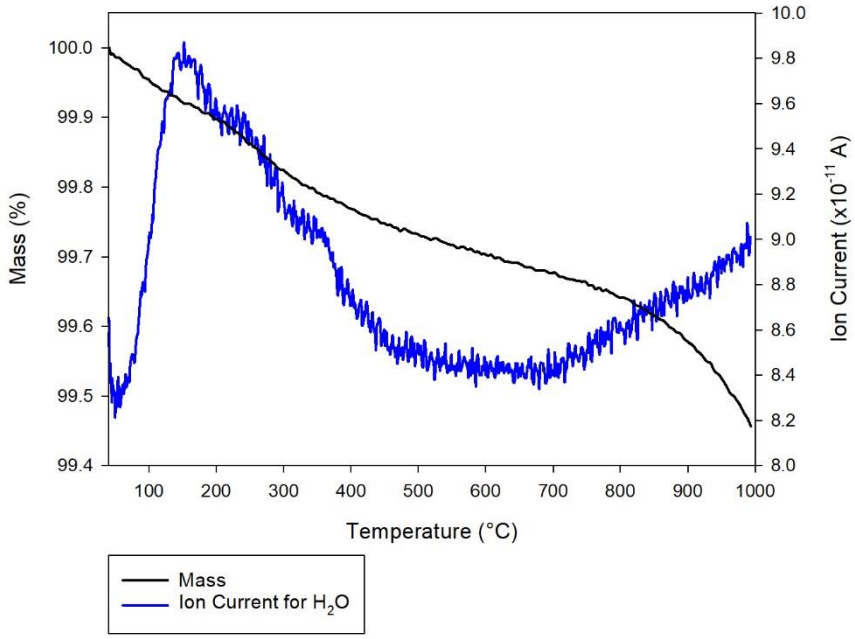


Figure 6.43: TGA and MS, up to a temperature of 1000°C, performed on $La_3PrNi_3O_{10-\delta}$ heated in humid N_2. Mass loss (black) and H_2O loss (blue).

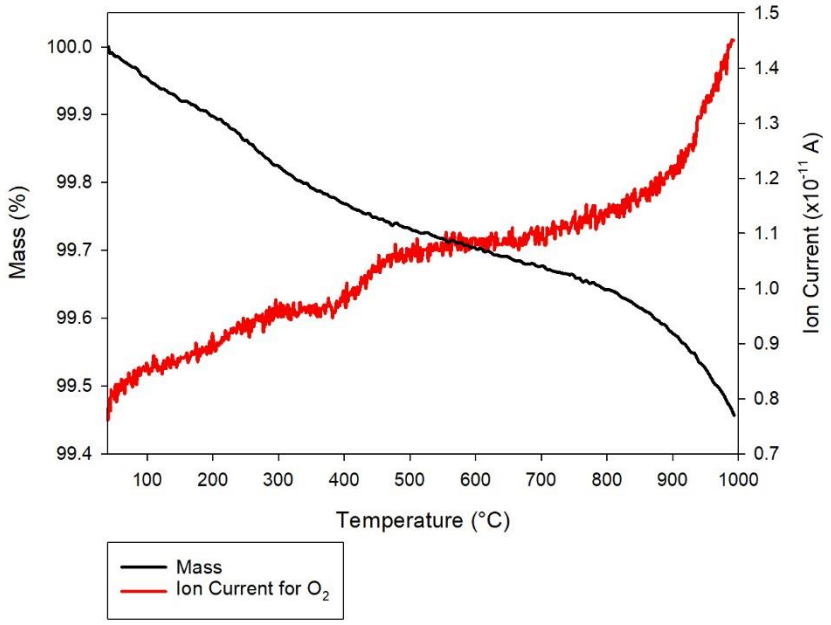


Figure 6.44: TGA and MS, up to a temperature of 1000°C, performed on $La_3PrNi_3O_{10-\delta}$ heated in humid. Mass loss (black) and O_2 loss (red).

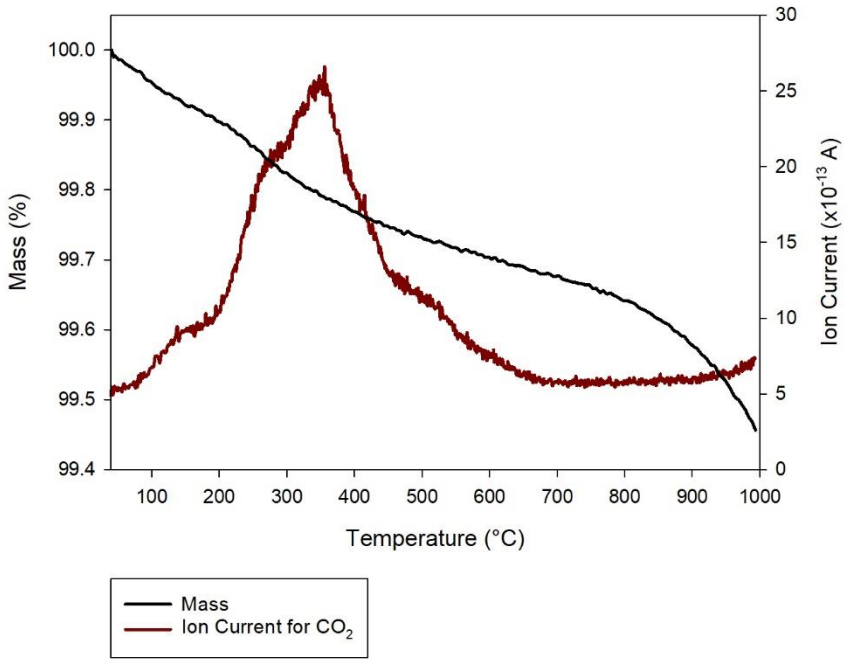


Figure 6.45: TGA and MS, up to a temperature of 1000°C, performed on $La_3PrNi_3O_{10-\delta}$ heated in humid N_2. Mass loss (black) and CO_2 loss (dark red).

Overall, $La_4Ni_3O_{10-\delta}$, $La_{3.75}Pr_{0.25}Ni_3O_{10-\delta}$ and $La_3PrNi_3O_{10-\delta}$ remained stable in humid N_2, humid O_2 and dry N_2. In contrast $La_{3.5}Pr_{0.5}Ni_3O_{10-\delta}$ degraded in humid N_2. Further work is required to understand the cause of this anomaly. $La_4Ni_3O_{10-\delta}$ showed varying changes in lattice parameters when annealed in the various atmospheres. In humid conditions the volume decreased while in dry conditions it increased. $La_{3.75}Pr_{0.25}Ni_3O_{10-\delta}$ and $La_3PrNi_3O_{10-\delta}$ showed no change in lattice parameters, when heated in humid N_2.

6.4.2 Analysis of Variable Temperature XRD on Samples treated in a Humid Atmosphere

VT-XRD was performed on all samples that showed no degradation when heated in humid N_2. Initial analysis of all XRD patterns showed that on heating there was a shift to lower 2θ values, suggesting an increase in the size of the unit cell. For all samples there was a decrease in the distance between the (020) and (200) peaks, on heating an indication that the difference between the *a* and *b* parameters was decreasing. Eventually the doublets formed a singular peak, implying a change from an orthorhombic to tetragonal structure. Previous studies regarding $La_4Ni_3O_{10-\delta}$ have shown this phase change at varying

temperatures [135, 218]. $Pr_4Ni_3O_{10-\delta}$ is able to maintain its original phase up to 1000°C, hence doping Pr may be the cause of the change in symmetry occurring at higher temperatures [218].

6.4.2.1 $La_4Ni_3O_{10-\delta}$

VT-XRD of $La_4Ni_3O_{10-\delta}$ shows a complete phase change from orthorhombic to tetragonal at 425°C (Figure 6.46), a lower temperature than previously stated within literature [135, 218]. Throughout the VT-XRD measurements an increase in all parameters was observed (Figure 6.47 to Figure 6.49). After the change in phase, the sample continued to show an increase in all lattice parameters. The sequential refinement did not show any noticeable change that would indicate H_2O or CO_2 loss although, that was identified from TGA/MS.

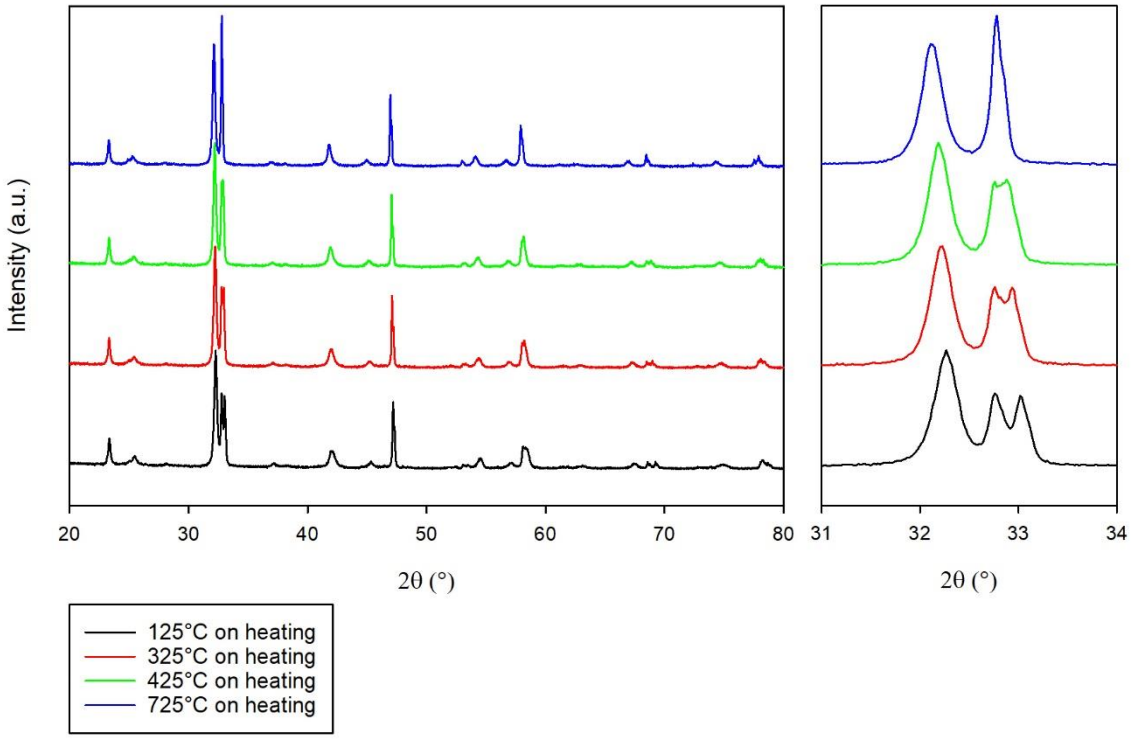


Figure 6.46: VT-XRD pattern of humid $La_4Ni_3O_{10-\delta}$ showing phase change, from orthorhombic to tetragonal, during heating. Specifically, peaks between 32.5° and 33.5° form a singular peak. In ascending order the temperatures are 125°C on heating (black), 325°C on heating (red), 425°C on heating (green) and 725°C on heating (blue).

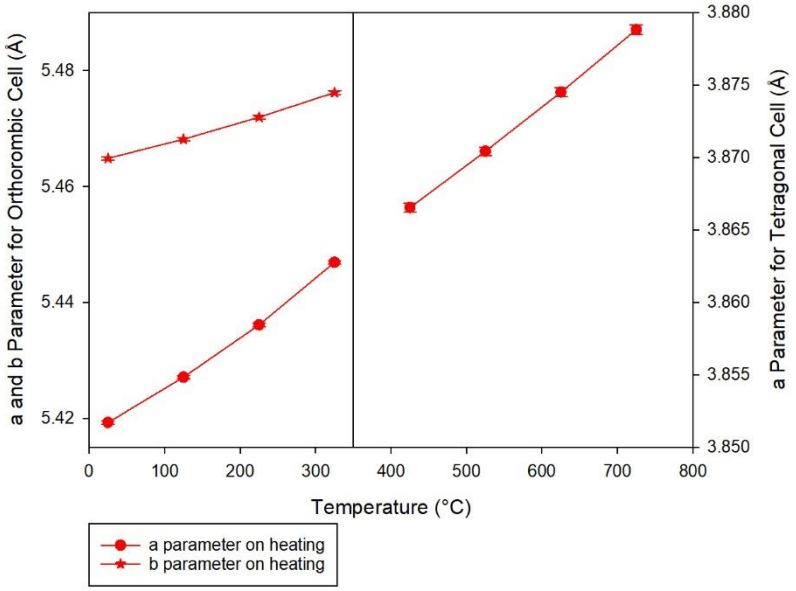


Figure 6.47: VT-XRD data showing the variation in *a* (circle) and *b* (star) parameter of humidifed $La_4Ni_3O_{10-\delta}$ versus temperature. At 425°C, the orthorhombic phase turns tetragonal. A black line is drawn to show this split in symmetry.

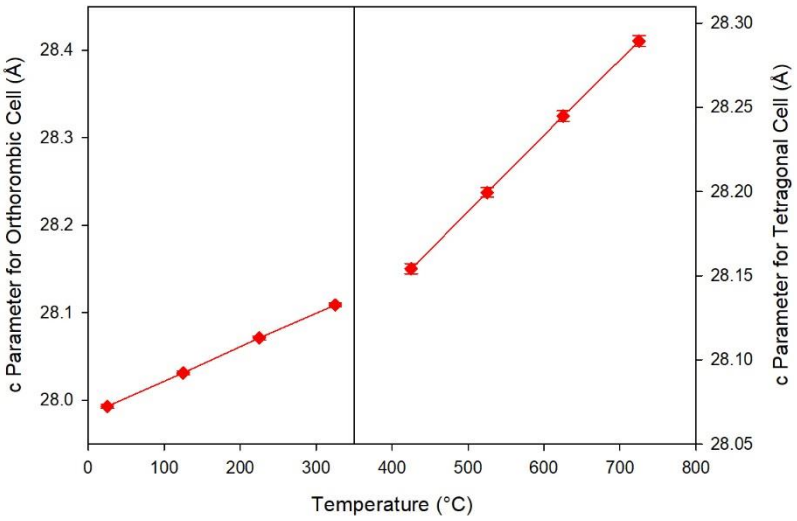


Figure 6.48: VT-XRD data showing the variation in *c* parameter of humidifed $La_4Ni_3O_{10-\delta}$ versus temperatures. At 425°C, the orthorhombic phase turns tetragonal. A black line is drawn to show this change in symmetry.

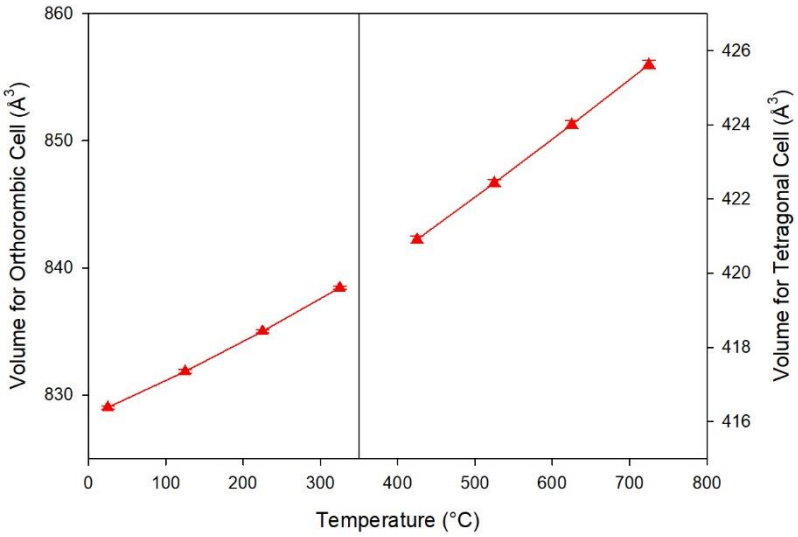


Figure 6.49: VT-XRD data showing the variation in volume (triangle) of humidifed $La_4Ni_3O_{10-\delta}$ versus temperatures. At 425°C, the orthorhombic phase turns tetragonal. A black line is drawn to show this change in symmetry.

6.4.2.2 $La_{3.75}Pr_{0.25}Ni_3O_{10-\delta}$

VT-XRD performed on humid $La_{3.75}Pr_{0.25}Ni_3O_{10-\delta}$ showed a phase change occurring at 425°C (Figure 6.50). Sequential refinement showed a general increase in all lattice parameters (Figure 6.51 to Figure 6.53), which was expected from thermal expansion. A closer look at the lattice parameters showed that at a temperature of 225°C and 275°C the *c* parameter was near identical when considering experimental errors, 28.0846 Å ± 0.0030 Å and 28.0863 Å ± 0.0034 Å, respectively. At these temperatures, H_2O and CO_2 lost would have been expected to have begun. Despite this, the volume increased between these two temperature points. This was thought to be due to the other parameters of the cell compensating for the change.

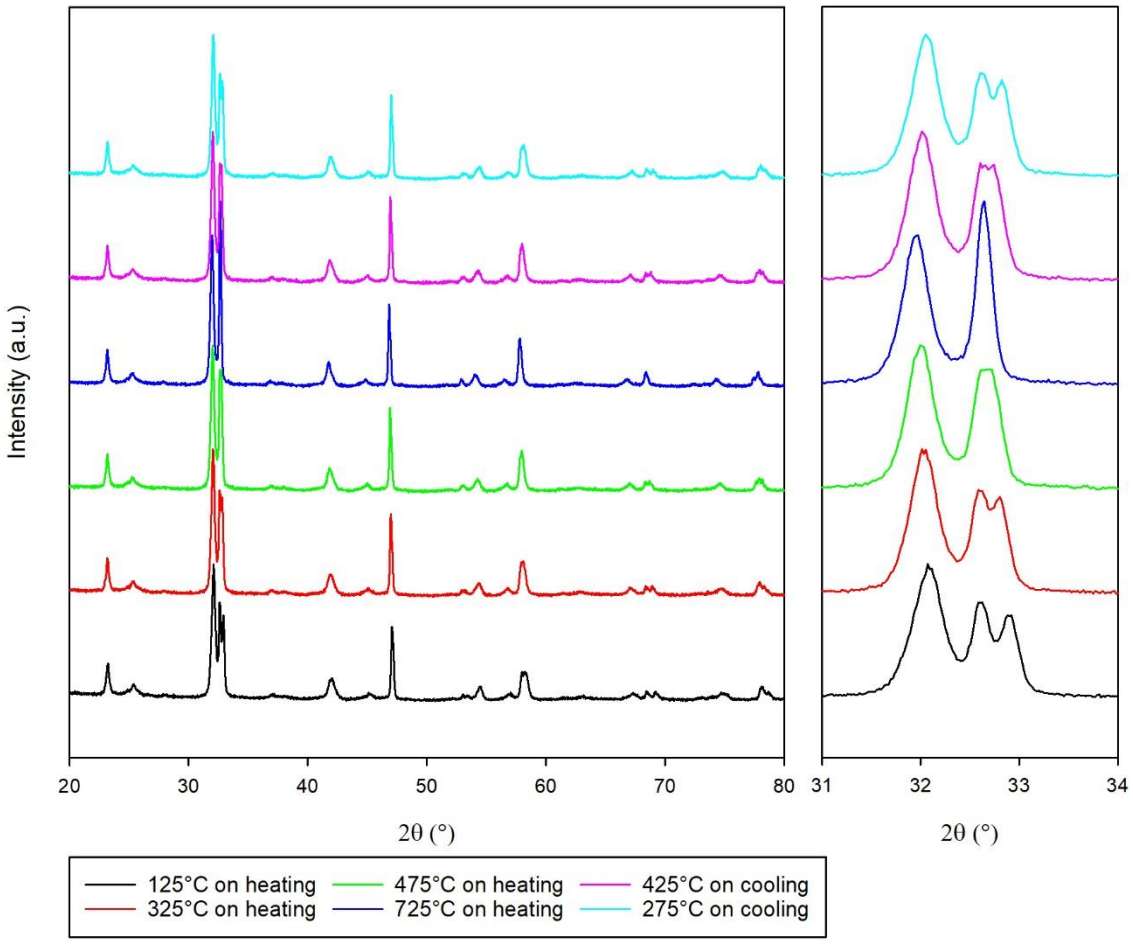


Figure 6.50: VT-XRD pattern of humid $La_{3.75}Pr_{0.25}Ni_3O_{10-\delta}$ showing phase change, from orthorhombic to tetragonal, during heating. Specifically, peaks between 32.5° and 33.5° form a singular peak. During cooling the tetragonal phase reverted to an orthorhombic structure. In ascending order the temperatures are 125°C on heating (black), 325°C on heating (red), 475°C on heating (green), 725°C on heating (blue), 425°C on cooling (pink) and 275°C on cooling (cyan).

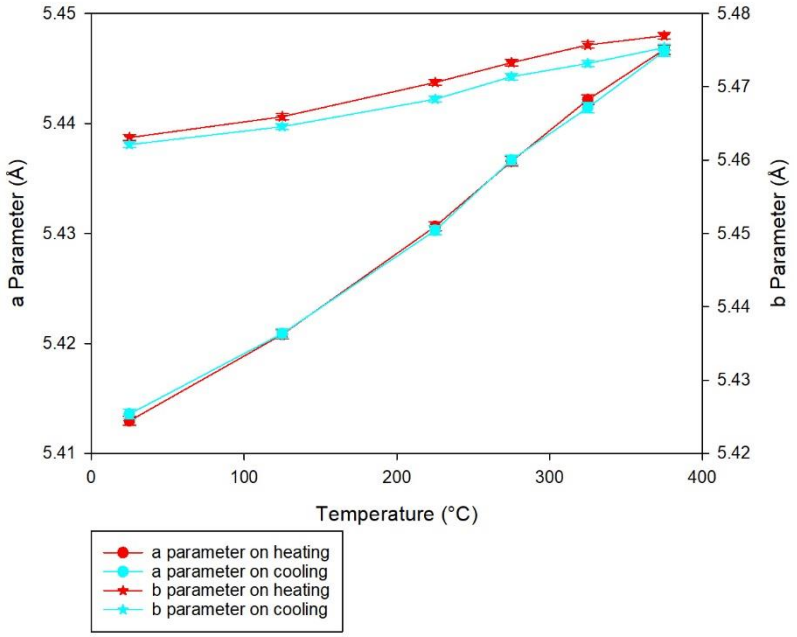


Figure 6.51: VT-XRD data showing the variation in *a* (circle) and *b* (star) parameter of humidified $La_{3.75}Pr_{0.25}Ni_3O_{10-\delta}$ versus temperature.

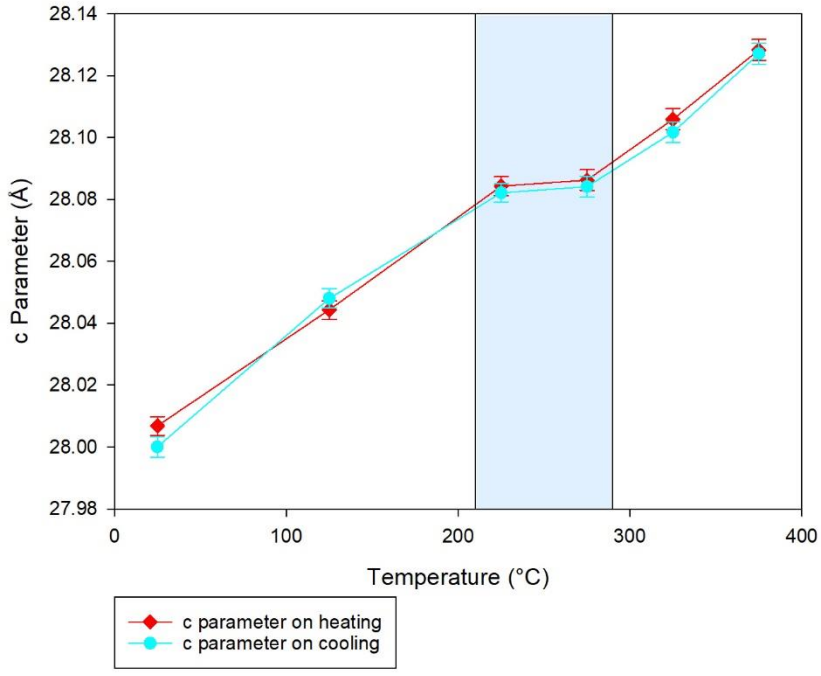


Figure 6.52: VT-XRD data showing the variantion in *c* parameter of humidified $La_{3.75}Pr_{0.25}Ni_3O_{10-\delta}$ against temperature. Deviations in the linearity of results are highlighted in blue.

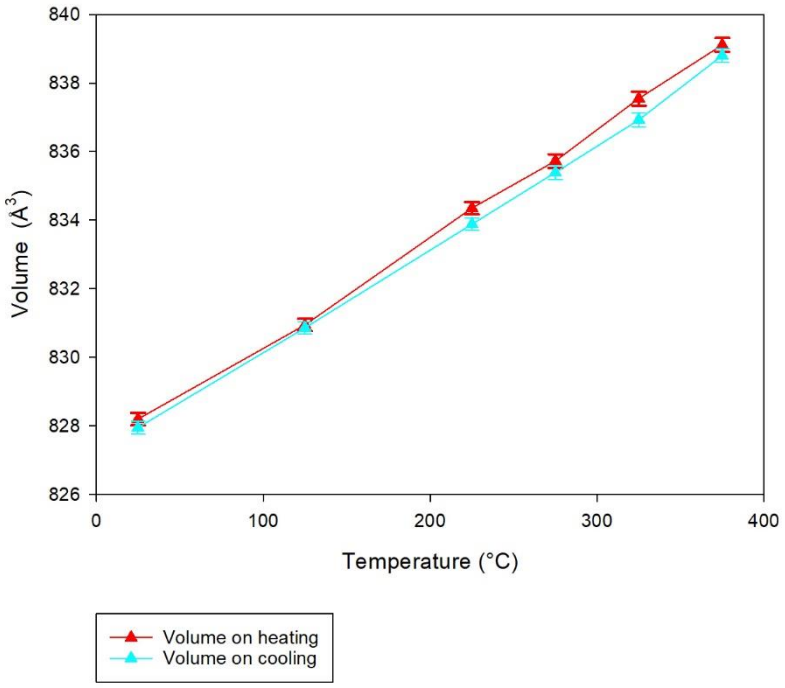


Figure 6.53: VT-XRD data showing the variation in volume of humidified $La_{3.75}Pr_{0.25}Ni_3O_{10-\delta}$ versus temperature.

On cooling, VT-XRD analysis showed that for $La_{3.75}Pr_{0.25}Ni_3O_{10-\delta}$ the same trend in lattice parameters could be seen. The *a* and *c* parameters remained similar to their respective values while heating, within experimental error. However, there was a slight variation in the cooling and heating of the *b* parameters. This may be due to the loss of various gaseous species, identified through TGA/MS. The gaseous species were then not reincorporated back into the crystal structure as VT-XRD was performed with N_2 flowing across the sample. The heating and cooling parameters, after 425°C, were linear and matched one another. No other gases species are released in between 425°C and 725°C, so this was expected.

6.4.2.3 $La_3PrNi_3O_{10-\delta}$

Humidified $La_3PrNi_3O_{10-\delta}$ showed a phase change at 725°C (Figure 6.54). Sequential refinement shows a linear increase in the a parameter (Figure 6.54), while deviations from the linearity were seen in the b parameter (Figure 6.56) between 225°C and 375°C. The change in lattice parameters correlated to when H_2O and CO_2 loss was expected, shown by TGA/MS data. In this temperature range there was a difference between the lattice parameters during heating and cooling. Although no deviations are seen

in the *c* parameter (Figure 6.57) and volume (Figure 6.58). At 725°C the crystal structure was refined to a tetragonal cell *I4/mmm* space group, as the doublet can be seen to have formed a singular peak.

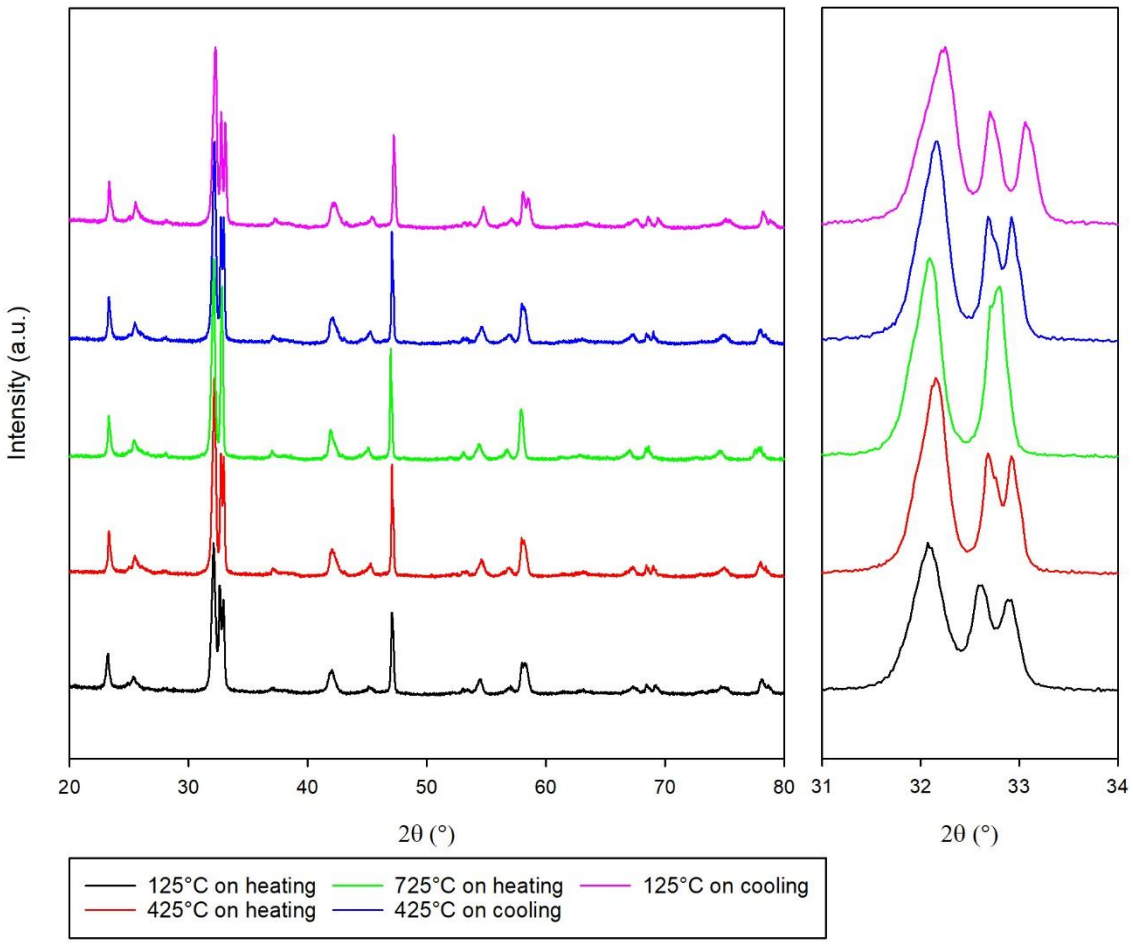


Figure 6.54: VT-XRD pattern of humid $La_3PrNi_3O_{10-\delta}$. The sample is orthorhombic at lower temperatures. During heating the distance between 32.5° and 33.5° peaks reduced. During cooling the previously mentioned peaks separated. In ascending order the temperatures are 125°C on heating (black), 425°C on heating (red), 775°C on heating (green), 425°C on cooling (blue) 125°C on cooling (pink).

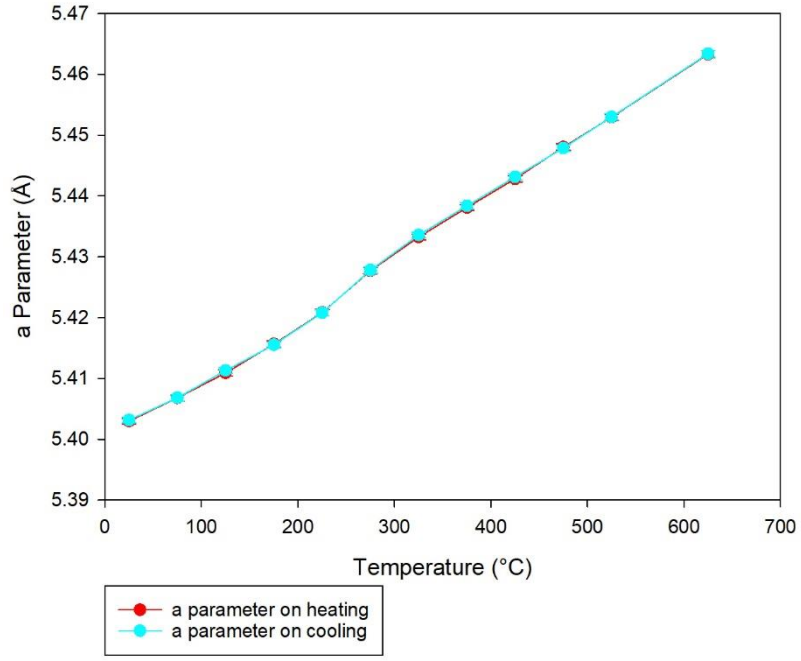


Figure 6.55: VT-XRD data showing the variation in *a* (circle) and *b* (star) parameter of humidified $La_3PrNi_3O_{10-\delta}$ versus temperature.

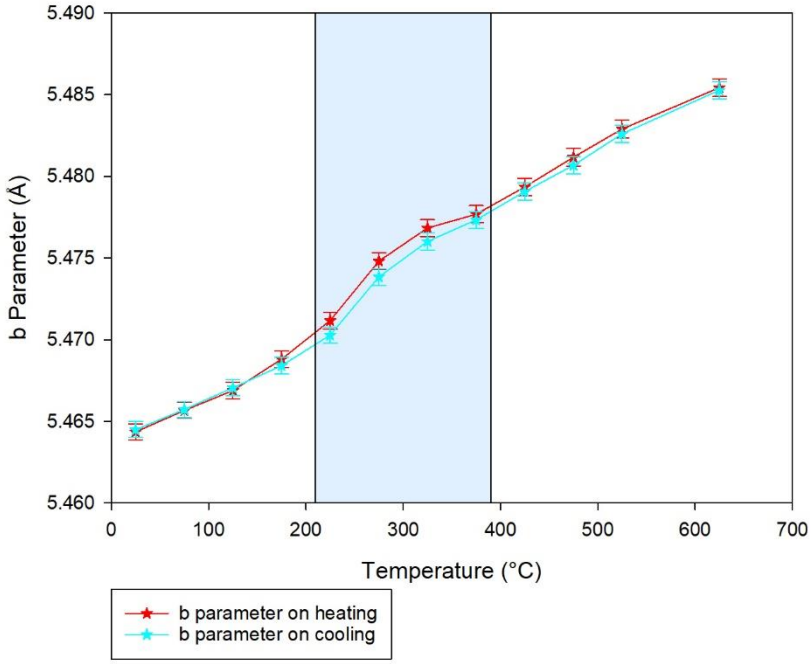


Figure 6.56: VT-XRD data showing the variantion in *b* parameter of humidified $La_3PrNi_3O_{10-\delta}$ against temperature. Slight deviations in linearity of results are highlighted in blue.

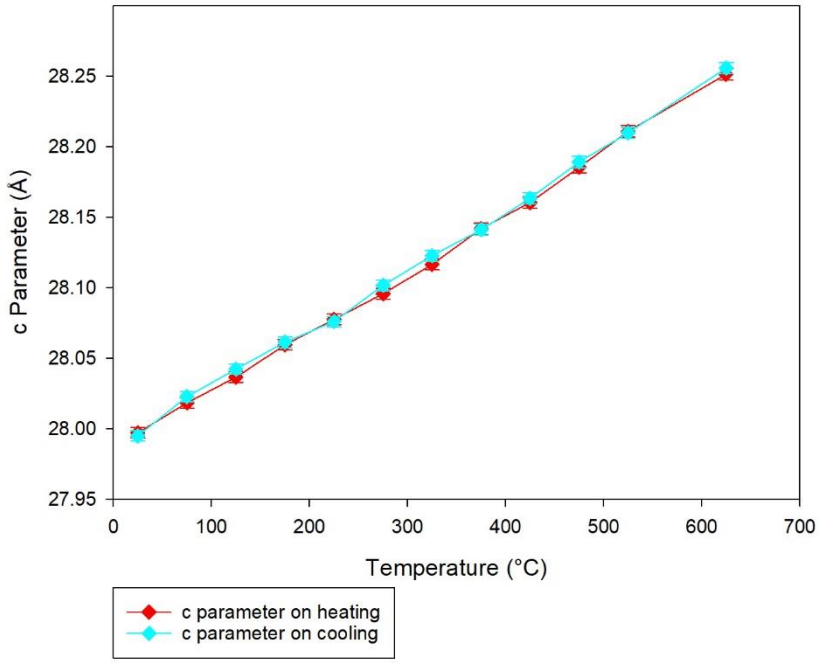


Figure 6.57: VT-XRD data showing the variation in *c* parameter of humidified $La_3PrNi_3O_{10-\delta}$ versus temperature.

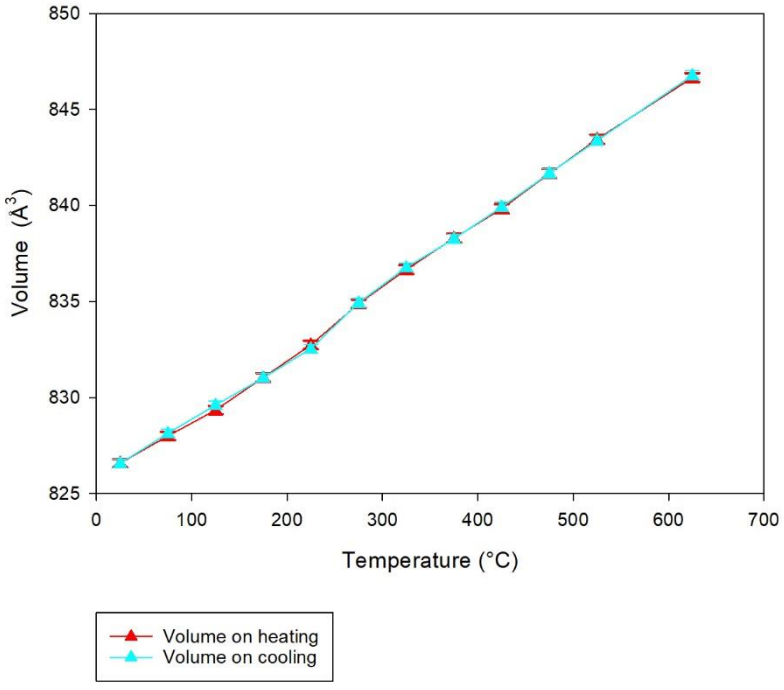


Figure 6.58: VT-XRD showing the variation in volume parameter of humidified $La_3PrNi_3O_{10-\delta}$ versus temperature.

6.4.3 Conductivity Data

$La_4Ni_3O_{10-\delta}$ showed the highest conductivity of all undoped Ruddlesden-Popper samples, due to the increased quantity of Ni-O layers, these being the main pathway for charge transport [213]. $La_4Ni_3O_{10-\delta}$ showed a similar trend in conductivity (Figure 6.59) as previously seen by Takahashi *et al.* [213] and Song *et al.* [218]. The decrease in conductivity at higher temperatures was attributed to a loss of O_2 at higher temperatures reducing the content of Ni^{3+}.

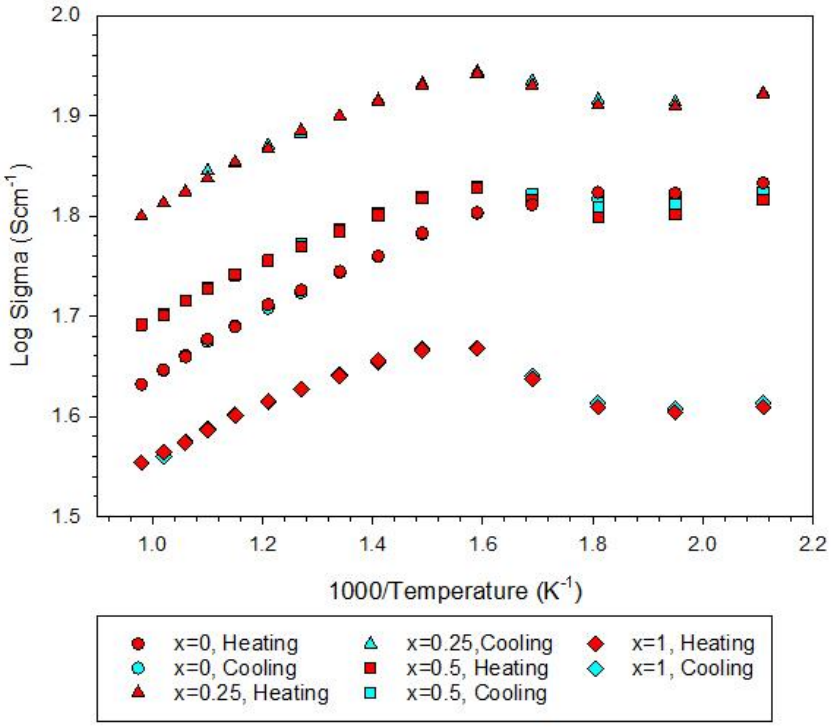


Figure 6.59: Conductivity data for $La_{4-x}Pr_xNi_3O_{10-\delta}$ where x=0 (circle) , 0.25 (triangle) and 0.5 (square) and 1 (diamond). Red fill indicates heating and cyan fill indicates cooling, data shown between 200°C and 750°C.

Pr doped samples did not follow this same trend. Instead, they showed a similar trend to that of $Pr_4Ni_3O_{10-\delta}$ and $La_3Ni_2O_{7-\delta}$ [213, 219, 240, 241]. Above 357°C the conductivity of the samples decreased. Tsai *et al.* [241] saw this same overall trend in $Pr_4Ni_3O_{10-\delta}$ and concluded that the change in characteristics of the electrical conductivity was due to the rearrangement of the crystal structure, caused by a change in oxygen stoichiometry.

$La_{3.75}Pr_{0.25}Ni_3O_{10-\delta}$ showed the highest conductivity throughout the whole temperature range (Table 6.15). $La_{3.5}Pr_{0.5}Ni_3O_{10-\delta}$ showed greater conductivity than $La_4Ni_3O_{10-\delta}$ above 357°C, while at lower temperatures the opposite was true. The results suggest that Pr doping can improve electrical conductivity at higher temperatures, possibly due to Pr having mixed valency, Pr^{3+} or Pr^{4+} [210]. Introducing too much Pr can have the opposite effect, possibly due to Pr interfering with conduction along the Ni-O layers.

Table 6.15: Conductivity for $La_{4-x}Pr_xNi_3O_{10-\delta}$ (x=0, 0.25, 0.5 and 1), conductivity at 200°C, 357°C and 750°C.

Composition	**Conductivity (Scm^{-1})**		
	200°C (2.11 K^{-1})	357°C (1.59 K^{-1})	750°C (0.98 K^{-1})
$La_4Ni_3O_{10-\delta}$	68.06	63.62	42.84
$La_{3.75}Pr_{0.25}Ni_3O_{10-\delta}$	83.46	87.51	63.06
$La_{3.5}Pr_{0.5}Ni_3O_{10-\delta}$	65.53	67.33	49.18
$La_3PrNi_3O_{10-\delta}$	40.71	46.53	35.80

6.4.4 Conclusions

$La_{4-x}Pr_xNi_3O_{10-\delta}$ (x=0, 0.25, 0.5 and 0.75) were successfully synthesised and all sample structures were refined to the orthorhombic structure. $La_4Ni_3O_{10-\delta}$, $La_{3.75}Pr_{0.25}Ni_3O_{10-\delta}$ and $La_3PrNi_3O_{10-\delta}$ retained their orthorhombic structure when heated in humid N_2, dry N_2 and humid O_2. While $La_{3.5}Pr_{0.5}Ni_3O_{10-\delta}$ was shown to degrade in humid N_2, despite being stable in dry N_2 and humid O_2. The estimated H_2O and CO_2 loss of the samples that remained chemically stable in humid N_2 is shown in Table 6.16. As Pr content increased so did the molar quantity of H_2O/CO_2 loss.

Table 6.16: H_2O loss (below 600°C) and CO_2 loss of $La_{4-x}Pr_xNi_3O_{10-\delta}$ (x=0, 0.25, 5 and 1) heated in humid N_2 as well as electrical conductivity.

Composition	H_2O loss below 600°C of humid N_2 sample (mol)	CO_2 loss of humid N_2 sample (mol)	Maximum Electrical Conductivity (Scm^{-1})
$La_4Ni_3O_{10-\delta}$	0.037	0.014	68.06
$La_{3.75}Pr_{0.25}Ni_3O_{10-\delta}$	0.050	0.020	87.51
$La_{3.5}Pr_{0.5}Ni_3O_{10-\delta}$	N/A	N/A	67.33
$La_3PrNi_3O_{10-\delta}$	0.089	0.050	46.53

VT-XRD was performed on the samples that remained chemically stable in humid N_2, as the data showed some variation in lattice parameters when H_2O and CO_2 loss were expected. All samples also showed a change in symmetry from orthorhombic to tetragonal. Samples with a higher Pr content saw the change occur at higher temperatures. Finally, conductivity measurements showed $La_{3.75}Pr_{0.25}Ni_3O_{10-\delta}$ to have the highest conductivity of all samples (87.5 S cm^{-1}).

6.5 Summary

A summary of all samples which were successfully synthesised and maintained their structure, when heated in humid N_2, is shown in Table 6.17. These samples showed varying degrees of H_2O and CO_2 loss, with the maximum estimated quantities also shown in the table. An improvement in conductivity was found increasing Ni-O layers. Pr Doping of Ruddlesden-Popper phases has been shown to increase the conductivity, however excessive doping of Pr seemed to hinder the electrical conductivity. Overall, several viable compositions for symmetrical cell testing have been identified that been shown to be stable in humid atmospheres and have good electrical conductivity.

Table 6.17: Summary of compositions which were chemically stable when heated in various atmospheres along with their maximum electrical conductivity and temperature at which orthorhombic-tetragonal phase change occurred.

Composition	Maximum H_2O loss below 600°C of humid sample (mol)	Maximum Conductivity (S cm^{-1})	Orthorhombic – Tetragonal Phase Change Temperature (°C)
$La_3Ni_2O_{7-\delta}$	0.032	53.15	325
$La_2PrNi_2O_{7-\delta}$	0.044	38.25	N/A
$La_4Ni_3O_{10-\delta}$	0.037	68.06	425
$La_{3.75}Pr_{0.25}Ni_3O_{10-\delta}$	0.050	87.51	425
$La_3PrNi_3O_{10-\delta}$	0.089	46.53	725

Chapter 7: Proton Conducting Ceramic Cell Fabrication and Testing

7.1 Introduction

Proton conducting ceramics cells (PCCC) often consist of a doped barium cerate or barium zirconate perovskite as the electrolyte [1-5]. A key component of the PCCC is that a dense electrolyte is required. A dense electrolyte allows the separation of the gaseous reactants, while allowing for proton transport via oxide ions [2]. Proton conducting electrolytes are notorious for requiring high sintering temperatures to produce a dense electrolyte, which causes issues with Ba volatility. Therefore, sintering aids are often required to lower the sintering temperature.

Sintering aids, such as copper oxide (CuO), zinc oxide (ZnO) and nickel oxide (NiO), have been previously studied with proton conducting materials [6-12]. A small percentage either by wt% or mol% can be mixed with the electrolyte which then allows lower temperature sintering [7, 8, 13]. With a dense electrolyte, symmetrical cells can be made, which consist of the same electrode on either side. These can be used to preliminarily assess the electrode performance.

Developing on from symmetrical cells, a cell consisting of two different compositions of electrodes, can be created. The anode for a proton conducting ceramic fuel cell (PCCFC) is often a mixture of the electrolyte powder mixed with nickel oxide, to act as the catalyst [3]. Whilst the cathode is often a perovskite which contains barium on the A site, with varying quantities of strontium (Sr), cobalt (Co) and iron (Fe) on the B site [3, 14, 15].

A common manufacturing method for ceramic cells is through co-pressing, where the electrolyte and anode are pressed together using a pellet die, followed by deposition of the cathode [15, 16]. As the field in PCCC has continued to expand, tape casting has begun to be implemented [17, 18]. Tape casting

often requires large volumes of precursor material, so can be strenuous to execute when synthesising small quantities of powders.

Once a successful cell has been manufactured, cell testing can commence. On a fuel cell hydrogen enters at the anode, and air at the cathode [3]. As an electrolyser the electrodes are switched, the previous anode is now classed as the cathode, while the previous cathode is now classed as the anode. Water in the form of steam enters the anode and dry hydrogen is produced on the cathode side of the cell.

This chapter will investigate developing a dense electrolyte pellet with the density at least 90% of the theoretical density. The sintering aids lithium fluoride, copper oxide, zinc oxide and nickel oxide will be explored. The dense electrolyte will then be used for symmetrical cell testing using the previously synthesised electrode materials. This is followed by the development of a fuel cell with different compositions of the electrodes. The method of cell manufacturing that gives the best results will then be taken on for electrolyser testing.

7.2 Experimental

$BaCe_{0.9}Y_{0.1}O_{3-\delta}$ was synthesised as follows: stoichiometric amounts CeO_2 (≥99.0%) and Y_2O_3 (99.99%) were weighed out, with $BaCO_3$ (99.8%) weighed in 6% excess, to account for barium evaporation. 3 mL of hexane (Sigma-Aldrich, ≥95.0%) was also added to act as a lubricant. The powders were ball milled at 500 rpm for 15 min intervals 4 times using a Fritsch Pulverisette 7 Planetary Micro Mill, 12 mL pots and four 10 mm zirconium oxide (ZrO_2) balls. The powders were then heated to 1400°C in a Vecstar Ltd. VF2 muffle furnace. $BaZr_{0.8}Y_{0.2}O_{3-\delta}$ was synthesised through a sol-gel method, $Ba(NO_3)_2$ (Alfa Aesar, ≥99.0%), $ZrO(NO_3)_2.xH_2O$ (Sigma-Aldrich, 99.0%) and $Y(NO_3)_3.6H_2O$ (Sigma-Aldrich, 99.8%) were weighed out, with 3% excess $Ba(NO_3)_2$ and dissolved in water. Ethylene glycol (VWR, ≥99.0%) and citric acid (Sigma-Aldrich, 99.0%) were added and mixed until dissolved. The solution was heated at 80°C until a gel formed, which was then heated in an oven at 350°C for 1 h. The powders were then ground using a pestle and mortar and heated to 1100°C. $BaCe_{0.6}Zr_{0.3}Y_{0.1}O_{3-\delta}$, using $Ce(NO_3)_3.6H_2O$ (Sigma-Aldrich, 99.0%), was synthesised through sol-gel synthesis method, which followed the same procedure as for as $BaZr_{0.8}Y_{0.2}O_{3-\delta}$, in this case the powders were heated up to 1400°C.

X-ray diffraction (XRD) analysis was primarily performed using a Bruker D8 diffractometer with Cu K_α radiation. Rietveld refinement was performed using the GSAS-II suite of programmes to determine the cell parameters and hence theoretical density of $BaZr_{0.8}Y_{0.2}O_{3-\delta}$ and $BaCe_{0.6}Zr_{0.3}Y_{0.1}O_{3-\delta}$ [19]. All samples except for $BaCe_{0.6}Zr_{0.3}Y_{0.1}O_{3-\delta}$ exposed in humid N_2 was analysed using this instrument. XRD analysis for this latter sample was performed using a Bruker D2 Co K_α radiation, as the Bruker D8 diffractometer was inoperable at the end of the project. In this instance XRD analysis was performed on $BaCe_{0.6}Zr_{0.3}Y_{0.1}O_{3-\delta}$ again to show a visual comparison.

Lithium fluoride (LiF, Sigma-Aldrich, 99.99%), copper (II) oxide (CuO, Sigma-Aldrich, 99.99%), zinc oxide (ZnO, Sigma-Aldrich, 99.9%) and nickel oxide (NiO, Sigma-Aldrich, 99%) were explored as sintering aids, with details given in section 7.4. XRD was performed on the pellets and DIFFRAC.EVA software and the Crystallography Open Database were used for peak identification. Pellets made of $BaCe_{0.6}Zr_{0.3}Y_{0.1}O_{3-\delta}$ electrolyte with NiO as a sintering aid were used pellets for performing symmetrical cell tests. The electrodes were made using the previously studied $La_2NiO_{4+\delta}$, $La_{1.5}Sr_{0.5}NiO_{4+\delta}$, $La_3Ni_2O_{7-\delta}$, $La_2PrNi_2O_{7-\delta}$, $La_4Ni_3O_{10-\delta}$, $La_{3.75}Pr_{0.25}Ni_3O_{10-\delta}$, and $La_3PrNi_3O_{10-\delta}$ electrodes. Electrode ink was prepared by mixing the powder with a Terpinol-based ink vehicle (Fuel Cell Materials) in a ratio of 2:1, using a EXAKT 35 three roll mill. The electrode ink was painted onto the surface of the electrolyte pellet and sintered at 1000°C for 4 h, using a Carbolite Gero Ltd. CWF 13/13. A similar process was preformed to make anode inks for fuel cell and electrolyser testing, with sintering temperatures detailed in Section 7.6.

Electrochemical impedance spectroscopy (EIS) measurements were taken between 400°C and 700°C at intervals of 50°C using a Solartron 1470E and 1455 FRA analyser, between the frequencies 0.01 Hz and 10^5 Hz with an amplitude of 10 mV. Measurements were first taken in air (dry) with a flow rate of 40 $mLmin^{-1}$, with each cell given 2 h to equilibrate before measurements were taken. Once complete, the rig was then cooled to 400°C and 40 $mLmin^{-1}$ of air was flown through a bubbler containing deionised water. Measurements were taken at the same temperature points. Equivalent circuits and polarisation resistance were determined for the recorded measurements using the ZView software.

Following this, various methods of manufacturing a cell were attempted using a $La_2NiO_{4+\delta}$ electrode, which are discussed in section 7.6 along with the flow rates used for testing. The composition of the fuel electrode unless otherwise stated is shown in Table 7.1. The electrolyte powder used had the composition $BaCe_{0.6}Zr_{0.3}Y_{0.1}O_{3-\delta}$ and tapioca starch was used as a pore former. For all fuel cell tests, the fuel electrode was first purged of any air using 40 $mLmin^{-1}$ of nitrogen (N_2). Following this, the NiO containing electrode was reduced for 12 h at 700°C. To reduce the fuel electrode 40 $mLmin^{-1}$ of hydrogen (H_2) and 40 $mLmin^{-1}$ of nitrogen (N_2) was used, while 80 $mLmin^{-1}$ of air entered the air electrode. The flow rates were then changed to the required flow rates for testing. Potential stair step measurements were taken to observe the current density and power output of the cell. Electrolysis measurements where then performed using $La_2NiO_{4+\delta}$ and $La_3Ni_2O_{7-\delta}$ as air electrode.

Table 7.1: Fuel electrode composition used for cell fabrication.

Composition	Quantity in mixture (%)
$BaCe_{0.6}Zr_{0.3}Y_{0.1}O_{3-\delta}$	33
NiO	50
Pore former	16

The morphology of the cells and pellets were analysed by scanning electron microscopy (SEM) using a Hitachi TM3030 Plus tabletop microscope. Surface elemental analysis was conducted using an energy dispersive X-ray spectroscopy (EDXS) attachment on the SEM.

7.3 Investigation of the Chemical Stability of Various Electrolyte Materials in Humid Nitrogen

$BaCe_{0.9}Y_{0.1}O_{3-\delta}$, $BaZr_{0.8}Y_{0.2}O_{3-\delta}$ and $BaCe_{0.6}Zr_{0.3}Y_{0.1}O_{3-\delta}$ were considered as electrolytes for the use in a PCCC. To explore the chemical stability of these materials they were heated in humid N_2 and XRD was performed after the heat treatment. $BaCe_{0.9}Y_{0.1}O_{3-\delta}$ was shown to degrade into a $Ce_{0.8}Y_{0.2}O_{1.9}$, Y_2O_3 and BaO phases (Figure 7.1). It should be noted that the humidity of the N_2 was approximately 3%. Some

degradation would be expected as $BaCe_{0.9}Y_{0.1}O_{3-\delta}$, is known to have poor chemical stability [20]. However, complete degradation of $BaCe_{0.9}Y_{0.1}O_{3-\delta}$ was surprising as it is a commonly used electrolyte material for proton conducting cells (PCCs). Another sample of $BaCe_{0.9}Y_{0.1}O_{3-\delta}$ was removed from the furnace with flowing humid N_2, at 200°C. XRD was performed on the sample and showed little degradation had occurred, suggesting that $BaCe_{0.9}Y_{0.1}O_{3-\delta}$ sees the most decomposition in humid atmospheres below 200°C. When heating $BaZr_{0.8}Y_{0.2}O_{3-\delta}$ and $BaCe_{0.6}Zr_{0.3}Y_{0.1}O_{3-\delta}$ in humid N_2, degradation was not observed on the samples, suggesting both as being chemically stable, this is expected as both compositions had a sufficient amount of zirconium (Zr).

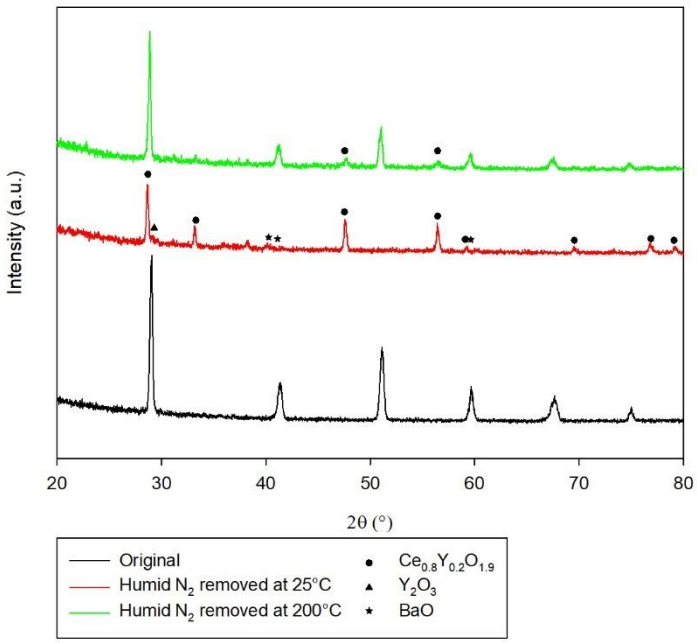


Figure 7.1: XRD of $BaCe_{0.9}Y_{0.1}O_{3-\delta}$ as synthesised (black), heated in humid N_2 and removed from furnace at room temperature (red), heated in humid N_2 and removed from furnace at 200°C.

7.4 Investigation into Developing Dense Electrolyte Pellets through the Addition of Sintering Aids

$BaZr_{0.8}Y_{0.2}O_{3-\delta}$ and $BaCe_{0.6}Zr_{0.3}Y_{0.1}O_{3-\delta}$ were taken further as they were shown to be chemically stable in humid N_2. As a dense electrolyte is required for cell testing, various sintering aids were attempted to develop dense pellets. Sintering aids were required as sintering temperatures above 1500°C could not be utilised, due to limitations in the muffle furnaces operating temperature. LiF, CuO, and ZnO were explored as sintering aids for $BaZr_{0.8}Y_{0.2}O_{3-\delta}$, followed by NiO for $BaCe_{0.6}Zr_{0.3}Y_{0.1}O_{3-\delta}$. During sintering, weights were applied to all pellets to prevent curvature of the pellet on sintering. The aim was to achieve a density of at least 90% of the theoretical density.

7.4.1 Exploration of LiF as a Sintering Aid

Lithium fluoride (LiF) was explored as a sintering aid for use with $BaZr_{0.8}Y_{0.1}O_{3-\delta}$. LiF has been previously used as a sintering aid for PCCC on a single occasion [21]. Varying quantities of LiF were applied; these were: 1 mol%, 2 mol% and 4 mol% (Figure 7.2). The pellets were sintered at 1400°C for 4 h to see if using LiF would be viable as a sintering aid. The sintering temperature was 300°C higher than the synthesis temperature of the material. Visually, the 2 mol% LiF sample appeared to have some small blemishes, with a greater number on the 4 mol%. The XRD pattern (Figure 7.3) of the 1 mol% sample showed a ZrO_2 peak at ca. 30° due to barium (Ba) evaporation. While 2 and 4 mol% samples did not show any impurities.

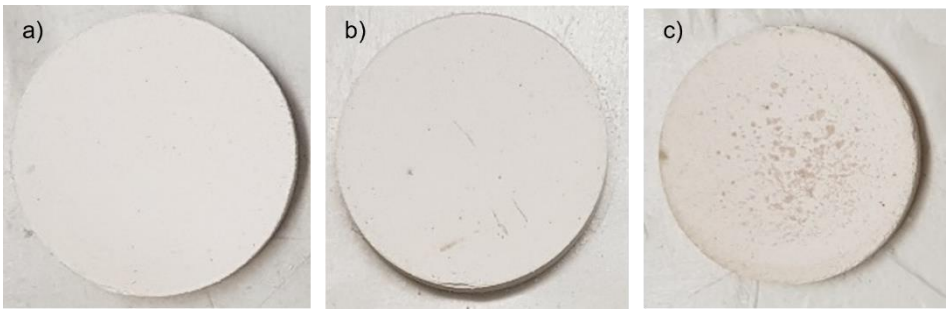


Figure 7.2: LiF doped samples a) 1 mol%, b) 2 mol% and c) 4 mol%.

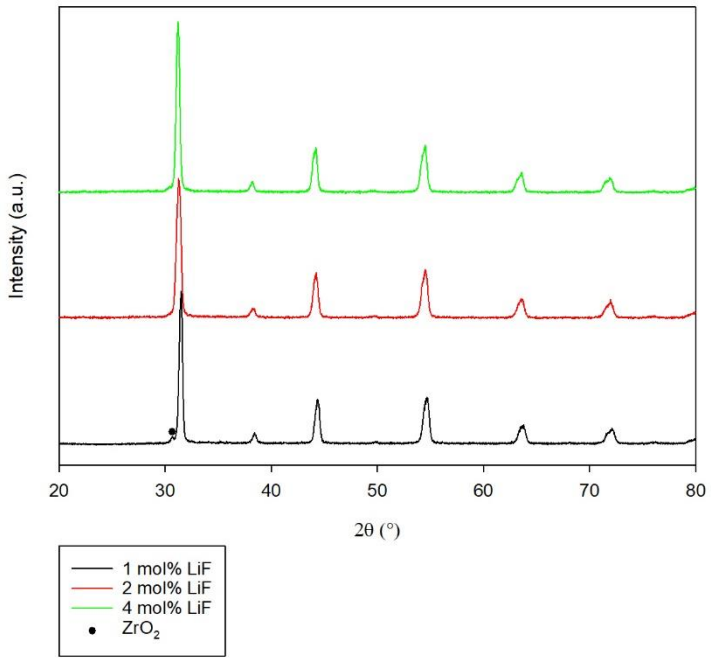


Figure 7.3: XRD patterns of $BaZr_{0.8}Y_{0.3}O_{3-\delta}$ pellets, sintered with varying quantities of LiF: 1 mol% (black), 2 mol% (red) and 4 mol% (green).

Densities of each pellet were determined and compared to the theoretical density, to determine how dense each pellet was (Table 7.2). The density ranged from 35.4% to 44.1 % of the theoretical density. No trend in density can be observed with increasing LiF, it can be concluded that LiF was not a sufficient sintering aid, as the density did not even exceed 50% of the theoretical value and the surface of the pellets became deformed.

Table 7.2: Table showing the densities of the $BaZr_{0.8}Y_{0.3}O_{3-\delta}$ sintered pellets using LiF as a sintering aid.

LiF (mol%)	**1**	**2**	**4**
Density (%)	44.13	35.42	41.85

7.4.2 Exploration of ZnO as a Sintering Aid

ZnO has been previously explored as a sintering aid for proton conducting ceramics [7-9]. Babilo *et al.* [7] had previously shown that an addition of 4 mol% of ZnO to $BaZr_{0.8}Y_{0.1}O_{3-\delta}$ could achieve a pellet that was 93% dense. While Tao et a*l.* [8] showed that sintering at 1325°C for 10 h with 1 wt% of ZnO was able to create a 96% dense pellet. Varying quantities of ZnO were used as a sintering aid for $BaZr_{0.8}Y_{0.1}O_{3-\delta}$. 1 mol%, 4 mol% and 10 mol% were originally used at a sintering temperature of 1300°C for 4 h, with prospects of increasing the temperature or duration.

Addition of 10 mol% ZnO appeared to completely deform the surface appearance of the pellet (Figure 7.4), with XRD patterns showing a peak for ZrO_2 due to Ba evaporation during sintering. The XRD pattern (Figure 7.5) for the 10 mol% sample showed the same ZrO_2 peak as well as several peaks for Al_2O_3, suggesting that the results for the use of ZnO as a sintering aid. Therefore, did not appear promising.

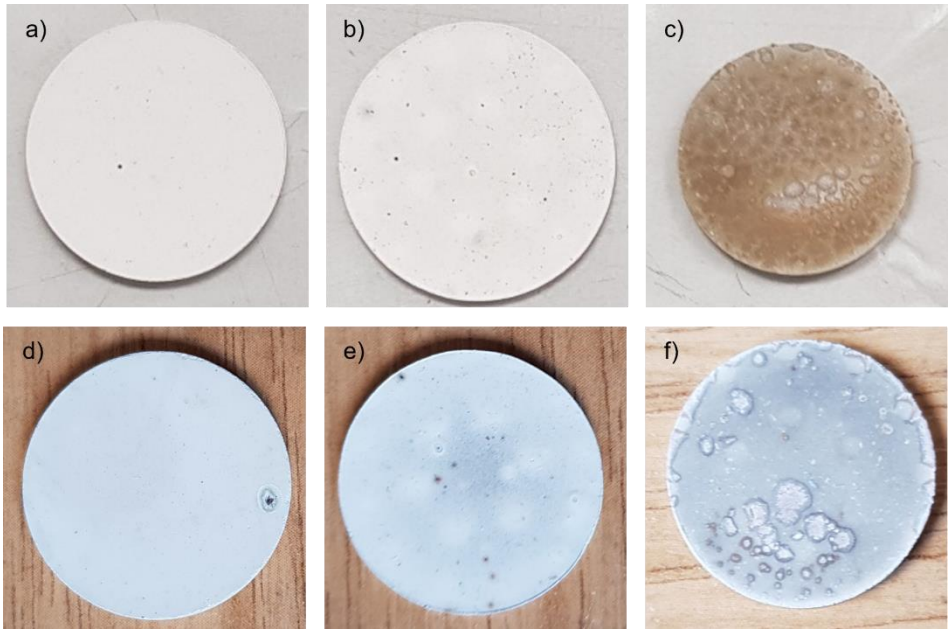


Figure 7.4: a) 1 mol% of ZnO sintered at 1300°C for 4 h. b) 4 mol% of ZnO sintered at at 1300°C for 4 h. c) 10 mol % of ZnO sintered at 1300°C for 4h d) 1 mol% of ZnO sintered at 1400°C for 4 h. e) 4 mol% of ZnO sintered at 1400°C for 4 h. f) 10 mol % of ZnO sintered at 1400°C for 4 h.

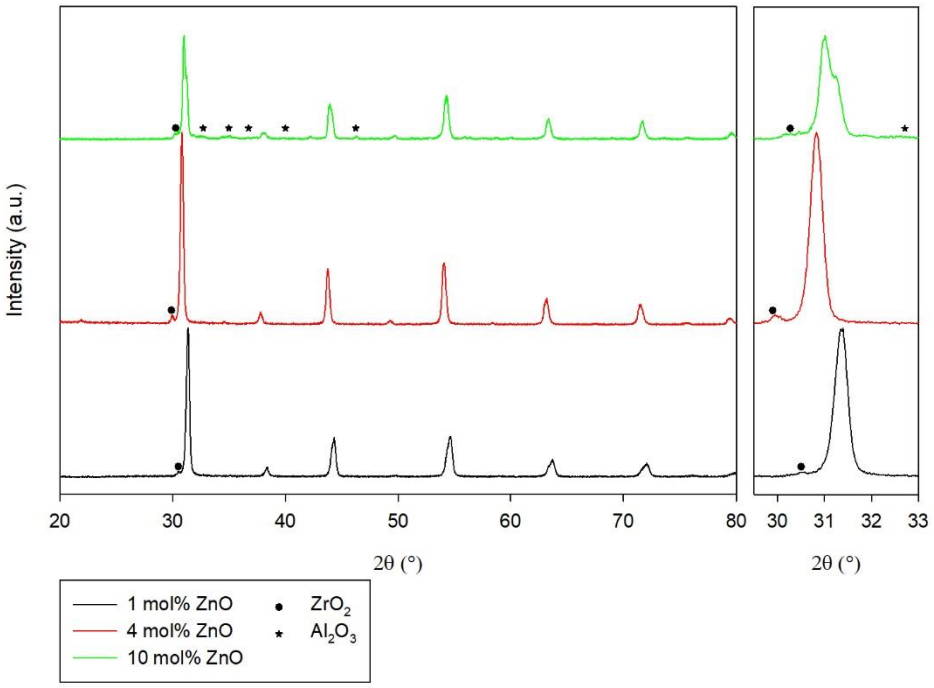


Figure 7.5: XRD patterns of $BaZr_{0.8}Y_{0.3}O_{3-\delta}$ pellets sintered at 1300°C for 4 h with ZnO as a sintering aid. 1 mol% ZnO (black), 4 mol% ZnO (red) and 10 mol% ZnO (green).

Increasing the sintering temperature to 1400°C for 4 h showed the same visual effects (Figure 7.4). The XRD patterns (Figure 7.6) for these samples had the same ZrO_2 peak due to Ba evaporation. The 10 mol% sample had several additional peaks form, so much so that it was difficult to identify whether the original composition was still present. Densities of the samples appeared to increase both with increasing temperature and increasing ZnO mol% (Table 7.3). However, even though the sample sintered at 1400°C with 10 mol% had the highest density, it was questionable how much of the sample was still $BaZr_{0.8}Y_{0.2}O_{3-\delta}$.

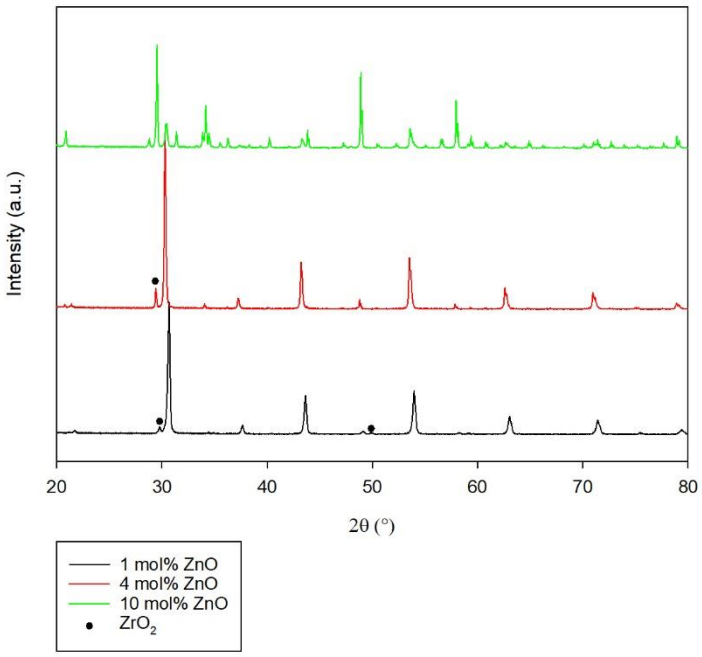


Figure 7.6: XRD patterns of $BaZr_{0.8}Y_{0.3}O_{3-\delta}$ pellets sintered at 1400°C for 4 h with ZnO as a sintering aid. 1 mol% ZnO (black), 4 mol% ZnO (red) and 10 mol% ZnO (green).

Table 7.3: Table showing the sintering temperatures and densities of $BaZr_{0.8}Y_{0.3}O_{3-\delta}$ pellets using ZnO as a sintering aid

	Density at Varying mol% of ZnO (%)		
Temperature (°C)	1	4	10
1300	46.8	54.86	84.45
1400	49.38	71.28	78.17

An excess of barium carbonate ($BaCO_3$) was mixed into the $BaZr_{0.8}Y_{0.1}O_{3-\delta}$ along with the sintering aid (1 mol% ZnO) to compensate for any Ba evaporation and sintered at 1300°C for 10 h. 1 mol% and 10 mol% excess of $BaCO_3$ was attempted, which resulted in pellets of with a density of 53.6% and 63.6%, respectively. The XRD patterns (Figure 7.7) for these samples do not show the same ZrO_2 peaks that were present on previous XRD patterns, indicating that the addition of excess Ba was successful in maintaining the perovskite phase.

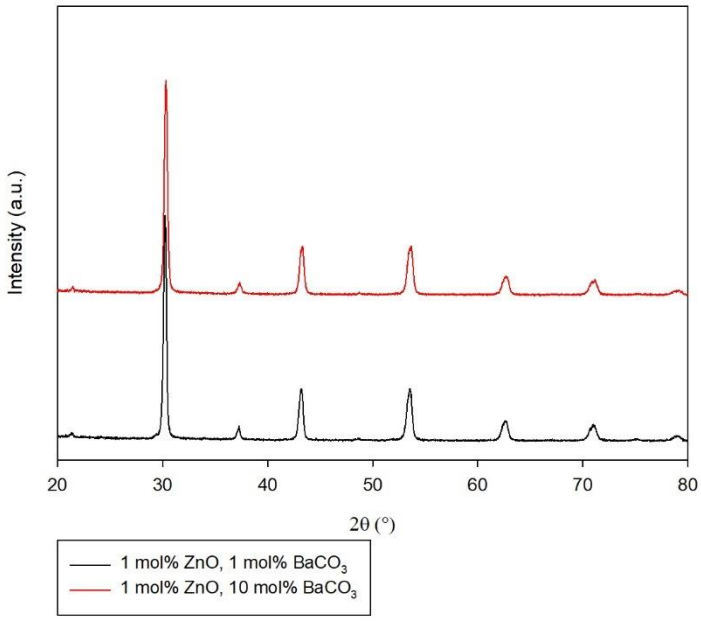


Figure 7.7: XRD pattern of $BaZr_{0.8}Y_{0.3}O_{3-\delta}$ with 1 mol% $BaCO_3$ (black) and 10 mol% $BaCO_3$ (red) sintered at 1300°C for 10 h.

Increasing the sintering temperature to 1500°C for 12 h was attempted to create a dense pellet, once again a discolouration on the surface of the pellets was observed. These pellets contained 1 mol% ZnO along with either 1 mol% $BaCO_3$ and 10 mol% $BaCO_3$ (Figure 7.8). The 1 mol% sample showed the greatest discolouration, this is possibly due to Ba loss and there being insufficient $BaCO_3$ to compensate for the loss, which is further supported by the XRD pattern (Figure 7.9) which showed an additional Ba deficient phase. The sample consisting of 10 mol% of $BaCO_3$ showed the least discolouration, possibly due to the larger excess of $BaCO_3$ compensating for the Ba evaporation. On this occasion the sample appears to form a phase consisting of Y-Zr-O (Figure 7.9).

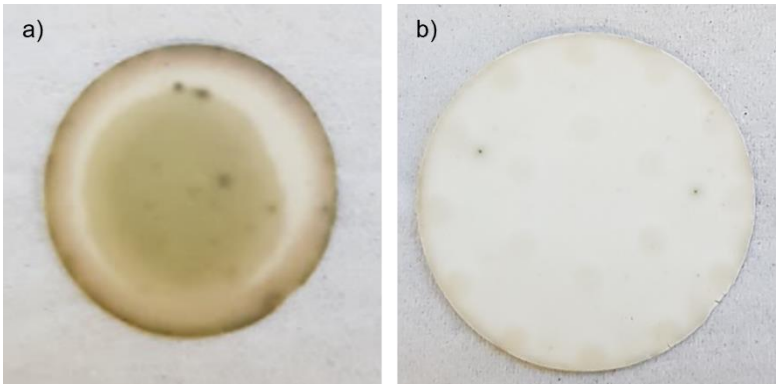


Figure 7.8: Images of $BaZr_{0.8}Y_{0.3}O_{3-\delta}$ containing 1 mol% ZnO, sintered at 1500°C for 12 h. a) 1 mol% $BaCO_3$, b) 10 mol% $BaCO_3$.

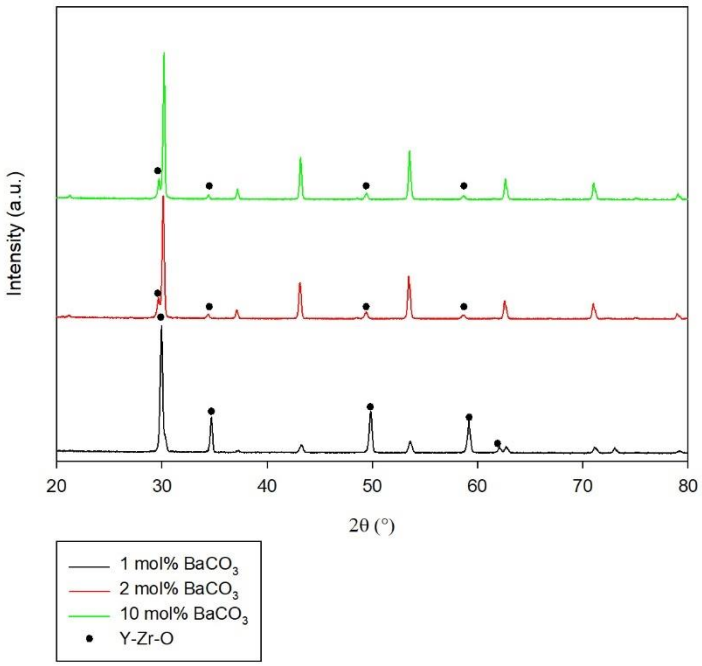


Figure 7.9: XRD patterns of $BaZr_{0.8}Y_{0.3}O_{3-\delta}$, 1 mol% ZnO with 1 mol% $BaCO_3$ (black), 2 mol% $BaCO_3$ (red) and 10 mol% $BaCO_3$ (green).

The results therefore show that the addition of the $BaCO_3$, while not improving the density of the pellet, did reduce the impurity within the sample.

7.4.3 Exploration of CuO as a Sintering Aid

Previous studies have shown that CuO can also be used as a sintering aid [7, 10]. 4 wt % of CuO was applied, with the addition of excess $BaCO_3$; one sample had 1 mol% $BaCO_3$ while another sample has 10 mol% $BaCO_3$. Samples were sintered at 1500°C for 5 h, as it had become clear that sintering temperatures below this level would most likely be insufficient.

The 1 mol% $BaCO_3$ sample is shown to have a density of 64.1% and the 10 mol% sample had a density of 66.0%. XRD patterns (Figure 7.9) of the pellets showed that an additional peak formed at lower angles attributed to impurities due to barium evaporation at higher temperatures. To compensate for this, a greater amount of excess Ba was required. As only 66.0% of the theoretical density was achieved, to create a dense pellet a mixture of higher sintering temperature and longer sintering time would possibly be required to form a dense pellet if CuO was used as a sintering aid.

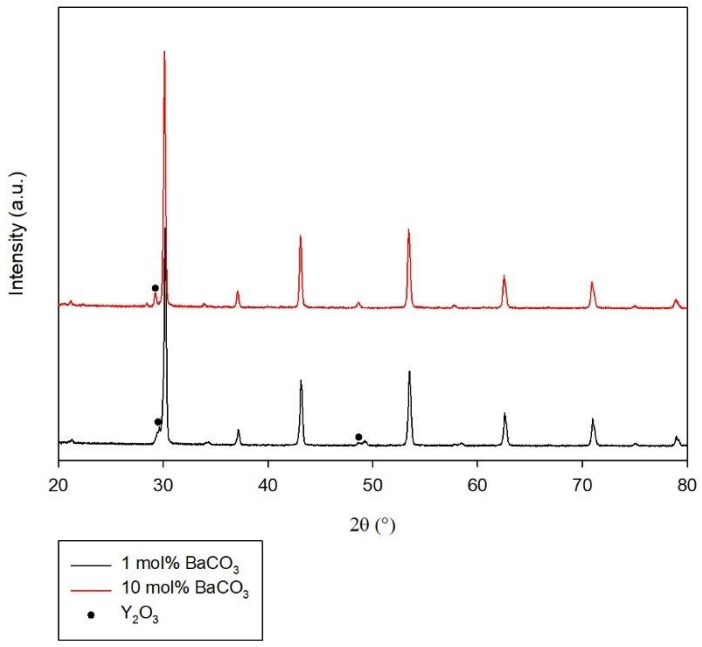


Figure 7.10: XRD pattern of $BaZr_{0.8}Y_{0.3}O_{3-\delta}$ with 4 wt% CuO. 1 mol% $BaCO_3$ (black) and 10 mol% $BaCO_3$ (red).

7.4.4 Exploration of NiO as a Sintering Aid

NiO has previously been shown to be a common sintering aid for proton conducting ceramics [3, 7]. Hence, it was trialled as a sintering aid for $BaCe_{0.6}Zr_{0.3}Y_{0.1}O_{3-\delta}$. From previous experience with sintering $BaZr_{0.8}Y_{0.2}O_{3-\delta}$, excess $BaCO_3$ was required to mitigate Ba evaporation. For temperatures above 1300°C an additional method is required to further reduce Ba loss. The $BaCe_{0.6}Zr_{0.3}Y_{0.1}O_{3-\delta}$ samples were covered with extra $BaCe_{0.6}Zr_{0.3}Y_{0.1}O_{3-\delta}$ powders to further help mitigate Ba loss [22].

Previous results had shown blemishes on some of the pellets, particularly the 10 mol% ZnO samples, which may be a result of the alumina weight reacting with the pellet. Thus, covering the pellets in electrolyte powder may also help to prevent this.

Sintering $BaCe_{0.6}Zr_{0.3}Y_{0.1}O_{3-\delta}$ with varying quantities of NiO was attempted. In this case pellets were placed on a bed of $BaCe_{0.6}Zr_{0.3}Y_{0.1}O_{3-\delta}$ powders (2 g) and again covered with more $BaCe_{0.6}Zr_{0.3}Y_{0.1}O_{3-\delta}$ powders (2 g), to reduce Ba evaporation and prevent the alumina plate from reacting with the electrolyte pellet. The pellet was sintered with the alumina weight applied. Without the addition of a weight the pellet would physically deform (Figure 7.12a). Pellets were sintered at 1500°C for 10 h, as this was the highest temperature that could be reached by the furnace.

Sintering of the pellets with 1 wt% NiO and 10 mol% $BaCO_3$ excess saw the formation of ZrO_2 peaks on the XRD pattern (Figure 7.11) similar to other samples. Therefore $BaCO_3$ excess was increased to 20 mol%. The XRD pattern of the 20 mol% $BaCO_3$ sample showed a sample with no visible Ba deficient peaks and a good pellet density 91.4% of the theoretical. The SEM image (Figure 7.12c) showed clear grain boundaries within the sample, although some small pores were present.

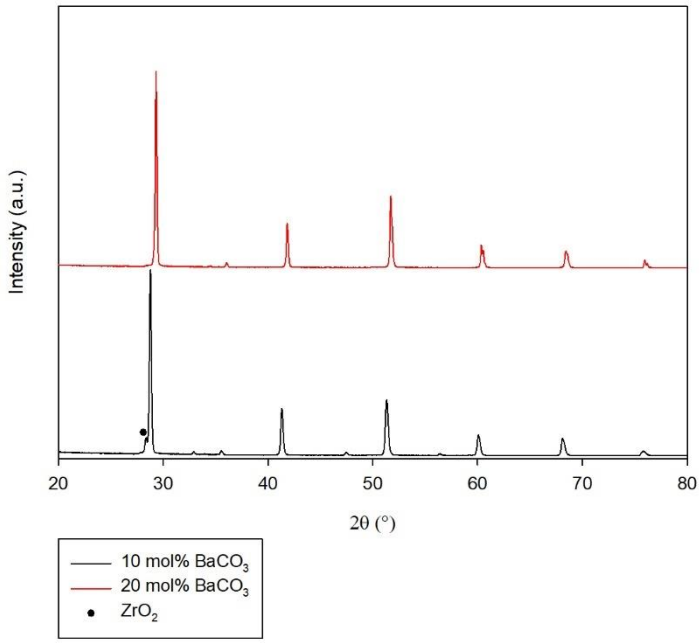


Figure 7.11: $BaCe_{0.6}Zr_{0.3}Y_{0.1}O_{3-\delta}$ sintered with 1 wt% NiO. 10 mol% $BaCO_3$ added (black) and 20 mol% $BaCO_3$ (red).

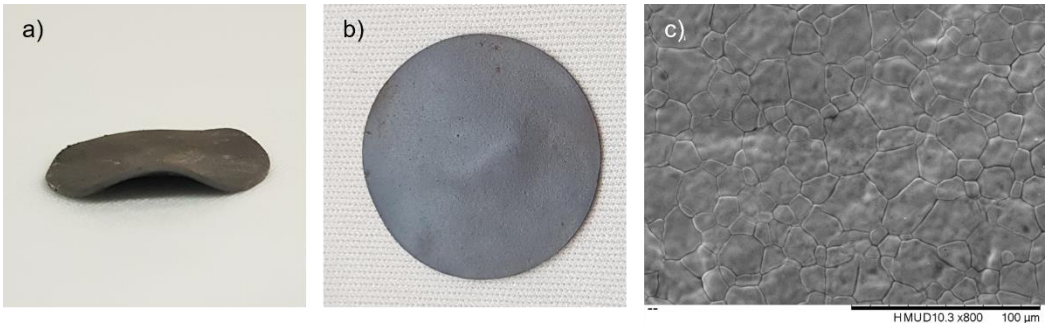


Figure 7.12: $BaCe_{0.6}Zr_{0.3}Y_{0.1}O_{3-\delta}$ with 1 wt% NiO sintered pellets. a) shows sintered pellet with no weight on top b) shows pellet with weight applied c) SEM surface image of $BaCe_{0.6}Zr_{0.3}Y_{0.1}O_{3-\delta}$ with 1 wt% NiO.

Increasing the quantity of NiO to 4 wt% was also attempted. This caused the pellet to crack during sintering (Figure 7.13). Pellets also appeared to be fused to the sacrificial powder, which in turn fused to the alumina weight, making the pellets unusable. Hence, it was decided to continue to produce $BaCe_{0.6}Zr_{0.3}Y_{0.1}O_{3-\delta}$ pellets with 1 wt% of NiO as a sintering aid.

Overall the various studies performed on the use of different sintering aids showed that NiO was the best sintering aid to give ≥90% density. Moreover, it was also shown that $BaCO_3$ excess, along with covering with sacrificial powder, was required to account for Ba volatility. It is interesting to note that

in the literature not many studies mention the use of excess Ba to compensate for Ba evaporation, and very few also mention covering the sample with electrolyte powder to mitigate loss further. From the results presented here, this appears to be a serious omission in the literature.

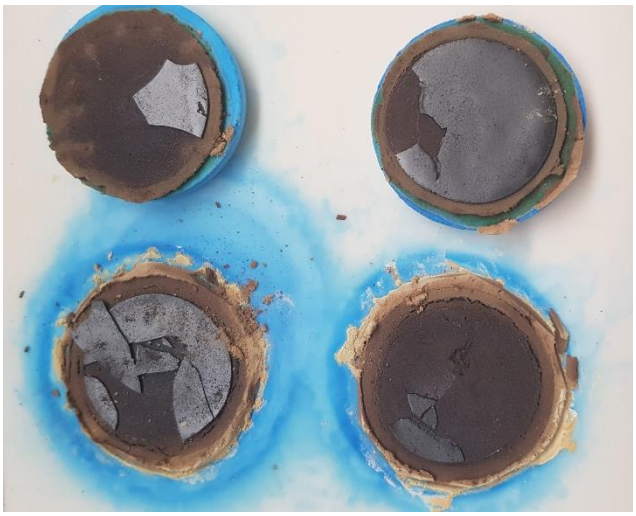


Figure 7.13: Image showing $BaCe_{0.6}Zr_{0.3}Y_{0.1}O_{3-\delta}$ pellets after sintering with 4 wt% NiO. The image shows the bed of $BaCe_{0.6}Zr_{0.3}Y_{0.1}O_{3-\delta}$ that the pellets were placed on during sintering, the cracked pellets and the sacrificial powder (that has fused to the alumina weights) used to cover the pellets.

7.5 Investigation into the Effect of Dry Air and Humid Air on Symmetrical Cells

$La_2NiO_{4+\delta}$, $La_3Ni_2O_{7-\delta}$ and $La_4Ni_3O_{10-\delta}$ were chosen for symmetrical cell testing as a benchmark for the doped samples. $La_{1.5}Sr_{0.5}NiO_{4+\delta}$ was selected as it had the highest electrical conductivity of the Sr doped samples. $La_2PrNi_2O_{7-\delta}$ was tested as no changes were observed in the XRD patterns when the sample was heated in humid N_2 or humid O_2. Finally, $La_{3.75}Pr_{0.25}Ni_3O_{10-\delta}$ and $La_3PrNi_3O_{10-\delta}$ were selected as neither decomposed in humid N_2. Symmetrical cell testing was performed between 400°C and 700°C at 50°C intervals in dry air and humid air. The impedance measurements were compared to observe any differences. The polarisation resistance (R_{pol}) was calculated as the difference between the high frequency and low frequency intercept; as symmetrical cells were being tested the difference was divided by two to account for the two electrodes [23]. It should be noted that the electrolyte material is a mixed ionic and electronic conductor so the actual R_{pol} may actually be higher than the measured value as some electronic conductivity was expected [24].

For $La_2NiO_{4+\delta}$ symmetrical cells the $R_{pol,\ humid}$ was less than the $R_{pol,\ dry}$ for 400°C to 550°C (Figure 7.14 and Figure 7.15), while for $La_{1.5}Sr_{0.5}NiO_{4+\delta}$ $R_{pol,\ humid}$ was only less than $R_{pol,\ dry}$ at 400°C. The lower $R_{pol,\ humid}$ compared to $R_{pol,\ dry}$ has been previously shown for proton conducting symmetrical cells and is thought to be due to proton conduction as a result of equation (1.3). Equation (1.3) shows the binding of OH^- to oxygen vacancies this, suppresses oxide ion conduction and allows proton conduction to surpass it.

$$H_2O + O_O{}^{\times} + V_O{}^{\bullet\bullet} \leftrightarrow 2OH_O{}^{\bullet} \qquad (7.1)$$

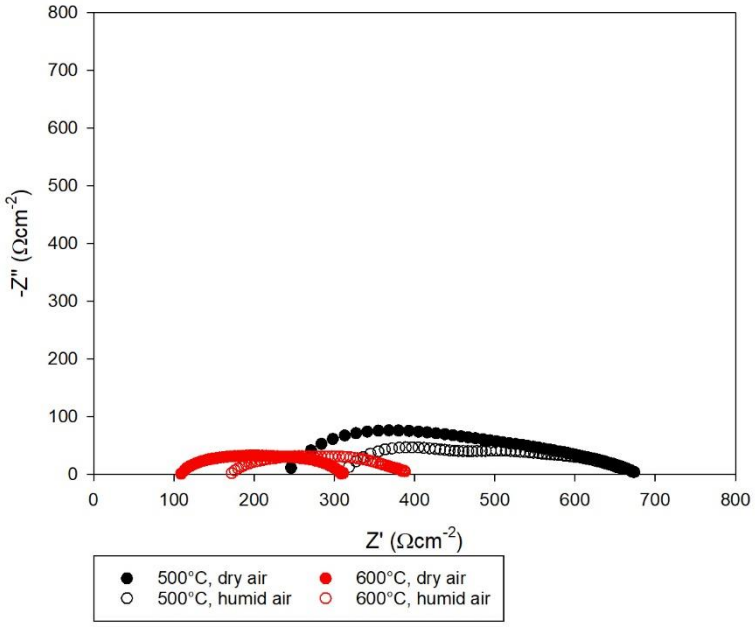


Figure 7.14: Nyquist plot for $La_2NiO_{4+\delta}$, at 500°C in dry air (black filled circle), and humid air (black open circle), and at 600°C in dry air (red filled circle), and humid air (red open circle).

$R_{pol,\ dry}$ was greater than $R_{pol,\ humid}$ for $La_2NiO_{4+\delta}$ at 600°C (Figure 7.14 and Figure 7.15) and above. At 700°C $R_{pol,\ dry}$ and $R_{pol,\ humid}$ were 57.47 Ωcm^{-2} and 130.20 Ωcm^{-2}, respectively. $La_{1.5}Sr_{0.5}NiO_{4+\delta}$ had higher $R_{pol,\ dry}$ values at temperatures of 450°C. Proton conduction was still expected to occur despite $R_{pol,\ dry}$ being less than $R_{pol,\ humid}$. If proton conduction was not occurring then there would not be any difference between $R_{pol,\ dry}$ and $R_{pol,\ humid}$ as previously seen by Sozal *et al.* [25]. Greater $R_{pol,\ humid}$ values have previously been seen by Li *et al.* and Sun *et al.* [24, 26]. It was speculated that the increase in

$R_{pol,\ humid}$ was due to predominant p-type conduction in these compounds, with humid air resulting in a reduction in electron holes as shown by equation (7.2) [24, 26-28]. This is also possibly why there is an increase in ohmic resistance (R_O) when EIS is performed in humid air.

$$4h^{\bullet} + 4O_O{}^{\times} + 2H_2O \leftrightarrow 4(OH)_O{}^{\bullet} + O_2 \qquad (7.2)$$

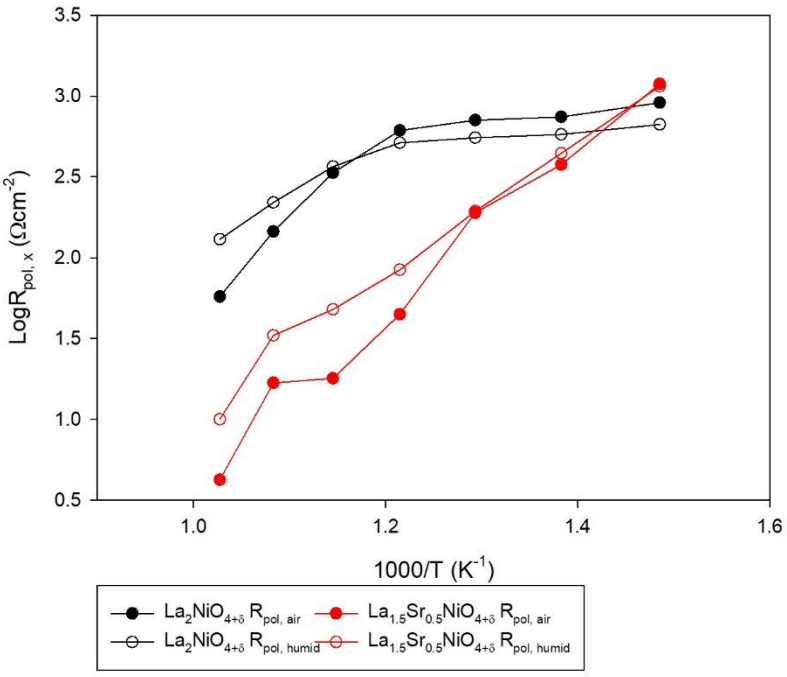


Figure 7.15: $R_{pol,\ air}$ (filled circle) and $R_{pol,\ humid}$ (empty circle) for $La_2NiO_{4+\delta}$ (black) and $La_{1.5}Sr_{0.5}NiO_{4+\delta}$ (red).

It has also been speculated that this difference occurs in electrode materials with high electrical conductivity as they have high electron hole concentration [27]. In this respect, $R_{pol,\ dry} > R_{pol,\ humid}$ was seen for the complete temperature range measured for $La_{3-x}Pr_xNi_2O_{7-\delta}$, and $La_{4-x}Pr_xNi_3O_{10-\delta}$ samples (Figure 7.16 and Figure 7.17). These samples all showed greater electronic conductivity than $La_2NiO_{4+\delta}$ (Chapter 5 and Chapter 6).

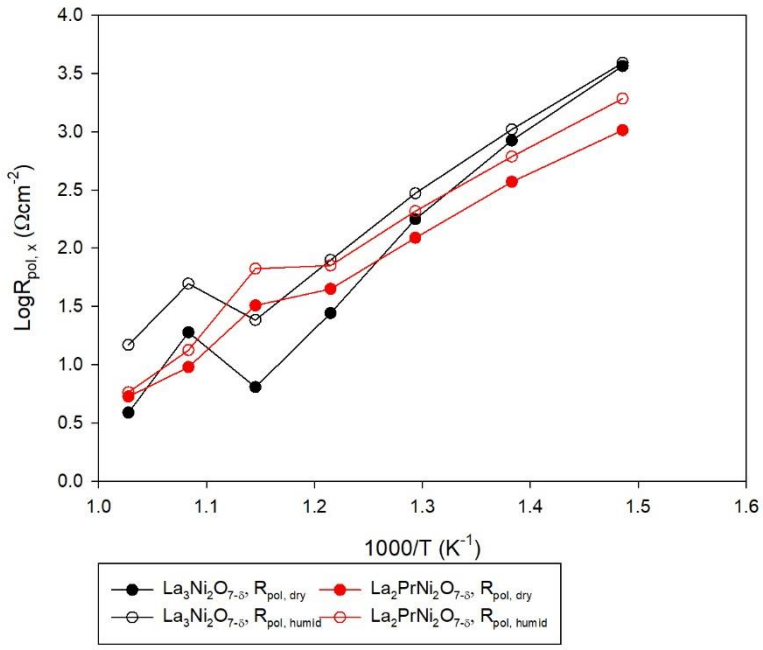


Figure 7.16: $R_{pol, air}$ (filled circle) and $R_{pol, humid}$ (empty circle) for $La_3Ni_2O_{7-\delta}$ (black) and $La_2PrNi_2O_{7-\delta}$ (red).

$La_{3-x}Pr_xNi_2O_{7-\delta}$ generally showed better R_{pol} values than $La_{2-x}Sr_xNiO_{4+\delta}$, which can be expected as $La_{3-x}Pr_xNi_2O_{7-\delta}$ showed better ionic conductivity. There was no drastic difference between the R_{pol} for $La_3Ni_2O_{7-\delta}$ and $La_2Pr_xNi_2O_{7-\delta}$, as there was no drastic difference in the 4 probe measurements for the two samples (Chapter 6). Generally, as the temperature increased R_{pol} decreases suggesting an increase in ionic conductivity, however for $La_3Ni_2O_{7-\delta}$ there was a slight increase in R_{pol} at 650°C, which did not correlate to a phase change or the previously shown 4-probe data. It should be noted though that the Pr doped sample saw this same increase in R_{pol} values at a lower temperature (600°C), however once again it does not correlate with a phase change, or the previously shown 4-probe data.

Symmetrical cell tests of $La_{4-x}Pr_xNi_3O_{10-\delta}$ samples showed improved R_{pol} (Figure 7.17) values compared to the other Ruddlesden-Popper samples. Doping of Pr showed an increase in R_{pol}; again $R_{pol, dry}$ was always greater than $R_{pol, humid}$ (Figure 7.18), attributed to the reduction of electron holes in humid air [24, 27]. $La_4Ni_3O_{10-\delta}$ achieved a maximum $R_{pol, dry}$ and $R_{pol, humid}$ value of 3.66 Ωcm^{-2} and 7.54 Ωcm^{-2}, respectively. $La_{3.75}Pr_{0.25}Ni_3O_{10-\delta}$ and $La_3PrNi_3O_{10-\delta}$ achieved a $R_{pol, dry}$ of 1.13 Ωcm^{-2} and 0.97 Ωcm^{-2}, respectively showing very little difference between the R_{pol} values.

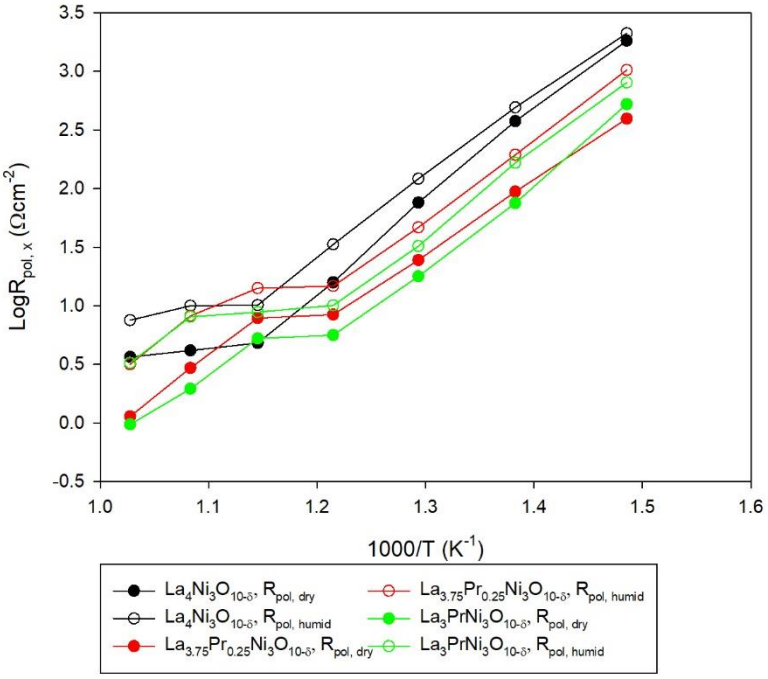


Figure 7.17: $R_{pol,\ air}$ (filled circles) and $R_{pol,\ humid}$ (open circles) for $La_4Ni_3O_{10-\delta}$ (black) and $La_{3.75}Pr_{0.25}Ni_3O_{10-\delta}$ (red) and $La_3PrNi_3O_{10-\delta}$ (green)

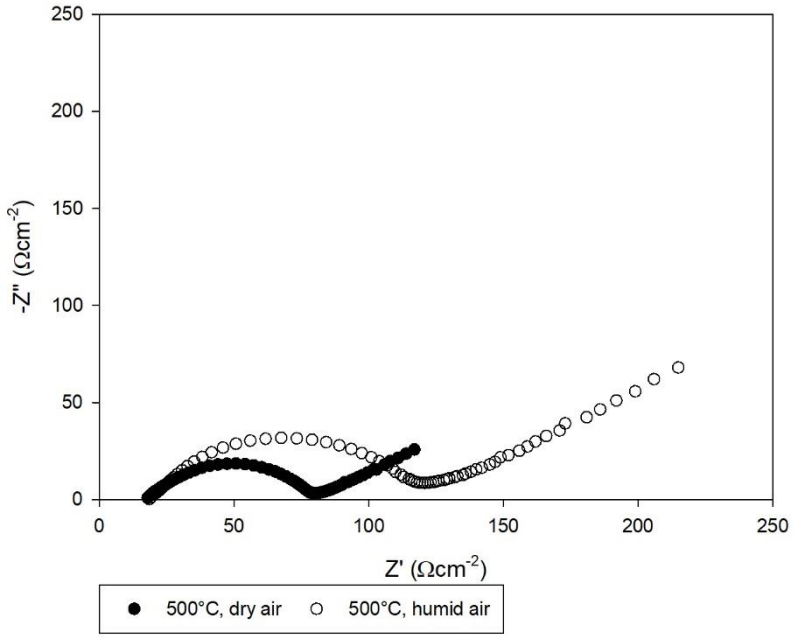


Figure 7.18: Nyquist plot for $La_4Ni_3O_{10-\delta}$, at 500°C in dry air (black filled circles), humid air (black open circles). The tail is observed coming from a semi-circle at low frequencies, possibly due to mass-transfer diffusion processes [9].

7.6 Cell Fabrication and Testing

To begin developing a PCCC, electrode materials need to be selected. When considering a fuel cell, the anode is a mixture of the electrolyte ($BaCe_{0.6}Zr_{0.3}Y_{0.1}O_{3-\delta}$) with NiO, whilst the cathode material varies. For the manufacturing of these cells $La_2NiO_{4+\delta}$ was selected as the cathode, as the symmetrical cell using $La_2NiO_{4+\delta}$ showed the conventional decrease in R_{pol} in humid air compared to dry air.

7.6.1 Attempt at Co-Pressing of Anode and Electrolyte

For the fabrication of proton conducting cells, a common method within the literature is through co-pressing. Co-pressing was attempted for fabricating cells. The fuel electrode composition shown in Table 7.1 was ball milled at 500 rpm for 15 min with 4 repetitions using a Fritsch Pulverisette 7 Planetary Micro Mill, 12 mL pots and four 10 mm zirconium oxide (ZrO_2) balls. The powders were then pressed using a 30 mm die press and a weight of 10 tons. The plunger was then removed and $BaCe_{0.6}Zr_{0.7}Y_{0.1}O_{3-\delta}$ spread onto the anode surface. 10 tons pressure was then applied to the pellet again. The pellet was then placed onto a bed of $BaCe_{0.6}Zr_{0.7}Y_{0.1}O_{3-\delta}$ sacrificial powder and further covered with more sacrificial powder to mitigate barium evaporation and any adverse reactions with the alumina plate or alumina weight. Finally, the pellet was sintered at 1400°C for 5 h similar to Lv *et al.* [15]. A lower temperature, compared to the electrolyte sintering temperature was used as the fuel electrode contained a large amount of Ni, and previously when using 4 wt% of NiO as a sintering aid at 1500°C for 10 h, the pellet cracked.

Once the pellet had finished sintering in the muffle furnace, it was taken out and the sacrificial powder removed. The pellet appeared to be cracked. In particular, the fuel electrode appeared to be separated into three pieces, possibly due to substantial contraction at the higher temperatures. The two sections of the pellet, fuel electrode and electrolyte, did appear to be well fused to one another. The cracking was possibly due to the difference in thermal expansion coefficients of the two components leading to the cell cracking and so unusable (Figure 7.19).



Figure 7.19: Image of co-pressed $BaCe_{0.6}Zr_{0.7}Y_{0.1}O_{3-\delta}$ fuel electrode and electrolyte. The surface layer is the fuel electrode which has broken into various segments.

The SEM (Figure 7.20) of the electrolyte showed a dense electrolyte, as well as a dense fuel electrode. EDXS of the fuel electrode showed that the NiO had formed distinct spots on the fuel electrode surface, instead of mixing with the electrolyte powder and becoming evenly distributed. Due to the state of the cell, it was decided an alternative method of producing cells would be attempted.

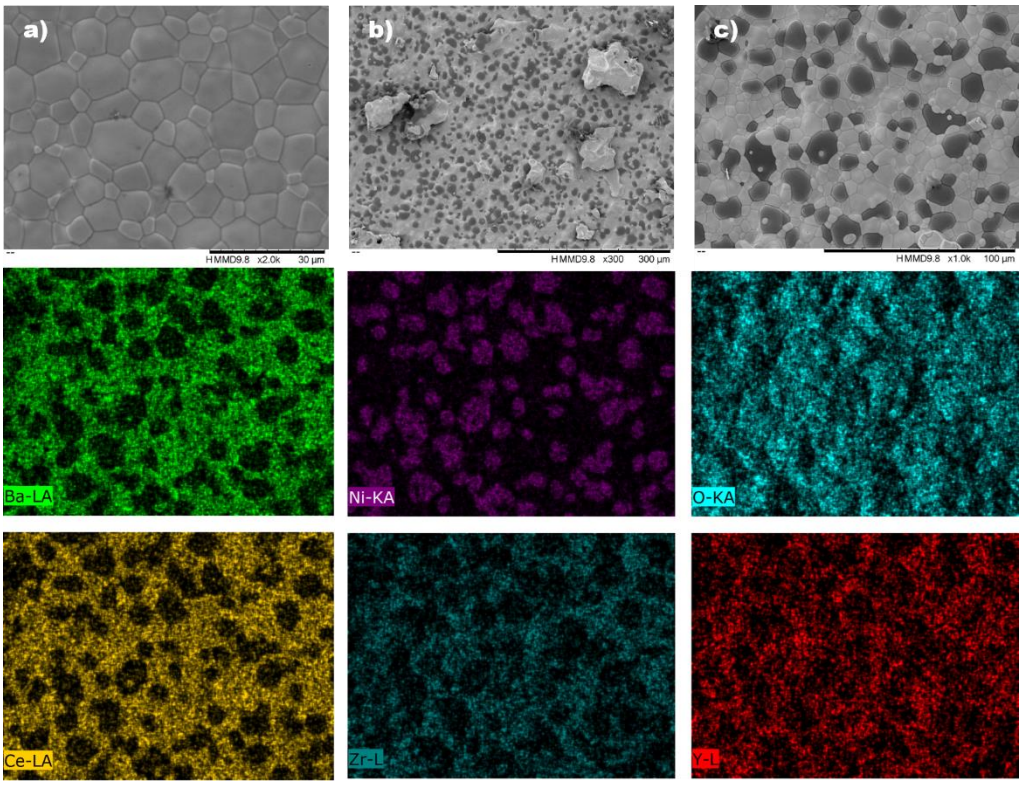


Figure 7.20: SEM and EDXS of co-pressed $BaCe_{0.6}Zr_{0.7}Y_{0.1}O_{3-\delta}$. a) shows the electrolyte side of the pellet, b) shows the anode side of the pellet at x300 magnification, c) shows x1000 magnification of the anode with EDXS analysis of the image in the following.

7.6.2 Anode Supported Cell

As co-pressing and co-sintering did not appear to be successful it was decided to attempt to make an fuel electrode supported cell, by pre-sintering the fuel electrode first and spin coating an electrolyte layer on top. The electrolyte would then be sintered at a higher temperature. Fuel electrode supported cells tend to have lower ohmic resistances, as they allow the use of thinner electrolytes. The fuel electrode mixture was first pressed using a 30 mm pellet die. The fuel electrode pellets were then sintered at 1300°C for 6 h. 1300°C was used as there was no requirement to make a dense electrolyte, but rather the fuel electrode should be porous.

On top of the anode pellets was then spin coated a mixture of electrolyte powder and ink vehicle. Three different amounts of solid loading were attempted to see which was the best: these were: 33%, 58% and 66% solid loading. 500 μL of electrolyte ink was spin coated ensuring that the surface of the fuel electrode was completely covered. Three layers were spin coated at 100 rpm for 15 s and then 2500 rpm for 25 s. Between each layer the pellet was left to dry at 30°C for 30 min. After the final layer was spin coated, the pellet was left to dry overnight at 30°C.

SEM images (Figure 7.21) of the sample post-sintering show the formation of several cracks throughout the electrolyte for each solid loading percentage. A solid loading of 33% appeared to show large pores due to lack of electrolyte material. Whilst a solid loading of 58% appeared to have the least number of visible cracks at a magnification of x30. Increasing the solid loading further to 66% showed an increase in the quantity of cracks throughout the surface of the electrolyte. The cracks may have been caused due to the fuel electrode shrinking more than the electrolyte during sintering. All cells were not suitable of a quality for cell testing due to the cracks, as this would allow the reactant gases to pass through the electrolyte.

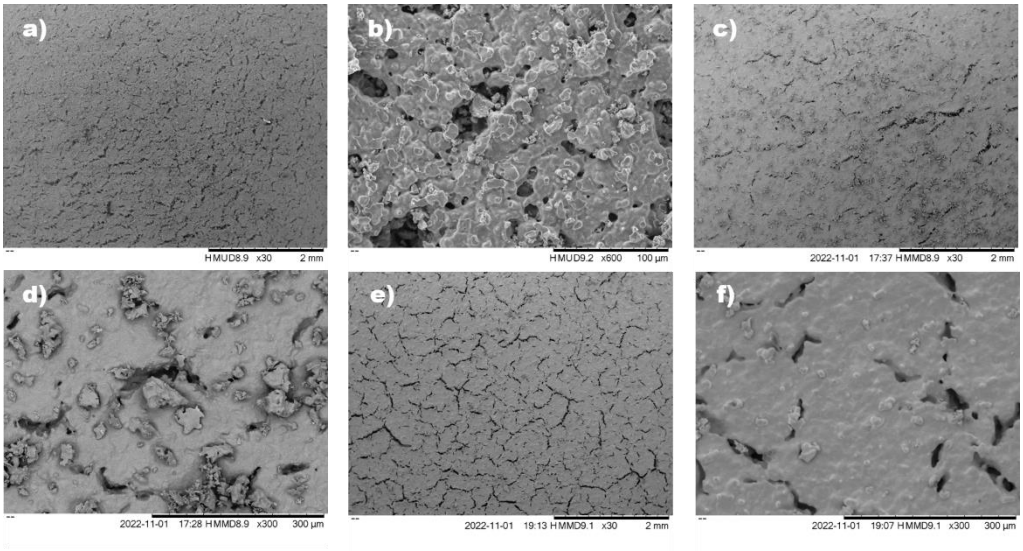


Figure 7.21: SEM images of the spin coated electrolyte after sintering a) and b) are the electrolyte with 33% solid loading, c) and d) are the electrolyte with 58% solid loading, e) and f) are the electrolyte with 66% solid loading.

7.6.3 Electrolyte Supported Cell

As previous attempts at making a successful cell had proven to be inadequate, the method of electrolyte supports to create dense electrolyte pellets for symmetrical cell testing was used to make a complete cell. Electrolyte pellets were pressed and sintered at 1500°C for 10 h. A mask was applied to one side of the electrolyte, 175 µL of fuel electrode ink was applied to one side of the electrolyte pellet and spread across the exposed area. The pellet was spin coated at 100 rpm for 5 s, to aid in distribution of the ink across the complete surface of the mask. Then the rotation speed was increased to 2500 rpm to ensure an even distribution of the ink and to remove any excess. The pellet was then dried at 40°C. Once dried, a second layer of fuel electrode ink was applied. For the second layer 125 µL was applied and the same spin coating programme was used. The second layer was also dried at 40°C (Figure 7.22). The fuel electrode was then sintered at 1100°C for 4 h. The fuel electrode was covered with sacrificial powder to mitigate barium evaporation. A air electrode was applied on the opposite side of the electrolyte and sintered at 1000°C for 4 h.

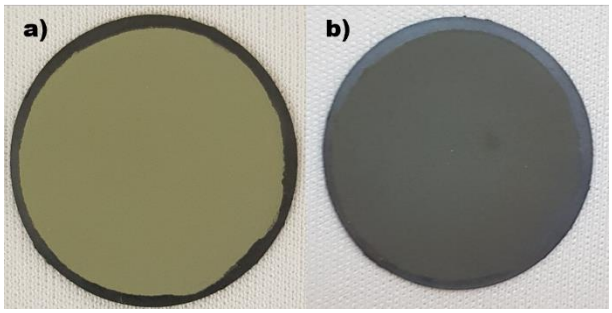


Figure 7.22: Images of spin coated half cells a) before sintering b) after sintering.

After sintering, SEM was performed (Figure 7.23) on the pellet and the fuel electrode appeared to be porous as to allow the diffusion of gases. SEM was also performed on the electrolyte to ensure the pellet had no cracks. An air electrode was applied on the opposite side of the electrolyte and sintered at 1000°C for 4 h.

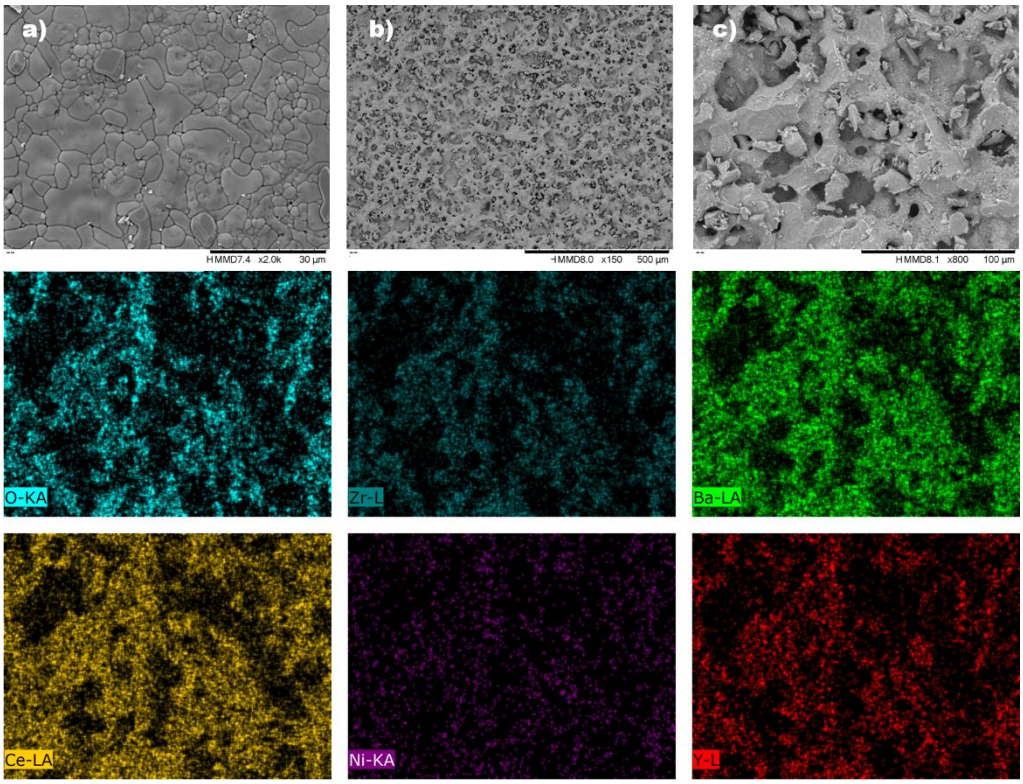


Figure 7.23: SEM images of the sintered half-cell. a) is the electrolyte, b) is the anode at x150 magnification, c) is the fuel electrode at x800 magnification followed by EDXS of the same surface.

The cell was tested in a custom-made fuel cell rig. Fuel cell tests were performed at 500°C, 550°C and 700°C. Proton conduction was expected to be predominant at 500°C and 550°C, while testing at 700°C

allowed the data to be compared to oxide ion conducting electrolyte literature, as testing is often done at this temperature. Measurements were taken under two flow rate profiles (Table 7.4), one used nitrogen as a carrier gas while the other did not. It was assumed that by introducing N_2, it would aid in H_2 flowing through the vertical rig, especially as the H_2 would have to enter from the top of the rig and would have to flow against gravity to reach the cell at the centre of the furnace (Figure 3.9). To compensate for the extra N_2, the flow rate of air was increased on the counter side.

Table 7.4: Flow rate profiles used when testing cells as a fuel cell.

Gas	**Profile 1 Flow rate (mL min^{-1})**	**Profile 2 Flow rate (mL min^{-1})**
Air	40	80
Hydrogen	40	40
Nitrogen	0	40

Fuel cell testing showed low current densities and power outputs (Figure 7.24) compared to the literature. At 500°C and 550°C, the OCV of the cells were drastically lower than the expected value, possibly due to the presence of small pores, which had been seen by SEM before testing (Figure 7.25). Increasing the temperature, the OCV would be expected to decrease, as per the Nernst equation, however instead the OCV increased. The increase was possibly due to the cell expanding during heating, causing the small pores to close. Despite this increase, the OCV was still lower than expected, possibly due to the triple conducting nature of the electrolyte material (some electronic conduction in the electrolyte).

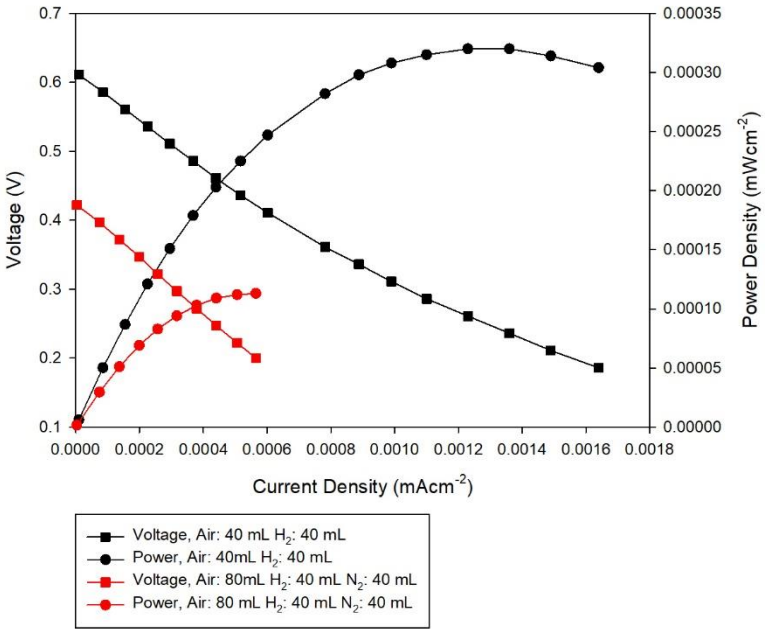


Figure 7.24: Voltage (square) and power density (circle) verses current density of the cell tested using the various flow rate profiles at 500°C

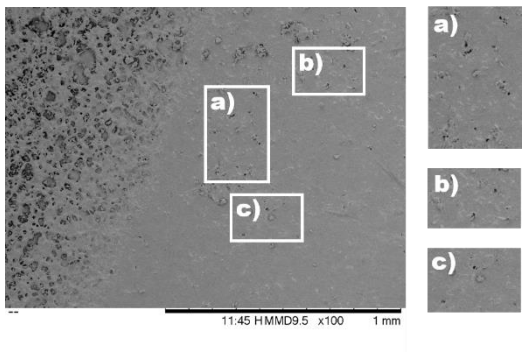


Figure 7.25: SEM image of cell before testing. The more porous section, to the left side of the larger image, is the fuel electrode. While the denser section is the electrolyte.

Profile 2 saw lower current densities at 500°C, which is possibly due to the greater air flow rate, leading to greater gas leakage. This may result in the OCV decreasing and therefore lower current densities and power outputs are observed. The OCV also possibly decreased due to the added N_2 diluting the H_2 partial pressure.

Increasing the temperature to 700°C (Figure 7.26) saw higher current and power densities. The maximum current density of profile 1 and 2 were 4.22×10^{-2} $mAcm^{-2}$ and 4.34×10^{-2} $mAcm^{-2}$, at 700°C

respectively. While the maximum power density was 1.16×10^{-2} $mWcm^{-2}$ and 1.29×10^{-2} $mWcm^{-2}$, respectively. Profile 2 saw a lower OCV due to the higher O_2 flow rate compared to the flow rate of H_2, while also the introduction of N_2 diluted the cathode feed stream further reducing the OCV as per the Nernst equation (Equation 3.29). However, a higher power density was achieved possibly due to the N_2 aiding the H_2 to flow through the vertical setup of the rig.

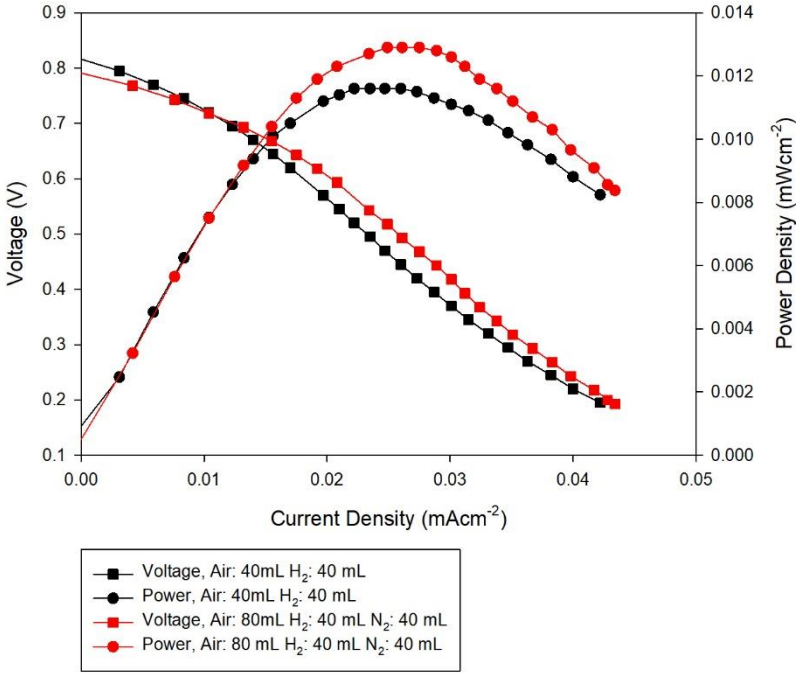


Figure 7.26: Voltage (square) and power density (circle) against current density of the cell tested using the various flow rate profiles, from Table 7.4, at 700°C.

Another cell was manufactured using a similar process. In this case the fuel electrode was sintered at 1300°C for 6 h. A sintering temperature higher than 1300°C was not attempted as it was expected that sintering a high Ni content at a higher temperature would cause the cell to crack, similar to that seen when sintering electrolyte pellets with NiO sintering aid. Increasing the sintering temperature was shown to improve the power output and current densities at 700°C (Figure 7.27). Once again, the two flow rate profiles were applied, with the OCV decreasing with the higher air flow rate, due to similar reasons as previously stated. For profile 1 a maximum current density and power density of 1.84 $mAcm^{-2}$ and

5.26×10^{-1} $mWcm^{-2}$, and for flow rate profile 2 values of 2.19 $mAcm^{-2}$ and 6.17×10^{-1} $mWcm^{-2}$ were achieved.

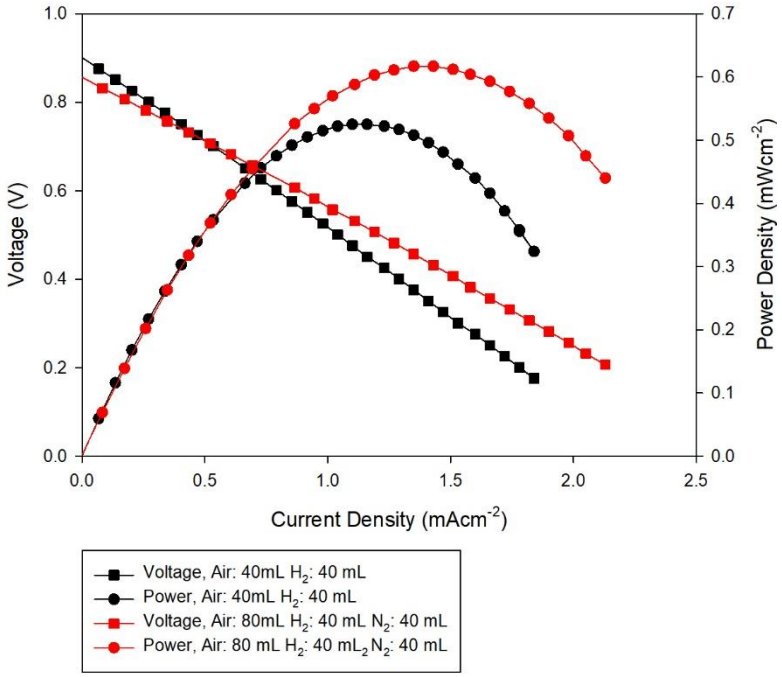


Figure 7.27: Voltage (square) and power density (circle) verses current density of the cell tested using the various flow rate profiles at 700°C. Fuel electrode was sintered at 1300°C for 6 h.

7.6.3.1 Effect of Adding a Water Bubbler on Cell Testing

The performance of the tested fuel cells was lower than those reported within the literature. A pre-treatment using a H_2O bubbler was then attempted. The previously tested cell, that was sintered at 1300°C and covered with sacrificial powder, was exposed to H_2 and N_2 which were passed through a bubbler containing deionised H_2O on the fuel electrode side. The H_2 and N_2 contained 3 vol% H_2O, it has been previously shown that a humid atmosphere may facilitate proton transport [29].

40 $mLmin^{-1}$ of H_2 and 40 $mLmin^{-1}$ N_2 with 3% H_2O entered the rig at 400°C which was then ramped to 700°C and held for 12 h. The N_2 mass flow controller was then turned off, the rig was cooled down to 500°C and the flow of H_2 was diverted so that it did not enter the bubbler but went straight to the rig. Potential stair step measurements were then taken again (Figure 7.28 and Figure 7.29). An improvement

could be seen in the OCV and performance of the cell, as the fuel electrode became hydrated facilitating OH^- incorporation and proton transport. At 700°C the maximum current density of 11.5 $mAcm^{-2}$ was achieved and the maximum power density 3.37 $mWcm^{-2}$ was achieved.

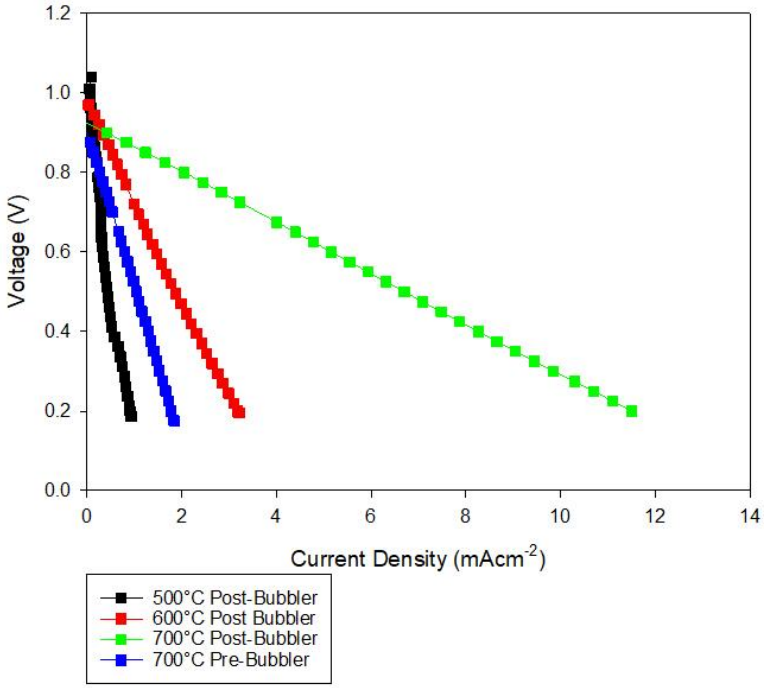


Figure 7.28: Voltage verses current density of cell before and after introduction of bubbler.

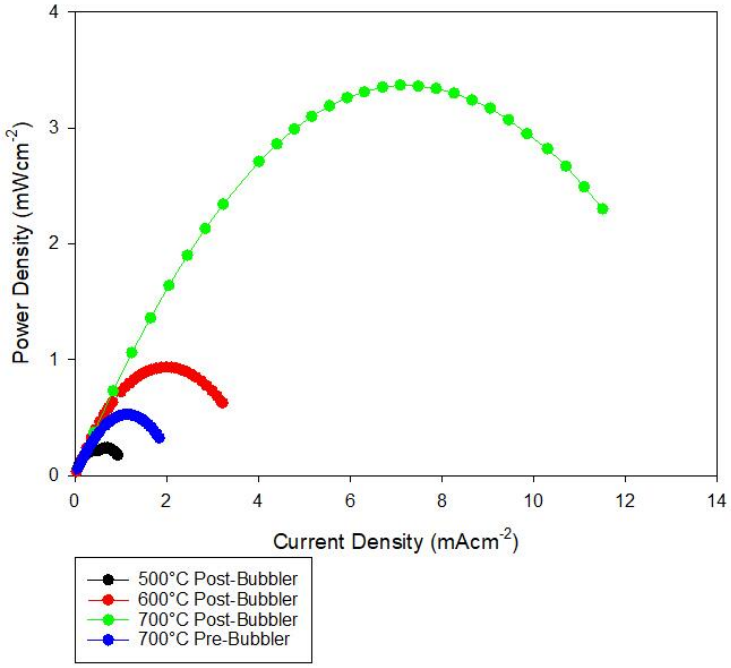


Figure 7.29: : Power density verses current density of cell before and after introduction of bubbler.

7.6.3.2 *Investigation of the Effect of emission of Sacrificial Powder*

When sintering the fuel electrode, the pellet had previously been covered with sacrificial powder. Within the literature, covering the fuel electrode with sacrificial powder is not often stated. Therefore, it was decided to explore whether removal of the sacrificial powder would have an impact on the performance of the cell. In addition, by not covering the cell with more sacrificial powder, less $BaCe_{0.6}Zr_{0.3}Y_{0.1}O_{3-\delta}$ electrolyte would need to be synthesised and used in the cell manufacture process.

After sintering the anode, without the sacrificial powder, SEM was performed (Figure 7.30). From the SEM images it was evident, that Ni was present. The Ni is represented by the darker spots on the SEM image, and these were not as observable on the anodes previously sintered with sacrificial powder.

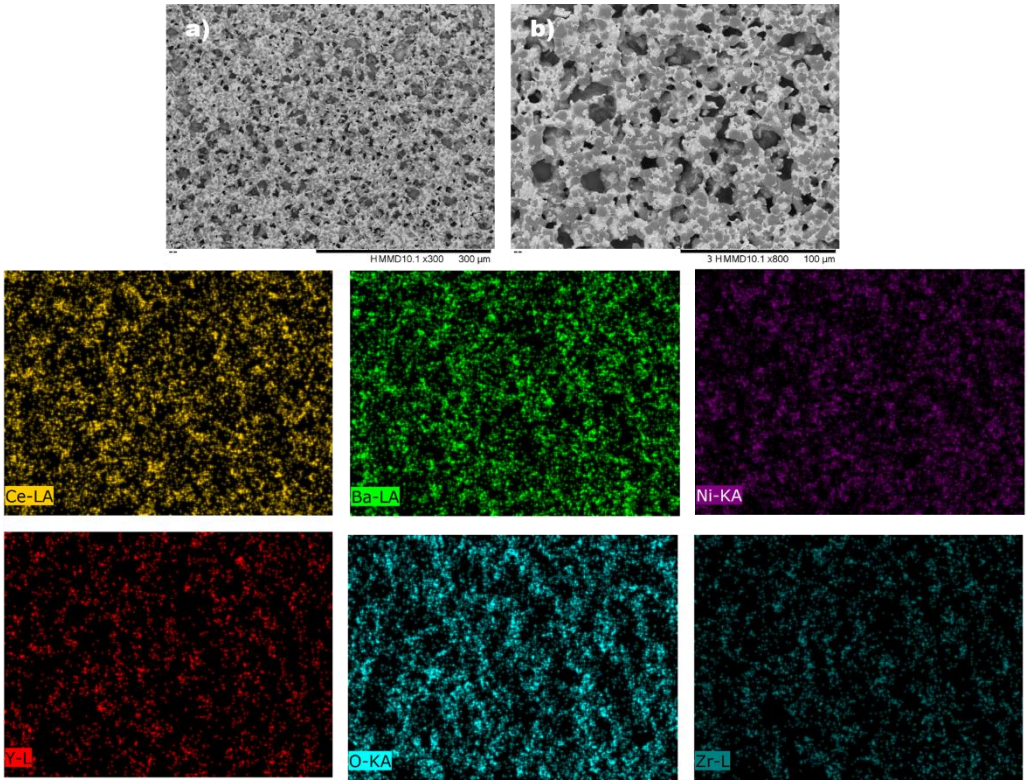


Figure 7.30: SEM of fuel electrode after sintering without sacrificial powder covering. a) x300 magnification and b) x800 magnification followed by EDXS of the image.

Testing of the cell was performed at 700°C (Figure 7.31). The OCV was lower than ideal at 500°C. Testing at 700°C showed higher OCV than previous cells. A higher OCV is an indication that there is better separation of the gases on either side of the cell, suggesting a dense electrolyte. However, the performance of this cell was lower compared to the previously tested cell, possibly due to Ba volatility. A maximum power density of 1.21 $mWcm^{-2}$ and current density of 3.70 $mAcm^{-2}$ was achieved after exposure to humid H_2. From the results it was determined that covering the fuel electrode with sacrificial powder helped to improve the performance of the cell.

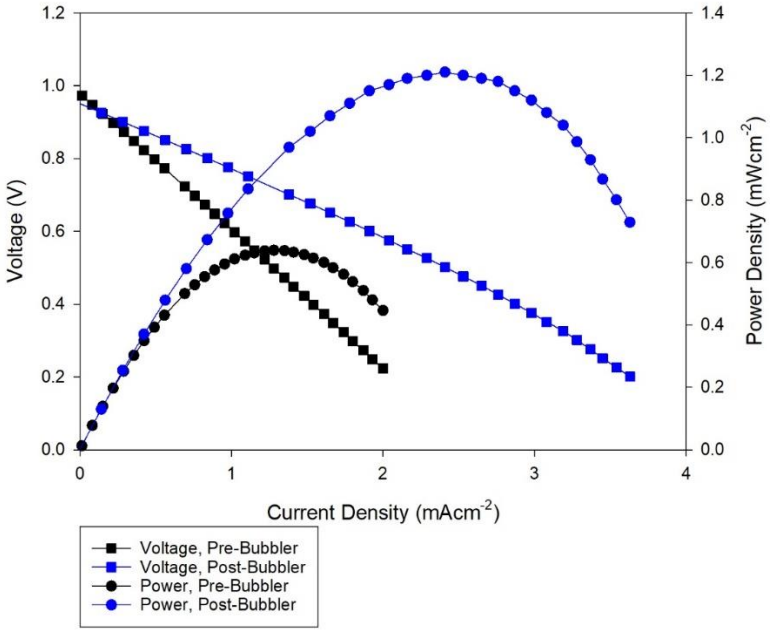


Figure 7.31: Voltage (square) and power density (circle) verses current density of the cell tested before and after introducing the bubbler. Measurements taken at 700°C.

7.6.3.3 *Effect of Polishing Electrolyte Surface on Current Density and Power*

Electrolyte pellets were polished using sandpaper in an attempt to remove any debris/Ba deficiency layer on the surface of the pellet. The debris was most likely due to some particles from the sacrificial powder agglomerating and sintering to the surface of the electrolyte. By polishing the surface, such particles were removed. Polishing, however, caused the pores within the electrolyte to be exposed to the surface (Figure 7.32). As the pores were small, the pellet was still taken further for testing, as applying fuel electrode ink could possibly cover the pores. Fuel electrode ink was applied in a similar manner as previously discussed and the cell sintered at 1300°C for 6 h. Measurements were taken first without H_2 passing through a bubbler. Followed by further measurements taken after exposing the fuel electrode to humid H_2 and N_2, as previously discussed in section 7.6.3.1 .

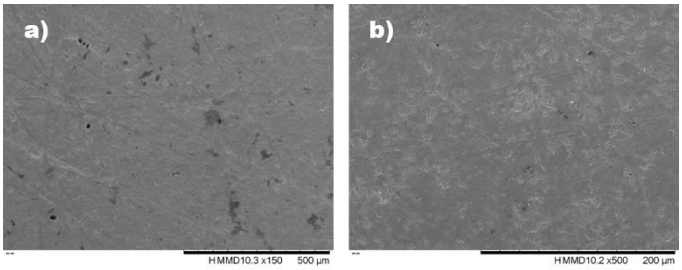


Figure 7.32: SEM images of surface of $BaCe_{0.6}Zr_{0.3}Y_{0.1}O_{3-\delta}$ pellet after polishing each image shows one side of the pellet.

The OCV of the cell at 700°C was lower than the previously tested cells, as could be expected (Figure 7.33), possibly due to the previously mentioned pores within the electrolyte being exposed. Introducing humid H_2 into the system was once again seen to increase the OCV and the performance of the cell. The maximum current density 8.45 $mAcm^{-2}$ and power density of 2.25 $mWcm^{-2}$, were similar to the unpolished cell. Therefore there was not a drastic improvement in values compared to the unpolished electrolyte cell.

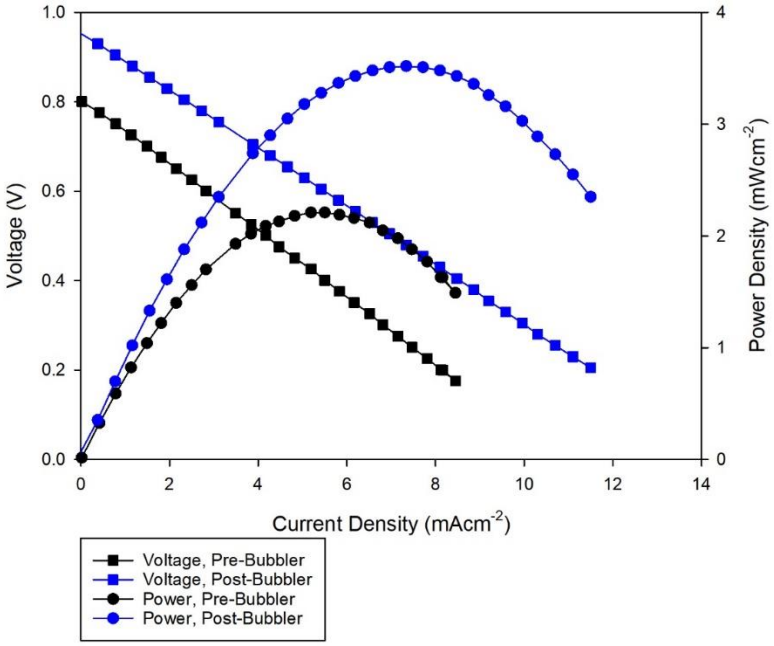


Figure 7.33: Voltage (square) and power density (circle) verses current density of the cell where the electrolyte was polished before the fuel electrode was applied. The cell was tested before and after introducing the bubbler, in the H_2 flowpath. Measurements taken at 700°C.

7.6.3.4 Investigation of Increasing Ni Content in the Anode of the Fuel Cell Anode

As the performance of these cells appeared to be low, increasing the Ni content in the fuel electrode was attempted as Ni catalyses the hydrogen oxidation reaction. To do this, the quantity of NiO in the anode powder was increased, requiring another component of the powder mixture to decrease. It was decided to decrease the quantity of the pore former as decreasing the quantity of $BaCe_{0.6}Zr_{0.3}Y_{0.1}O_{3-\delta}$ would reduce the number of oxygen vacancies. The new quantities for the anode mixture can be seen in Table 7.5. The anode mixture was developed into an ink once again and a similar process of sintering at 1300°C for 6 h with sacrificial powder was used, as this had previously shown to be useful. SEM (Figure 7.34) of the sintered anode, appears to show less porosity in the fuel electode which is to be expected as the quantity of pore former was decreased.

Table 7.5: Composition of new anode, with greater percentage of NiO and lower percentage of pore former.

Composition	Quantity in mixture (%)
$BaCe_{0.6}Zr_{0.3}Y_{0.1}O_{3-\delta}$	33
NiO	61
Pore former	5

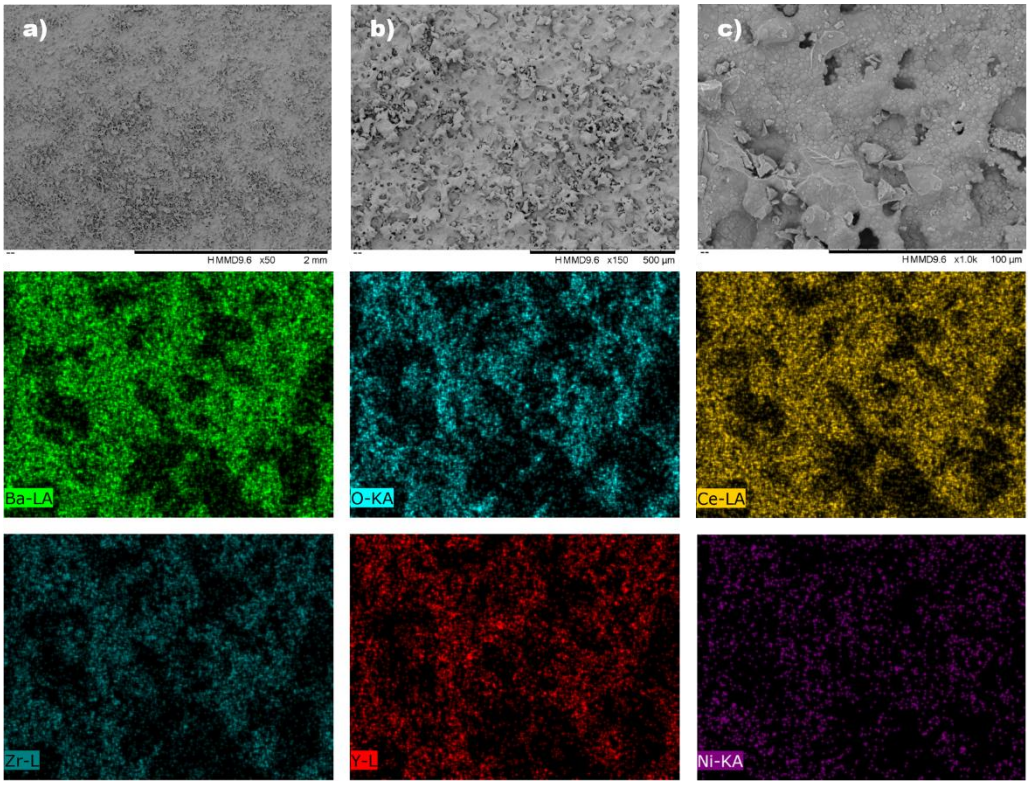


Figure 7.34: SEM images of new fuel electrode composition after sintering but before reducing a) x50 magnification b) x150 magnification and c) x1000 magnification followed by EDXS of image.

Potential stair step testing (Figure 7.35) was performed after exposing the anode to humid H_2; measurements were taken at 700°C and increases in current (7.43 $mAcm^{-2}$) and power density (3.32 $mWcm^{-2}$) were seen. At higher currents (where mass transport losses dominate), there is significant polarisation as shown by the plots. It is possible that at these high current densities are due to a reduction in pore former and hence porosity of the anode, there are less pathways for the reactant gases to diffuse through the cell were present, creating hurdle for species transport, in turn this had a negative effect on the power density of the cell.

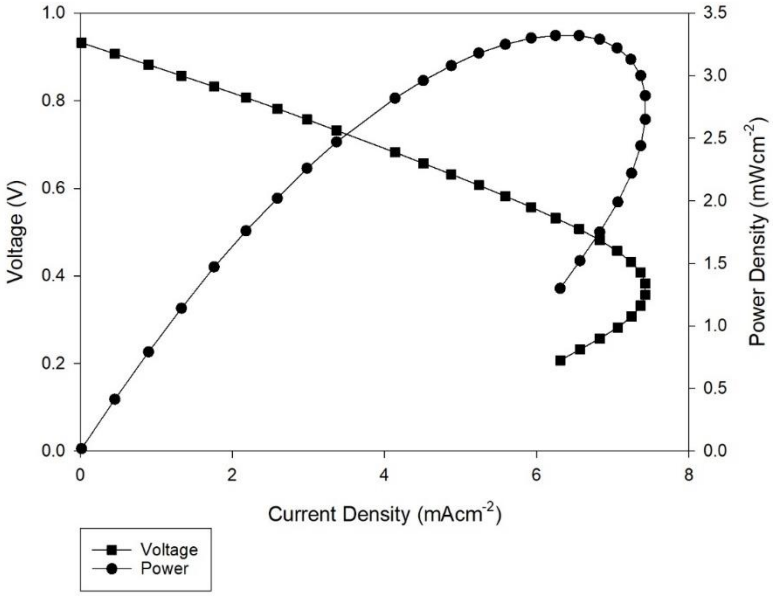


Figure 7.35: Voltage (square) and power density (circle) against current density of the cell with new fuel electrode compositions. Measurements taken at 700°C.

7.6.3.5 *Effect of Increasing Number of Spin Coated Anode Layers*

An alternative attempt to increase the performance of the cell by increasing the number of spin coated anode layers was attempted. Instead of two layers, four layers were applied. Drying and sintering performed in the same way as previously stated. Sacrificial powders were used to cover the fuel electrode, as not covering the fuel electrode showed a decrease in performance of the cell. SEM/EDXS (Figure 7.36) analysis showed a greater presence of Ni in particular regions, whilst also maintaining the porosity of the anode.

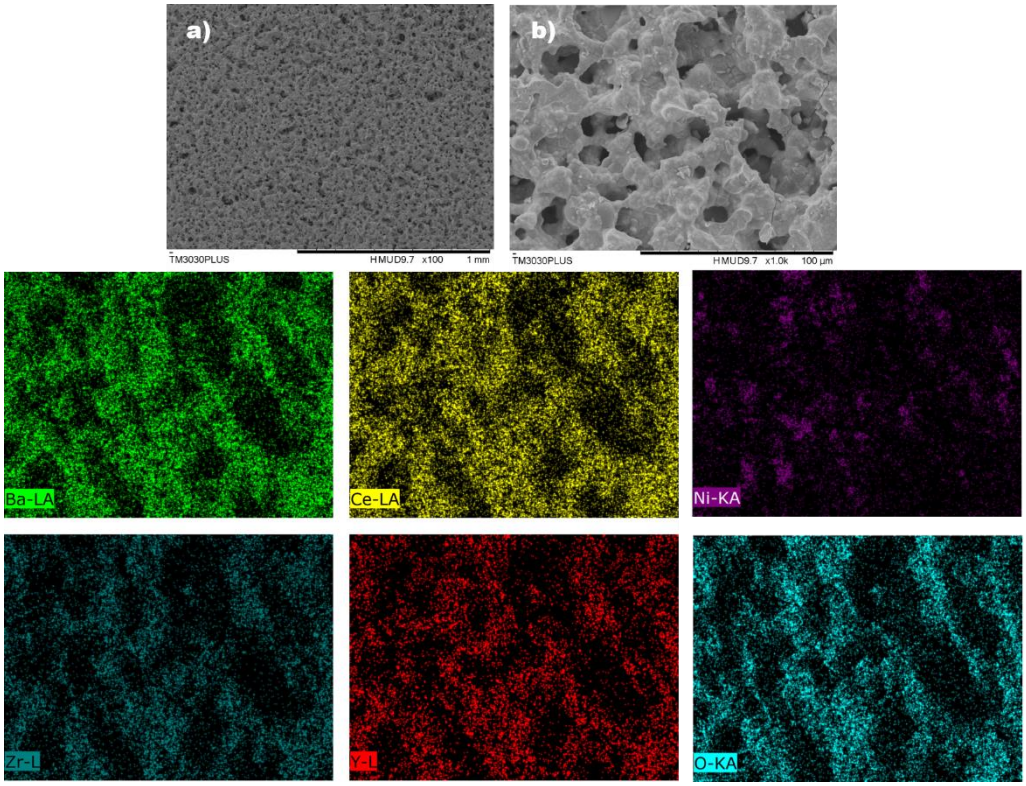


Figure 7.36: SEM images of the four layer anode after sintering. a) x100 magnification and b) x1000 magnification, followed by EDXS of the image.

The OCV at 700°C appeared to be similar to that of the previously tested cells, whilst at 500°C and 600°C the OCV was higher than with the previous cells at the same temperature, suggesting that the four-layer anode was able to cover the pores better than the two-layer version. Fuel cell testing was performed at 500°C where a current density of 0.37 $mAcm^{-2}$ and power density of 0.12 $mWcm^{-2}$ was achieved. Increasing the temperature to 700°C showed larger current density (14.8 $mAcm^{-2}$) and power densities (4.94 $mWcm^{-2}$) (Figure 7.37 and Figure 7.38). Unlike with the cell that was made with the ink containing a higher content of NiO and lower content of pore former, there did not appear to be unexpected deviations in the trend of the polarisation curve.

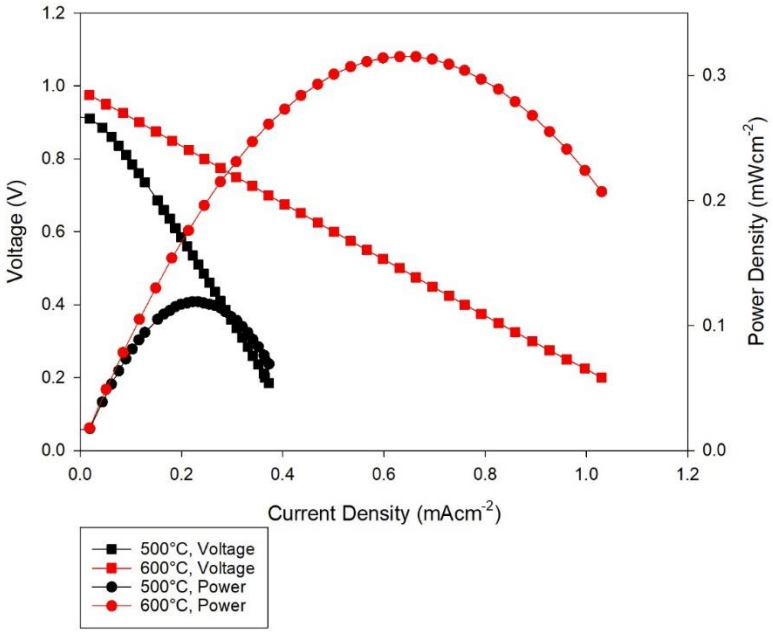


Figure 7.37: Voltage (square) and power density (circle) verses current density of the cell with four layers of fuel electrode spin coated on. Measurements taken at 500°C (black) and 600°C (red).

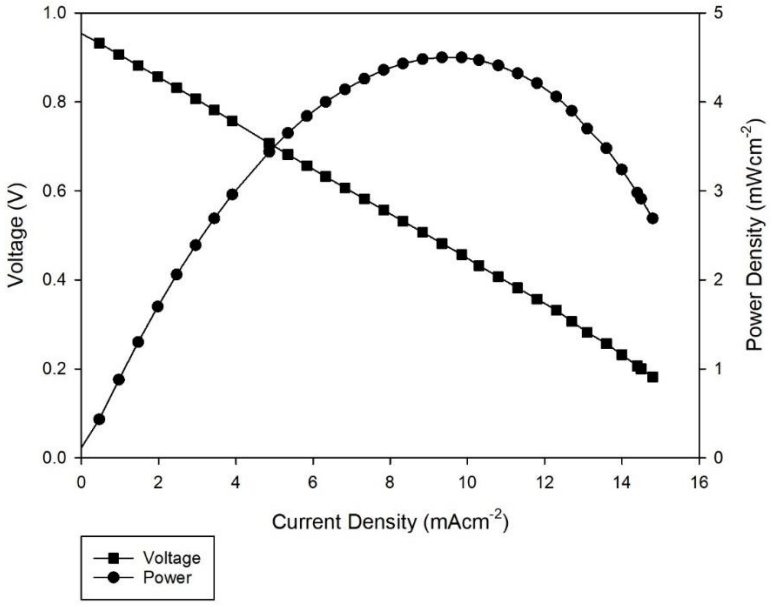


Figure 7.38: Voltage (square) and power density (circle) verses current density of the cell with four layers of fuel electrode spin coated on, measurements taken at 700°C.

7.7 Electrolysis Testing

A high temperature electrolysis test was performed on cells with a $La_2NiO_{4+\delta}$ and $La_3Ni_2O_{7-\delta}$ air electrode. The fuel electrode, previously the anode in fuel cell testing, composition was maintained as that shown in Table 7.1. Four layers of fuel electrode ink were applied, as this had been previously shown to give the highest current densities and power output, as well as covering the fuel electrode with sacrificial powders. Electrolysis tests for $La_2NiO_{4+\delta}$ were performed between 500°C and 700°C at 50°C intervals, with a H_2O flow rate of 0.82 gh^{-1}, 52 $mLmin^{-1}$ of air, a relative humidity of 80.3% was achieved. The hydrogen flow rate was set to 52 $mLmin^{-1}$ to ensure the OCV remained stable.

At 500°C and 550°C the OCV for the cell using $La_2NiO_{4+\delta}$ as the fuel electrode was 0.4 V and 0.6 V, suggesting leakage through pores in the electrolyte (Figure 7.39). The OCV at 600°C, 650°C and 700°C ranged between 0.85 V and 0.9 V. Suggesting that at higher temperatures the electrolyte expanded causing the tiny pores to reduce in size, similar to the effect seen during fuel cell testing. During electrolysis testing, increasing temperature resulted in an increase in the current density as could be expected. A maximum current density of -3.29 $mAcm^{-2}$ was achieved by the cell containing a $La_2NiO_{4+\delta}$ air electrode. The cell using a $La_3Ni_2O_{7-\delta}$ air electrode (Figure 7.40) showed an improvement in current density when operating as an electrolyser. The $La_3Ni_2O_{7-\delta}$ achieved a current density of -4.59 $mAcm^{-2}$ at 600°C and -21.3 $mAcm^{-2}$ at 700°C. At 700°C the cell using $La_3Ni_2O_{7-\delta}$ saw an improvement by a factor of over five, compared to the cell using $La_2NiO_{4+\delta}$. The improvement in electrolysis performance can be expected as $La_3Ni_2O_{7-\delta}$ had previously showed higher electrical conductivity (from 4 probe testing, Chapter 4) and better R_{pol} (from symmetrical cell testing).

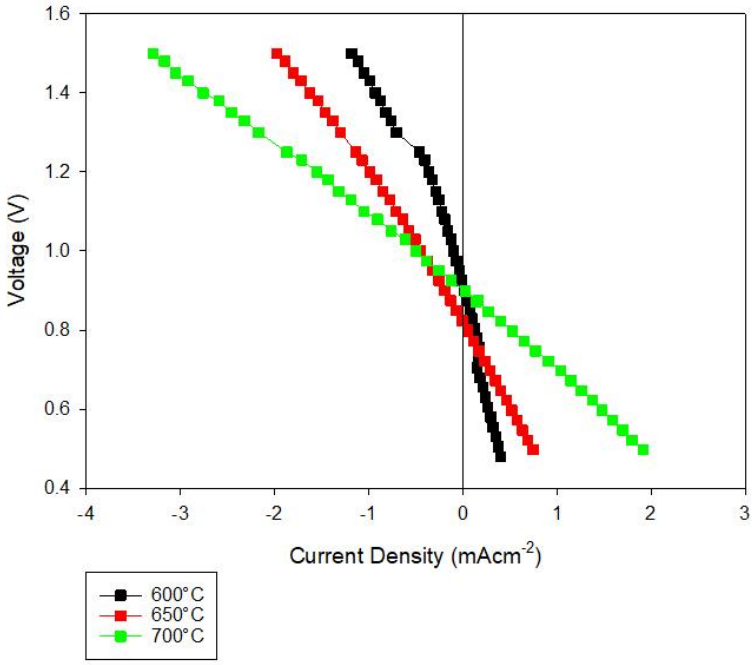


Figure 7.39: Electrolysis voltage against current density for cell with $La_2NiO_{4+\delta}$ air electrode. Measurements taken at 600°C (black square), 650°C (red square) and 700°C (green square).

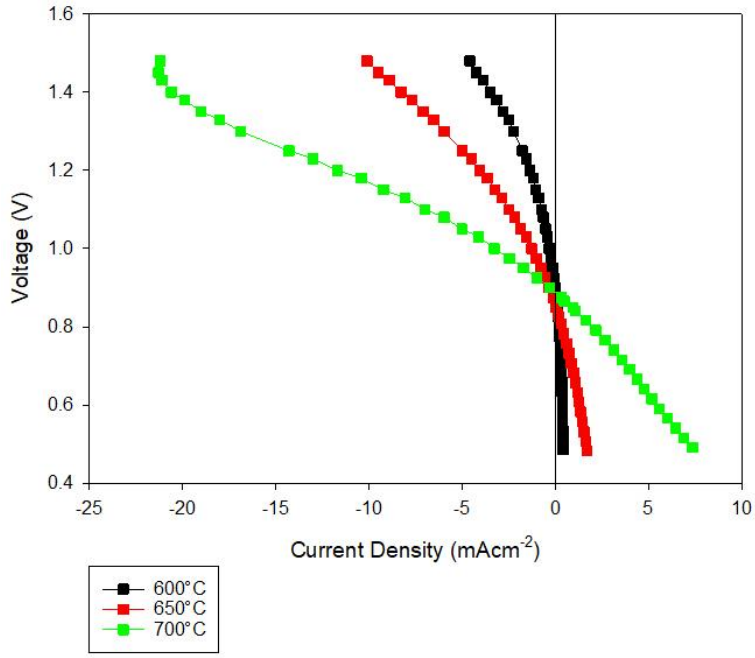


Figure 7.40: Electrolysis voltage against current density for cell with $La_3Ni_2O_{7-\delta}$ air electrode. Measurements taken at 600°C (black square), 650°C (red square) and 700°C (green square).

7.8 Conclusions

Various methods of cell fabrication were attempted. Fabricating of proton conducting ceramics was extremely difficult, as high sintering temperatures were required whilst also trying to mitigate loss of Ba. Ba evaporation was a key problem, which is rarely addressed in literature. The high sintering temperature was overcome through the use of NiO as a sintering aid. The issue of barium evaporation was overcome by adding Ba excess.

Using sintered $BaCe_{0.6}Zr_{0.3}Y_{0.1}O_{3-\delta}$ pellets, symmetrical cell tests were performed. Between 400°C and 550°C the $R_{pol,\ humid}$ was less than the $R_{pol,\ dry}$ for $La_2NiO_{4+\delta}$. Above 600°C, $R_{pol,\ dry} < R_{pol,\ humid}$. The higher order Ruddlesden-Popper phases showed similar characteristics regarding R_{pol} values, possibly a result of p-type conductivity.

Various methods of attempting to improve the performance of proton conducting ceramics were implemented. A maximum current density of 14.8 $mAcm^{-2}$ and power density of 4.94 $mWcm^{-2}$ were achieved, whilst at 500°C, when proton conducting was expected to be dominant, a maximum current density of 0.37 $mAcm^{-2}$ and power density of 0.12 $mWcm^{-2}$ was obtained, although values obtained from fuel cell testing were low compared to literature, electrolysis was attempted with $La_2NiO_{4+\delta}$ and $La_3Ni_2O_{7-\delta}$ air electrode, the latter showing the improved current density of -4.59 $mAcm^{-2}$ at 600°C and -21.3 $mAcm^{-2}$ at 700°C, respectively.

Chapter 8: Conclusion and Future Work

This thesis investigated applying cathodes for use in a proton conducting ceramics cells (PCCC)s. This chapter looks at the summaries and concludes the key findings from each chapter, as well as providing possibilities of future work.

8.1 Summary and Conclusions

8.1.1 Chapter 4

Chapter 4 looked at cobalt free electrodes, in particular barium ferrites ($BaFeO_{3-\delta}$) doped with bismuth (Bi) and niobium (Nb). Bi was chosen as even though it has been explored as a dopant for other perovskites for PCCC application, it has not been explored in particular for doping into lower cost $BaFeO_{3-\delta}$ for use in PCCCs. Nb doping was also explored similarly. Increasing the quantity of Bi or Nb was shown to increase the cell parameters mainly attributed to partial reduction of Fe to larger Fe^{3+}.

The various compositions synthesised were heated in humid nitrogen (N_2) to investigate whether the samples would incorporate water (H_2O). The samples were then heated in dry N_2 and a comparison of lattice parameters performed. The X-ray diffraction (XRD) patterns showed that the Bi doped samples were chemically stable in humid N_2, and Rietveld refinement showed an increase in lattice parameters. The XRD pattern of the sample heated in dry N_2 however, showed a second phase, which was confirmed through Rietveld refinement.

The Nb doped samples were also heated in humid N_2 and were shown to be chemically stable, with some H_2O incorporation shown from thermogravimetric analysis (TGA). When the Nb doped samples were heated in dry N_2, the XRD patterns remained similar to the original sample. Rietveld refinement showed an increase in the lattice parameters in both cases, with the increase in the lattice parameters of the humid N_2 sample being larger than the dry N_2 sample.

Electrical conductivity measurements were performed on all the samples; $BaFe_{0.925}Bi_{0.075}O_{3-\delta}$ showed the highest conductivity of the Bi doped samples, while $BaFe_{0.55}Nb_{0.45}O_{3-\delta}$ showed the highest

conductivity of the Nb doped samples. However, overall the conductivities of all the samples were quite low, and so it was concluded that the materials were not suitable for PCCC applications.

8.1.2 Chapter 5

Chapter 5 explored $La_2NiO_{4+\delta}$ and doping with strontium (Sr) and barium (Ba). Ba and Sr doping had been previously shown to improve the electrical and ionic conductivity of $La_2NiO_{4+\delta}$, although the stability of these materials in humid N_2, dry N_2 and humid O_2 had not been explored before. The samples were synthesised, and Rietveld refinement showed that the cell parameters decreased with increasing Ba/Sr quantities, which was attributed to the partial oxidation of Ni^{2+} to Ni^{3+}, for charge balance.

The synthesised samples were then heated in humid N_2, dry N_2 and humid O_2. The Ba doped samples heated in humid N_2 were shown to degrade, giving a range of impurities. In contrast $La_2NiO_{4+\delta}$ and the Sr doped samples remained chemically stable in all atmospheres. The samples that remained stable in humid N_2 showed some H_2O loss, as well as some carbon dioxide (CO_2) loss.

Variable temperature XRD (VT-XRD) was performed on $La_2NiO_{4+\delta}$ doped samples to investigate H_2O incorporation further. For $La_2NiO_{4+\delta}$ a change in symmetry was observed during heating, though the same symmetry change is not observed for the Sr doped samples. There was a small deviation in the a parameter on heating, which correlates with the temperature at which H_2O/CO_2 loss occurs. $La_{1.5}Sr_{0.5}NiO_{4+\delta}$ also showed a slight deviation in the a parameter (at 625°C), approximately when CO_2 loss was expected from the TGA results. Besides this, no other changes in lattice parameters indicate H_2O loss. The electrical conductivity of the samples shows an increased with increasing Sr content, attributed to the partial oxidation of Ni^{2+} to Ni^{3+}.

8.1.3 Chapter 6

Further Ruddlesden-Popper phases were explored in Chapter 6, specially $La_3Ni_2O_{7-\delta}$ and $La_4Ni_3O_{10-\delta}$ doped with Pr. Previous work had shown the incorporation of Pr doped $La_4Ni_3O_{10-\delta}$ for use in OC-SOCs, however the possibility to use in PCCC has not been investigated. Furthering this Pr doping has not been explored in $La_3Ni_2O_{7-\delta}$ for use either in OC-SOCs or PCCCs.

$La_3Ni_2O_{7-\delta}$ doping saw a decrease in the unit cell volume due to the smaller ionic radius of Pr^{3+} compared to La^{3+}. A similar decrease was observed with Pr doping in $La_4Ni_3O_{10-\delta}$ along with an increase in the orthorhombic strain.

Heating the samples in humid N_2, dry N_2 and humid O_2 saw no changes in XRD pattern for $La_3Ni_2O_{7-\delta}$ and $La_2PrNi_2O_{7-\delta}$. Both samples, showed some H_2O, CO_2 and O_2 loss when TGA/MS was performed, after being heated in humid N_2. The other samples saw varying effects when heated in the various atmospheres, $La_{2.75}Pr_{0.25}Ni_2O_{7-\delta}$ showed distinct increased preferred orientation when heated in humid N_2 and humid O_2. $La_{2.5}Pr_{0.5}Ni_2O_{7-\delta}$ degraded in dry N_2 and showed increased preferred orientation in humid O_2.

VT-XRD was performed on $La_3Ni_2O_{7-\delta}$, $La_{2.5}Pr_{0.5}Ni_2O_{7-\delta}$ and $La_2PrNi_2O_{7-\delta}$. All samples showed a change in symmetry during heating. Increasing the content of Pr led to the change in symmetry occurring at a higher temperature. $La_3Ni_2O_{7-\delta}$ did not show any noticeable deviation in lattice parameter during heating that would indicate loss of H_2O, while $La_{2.5}Pr_{0.5}Ni_2O_{7-\delta}$ and $La_2PrNi_2O_{7-\delta}$ showed a clear decrease in the c parameter at 275°C and 325°C, when H_2O and CO_2 loss was expected to occur from the TGA data. 4-probe conductivity data showed that all samples had similar conductivities, with $La_{2.5}Pr_{0.2}Ni_2O_{7-\delta}$ having the highest value overall electrical conductivity.

When heating $La_4Ni_3O_{10-\delta}$ and its Pr doped samples in humid N_2, the results showed that $La_4Ni_3O_{10-\delta}$, $La_{3.75}Pr_{0.25}Ni_3O_{10-\delta}$ and $La_3PrNi_3O_{10-\delta}$ maintained their original XRD patterns. The samples showed some H_2O, CO_2 and O_2 loss according to TGA experiments. All samples heated in dry N_2 and humid O_2, saw no change in XRD patterns. VT-XRD of the humid samples all showed an increase in lattice parameters as expected. All showed a change in symmetry during heating and once again an increase in Pr content resulted in the change in symmetry occurring at a higher temperature. VT-XRD of the humid $La_4Ni_3O_{10-\delta}$ showed no noticeable changes that could indicate H_2O loss, while $La_{3.75}Pr_{0.25}Ni_3O_{10-\delta}$, saw a small change in the c lattice parameter at 225°C and 275°C. $La_{3.5}Pr_{0.5}Ni_3O_{10-\delta}$ saw some deviations from the typical linear trend between 225°C and 375°C, in both cases H_2O and CO_2 loss are expected. On the

way of electrical properties $La_{3.75}Pr_{0.5}Ni_3O_{10-\delta}$ showed the highest electrical conductivity of all the samples.

8.1.4 Chapter 7

Chapter 7 investigated producing a dense electrolyte pellet for cell testing. $BaCe_{0.9}Y_{0.1}O_{3-\delta}$, $BaZr_{0.8}Y_{0.2}O_{3-\delta}$ and $BaCe_{0.6}Zr_{0.3}Y_{0.1}O_{3-\delta}$ were explored as electrolytes materials. $BaCe_{0.9}Y_{0.1}O_{3-\delta}$ was shown not to be chemically stable in humid N_2, whilst $BaZr_{0.8}Y_{0.2}O_{3-\delta}$ and $BaCe_{0.6}Zr_{0.3}Y_{0.1}O_{3-\delta}$ were stable. Various sintering aids were employed to improve sintering of $BaZr_{0.8}Y_{0.2}O_{3-\delta}$ pellets, although the results suggested Ba evaporation remained a common issue. A $BaCe_{0.6}Zr_{0.3}Y_{0.1}O_{3-\delta}$ pellets were successfully sintered with 1 wt% nickel oxide (NiO), with 20% excess $BaCO_3$ to mitigate Ba evaporation (as well as covering the pellet with $BaCe_{0.6}Zr_{0.3}Y_{0.1}O_{3-\delta}$ powder). The $BaCe_{0.6}Zr_{0.3}Y_{0.1}O_{3-\delta}$ powder covering the pellet also had the added benefit of protecting the pellet from reacting with the alumina weight used to prevent pellet distortion on sintering. The pellet was also placed on a bed of $BaCe_{0.6}Zr_{0.3}Y_{0.1}O_{3-\delta}$ powder to prevent the pellet from reacting with the alumina plate used.

Symmetrical cell tests were performed using this electrolyte and a range of electrodes examined, including $La_2NiO_{4+\delta}$, $La_3Ni_2O_{7-\delta}$ and $La_4Ni_3O_{10-\delta}$, $La_{1.5}Sr_{0.5}NiO_{4+\delta}$ (as it had the highest electrical conductivity of the Sr doped samples), $La_2PrNi_2O_{7-\delta}$, $La_{3.75}Pr_{0.25}Ni_3O_{10-\delta}$ and $La_3PrNi_3O_{10-\delta}$ (as these samples showed no change in their XRD patterns when heated in humid N_2, dry N_2 and humid O_2).

Symmetrical cells with $La_2NiO_{4+\delta}$ and $La_{1.5}Sr_{0.5}NiO_{4+\delta}$ showed a decrease in polarisation resistance (R_{pol}) when electrochemical impedance spectroscopy was performed in humid air, up to 600°C. At 600°C and above the R_{pol} in dry air was less than the R_{pol} in humid air, suggesting p-type conductivity. Lower R_{pol} in dry air was seen for all temperature ranges for the other electrode materials tested, for all temperatures.

Various attempts at making full cells for testing were investigated, but a number of these were unsuccessful. The only cell manufacturing method that created a dense electrolyte layer with no cracks, was when the electrolyte was first sintered, the anode spin coated on top and then sintered. This then

allowed the cathode ink to be painted on and heated to bond to the electrolyte. $La_2NiO_{4+\delta}$ was chosen as the cathode as symmetrical cell testing as this material showed the conventional decrease in R_{pol} in humid air that is seen in PCCC.

Numerous attempts were made to improve the power density of the cell, including applying several anode layers to the cell, sintering the anode at 1300°C and reducing the anode in humid H_2. Finally, the cells that gave the best results were tested in electrolyser mode, followed by electrolyser testing of $La_3Ni_2O_{7-\delta}$ as the air electrode. While overall electrolyser performances were low, the results suggested $La_3Ni_2O_{7-\delta}$ was a better anode compared to $La_2NiO_{4+\delta}$, achieving a current density five times better.

8.2 Future Work

Based on the findings of this thesis, the following future work is suggested:

1. Exploration into why $La_2PrNi_2O_{7-\delta}$ appears to be chemically stable in humid N_2, dry N_2 and humid O_2, whilst lower levels of Pr would lead to samples giving enhanced preferred orientation or decomposing in various atmospheres.
2. Attempting to pellet press thinner pellets and sinter at higher temperatures in an attempt to improve the performance of the PCCC.
3. Testing of other synthesised Ruddlesden-Popper electrode materials as an anode in an electrolyser cell, in particular, $La_4Ni_3O_{10-\delta}$ and Pr doped $La_4Ni_3O_{10-\delta}$, to compare with the systems examined above.
4. Attempt at making a composite electrode with the Ruddlesden-Popper electrode material and $BaCe_{0.6}Zr_{0.3}Y_{0.1}O_{3-\delta}$ and performing PCCC tests.

Chapter 9: References

1. Foot E. Circumstances Affecting the Heat of the Sun's Rays The American Journal of Science and Arts. 1856;22:383-4.

2. Schneider SH. The Greenhouse Effect: Science and Policy. Science. 1989;243(4892):771-81.

3. CO_2 and Greenhouse Gas Emissions [Internet]. Our World in Data 2020 [cited 06/08/2023]. Available from: https://ourworldindata.org/co2-and-greenhouse-gas-emissions.

4. Trends in globally-averaged CO2 determined from NOAA Global Monitoring Laboratory measurements [Internet]. 2023 [cited 06/08/2023]. Available from: https://gml.noaa.gov/ccgg/trends/global.html?doi=10.15138/9n0h-zh07.

5. Kyoto Protocol to the United Nations Framework Convention on Climate Change. Kyoto, Japan: United Nations 1998.

6. The Paris Agreement United Nations 2016.

7. Climate Change Act 2008. London: The Stationery Office; 2008.

8. Dale S. Statistical Review of World Energy. London bp; 2022.

9. Data & Statistics, Total primary energy supply (TPES) by source, World 1990-2019 [Internet]. IEA. [cited 29/05/2023]. Available from: ttps://www.iea.org/data-and-statistics/data-tools/energy-statistics-data-browser?country=WORLD&fuel=Energy%20supply&indicator=TESbySource.

10. Dale S. Energy Outlook. London: bp; 2023 2023/07/01.

11. Waters L. Digest of United Kingdom Energy Statistics 2022. In: Department for Business EIS, editor. London: Crown; 2022.

12. Marbán G, Valdés-Solís T. Towards the hydrogen economy? International Journal of Hydrogen Energy. 2007;32(12):1625-37.

13. Gómez SY, Hotza D. Current developments in reversible solid oxide fuel cells. Renewable and Sustainable Energy Reviews. 2016;61:155-74.

14. Ozturk M, Dincer I. A comprehensive review on power-to-gas with hydrogen options for cleaner applications. International Journal of Hydrogen Energy. 2021;46(62):31511-22.

15. JP Hodges WG, S Graham, P Hooker, R Goff. Injecting hydrogen into the gas network – a literature search. Buxton: Health and Safety Executive (HSE); 2015 2015.

16. IEA. Global Hydrogen Review 2022. Paris; 2022.

17. Isaac T. HyDeploy: The UK's First Hydrogen Blending Deployment Project. Clean Energy. 2019;3(2):114-25.

18. IEA. Global Hydrogen Review 2021. Paris; 2021.

19. Larminie J, Dicks A. Fuel Cell Systems Explained (2nd Edition). John Wiley & Sons.

20. Sharaf OZ, Orhan MF. An overview of fuel cell technology: Fundamentals and applications. Renewable and Sustainable Energy Reviews. 2014;32:810-53.

21. Salameh Z. Chapter 4 - Energy Storage. In: Salameh Z, editor. Renewable Energy System Design. Boston: Academic Press; 2014. p. 201-98.

22. Spiegel C. Designing and Building Fuel Cells: McGraw Hill; 2007.

23. Rashid NLRM, Samat AA, Jais AA, Somalu MR, Muchtar A, Baharuddin NA, et al. Review on zirconate-cerate-based electrolytes for proton-conducting solid oxide fuel cell. Ceramics International. 2019;45(6):6605-15.

24. Lin Y, Ran R, Guo Y, Zhou W, Cai R, Wang J, et al. Proton-conducting fuel cells operating on hydrogen, ammonia and hydrazine at intermediate temperatures. International Journal of Hydrogen Energy. 2010;35(7):2637-42.

25. Nowicki KM, Carins G, Bayne J, Tupberg C, Irvine GJ, Irvine JTS. Characterisation of direct ammonia proton conducting tubular ceramic fuel cells for maritime applications. Journal of Materials Chemistry A. 2023;11(1):352-63.

26. Barbir F. Chapter Six - Stack Design. In: Barbir F, editor. PEM Fuel Cells (Second Edition). Boston: Academic Press; 2013. p. 159-215.

27. Staffell I, Scamman D, Velazquez Abad A, Balcombe P, Dodds PE, Ekins P, et al. The role of hydrogen and fuel cells in the global energy system. Energy & Environmental Science. 2019;12(2):463-91.

28. Wang Y, Ruiz Diaz DF, Chen KS, Wang Z, Adroher XC. Materials, technological status, and fundamentals of PEM fuel cells – A review. Materials Today. 2020;32:178-203.

29. Dawood F, Anda M, Shafiullah GM. Hydrogen production for energy: An overview. International Journal of Hydrogen Energy. 2020;45(7):3847-69.

30. Incer-Valverde J, Korayem A, Tsatsaronis G, Morosuk T. "Colors" of hydrogen: Definitions and carbon intensity. Energy Conversion and Management. 2023;291:117294.

31. Ajanovic A, Sayer M, Haas R. The economics and the environmental benignity of different colors of hydrogen. International Journal of Hydrogen Energy. 2022;47(57):24136-54.

32. Min G, Choi S, Hong J. A review of solid oxide steam-electrolysis cell systems: Thermodynamics and thermal integration. Applied Energy. 2022;328:120145.

33. Dincer I, Acar C. Review and evaluation of hydrogen production methods for better sustainability. International Journal of Hydrogen Energy. 2015;40(34):11094-111.

34. Abdullah B, Abd Ghani NA, Vo D-VN. Recent advances in dry reforming of methane over Ni-based catalysts. Journal of Cleaner Production. 2017;162:170-85.

35. Barelli L, Bidini G, Gallorini F, Servili S. Hydrogen production through sorption-enhanced steam methane reforming and membrane technology: A review. Energy. 2008;33(4):554-70.

36. Iulianelli A, Liguori S, Wilcox J, Basile A. Advances on methane steam reforming to produce hydrogen through membrane reactors technology: A review. Catalysis Reviews. 2016;58(1):1-35.

37. LeValley TL, Richard AR, Fan M. The progress in water gas shift and steam reforming hydrogen production technologies – A review. International Journal of Hydrogen Energy. 2014;39(30):16983-7000.

38. Holladay JD, Hu J, King DL, Wang Y. An overview of hydrogen production technologies. Catalysis Today. 2009;139(4):244-60.

39. Simpson AP, Lutz AE. Exergy analysis of hydrogen production via steam methane reforming. International Journal of Hydrogen Energy. 2007;32(18):4811-20.

40. Nikolaidis P, Poullikkas A. A comparative overview of hydrogen production processes. Renewable and Sustainable Energy Reviews. 2017;67:597-611.

41. Midilli A, Kucuk H, Topal ME, Akbulut U, Dincer I. A comprehensive review on hydrogen production from coal gasification: Challenges and Opportunities. International Journal of Hydrogen Energy. 2021;46(50):25385-412.

42. Ji M, Wang J. Review and comparison of various hydrogen production methods based on costs and life cycle impact assessment indicators. International Journal of Hydrogen Energy. 2021;46(78):38612-35.

43. Brauns J, Turek T. Alkaline Water Electrolysis Powered by Renewable Energy: A Review. Processes. 2020;8(2):248.

44. Shiva Kumar S, Lim H. An overview of water electrolysis technologies for green hydrogen production. Energy Reports. 2022;8:13793-813.

45. David M, Ocampo-Martínez C, Sánchez-Peña R. Advances in alkaline water electrolyzers: A review. Journal of Energy Storage. 2019;23:392-403.

46. Ju H, Badwal S, Giddey S. A comprehensive review of carbon and hydrocarbon assisted water electrolysis for hydrogen production. Applied Energy. 2018;231:502-33.

47. El-Shafie M, Kambara S, Hayakawa Y. Hydrogen Production Technologies Overview. Journal of Power and Energy Engineering. 2019;Vol.07No.01:48.

48. Bi L, Boulfrad S, Traversa E. Steam electrolysis by solid oxide electrolysis cells (SOECs) with proton-conducting oxides. Chemical Society Reviews. 2014;43(24):8255-70.

49. Hossain S, Abdalla AM, Jamain SNB, Zaini JH, Azad AK. A review on proton conducting electrolytes for clean energy and intermediate temperature-solid oxide fuel cells. Renewable and Sustainable Energy Reviews. 2017;79:750-64.

50. Buttler A, Spliethoff H. Current status of water electrolysis for energy storage, grid balancing and sector coupling via power-to-gas and power-to-liquids: A review. Renewable and Sustainable Energy Reviews. 2018;82:2440-54.

51. Carmo M, Fritz DL, Mergel J, Stolten D. A comprehensive review on PEM water electrolysis. International Journal of Hydrogen Energy. 2013;38(12):4901-34.

52. Marshall A, Børresen B, Hagen G, Tsypkin M, Tunold R. Hydrogen production by advanced proton exchange membrane (PEM) water electrolysers—Reduced energy consumption by improved electrocatalysis. Energy. 2007;32(4):431-6.

53. The Future of Hydrogen. Paris: IEA; 2019.

54. Hauch A, Ebbesen SD, Jensen SH, Mogensen M. Highly efficient high temperature electrolysis. Journal of Materials Chemistry. 2008;18(20):2331-40.

55. Arifin NA, Afifi AA, Samreen A, Hafriz RSRM, Muchtar A. Characteristic and challenges of scandia stabilized zirconia as solid oxide fuel cell material – In depth review. Solid State Ionics. 2023;399:116302.

56. Laguna-Bercero MA. Recent advances in high temperature electrolysis using solid oxide fuel cells: A review. Journal of Power Sources. 2012;203:4-16.

57. Biswas S, Kaur G, Paul G, Giddey S. A critical review on cathode materials for steam electrolysis in solid oxide electrolysis. International Journal of Hydrogen Energy. 2023;48(34):12541-70.

58. Iwahara H, Esaka T, Uchida H, Maeda N. Proton conduction in sintered oxides and its application to steam electrolysis for hydrogen production. Solid State Ionics. 1981;3-4:359-63.

59. Iwahara H. High temperature proton conducting oxides and their applications to solid electrolyte fuel cells and steam electrolyzer for hydrogen production. Solid State Ionics. 1988;28-30:573-8.

60. Iwahara H. Proton Conduction in Sintered Oxides Based on BaCeO3. Journal of The Electrochemical Society. 1988;135(2):529.

61. Norby T, Wideroe M, Glockner R, Larring Y. Hydrogen in oxides. Dalton transactions (Cambridge, England : 2003). 2004(19):3012-8.

62. Malavasi L, Fisher CA, Islam MS. Oxide-ion and proton conducting electrolyte materials for clean energy applications: structural and mechanistic features. Chem Soc Rev. 2010;39(11):4370-87.

63. Sawant P, Varma S, Wani BN, Bharadwaj SR. Synthesis, stability and conductivity of BaCe0.8−xZrxY0.2O3−δ as electrolyte for proton conducting SOFC. International Journal of Hydrogen Energy. 2012;37(4):3848-56.

64. Gu Y-J, Liu Z-G, Ouyang J-H, Yan F-Y, Zhou Y. Structure and electrical conductivity of BaCe0.85Ln0.15O3−δ (Ln=Gd, Y, Yb) ceramics. Electrochimica Acta. 2013;105:547-53.

65. Iguchi F, Nagao Y, Sata N, Yugami H. Proton concentration in 15mol% Y-doped BaZrO3 proton conductors prepared at various temperatures. Solid State Ionics. 2011;192(1):97-100.

66. Bohn HG, Schober T. Electrical Conductivity of the High-Temperature Proton Conductor BaZr0.9Y0.1O2.95. Journal of the American Ceramic Society. 2000;83(4):768-72.

67. Dahl PI, Lein HL, Yu Y, Tolchard J, Grande T, Einarsrud M-A, et al. Microstructural characterization and electrical properties of spray pyrolyzed conventionally sintered or hot-pressed BaZrO3 and BaZr0.9Y0.1O3−δ. Solid State Ionics. 2011;182(1):32-40.

68. Zakowsky N, Williamson S, Irvine JTS. Elaboration of CO2 tolerance limits of BaCe0.9Y0.1O3–δ electrolytes for fuel cells and other applications. Solid State Ionics. 2005;176(39):3019-26.

69. Xie K, Yan R, Liu X. The chemical stability and conductivity of BaCe0.9−xYxSn0.1O3−δ solid proton conductor for SOFC. Journal of Alloys and Compounds. 2009;479(1):L36-L9.

70. Duan C, Kee R, Zhu H, Sullivan N, Zhu L, Bian L, et al. Highly efficient reversible protonic ceramic electrochemical cells for power generation and fuel production. Nature Energy. 2019;4(3):230-40.

71. Carpanese MP, Barbucci A, Canu G, Viviani M. BaCe0.85Y0.15O2.925 dense layer by wet powder spraying as electrolyte for SOFC/SOEC applications. Solid State Ionics. 2015;269:80-5.

72. Qian J, Sun W, Zhang Q, Jiang G, Liu W. Fabrication and performance of BaCe0.8Y0.2O3−δ–BaZr0.8Y0.2O3−δ bilayer electrolyte for anode-supported solid oxide fuel cells. Journal of Power Sources. 2014;249:131-6.

73. Xie K, Yan R, Xu X, Liu X, Meng G. The chemical stability and conductivity of BaCe0.9−xYxNb0.1O3−σ proton-conductive electrolyte for SOFC. Materials Research Bulletin. 2009;44(7):1474-80.

74. Xie K, Yan R, Liu X. Stable BaCe0.7Ti0.1Y0.2O3−δ proton conductor for solid oxide fuel cells. Journal of Alloys and Compounds. 2009;479(1):L40-L2.

75. Wang S, Shen J, Zhu Z, Wang Z, Cao Y, Guan X, et al. Further optimization of barium cerate properties via co-doping strategy for potential application as proton-conducting solid oxide fuel cell electrolyte. Journal of Power Sources. 2018;387:24-32.

76. Zhang Z, Chen L, Li Q, Song T, Su J, Cai B, et al. High performance In, Ta and Y-doped BaCeO3 electrolyte membrane for proton-conducting solid oxide fuel cells. Solid State Ionics. 2018;323:25-31.

77. P. Shafi S, Bi L, Boulfrad S, Traversa E. Yttrium and Nickel Co-Doped BaZrO3 as a Proton-Conducting Electrolyte for Intermediate Temperature Solid Oxide Fuel Cells. ECS Transactions. 2015;68(1):503.

78. Cervera RB, Oyama Y, Miyoshi S, Oikawa I, Takamura H, Yamaguchi S. Nanograined Sc-doped BaZrO3 as a proton conducting solid electrolyte for intermediate temperature solid oxide fuel cells (IT-SOFCs). Solid State Ionics. 2014;264:1-6.

79. Kreuer KD. Proton-Conducting Oxides. Annual Review of Materials Research. 2003;33(1):333-59.

80. Sun W, Shi Z, Liu M, Bi L, Liu W. An Easily Sintered, Chemically Stable, Barium Zirconate-Based Proton Conductor for High-Performance Proton-Conducting Solid Oxide Fuel Cells. Advanced Functional Materials. 2014;24(36):5695-702.

81. Kuroha T, Yamauchi K, Mikami Y, Tsuji Y, Niina Y, Shudo M, et al. Effect of added Ni on defect structure and proton transport properties of indium-doped barium zirconate. International Journal of Hydrogen Energy. 2020;45(4):3123-31.

82. Sun W, Zhu Z, Shi Z, Liu W. Chemically stable and easily sintered high-temperature proton conductor BaZr0.8In0.2O3−δ for solid oxide fuel cells. Journal of Power Sources. 2013;229:95-101.

83. Sun W, Liu M, Liu W. Chemically Stable Yttrium and Tin Co-Doped Barium Zirconate Electrolyte for Next Generation High Performance Proton-Conducting Solid Oxide Fuel Cells. Advanced Energy Materials. 2013;3(8):1041-50.

84. Yilmaz S, Kavici B, Ramakrishnan P, Celen C, Amini Horri B. Highly Conductive Cerium- and Neodymium-Doped Barium Zirconate Perovskites for Protonic Ceramic Fuel Cells. Energies. 2023;16(11):4318.

85. Dai H. Proton conducting solid oxide fuel cells with chemically stable BaZr0.75Y0.2Pr0.05O3-δ electrolyte. Ceramics International. 2017;43(9):7362-5.

86. Yoo Y, Lim N. Performance and stability of proton conducting solid oxide fuel cells based on yttrium-doped barium cerate-zirconate thin-film electrolyte. Journal of Power Sources. 2013;229:48-57.

87. Barison S, Battagliarin M, Cavallin T, Doubova L, Fabrizio M, Mortalo C, et al. High conductivity and chemical stability of BaCe 1− x− y Zr x Y y O 3− δ proton conductors prepared by a sol–gel method. Journal of Materials Chemistry. 2008;18(42):5120-8.

88. Ricote S, Bonanos N, Manerbino A, Coors WG. Conductivity study of dense BaCexZr(0.9−x)Y0.1O(3−δ) prepared by solid state reactive sintering at 1500 °C. International Journal of Hydrogen Energy. 2012;37(9):7954-61.

89. Lagaeva J, Medvedev D, Demin A, Tsiakaras P. Insights on thermal and transport features of BaCe0.8−xZrxY0.2O3−δ proton-conducting materials. Journal of Power Sources. 2015;278:436-44.

90. Bae K, Kim DH, Choi HJ, Son J-W, Shim JH. High-Performance Protonic Ceramic Fuel Cells with 1 μm Thick Y:Ba(Ce, Zr)O3 Electrolytes. Advanced Energy Materials. 2018;8(25):1801315.

91. An H, Lee H-W, Kim B-K, Son J-W, Yoon KJ, Kim H, et al. A 5 × 5 cm2 protonic ceramic fuel cell with a power density of 1.3 W cm–2 at 600 °C. Nature Energy. 2018;3(10):870-5.

92. Ling Y, Yu J, lin B, Zhang X, Zhao L, Liu X. A cobalt-free Sm0.5Sr0.5Fe0.8Cu0.2O3−δ–Ce0.8Sm0.2O2−δ composite cathode for proton-conducting solid oxide fuel cells. Journal of Power Sources. 2011;196(5):2631-4.

93. Wan Y, He B, Wang R, Ling Y, Zhao L. Effect of Co doping on sinterability and protonic conductivity of BaZr0.1Ce0.7Y0.1Yb0.1O3−δ for protonic ceramic fuel cells. Journal of Power Sources. 2017;347:14-20.

94. Ling Y, Chen H, Niu J, Wang F, Zhao L, Ou X, et al. Bismuth and indium co-doping strategy for developing stable and efficient barium zirconate-based proton conductors for high-performance H-SOFCs. Journal of the European Ceramic Society. 2016;36(14):3423-31.

95. Ruiz-Trejo E, Irvine JTS. Electrolysis of CO2 in a proton conducting membrane. Solid State Ionics. 2013;252:157-64.

96. Tseng C-J, Chang J-K, Lee K-R, Hung IM, Lin J-C, Jang S-C, et al. Potassium doping optimization in proton-conducting Ba1-xKxCe0.6Zr0.2Y0.2O3-δ oxides for fuel cell applications. Journal of Alloys and Compounds. 2017;696:251-6.

97. Xia Y, Jin Z, Wang H, Gong Z, Lv H, Peng R, et al. A novel cobalt-free cathode with triple-conduction for proton-conducting solid oxide fuel cells with unprecedented performance. Journal of Materials Chemistry A. 2019;7(27):16136-48.

98. Xu X, Bi L, Zhao XS. Highly-conductive proton-conducting electrolyte membranes with a low sintering temperature for solid oxide fuel cells. Journal of Membrane Science. 2018;558:17-25.

99. Yang L, Zuo C, Liu M. High-performance anode-supported Solid Oxide Fuel Cells based on Ba(Zr0.1Ce0.7Y0.2)O3−δ (BZCY) fabricated by a modified co-pressing process. Journal of Power Sources. 2010;195(7):1845-8.

100. Wang N, Hinokuma S, Ina T, Zhu C, Habazaki H, Aoki Y. Mixed proton–electron–oxide ion triple conducting manganite as an efficient cobalt-free cathode for protonic ceramic fuel cells. Journal of Materials Chemistry A. 2020;8(21):11043-55.

101. Xiao J, Sun W, Zhu Z, Tao Z, Liu W. Fabrication and characterization of anode-supported dense BaZr0.8Y0.2O3−δ electrolyte membranes by a dip-coating process. Materials Letters. 2012;73:198-201.

102. Hou J, Qian J, Bi L, Gong Z, Peng R, Liu W. The effect of oxygen transfer mechanism on the cathode performance based on proton-conducting solid oxide fuel cells. Journal of Materials Chemistry A. 2015;3(5):2207-15.

103. Duan C, Tong J, Shang M, Nikodemski S, Sanders M, Ricote S, et al. Readily processed protonic ceramic fuel cells with high performance at low temperatures. Science. 2015;349(6254):1321-6.

104. Liu W, Kou H, Wang X, Bi L, Zhao XS. Improving the performance of the Ba0.5Sr0.5Co0.8Fe0.2O3-δ cathode for proton-conducting SOFCs by microwave sintering. Ceramics International. 2019;45(16):20994-8.

105. Nasani N, Ramasamy D, Mikhalev S, Kovalevsky AV, Fagg DP. Fabrication and electrochemical performance of a stable, anode supported thin BaCe0.4Zr0.4Y0.2O3-δ electrolyte Protonic Ceramic Fuel Cell. Journal of Power Sources. 2015;278:582-9.

106. Bae H, Choi J, Kim KJ, Park D, Choi GM. Low-temperature fabrication of protonic ceramic fuel cells with BaZr0.8Y0.2O3−δ electrolytes coated by aerosol deposition method. International Journal of Hydrogen Energy. 2015;40(6):2775-84.

107. Sun W, Yan L, Shi Z, Zhu Z, Liu W. Fabrication and performance of a proton-conducting solid oxide fuel cell based on a thin BaZr0.8Y0.2O3−δ electrolyte membrane. Journal of Power Sources. 2010;195(15):4727-30.

108. Yamaura H, Ikuta T, Yahiro H, Okada G. Cathodic polarization of strontium-doped lanthanum ferrite in proton-conducting solid oxide fuel cell. Solid State Ionics. 2005;176(3):269-74.

109. Sozal MSI, Tang W, Das S, Li W, Durygin A, Drozd V, et al. Electrical, thermal, and H2O and CO2 poisoning behaviors of PrNi0.5Co0.5O3-δ electrode for intermediate temperature protonic ceramic electrochemical cells. International Journal of Hydrogen Energy. 2022;47(51):21817-27.

110. Uchida H, Tanaka S, Iwahara H. Polarization at Pt electrodes of a fuel cell with a high temperature-type proton conductive solid electrolyte. Journal of Applied Electrochemistry. 1985;15(1):93-7.

111. Meng X, Yang N, Song J, Tan X, Ma Z-F, Li K. Synthesis and characterization of terbium doped barium cerates as a proton conducting SOFC electrolyte. International Journal of Hydrogen Energy. 2011;36(20):13067-72.

112. Yang L, Zuo C, Wang S, Cheng Z, Liu M. A Novel Composite Cathode for Low-Temperature SOFCs Based on Oxide Proton Conductors. Advanced Materials. 2008;20(17):3280-3.

113. Liu M, Gao J, Liu X, Meng G. High performance of anode supported BaZr0.1Ce0.7Y0.2O3−δ(BZCY) electrolyte cell for IT-SOFC. International Journal of Hydrogen Energy. 2011;36(21):13741-5.

114. Dailly J, Taillades G, Ancelin M, Pers P, Marrony M. High performing BaCe0.8Zr0.1Y0.1O3-δ-Sm0.5Sr0.5CoO3-δ based protonic ceramic fuel cell. Journal of Power Sources. 2017;361:221-6.

115. Wang B, Bi L, Zhao XS. Exploring the role of NiO as a sintering aid in BaZr0.1Ce0.7Y0.2O3-δ electrolyte for proton-conducting solid oxide fuel cells. Journal of Power Sources. 2018;399:207-14.

116. Dai H, Da'as EH, Shafi SP, Wang H, Bi L. Tailoring cathode composite boosts the performance of proton-conducting SOFCs fabricated by a one-step co-firing method. Journal of the European Ceramic Society. 2018;38(7):2903-8.

117. Sun W, Yan L, Lin B, Zhang S, Liu W. High performance proton-conducting solid oxide fuel cells with a stable Sm0.5Sr0.5Co3−δ–Ce0.8Sm0.2O2−δ composite cathode. Journal of Power Sources. 2010;195(10):3155-8.

118. Fabbri E, Bi L, Rupp JLM, Pergolesi D, Traversa E. Electrode tailoring improves the intermediate temperature performance of solid oxide fuel cells based on a Y and Pr co-doped barium zirconate proton conducting electrolyte. RSC Advances. 2011;1(7):1183-6.

119. Pergolesi D, Fabbri E, Traversa E. Chemically stable anode-supported solid oxide fuel cells based on Y-doped barium zirconate thin films having improved performance. Electrochemistry Communications. 2010;12(7):977-80.

120. Li M, Ni M, Su F, Xia C. Proton conducting intermediate-temperature solid oxide fuel cells using new perovskite type cathodes. Journal of Power Sources. 2014;260:197-204.

121. Mao X, Yu T, Ma G. Performance of cobalt-free double-perovskite NdBaFe2−xMnxO5+δ cathode materials for proton-conducting IT-SOFC. Journal of Alloys and Compounds. 2015;637:286-90.

122. Bi L, Zhang S, Lin B, Fang S, Xia C, Liu W. Screen-printed BaCe0.8Sm0.2O3−δ thin membrane solid oxide fuel cells with surface modification by spray coating. Journal of Alloys and Compounds. 2009;473(1):48-52.

123. Yan L, Ding H, Zhu Z, Xue X. Investigation of cobalt-free perovskite Ba0.95La0.05FeO3−δ as a cathode for proton-conducting solid oxide fuel cells. Journal of Power Sources. 2011;196(22):9352-5.

124. Shang M, Tong J, O'Hayre R. A promising cathode for intermediate temperature protonic ceramic fuel cells: BaCo0.4Fe0.4Zr0.2O3−δ. RSC Advances. 2013;3(36):15769-75.

125. Zhao Z, Cui J, Zou M, Mu S, Huang H, Meng Y, et al. Novel twin-perovskite nanocomposite of Ba–Ce–Fe–Co–O as a promising triple conducting cathode material for protonic ceramic fuel cells. Journal of Power Sources. 2020;450:227609.

126. Tong J, Yang W, Zhu B, Cai R. Investigation of ideal zirconium-doped perovskite-type ceramic membrane materials for oxygen separation. Journal of Membrane Science. 2002;203(1):175-89.

127. Ding X, Gao X, Zhu W, Wang J, Jiang J. Electrode redox properties of Ba1−xLaxFeO3−δ as cobalt free cathode materials for intermediate-temperature SOFCs. International Journal of Hydrogen Energy. 2014;39(23):12092-100.

128. Wei Z, Li Z, Wang Z, Zhao Y, Wang J, Chai J. A free-cobalt barium ferrite cathode with improved resistance against CO2 and water vapor for protonic ceramic fuel cells. International Journal of Hydrogen Energy. 2022;47(27):13490-501.

129. Kim J, Choi S, Jun A, Jeong HY, Shin J, Kim G. Chemically Stable Perovskites as Cathode Materials for Solid Oxide Fuel Cells: La-Doped Ba0.5Sr0.5Co0.8Fe0.2O3−δ. ChemSusChem. 2014;7(6):1669-75.

130. Wu Y, Li K, Yang Y, Song W, Ma Z, Chen H, et al. Investigation of Fe-substituted in BaZr0.8Y0.2O3-δ proton conducting oxides as cathode materials for protonic ceramics fuel cells. Journal of Alloys and Compounds. 2020;814:152220.

131. Wei Z, Wang J, Yu X, Li Z, Zhao Y, Chai J. Study on Ce and Y co-doped BaFeO3-δ cubic perovskite as free-cobalt cathode for proton-conducting solid oxide fuel cells. International Journal of Hydrogen Energy. 2021;46(46):23868-78.

132. Choi S, Kucharczyk CJ, Liang Y, Zhang X, Takeuchi I, Ji H-I, et al. Exceptional power density and stability at intermediate temperatures in protonic ceramic fuel cells. Nature Energy. 2018;3(3):202-10.

133. Ma J, Tao Z, Kou H, Fronzi M, Bi L. Evaluating the effect of Pr-doping on the performance of strontium-doped lanthanum ferrite cathodes for protonic SOFCs. Ceramics International. 2020;46(3):4000-5.

134. Orera A, Slater PR. New Chemical Systems for Solid Oxide Fuel Cells. Chemistry of Materials. 2010;22(3):675-90.

135. Amow G, Davidson IJ, Skinner SJ. A comparative study of the Ruddlesden-Popper series, Lan+1NinO3n+1 (n=1, 2 and 3), for solid-oxide fuel-cell cathode applications. Solid State Ionics. 2006;177(13):1205-10.

136. Grimaud A, Mauvy F, Marc Bassat J, Fourcade S, Marrony M, Claude Grenier J. Hydration and transport properties of the Pr2−xSrxNiO4+δ compounds as H+-SOFC cathodes. Journal of Materials Chemistry. 2012;22(31):16017-25.

137. Dailly J, Marrony M, Taillades G, Taillades-Jacquin M, Grimaud A, Mauvy F, et al. Evaluation of proton conducting BCY10-based anode supported cells by co-pressing method: Up-scaling, performances and durability. Journal of Power Sources. 2014;255:302-7.

138. Dailly J, Marrony M. BCY-based proton conducting ceramic cell: 1000 h of long term testing in fuel cell application. Journal of Power Sources. 2013;240:323-7.

139. Hou J, Zhu Z, Qian J, Liu W. A new cobalt-free proton-blocking composite cathode La2NiO4+δ–LaNi0.6Fe0.4O3−δ for BaZr0.1Ce0.7Y0.2O3−δ-based solid oxide fuel cells. Journal of Power Sources. 2014;264:67-75.

140. Dailly J, Fourcade S, Largeteau A, Mauvy F, Grenier JC, Marrony M. Perovskite and A2MO4-type oxides as new cathode materials for protonic solid oxide fuel cells. Electrochimica Acta. 2010;55(20):5847-53.

141. Ma Y, Huang J, He B. Scalable fabrication process for new structure BaZr0.8Y0.2O3-δ-based protonic ceramic fuel cells. Ceramics International. 2021;47(10, Part A):14680-8.

142. Tong J, Clark D, Hoban M, O'Hayre R. Cost-effective solid-state reactive sintering method for high conductivity proton conducting yttrium-doped barium zirconium ceramics. Solid State Ionics. 2010;181(11):496-503.

143. Osman N, Talib IA, Hamid HA. Preparation and characterization of Yb-doped Ba(Ce,Zr)O3 nanopowders with high sinterability. Ionics. 2010;16(6):561-9.

144. Shao Z, Zhou W, Zhu Z. Advanced synthesis of materials for intermediate-temperature solid oxide fuel cells. Progress in Materials Science. 2012;57(4):804-74.

145. Duval SBC, Holtappels P, Vogt UF, Pomjakushina E, Conder K, Stimming U, et al. Electrical conductivity of the proton conductor BaZr0.9Y0.1O3−δ obtained by high temperature annealing. Solid State Ionics. 2007;178(25):1437-41.

146. Babilo P, Haile SM. Enhanced Sintering of Yttrium-Doped Barium Zirconate by Addition of ZnO. Journal of the American Ceramic Society. 2005;88(9):2362-8.

147. Tao S, Irvine JTS. Conductivity studies of dense yttrium-doped BaZrO3 sintered at 1325oC. Journal of Solid State Chemistry. 2007;180(12):3493-503.

148. Tong J, Clark D, Bernau L, Sanders M, O'Hayre R. Solid-state reactive sintering mechanism for large-grained yttrium-doped barium zirconate proton conducting ceramics. Journal of Materials Chemistry. 2010;20(30):6333-41.

149. Sun Z, Fabbri E, Bi L, Traversa E. Electrochemical Properties and Intermediate-Temperature Fuel Cell Performance of Dense Yttrium-Doped Barium Zirconate with Calcium Addition. Journal of the American Ceramic Society. 2012;95(2):627-35.

150. Sun Z, Fabbri E, Bi L, Traversa E. Lowering grain boundary resistance of BaZr0.8Y0.2O3−δ with LiNO3 sintering-aid improves proton conductivity for fuel cell operation. Physical Chemistry Chemical Physics. 2011;13(17):7692-700.

151. Choi SM, Lee J-H, Ji HI, Yoon KJ, Son J-W, Kim B-K, et al. Fabrication and characterization of Ba(Zr0.84Y0.15Cu0.01)O3−δ electrolyte-based protonic ceramic fuel cells. Ceramics International. 2013;39(8):9605-11.

152. Peng C, Melnik J, Luo J-L, Sanger AR, Chuang KT. BaZr0.8Y0.2O3−δ electrolyte with and without ZnO sintering aid: Preparation and characterization. Solid State Ionics. 2010;181(29):1372-7.

153. Peng C, Melnik J, Li J, Luo J, Sanger AR, Chuang KT. ZnO-doped BaZr0.85Y0.15O3−δ proton-conducting electrolytes: Characterization and fabrication of thin films. Journal of Power Sources. 2009;190(2):447-52.

154. Tao SW, Irvine JTS. A Stable, Easily Sintered Proton- Conducting Oxide Electrolyte for Moderate-Temperature Fuel Cells and Electrolyzers. Advanced Materials. 2006;18(12):1581-4.

155. Han D, Uemura S, Hiraiwa C, Majima M, Uda T. Detrimental Effect of Sintering Additives on Conducting Ceramics: Yttrium-Doped Barium Zirconate. ChemSusChem. 2018;11(23):4102-13.

156. Han D, Shinoda K, Tsukimoto S, Takeuchi H, Hiraiwa C, Majima M, et al. Origins of structural and electrochemical influence on Y-doped BaZrO3 heat-treated with NiO additive. Journal of Materials Chemistry A. 2014;2(31):12552-60.

157. Kim E, Yamazaki Y, Haile SM, Yoo HI. Effect of NiO sintering-aid on hydration kinetics and defect-chemical parameters of BaZr0.8Y0.2O3−Δ. Solid State Ionics. 2015;275:23-8.

158. Shimada H, Yamaguchi T, Sumi H, Yamaguchi Y, Nomura K, Fujishiro Y. Effect of Ni diffusion into BaZr0.1Ce0.7Y0.1Yb0.1O3−δ electrolyte during high temperature co-sintering in anode-supported solid oxide fuel cells. Ceramics International. 2018;44(3):3134-40.

159. Bi L, Fabbri E, Sun Z, Traversa E. Sinteractive anodic powders improve densification and electrochemical properties of BaZr0.8Y0.2O3−δ electrolyte films for anode-supported solid oxide fuel cells. Energy & Environmental Science. 2011;4(4):1352-7.

160. Luisetto I, Licoccia S, D'Epifanio A, Sanson A, Mercadelli E, Di Bartolomeo E. Electrochemical performance of spin coated dense BaZr0.80Y0.16Zn0.04O3-δ membranes. Journal of Power Sources. 2012;220:280-5.

161. Oghbaei M, Mirzaee O. Microwave versus conventional sintering: A review of fundamentals, advantages and applications. Journal of Alloys and Compounds. 2010;494(1):175-89.

162. Beyribey B, Bayne J, Persky J. The effect of dip-coating parameters on the thickness and uniformity of BCZYZ electrolyte layer on porous NiO-BCZYZ tubular supports. Ceramics International. 2022;48(5):6046-51.

163. Shimada H, Yamaguchi T, Sumi H, Yamaguchi Y, Nomura K, Mizutani Y, et al. A Key for Achieving Higher Open-Circuit Voltage in Protonic Ceramic Fuel Cells: Lowering Interfacial Electrode Polarization. ACS Applied Energy Materials. 2019;2(1):587-97.

164. Lei L, Tao Z, Wang X, Lemmon JP, Chen F. Intermediate-temperature solid oxide electrolysis cells with thin proton-conducting electrolyte and a robust air electrode. Journal of Materials Chemistry A. 2017;5(44):22945-51.

165. Ricote S, Bonanos N, Wang HJ, Boukamp BA. Conductivity study of dense BaZr0.9Y0.1O(3−δ) obtained by spark plasma sintering. Solid State Ionics. 2012;213:36-41.

166. Wallis J, Urban L, Grimmer C, Bodnar W, Zimmermann R, Ricote S, et al. Structural and electrical properties of BaZr0.7Ce0.2Y0.1O3−δ proton conducting ceramic fabricated by spark plasma sintering. Solid State Ionics. 2020;345:115118.

167. Wallis J, Ricote S, Weltmann KD, Burkel E, Kruth A. The influence of the sintering temperature on BaZr0·7Ce0·2Y0·1O3-δ proton conductors prepared by Spark Plasma Sintering. Ceramics International. 2021;47(11):15349-56.

168. Sari SN, Nieroda P, Pasierb P. The BaCeO3-based composite protonic conductors prepared by Spark Plasma Sintering (SPS) and free-sintering methods. International Journal of Hydrogen Energy. 2023;48(76):29748-58.

169. Leonard K, Okuyama Y, Takamura Y, Lee Y-S, Miyazaki K, Ivanova ME, et al. Efficient intermediate-temperature steam electrolysis with Y : SrZrO3–SrCeO3 and Y : BaZrO3–BaCeO3 proton conducting perovskites. Journal of Materials Chemistry A. 2018;6(39):19113-24.

170. Gan L, Ye L, Liu M, Tao S, Xie K. A scandium-doped manganate anode for a proton-conducting solid oxide steam electrolyzer. RSC Advances. 2016;6(1):641-7.

171. Li W, Guan B, Ma L, Hu S, Zhang N, Liu X. High performing triple-conductive Pr2NiO4+δ anode for proton-conducting steam solid oxide electrolysis cell. Journal of Materials Chemistry A. 2018;6(37):18057-66.

172. Bi L, Shafi SP, Traversa E. Y-doped BaZrO3 as a chemically stable electrolyte for proton-conducting solid oxide electrolysis cells (SOECs). Journal of Materials Chemistry A. 2015;3(11):5815-9.

173. He F, Song D, Peng R, Meng G, Yang S. Electrode performance and analysis of reversible solid oxide fuel cells with proton conducting electrolyte of BaCe0.5Zr0.3Y0.2O3−δ. Journal of Power Sources. 2010;195(11):3359-64.

174. Wu W, Ding D, He T. Development of High Performance Intermediate Temperature Proton-Conducting Solid Oxide Electrolysis Cells. ECS Transactions. 2017;80(9):167-73.

175. Gan Y, Zhang J, Li Y, Li S, Xie K, Irvine JTS. Composite Oxygen Electrode Based on LSCM for Steam Electrolysis in a Proton Conducting Solid Oxide Electrolyzer. Journal of The Electrochemical Society. 2012;159(11):F763.

176. Zhu H, Ricote S, Kee RJ. Faradaic efficiency in protonic-ceramic electrolysis cells. Journal of Physics: Energy. 2022;4(1):014002.

177. Irvine JTS, Sinclair DC, West AR. Electroceramics: Characterization by Impedance Spectroscopy. Advanced Materials. 1990;2(3):132-8.

178. Mingyi L, Bo Y, Jingming X, Jing C. Thermodynamic analysis of the efficiency of high-temperature steam electrolysis system for hydrogen production. Journal of Power Sources. 2008;177(2):493-9.

179. Nitsch J, Winter CJ. Hydrogen as an energy carrier : technologies, systems, economy / Carl-Jochen Winter, Joachim Nitsch, eds. Berlin: Springer-Verlag Berlin Heidelberg; 1988.

180. Xu X, Wang H, Fronzi M, Wang X, Bi L, Traversa E. Tailoring cations in a perovskite cathode for proton-conducting solid oxide fuel cells with high performance. Journal of Materials Chemistry A. 2019;7(36):20624-32.

181. Zhang Y, Knibbe R, Sunarso J, Zhong Y, Zhou W, Shao Z, et al. Recent Progress on Advanced Materials for Solid-Oxide Fuel Cells Operating Below 500 °C. Advanced Materials. 2017;29(48):1700132.

182. Wang M, Su C, Zhu Z, Wang H, Ge L. Composite cathodes for protonic ceramic fuel cells: Rationales and materials. Composites Part B: Engineering. 2022;238:109881.

183. Shan D, Gong Z, Wu Y, Miao L, Dong K, Liu W. A novel BaCe0.5Fe0.3Bi0.2O3–δ perovskite-type cathode for proton-conducting solid oxide fuel cells. Ceramics International. 2017;43(4):3660-3.

184. Dong F, Chen Y, Ran R, Chen D, Tadé MO, Liu S, et al. BaNb0.05Fe0.95O3−δ as a new oxygen reduction electrocatalyst for intermediate temperature solid oxide fuel cells. Journal of Materials Chemistry A. 2013;1(34):9781-91.

185. Mori S. Phase Transformation in Barium Orthoferrate, BaFeO3-x. Journal of the American Ceramic Society. 1966;49(11):600-5.

186. Gonzalez-Calbet J, Parras M, Vallet-Regi M, Grenier J. Nonstoichiometry in BaFeO3− y (0.35< y< 0.50). Journal of Solid State Chemistry. 1990;86(2):149-59.

187. Knöchel PL, Keenan PJ, Loho C, Reitz C, Witte R, Knight KS, et al. Synthesis, structural characterisation and proton conduction of two new hydrated phases of barium ferrite BaFeO2.5−x(OH)2x. Journal of Materials Chemistry A. 2016;4(9):3415-30.

188. He S, Le S, Guan L, Liu T, Sun K. Bismuth and niobium co-doped barium cobalt oxide as a promising cathode material for intermediate temperature solid oxide fuel cells. Journal of Power Sources. 2015;295:33-40.

189. Song X, Le S, Zhu X, Qin L, Luo Y, Li Y, et al. High performance BaFe1−xBixO3−δ as cobalt-free cathodes for intermediate temperature solid oxide fuel cells. International Journal of Hydrogen Energy. 2017;42(24):15808-17.

190. Wang S, Xu JC, Wu M, Song Z, Wang L, Zhang L, et al. Cobalt–free perovskite cathode BaFe0.9Nb0.1O3– for intermediate–temperature solid oxide fuel cell. Journal of Alloys and Compounds. 2021;872:159701.

191. Wang J, Saccoccio M, Chen D, Gao Y, Chen C, Ciucci F. The effect of A-site and B-site substitution on BaFeO3−δ: An investigation as a cathode material for intermediate-temperature solid oxide fuel cells. Journal of Power Sources. 2015;297:511-8.

192. Gao L, Zhu M, Xia T, Li Q, Li T, Zhao H. Ni-doped BaFeO3−δ perovskite oxide as highly active cathode electrocatalyst for intermediate-temperature solid oxide fuel cells. Electrochimica Acta. 2018;289:428-36.

193. Farid MA, Zhang H, Lin X, Yang A, Yang S, Li G, et al. Structural and magnetic properties of tetragonal perovskite BaFe1−xBixO3−δ. RSC Advances. 2015;5(17):12866-71.

194. Ray R, Himanshu AK, Mandal GK, Kumar U, Jha SN, Patra N, et al. Revised crystal structure and electronic properties of high dielectric Ba(Fe1/2Nb1/2)O3 ceramics. Journal of Applied Physics. 2021;130(21):214101.

195. Gao Y, Zhang M, Fu M, Hu W, Tong H, Tao Z. A comprehensive review of recent progresses in cathode materials for Proton-conducting SOFCs. Energy Reviews. 2023;2(3):100038.

196. Tao Z, Bi L, Yan L, Sun W, Zhu Z, Peng R, et al. A novel single phase cathode material for a proton-conducting SOFC. Electrochemistry Communications. 2009;11(3):688-90.

197. Shao Z, Xiong G, Cong Y, Yang W. Synthesis and oxygen permeation study of novel perovskite-type BaBixCo0.2Fe0.8−xO3−δ ceramic membranes. Journal of Membrane Science. 2000;164(1):167-76.

198. Chen R-Y, Zhou D-F, Zhu X-F, Wang N, Bai J-H, Guo C-Q, et al. A promising Nb-doped La0.5Sr0.5Co0.8Cu0.2O3–δ cathode materials for intermediate temperature solid oxide fuel cells. Journal of Alloys and Compounds. 2022;924:166526.

199. Qiu Y, Li H, Liu Y, Chi B, Pu J, Li J. Effects of niobium doping on the stability of SrCo0.2Fe0.8O3-δ cathodes for intermediate temperature solid oxide fuel cells. Journal of Alloys and Compounds. 2020;829:154503.

200. Norby T, Larring Y. Concentration and transport of protons in oxides. Current Opinion in Solid State and Materials Science. 1997;2(5):593-9.

201. Jiang S, Sunarso J, Zhou W, Shen J, Ran R, Shao Z. Cobalt-free SrNbxFe1−xO3−δ (x = 0.05, 0.1 and 0.2) perovskite cathodes for intermediate temperature solid oxide fuel cells. Journal of Power Sources. 2015;298:209-16.

202. Yao C, Zhang H, Liu X, Meng J, Meng J, Meng F. A niobium and tungsten co-doped SrFeO3-δ perovskite as cathode for intermediate temperature solid oxide fuel cells. Ceramics International. 2019.

203. Toby BH, Von Dreele RB. GSAS-II: the genesis of a modern open-source all purpose crystallography software package. Journal of Applied Crystallography. 2013;46(2):544-9.

204. Song R, Zhang X, Huan D, Li X, Shi N, Xia C, et al. A novel triple-conductive cathode with high efficiency and stability for protonic ceramic fuel cells. International Journal of Hydrogen Energy. 2023.

205. Hui Z, Michèle P. Preparation, chemical stability, and electrical properties of Ba(Ce1 − xBix)O3 (x = 0.0–0.5). Journal of Materials Chemistry. 2002;12(12):3787-91.

206. Jarvis A, Berry FJ, Marco JF, Sanchez-Arenillas M, Cibin G, Clemens O, et al. Synthesis and characterisation of Sr4Fe3-xCrxO10-δ: Stabilisation of n=3 Ruddlesden-Popper phases through Cr doping. Journal of Solid State Chemistry. 2020;287:121372.

207. Shen Y, Zhao H, Xu J, Zhang X, Zheng K, Świerczek K. Effect of ionic size of dopants on the lattice structure, electrical and electrochemical properties of La2−xMxNiO4+δ (M = Ba, Sr) cathode materials. International Journal of Hydrogen Energy. 2014;39(2):1023-9.

208. Lee Y, Kim H. Electrochemical performance of La2NiO4+δ cathode for intermediate-temperature solid oxide fuel cells. Ceramics International. 2015;41(4):5984-91.

209. Sharma RK, Burriel M, Dessemond L, Bassat J-M, Djurado E. Lan+1NinO3n+1 (n = 2 and 3) phases and composites for solid oxide fuel cell cathodes: Facile synthesis and electrochemical properties. Journal of Power Sources. 2016;325:337-45.

210. Yatoo MA, Du Z, Zhao H, Aguadero A, Skinner SJ. La2Pr2Ni3O10±δ Ruddlesden-Popper phase as potential intermediate temperature-solid oxide fuel cell cathodes. Solid State Ionics. 2018;320:148-51.

211. Yatoo MA, Aguadero A, Skinner SJ. LaPr3Ni3O9.76 as a candidate solid oxide fuel cell cathode: Role of microstructure and interface structure on electrochemical performance. APL Materials. 2019;7(1):013204.

212. Yatoo MA, Du Z, Yang Z, Zhao H, Skinner SJ. LaxPr4−xNi3O10−δ: Mixed A-Site Cation Higher-Order Ruddlesden-Popper Phase Materials as Intermediate-Temperature Solid Oxide Fuel Cell Cathodes. Crystals. 2020;10(6):428.

213. Takahashi S, Nishimoto S, Matsuda M, Miyake M. Electrode Properties of the Ruddlesden–Popper Series, Lan+1NinO3n+1 (n=1, 2, and 3), as Intermediate-Temperature Solid Oxide Fuel Cells. Journal of the American Ceramic Society. 2010;93(8):2329-33.

214. Tong X, Zhou F, Yang S, Zhong S, Wei M, Liu Y. Performance and stability of Ruddlesden-Popper La2NiO4+δ oxygen electrodes under solid oxide electrolysis cell operation conditions. Ceramics International. 2017;43(14):10927-33.

215. Amow G, Skinner SJ. Recent developments in Ruddlesden–Popper nickelate systems for solid oxide fuel cell cathodes. Journal of Solid State Electrochemistry. 2006;10(8):538-46.

216. Lou Z, Peng J, Dai N, Qiao J, Yan Y, Wang Z, et al. High performance La3Ni2O7 cathode prepared by a facile sol–gel method for intermediate temperature solid oxide fuel cells. Electrochemistry Communications. 2012;22:97-100.

217. Vibhu V, Rougier A, Nicollet C, Flura A, Fourcade S, Penin N, et al. Pr4Ni3O10+δ: A new promising oxygen electrode material for solid oxide fuel cells. Journal of Power Sources. 2016;317:184-93.

218. Song J, Ning D, Boukamp B, Bassat J-M, Bouwmeester HJM. Structure, electrical conductivity and oxygen transport properties of Ruddlesden–Popper phases Lnn+1NinO3n+1 (Ln = La, Pr and Nd; n = 1, 2 and 3). Journal of Materials Chemistry A. 2020;8(42):22206-21.

219. Zhang Z, Greenblatt M. Synthesis, Structure, and Properties of Ln4Ni3O10-δ (Ln = La, Pr, and Nd). Journal of Solid State Chemistry. 1995;117(2):236-46.

220. Harrison CM, Slater PR, Steinberger-Wilckens R. Lanthanum nickelates and their application in Solid Oxide Cells – The LaNi1-xFexO3 system and other ABO3-type nickelates. Solid State Ionics. 2021;373:115799.

221. Vashook VV, Yushkevich II, Kokhanovsky LV, Makhnach LV, Tolochko SP, Kononyuk IF, et al. Composition and conductivity of some nickelates. Solid State Ionics. 1999;119(1):23-30.

222. Akbari-Fakhrabadi A, Toledo EG, Canales JI, Meruane V, Chan SH, Gracia-Pinilla MA. Effect of Sr2+ and Ba2+ doping on structural stability and mechanical properties of La2NiO4+δ. Ceramics International. 2018;44(9):10551-7.

223. Zhong P, Toyoura K, Jiang L, Chen L, Ismail SA, Hatada N, et al. Protonic Conduction in La2NiO4+δ and La2-xAxNiO4+δ (A = Ca, Sr, Ba) Ruddlesden–Popper Type Oxides. Advanced Energy Materials. 2022;12(22):2200392.

224. Sadykov VA, Sadovskaya EM, Pikalova EY, Kolchugin AA, Filonova EA, Pikalov SM, et al. Transport features in layered nickelates: correlation between structure, oxygen diffusion, electrical and electrochemical properties. Ionics. 2018;24(4):1181-93.

225. Pikalova EY, Bogdanovich NM, Kolchugin AA, Osinkin DA, Bronin DI. Electrical and Electrochemical Properties of La2NiO4+δ-Based Cathodes in Contact with Ce0.8Sm0.2O2-δ Electrolyte. Procedia Engineering. 2014;98:105-10.

226. Vashook VV, Tolochko SP, Yushkevich II, Makhnach LV, Kononyuk IF, Altenburg H, et al. Oxygen nonstoichiometry and electrical conductivity of the solid solutions La2−xSrxNiOy (0≤x≤0.5). Solid State Ionics. 1998;110(3):245-53.

227. Mehta A, Heaney PJ. Structure of $La_2NiO_{4.18}$. Physical Review B. 1994;49(1):563-71.

228. Skinner SJ. Characterisation of La2NiO4+δ using in-situ high temperature neutron powder diffraction. Solid State Sciences. 2003;5(3):419-26.

229. Aguadero A, Escudero MJ, Pérez M, Alonso JA, Pomjakushin V, Daza L. Effect of Sr content on the crystal structure and electrical properties of the system La2−xSrxNiO4+δ (0 ≤ x ≤ 1). Dalton Transactions. 2006(36):4377-83.

230. McSloy AJ, Trussov I, Jarvis A, Cooke DJ, Slater PR, Panchmatia PM. Mechanism of Carbon Dioxide and Water Incorporation in Ba2TiO4: A Joint Computational and Experimental Study. The Journal of Physical Chemistry C. 2018;122(2):1061-9.

231. Park J-C, Kim D-K, Byeon S-H, Kim D. XANES study on Ruddlesden-Popper phase, Lan+1NinO3n+1 (n = 1, 2, and ∞). Journal of Synchrotron Radiation. 2001;8(2):704-6.

232. Kovalevsky AV, Kharton VV, Yaremchenko AA, Pivak YV, Naumovich EN, Frade JR. Stability and oxygen transport properties of Pr2NiO4+δ ceramics. Journal of the European Ceramic Society. 2007;27(13):4269-72.

233. Deus Carvalho M, Madalena A. Costa F, da Silva Pereira I, Wattiaux A, Marc Bassat J, Claude Grenier J, et al. New preparation method of Lan+1NinO3n+1–δ (n=2, 3). Journal of Materials Chemistry. 1997;7(10):2107-11.

234. Zhang Z, Greenblatt M, Goodenough JB. Synthesis, Structure, and Properties of the Layered Perovskite La3Ni2O7-δ. Journal of Solid State Chemistry. 1994;108(2):402-9.

235. Ling CD, Argyriou DN, Wu G, Neumeier JJ. Neutron Diffraction Study of La3Ni2O7: Structural Relationships Among n=1, 2, and 3 Phases Lan+1NinO3n+1. Journal of Solid State Chemistry. 2000;152(2):517-25.

236. Hancock CA, Porras-Vazquez JM, Keenan PJ, Slater PR. Oxyanions in perovskites: from superconductors to solid oxide fuel cells. Dalton Transactions. 2015;44(23):10559-69.

237. Bannikov DO, Cherepanov VA. Thermodynamic properties of complex oxides in the La–Ni–O system. Journal of Solid State Chemistry. 2006;179(8):2721-7.

238. Sharma RK, Burriel M, Djurado E. La4Ni3O10−δ as an efficient solid oxide fuel cell cathode: electrochemical properties versus microstructure. Journal of Materials Chemistry A. 2015;3(47):23833-43.

239. Yamaura K, Huang Q, Lynn JW, Erwin RW, Cava RJ. Synthesis, Crystal Structure, and Magnetic Order of the Layered Iron Oxycarbonate Sr4Fe2O6CO3. Journal of Solid State Chemistry. 2000;152(2):374-80.

240. Bassat JM, Allançon C, Odier P, Loup JP, Carvalho MD, Wattiaux A. Electronic properties of Pr4Ni3O10±δ. European Journal of Solid State and Inorganic Chemistry. 1998;35(2):173-88.

241. Tsai C-Y, Aguadero A, Skinner SJ. High electrical conductivity and crystal structure of the solid oxide cell electrode Pr4Ni3O10-δ. Journal of Solid State Chemistry. 2020;289:121533.

242. Qian J, Sun W, Shi Z, Tao Z, Liu W. Chemically stable BaZr0.7Pr0.1Y0.2O3-δ-BaCe0.8Y0.2O3-δ bilayer electrolyte for intermediate temperature solid oxide fuel cells. Electrochimica Acta. 2015;151:497-501.

243. Hossain S, Abdalla A, Radenahmad N, Zakaria AKM, H. Zaini J, Rahman S, et al. Highly dense and chemically stable proton conducting electrolyte sintered at 1200 °C2018. 894-907 p.

244. Ji H-I, Kim B-K, Son J-W, Yoon KJ, Lee J-H. Influence of sintering activators on electrical property of BaZr0.85Y0.15O3-δ proton-conducting electrolyte. Journal of Power Sources. 2021;507:230296.

245. Marder R, Chaim R, Chevallier G, Estournès C. Effect of 1wt% LiF additive on the densification of nanocrystalline Y2O3 ceramics by spark plasma sintering. Journal of the European Ceramic Society. 2011;31(6):1057-66.

246. Nikodemski S, Tong J, Duan C, o Hayre R. Ionic transport modification in proton conducting BaCe 0.6 Zr 0.3 Y 0.1 O U ´ with transition metal oxide dopants. Solid State Ionics. 2016;294:37-42.

247. Lv H, Jin Z, Peng R, Liu W, Gong Z. BaCoxFe0.7-xZr0.3O3-δ(0.2≤x≤0.5) as cathode materials for proton-based SOFCs. Ceramics International. 2019;45(18, Part A):23948-53.

248. Mercadelli E, Gondolini A, Montaleone D, Pinasco P, Sanson A. Innovative strategy for designing proton conducting ceramic tapes and multilayers for energy applications. Journal of the European Ceramic Society. 2021;41(1):488-96.

249. Kim D, Son SJ, Kim M, Park HJ, Joo JH. PrBaFe2O5+δ promising electrode for redox-stable symmetrical proton-conducting solid oxide fuel cells. Journal of the European Ceramic Society. 2021;41(12):5939-46.

250. Medvedev D, Lyagaeva J, Plaksin S, Demin A, Tsiakaras P. Sulfur and carbon tolerance of BaCeO3–BaZrO3 proton-conducting materials. Journal of Power Sources. 2015;273:716-23.

251. VahidMohammadi A, Cheng Z. Fundamentals of Synthesis, Sintering Issues, and Chemical Stability of BaZr0.1Ce0.7Y0.1Yb0.1O3-δ Proton Conducting Electrolyte for SOFCs. Journal of The Electrochemical Society. 2015;162(8):F803.

252. Mauvy F, Lalanne C, Fourcade S, Bassat JM, Grenier JC. Impedance spectroscopy study of Nd2NiO4+δ, LSM and platinum electrodes by micro-contact technique. Journal of the European Ceramic Society. 2007;27(13):3731-4.

253. Li W, Sozal MSI, Drozd V, Durygin A, Cheng Z. BaCo0.4Fe0.4Zr0.1Y0.1O3−σ Cathode Performance for Proton Conducting Solid Oxide Fuel Cells with BaZr0.8−xCexY0.1Yb0.1O3−δ Electrolytes. ECS Advances. 2023;2(4):044502.

254. Sun S, Cheng Z. Electrochemical Behaviors for Ag, LSCF and BSCF as Oxygen Electrodes for Proton Conducting IT-SOFC. Journal of The Electrochemical Society. 2017;164(10):F3104.

255. Hong T, Lu W, Ren K, Liu T. The two-fold diffusion process for proton uptake reaction in BCFZY e-/H+/O2- triple conductor measured by electrical conductivity relaxation. Ionics. 2020;26(10):5293-7.

256. Chen Y, Hong T, Wang P, Brinkman K, Tong J, Cheng J. Investigate the proton uptake process of proton/oxygen ion/hole triple conductor BaCo0.4Fe0.4Zr0.1Y0.1O3-δ by electrical conductivity relaxation. Journal of Power Sources. 2019;440:227122.

257. Taherparvar H, Kilner JA, Baker RT, Sahibzada M. Effect of humidification at anode and cathode in proton-conducting SOFCs. Solid State Ionics. 2003;162-163:297-303.

Chapter 10: Appendix

10.1 Chapter 4

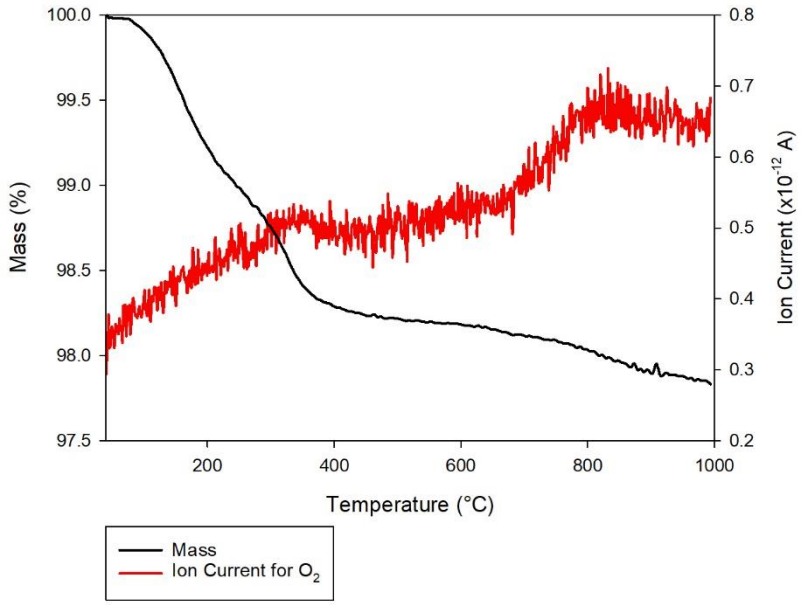


Figure 10.1: TGA and MS data for humidified $BaFe_{0.925}Bi_{0.075}O_{3-\delta}$ when heated to 1000°C showing mass loss (black) and O_2 loss (red).

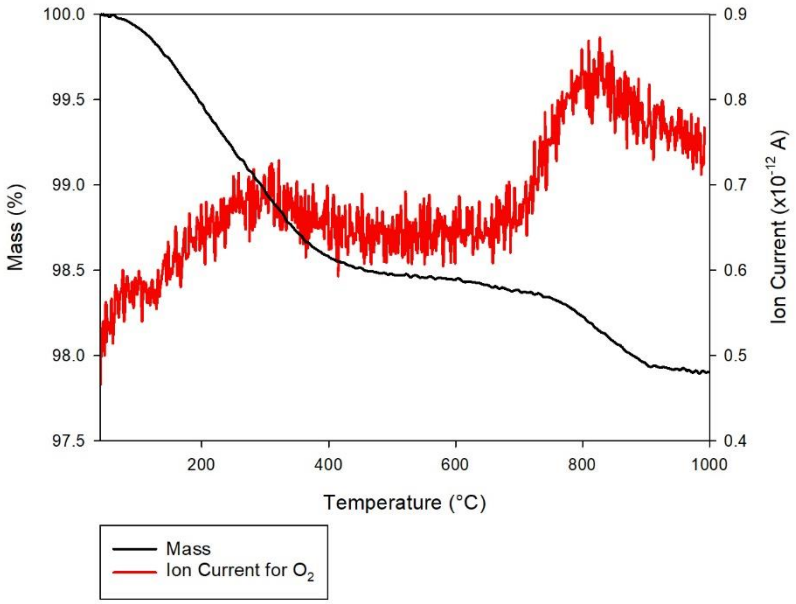


Figure 10.2: TGA and MS data for humidified $BaFe_{0.9}Bi_{0.1}O_{3-\delta}$ of sample when heated to 1000°C showing mass loss (black) and O_2 loss (red).

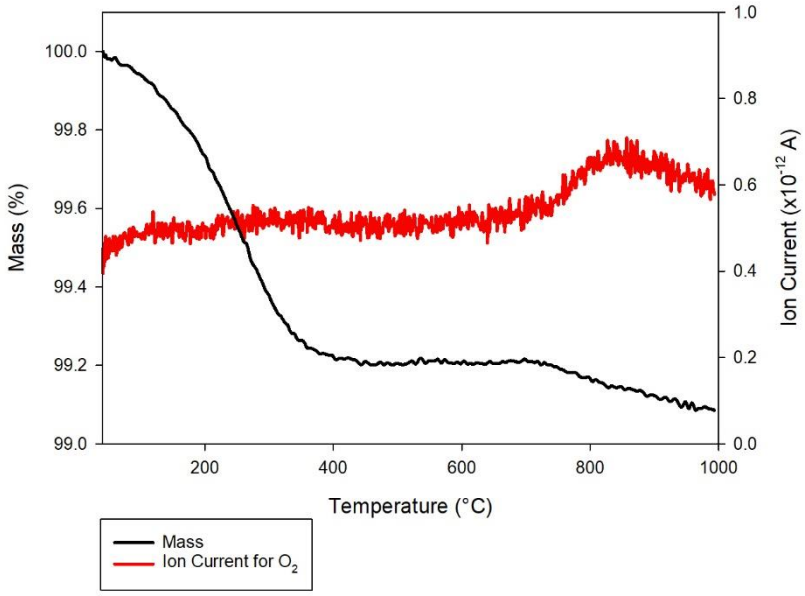


Figure 10.3: TGA and MS data for humidified $BaFe_{0.85}Bi_{0.15}O_{3-\delta}$ of sample when heated to 1000°C showing mass loss (black) and O_2 loss (red).

10.2 Chapter 5

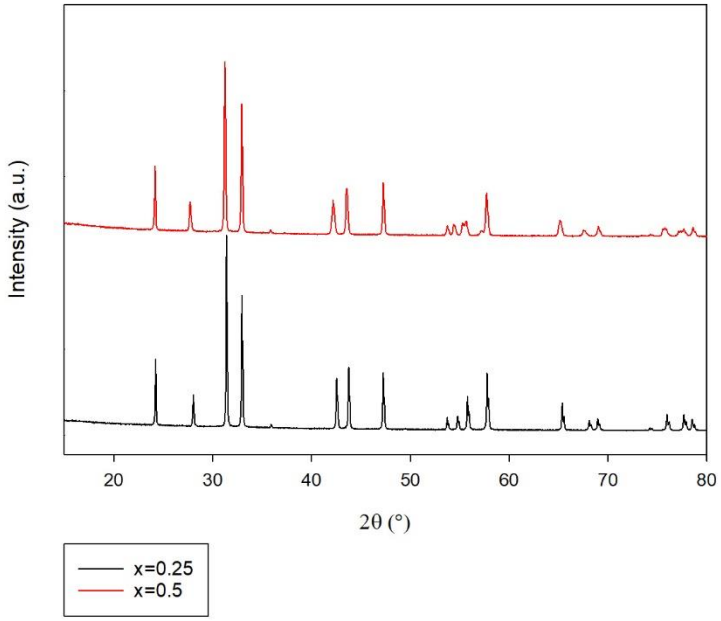


Figure 10.4: XRD pattern of $La_{2-x}Ba_xNiO_{4+\delta}$ where x=0.25 and 0.5, heated in dry N_2. In ascending order $La_{1.75}Ba_{0.25}NiO_{4+\delta}$, $La_{1.5}Ba_{0.5}NiO_{4+\delta}$.

10.3 Chapter 6

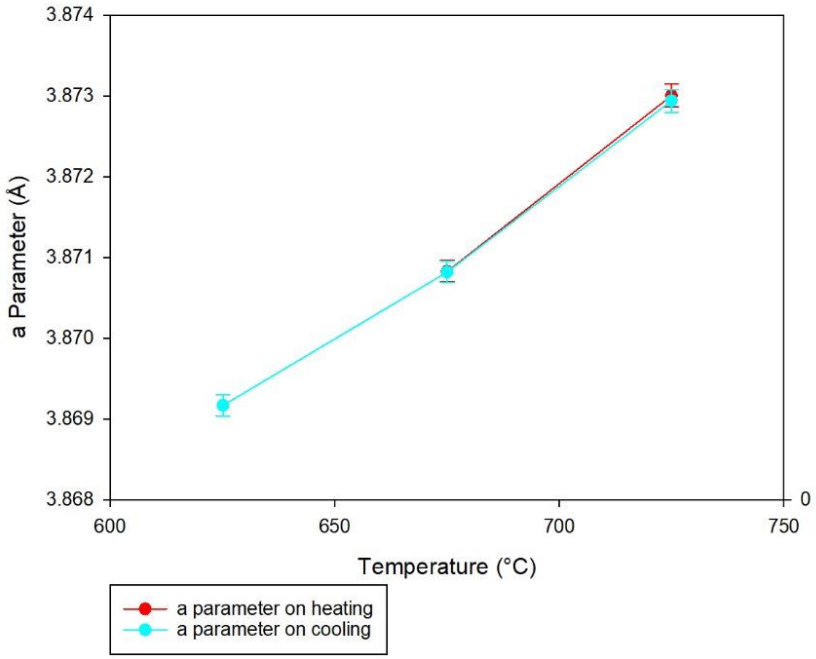


Figure 10.5: VT-XRD data showing the variation in a (circle) parameter of humidified $La_{2.5}Pr_{0.5}Ni_2O_{7-\delta}$ versus temperature, between 625°C and 725°C.

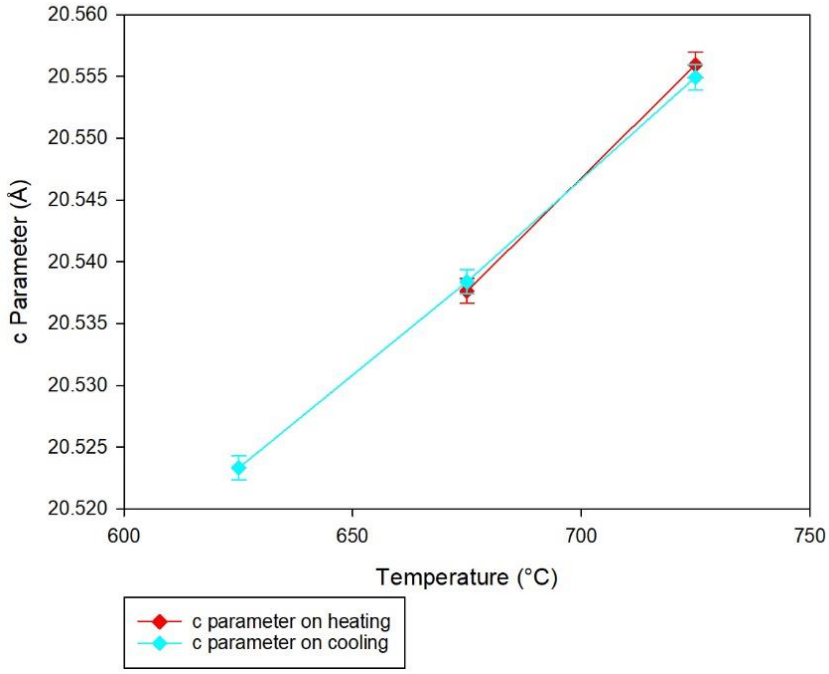


Figure 10.6: VT-XRD data showing the variantion in c parameter of humidified $La_{2.5}Pr_{0.5}Ni_2O_{7-\delta}$ against temperature, between 625°C and 725°C.

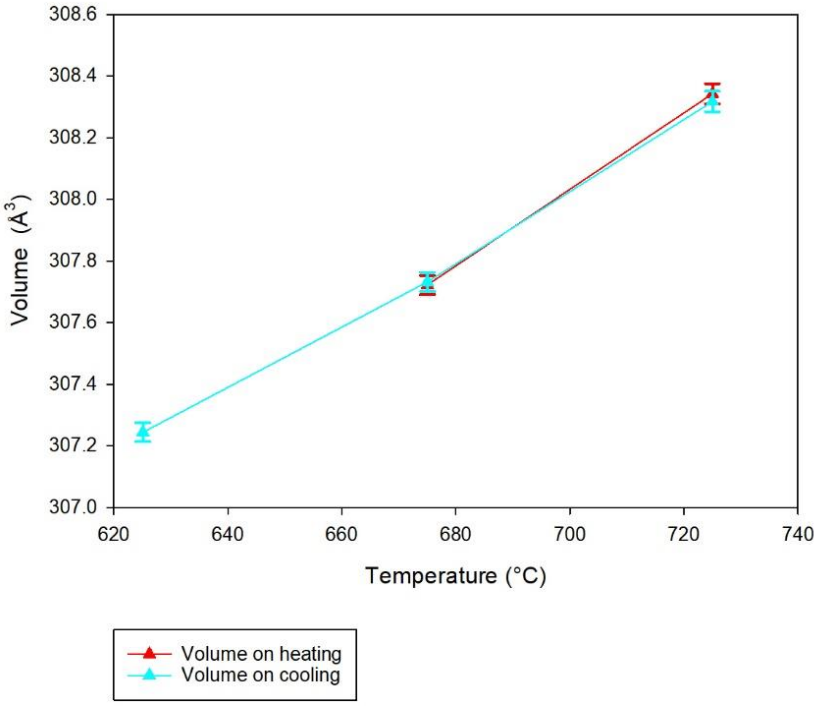


Figure 10.7: VT-XRD data showing the variation in volume of humidified $La_{2.5}Pr_{0.5}Ni_2O_{7-\delta}$ versus temperature, between 625°C and 725°C.

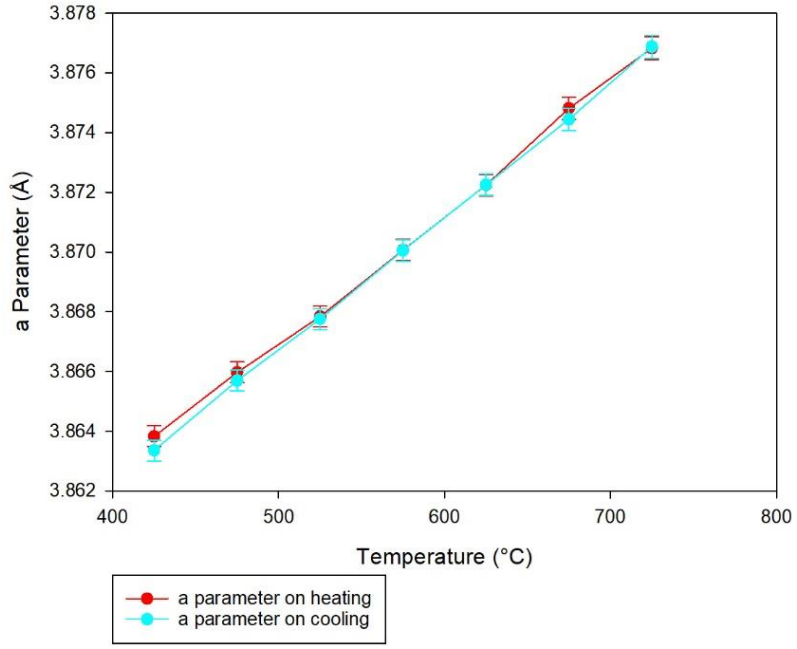


Figure 10.8: VT-XRD data showing the variation in a (circle) parameter of humidified $La_{3.75}Pr_{0.25}Ni_3O_{10-\delta}$ versus temperature, between 425°C and 725°C.

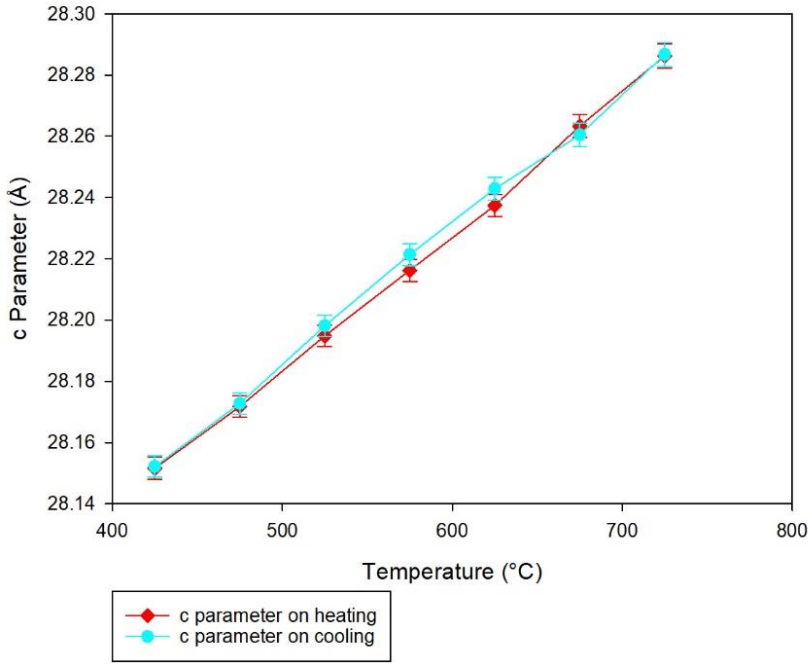


Figure 10.9: VT-XRD data showing the variantion in c parameter of humidified $La_{3.75}Pr_{0.25}Ni_3O_{10-\delta}$ against temperature, between 425°C and 725°C.

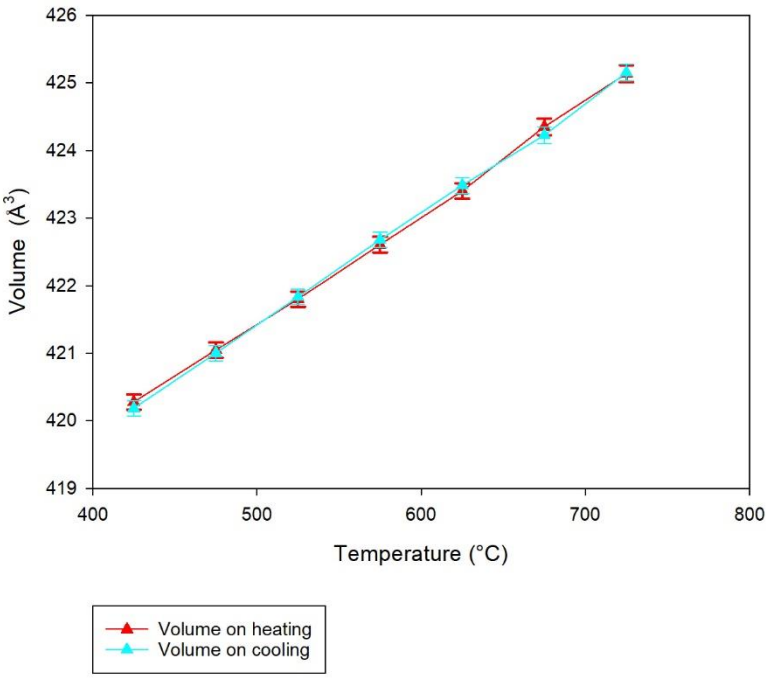


Figure 10.10: VT-XRD data showing the variation in volume of humidified $La_{3.75}Pr_{0.25}Ni_3O_{10-\delta}$ versus temperature, between 425°C and 725°C.

Table 10.1: Lattice parameters for $La_3PrNi_3O_{10-\delta}$ at 725°C, during heating and cooling.

Condition	a Parameter (Å)	c parameter (Å)	Volume (Å^3)
Heating	3.8753(3)	28.3022(36)	425.04(11)
Cooling	3.8750(3)	28.3006(36)	424.96(11)

10.4 Chapter 7

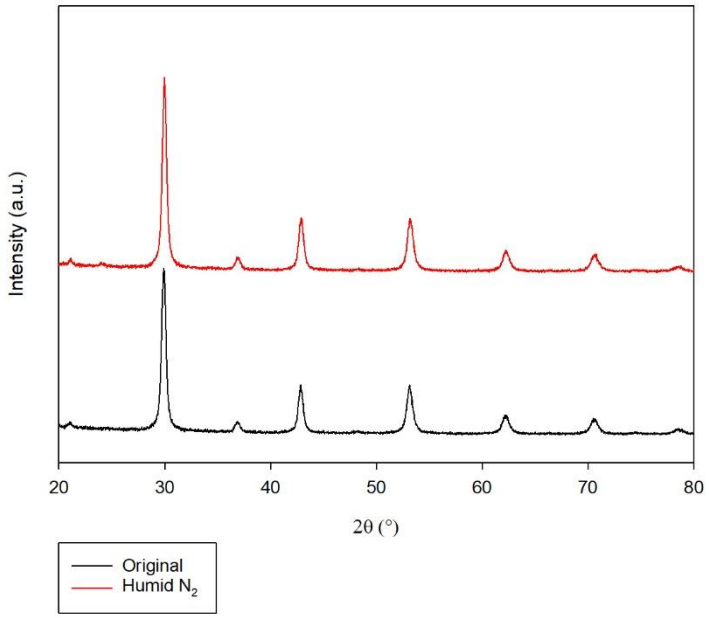


Figure 10.11: XRD pattern of $BaZr_{0.8}Y_{0.2}O_{3-\delta}$ original (black) and heated in humid N_2 (red).

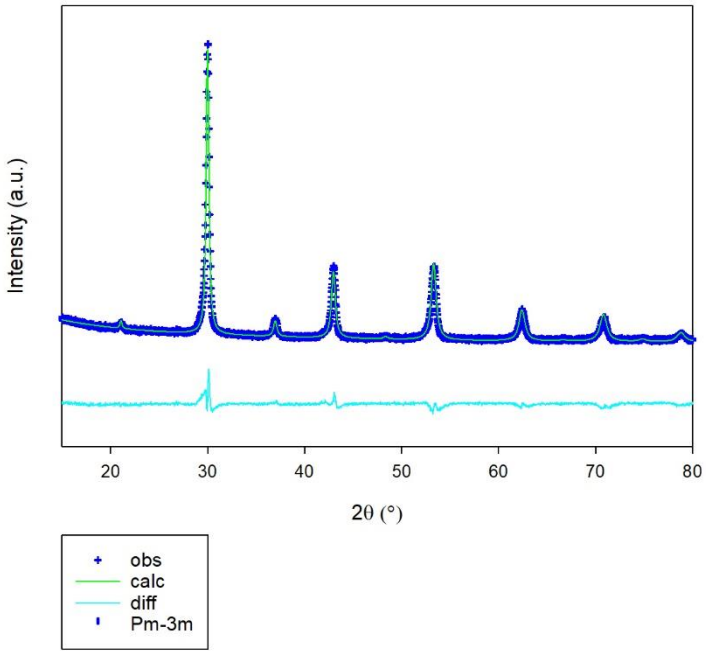


Figure 10.12: Example of observed (blue cross), calculated (green) and difference (cyan) profiles for Rietveld refinement performed on $BaZr_{0.8}Y_{0.2}O_{3-\delta}$ (cubic *Pm-3m* space group, R_w=5.72%).

Table 10.2: Lattice parameters (cubic *Pm-3m*) for Rietveld refinement performed on $BaZr_{0.8}Y_{0.2}O_{3-\delta}$.

Composition	**Unit Cell Parameters (Å)**	**Unit Cell Volume (Å^3)**	**Density (gcm^{-2})**
	a		
$BaZr_{0.8}Y_{0.2}O_{3-\delta}$	4.2054(2)	74.37(1)	5.977

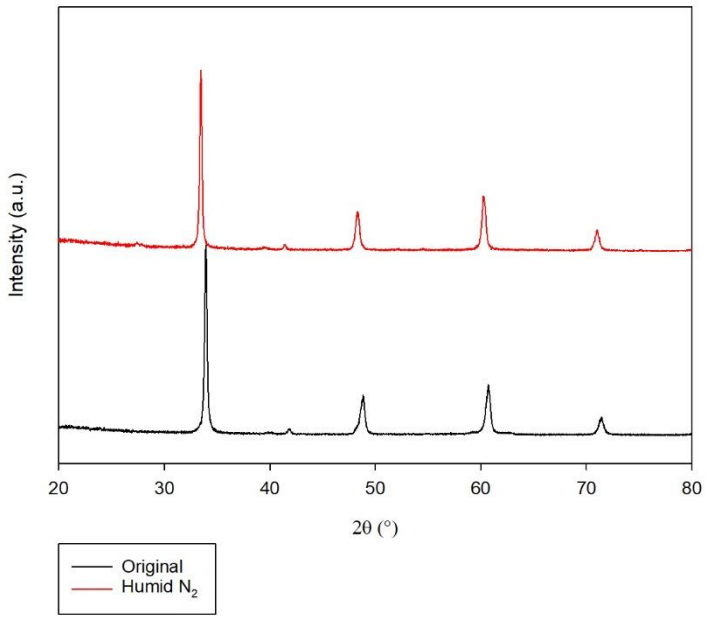


Figure 10.13: XRD pattern of $BaCe_{0.6}Zr_{0.3}Y_{0.1}O_{3-\delta}$ original (black) and heated in humid N_2 (red).

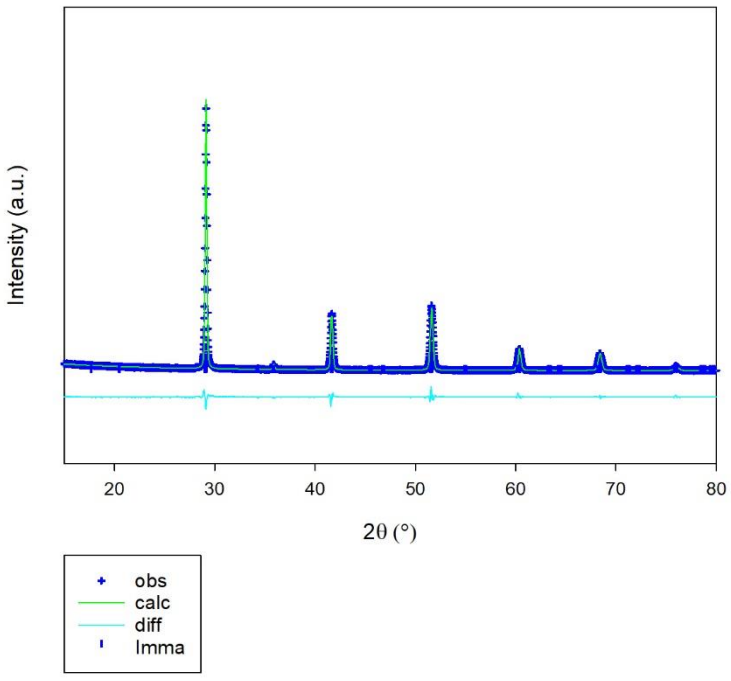


Figure 10.14: Example of observed (blue cross), calculated (green) and difference (cyan) profiles for Rietveld refinement performed on $BaCe_{0.6}Zr_{0.3}Y_{0.1}O_{3-\delta}$ (orthorhombic *Imma* space group, R_w=6.89%).

Table 10.3: Lattice parameters (orthorhombic *Imma*) for Rietveld refinement performed on $BaCe_{0.6}Zr_{0.3}Y_{0.1}O_{3-\delta}$.

Composition	**Unit Cell Parameters (Å)**			**Unit Cell Volume ($Å^3$)**	**Density (gcm^{-2})**
	a	b	c		
$BaCe_{0.6}Zr_{0.3}Y_{0.1}O_{3-\delta}$	6.1235(2)	8.6576(2)	6.1520(1)	326.15(1)	6.22